Array-Based Measurements of Surface Wave Dispersion and Attenuation Using Frequency-Wavenumber Analysis

A Thesis
Presented to
The Academic Faculty

by

Sungsoo Yoon

In Partial Fulfillment
of the Requirements for the Degree
Doctor of Philosophy in the
School of Civil and Environmental Engineering

Georgia Institute of Technology
August 2005

Array-Based Measurements of Surface Wave Dispersion and Attenuation Using Frequency-Wavenumber Analysis

Approved by:

Dr. Glenn J. Rix, Advisor
School of Civil and Environmental Engineering
Georgia Institute of Technology

Dr. Paul W. Mayne
School of Civil and Environmental Engineering
Georgia Institute of Technology

Dr. J. Carlos Santamarina
School of Civil and Environmental Engineering
Georgia Institute of Technology

Dr. L. Timothy Long
School of Earth and Atmospheric Sciences
Georgia Institute of Technology

Dr. Laurence J. Jacobs
School of Civil and Environmental Engineering
Georgia Institute of Technology

Date Approved: July 5, 2005

DEDICATION

To my wife, daughter, and family

ACKNOWLEDGMENTS

I would like to express my sincere gratitude to my advisor, Dr. Glenn J. Rix for his guidance and support during my doctoral studies. I have benefited tremendously from his experience and clear thought in engineering research. He has provided for me not only his knowledge but also his deep and kind consideration.

I would like to thank the other members of my committee, Dr. J. Carlos Santamarina, Dr. Paul W. Mayne, Dr. Laurence J. Jacobs, and Dr. L. Timothy Long for their valuable comments and suggestions. I would also like to extend my gratitude to the other members of the Geosystems faculty, Dr. J. David Frost, Dr. Leonid Germanovich, and Dr. Alexander M. Puzrin for their contributions to my education.

I would also like to thank:

- Greg Hebeler for unselfishly passing to me much of his knowledge of surface wave methods;

- Dr. Jong-Sub Lee, Dr. Young-Jong Sim, Jong-Won Choi, Jose Alvarellos, Dr. Jiewu Meng and Dr. Vitantonio Roma for helpful discussions and friendships;

- John Rhodes for his assistance in collecting much of the experimental data in this dissertation;

- Ms. Carol Maddox for her help and friendship;

- Matt Evans, Alfredo Fernadez, Andrew Fuggle, DuHwan Kim, Hyunki Kim, Jong Hee Kim, Sihyun Kim, Jenniffer Knapp, Brian Lawrence, Joo-Yong Lee, Alec McGillivray, Hosung Shin, Angel Palomino, Tae Sup Yun and Guillermo Zavala for their friendships.

I am deeply indebted to my parents, parents-in-law, and family for their patience, understanding and encouragement.

Finally and above all, I would like to thank my wife, Soojin and daughter, Heewon for their love, support, encouragement and smile during this difficult time. They have made this possible.

Atlanta

July 18, 2005

TABLE OF CONTENTS

DEDICATION iii

ACKNOWEDGMENTS iv

LIST OF TABLES x

LIST OF FIGURES xii

SUMMARY xix

I INTRODUCTION 1

1.1 MOTIVATION 1

1.2 RESEARCH OBJECTIVES 2

1.3 DISSERTATION OUTLINE 4

II RAYLEIGH WAVES IN VERTICALLY HETEROGENEOUS MEDIA 6

2.1 INTRODUCTION 6

2.2 CHARACTERISTICS OF BODY AND SURFACE WAVES 7

2.3 RAYLEIGH WAVES IN A HOMOGENEOUS HALF-SPACE 10

2.3.1 Rayleigh Wave Equation 10
2.3.2 Displacements Due to Rayleigh Waves 16

2.4 RAYLEIGH WAVES IN LAYERED MEDIA 17

2.4.1 Rayleigh Dispersion Equation 17
2.4.2 Techniques to Solve the Rayleigh Dispersion Equation 22
2.4.3 Green's Function for Plane Rayleigh Waves 23
2.4.4 Green's Function for Full Wavefield (PUNCH) 26

III OVERVIEW OF SURFACE WAVE METHODS 31

3.1 SPECTRAL ANALYSIS OF SURFACE WAVE (SASW) METHOD 31

3.2 ARRAY-BASED SURFACE WAVE METHOD 31

3.2.1 Field Measurements 32
3.2.2 Dispersion Calculations 42
3.2.3 Inversion 50

3.3 SPATIAL SAMPLING ISSUES 54

3.3.1 Array Characteristics 54
3.3.2 Effects of Finite Sampling in Space 55
3.3.3 Examples of Array Effects 64

IV NEAR-FIELD EFFECTS ON ARRAY-BASED SURAFE WAVE METHOD 67

4.1 INTRODUCTION AND STATEMENT OF THE PROBLEM 67

4.2 NUMERICAL SIMULATIONS 71

4.2.1 Typical Soil Profiles 71
4.2.2 Two Normalized Parameters to Evaluate Near-Field Effects 73
4.2.3 Array Center as an Indicator of Near-Field Effects 74
4.2.4 Influence of Medium Properties on Near-Field Effects 76
4.2.5 Array Configurations 78
4.2.6 Results of Numerical Simulations 80

4.3 LABORATORY SIMULATIONS 96

4.3.1 Waves in a Thin PMMA Plate 96
4.3.2 System and Source Identification 100
4.3.3 Laboratory Simulation Procedure to Investigate Near-Field Effects 112
4.3.4 Results of Laboratory Simulations 113

4.4 FIELD TESTS 116

4.4.1 Oakridge Landfill Site 116
4.4.2 Test Configuration 117
4.4.3 Passive Test Results as Reference 118
4.4.4 Results of Filed Tests 118

4.5 COMPARISON AND SYNTESIS OF NUMERICAL, LABORATORY, AND FIELD RESULTS 127

4.5.1 Comparison of Numerical, Laboratory, and Field Results 127
4.5.2 Summary of Errors Due to Near-Field Effects 131

4.6 SUMMARY AND CONCLUSIONS 132

V COMBINED ACTIVE-PASSIVE SURFACE WAVE MEASUREMENTS 135

5.1 INTRODUCTION AND STATEMENT OF THE PROBLEM 135

5.2 FIELD MEASUREMENTS 136

5.2.1 Williams Street Park Site 136
5.2.2 Active and Passive Measurements 137
5.2.3 Differences between Active and Passive Dispersion Curves 144

5.3 WAVENUMBER PRECISOIN 145

5.4 WAVENUMBER RESOLUTION AND SIDELOBE LEAKAGE 146

5.4.1 Wavenumber Resolution 147
5.4.2 Sidelobe Leakage 153
5.4.3 Threshold Ratios Associated with Errors in Passive Data 155
5.4.4 Two Waves with Different Amplitudes 158

5.5 RECOMMENDATIONS FOR IMPROVING PASSIVE MEASUREMENTS 159

5.5.1 Improvement of Array Characteristics 159
5.5.2 Refining Process to Remove Passive Data with Significant Errors 164
5.5.3 Validation of the Recommendations 169
5.5.4 Shear Wave Velocity Profiles from Composite Dispersion Curves 172

5.6 SUMMARY AND CONCLUSIONS 175

VI ATTENUATION MEASUREMENTS BY FREQUENCY-WAVENUMBER ANALYSIS 178

6.1 INTRODUCTION AND STATEMENT OF THE PROBLEM 178

6.2 MECHANISMS AND DEFINITIONS OF ATTENUATION 180

6.2.1 Mechanisms of Attenuation 180
6.2.2 Definitions of Material Attenuation 183
6.2.3 Attenuation of Rayleigh Waves in Homogeneous Media 186

6.3 MEASUREMENT OF SURFACE WAVE ATTENUATION 186

6.3.1 Rayleigh Wave Attenuation in Vertically Heterogeneous Media 186

6.3.2 Frequency-Wavenumber (f-k) Estimation Method 188

6.4 NUMERICAL SIMULATION RESULTS 190

6.4.1 Soil Profiles Used in Numerical Simulations 191
6.4.2 Validation of Two Attenuation Estimation Methods 192
6.4.3 Near-Field Effects 194
6.4.4 Effect of the Number of Receivers in Each Sub-Array 201
6.4.5 Noise Inclusion Effects 207
6.4.6 Improvement of the Methods by Increasing the Total Number of Receivers in an Array 209

6.5 FIELD EXPERIMENTAL RESULTS 212

6.5.1 Surface Wave Field Tests with Various Arrays 212
6.5.2 Measurements of Displacement Amplitudes 214
6.5.3 Validation of the Recommendation for Near-Field Effects 215
6.5.4 Validation of the Recommendation for Effect of the Number of Receivers in Each Sub-Array 218

6.6 SUMMARY AND CONCLUSIONS 219

VII SUMMARY, CONCLUSIONS AND RECOMMENDATIONS 221

7.1 SUMMARY AND CONCLUSIONS 221

7.2 RECOMMENDATIONS 224

REFERENCES 226

VITA 235

LIST OF TABLES

Table		Page
2.1	Relationships among elastic constants (modified from Achenbach, 1972)	11
2.2	Properties of a normally dispersive medium	26
2.3	Properties of an inversely dispersive medium	26
2.4	Properties of an elastic homogeneous medium used for validation of PUNCH	29
2.5	Properties of a viscoelastic homogeneous medium used for validation of PUNCH	29
3.1	Comparison of characteristics of three linear arrays with 15 receivers	60
4.1	Summary of filtering criteria for near-field effects on SASW tests	70
4.2	Medium properties of a soil profile (Case 1)	72
4.3	Medium properties of a soil profile (Case 2)	72
4.4	Medium properties of a soil profile (Case 3)	72
4.5	Medium properties of a soil profile (Case 4)	72
4.6	Soil profiles for investigating medium property effect on near-field effects	77
4.7	Array sets used for numerical simulation to investigate near-field effects	79
4.8	Wave velocities in PMMA	103
4.9	Array sets used for laboratory simulation to investigate near-field effects	112
4.10	Lower-bound normalized Rayleigh wave velocity based on numerical results	131
4.11	Lower-bound normalized Rayleigh wave velocity based on laboratory and field results	131
5.1	Classification of surface wave methods (after Tokimastu, 1995)	135
5.2	Important features associated with α_t^{1st} and α_t^{2nd}	156

5.3 Values of α_t^{1st} and α_t^{2nd} associated with various amplitude ratios between two waves 159

6.1 Properties of a soil profile (Case 1) 191

6.2 Properties of a soil profile (Case 2) 191

6.3 Properties of a soil profile (Case 3) 192

6.4 Properties of a soil profile (Case 4) 192

6.5 Array sets used to investigate near-field effects on attenuation estimates 196

LIST OF FIGURES

Figure		Page
2.1	Body waves ((a) and (b)) and surface waves ((c) and (d)) (Bolt, 1993)	9
2.2	Cartesian coordinate system	10
2.3	Coordinate system in a homogeneous half-space	13
2.4	Ratio of V_R to V_S with Poisson's ratio	15
2.5	Vertical and horizontal displacements of Rayleigh waves in homogeneous half-space media (after Richart et al., 1970)	17
2.6	Elastic layered media model	18
2.7	Vertical particle motion of two Rayleigh waves with different wavelengths (Rix, 2000)	20
2.8	Vertical displacement of Rayleigh waves at various offsets: (a) normally dispersive medium and (b) inversely dispersive medium	25
2.9	Comparison of solutions from Lamb (1904) and PUNCH for vertical displacement amplitudes and phases in elastic ((a) and (b)) and viscoelastic ((c) and (d)) homogeneous media for a frequency of 5 Hz	30
3.1	Vertically-oscillating harmonic point source acting on a homogeneous, isotropic, and elastic half-space: (a) complete wavefield generated by the source and (b) energy portion associated with different types of waves (Woods, 1968)	33
3.2	Examples of two different transient sources and their frequency contents: (a) dropped heavy weight, (b) sledge hammer, (c) frequency content for the dropped heavy weight, and (d) frequency content for the sledge hammer	34
3.3	Active harmonic source (electromechanical shaker)	36
3.4	Array and wave: (a) active tests, and (b) passive tests	38
3.5	Data acquisition system used for array-based surface wave measurements	39
3.6	Receiver used for array-based surface wave measurements	40

3.7 Source and data acquisition system for array-based surface wave measurements 42

3.8 Example of time history plots from a harmonic active test 45

3.9 Example of graphical representation of a spaciospectral correlation matrix 46

3.10 Example of a steered response power spectrum at a frequency of 10 Hz 47

3.11 Example of a frequency-wavenumber spectrum 48

3.12 Example of a dispersion curve from a harmonic active test 48

3.13 Example of a 2-D wavenumber spectrum at frequency of 5.9584 Hz 49

3.14 Example of a dispersion curve from a passive test 50

3.15 Flow chart of inversion algorithm (Rix, 2000) 51

3.16 Fourier transform of the spatial window w(x) 57

3.17 Geometries of three linear arrays with 15 receivers 59

3.18 Comparison of ASFs of three linear arrays with 15 receivers 60

3.19 Comparison of wavenumber spectra using the three different linear arrays 62

3.20 Array smoothing function of a 16-receiver circular array with a radius of 30 m 64

3.21 Array effects on array-based surface wave methods in (a) normally, and (b) inversely dispersive soil profiles 66

4.1 Shear wave velocity profiles of four typical soil profiles 73

4.2 Comparison of dispersion curves associated with various arrays in a homogeneous half-space 75

4.3 Near-field effects on array-based surface wave tests with the first array set in a homogeneous half-space captured by: (a) normalized AC and (b) normalized SR distance 76

4.4 Near-field effects on array-based surface wave tests with the second array set in a homogeneous half-space captured by: (a) normalized AC and (b) normalized SR distance 76

4.5 Influence of medium properties on near-field effects: (a) V_S effect, (b) Poisson's ratio effect, (c) damping ratio effect, and (d) mass density effect 78

4.6 Comparison of dispersion curves of full wavefield for the Case 1 soil profile 81

4.7 Comparison of dispersion curves of full wavefield for the Case 2 soil profile 82

4.8 Comparison of dispersion curves of full wavefield for the Case 3 soil profile 83

4.9 Comparison of dispersion curves of full wavefield for the Case 4 soil profile 84

4.10 Comparison of dispersion curves of plane Rayleigh Green's function for the Case 2 soil profile 85

4.11 Comparison of dispersion curves of plane Rayleigh Green's function for the Case 3 soil profile 86

4.12 Comparison of dispersion curves of plane Rayleigh Green's function for the Case 4 soil profile 87

4.13 Near-field effects on array-based active methods in homogeneous half-spaces (Case1) 89

4.14 Near-field effects on the array-based active methods in normally dispersive soil profiles (Case2) 90

4.15 Near-field effects on the array-based active methods in inversely dispersive soil profiles (Case 3) 91

4.16 Near-field effects on the array-based active methods in inversely dispersive soil profiles (Case 4) 92

4.17 Near-field effects on the array-based active methods in various soil profiles with emphasis on small normalized array centers: (a) homogeneous half-space (Case 1), (b) normally dispersive (Case 2), (c) inversely dispersive (Case 3), and (d) inversely dispersive (Case 4) 94

4.18 Coordinate system for a thin plate in an upright position 97

4.19 Viscoelastic properties of PMMA (modified from Kopplemann (1958), Ferry, 1980) 102

4.20 Frequency-wavenumber spectra of Lamb waves in a thin PMMA plate for (a) frequencies up to 20 kHz and (b) frequencies up to 5 kHz 104

4.21 Dispersion curves of Lamb waves in a thin PMMA plate for (a) frequencies up to 20 kHz and (b) frequencies up to 8 kHz 105

4.22 PMMA plate used for laboratory simulations 106

4.23 WR F7 piezoelectric vibrator 107

4.24 Equipment configuration for laboratory simulations 108

4.25 Test results of laboratory simulation with 15 receivers placed simultaneously: (a) f-k spectrum and (b) dispersion curve 109

4.26 Test results with the minimized receiver mass effect: (a) f-k spectrum and (b) dispersion curve 111

4.27 Comparison of dispersion curves from laboratory simulations with various arrays of (a) 10 receivers, (b) 15 receivers, and (c) 20 receivers 114

4.28 Near-field effects captured by normalized parameters with laboratory simulation results 115

4.29 Soil profile at Oakridge landfill site 117

4.30 Comparison of dispersion curves from the filed tests for (a) frequencies up to 100 Hz and (b) frequencies ranging 2 to 16 Hz 120

4.31 Frequency contents of energies generated by a transient source in tests with three arrays: (a) true magnitude and (b) normalized magnitude 121

4.32 Frequency-wavenumber spectra for active tests using a transient source: (a) standard array, (b) standard + 3 m array, and (c) standard + 9.1 m array 123

4.33 Comparison of dispersion curves of active tests using a transient source and a harmonic source: (a) standard array, (b) standard + 3 m array, and (c) standard + 9.1 m array 125

4.34 Near-field effects captured by normalized parameters with field test results 126

4.35 Comparison of near-field effect criteria in terms of normalized parameters from laboratory simulation results and numerical simulation results for Case 1 128

4.36 Shear wave velocity profiles at Oakridge landfill site 129

4.37 Comparison of near-field effect criteria in terms of normalized parameters from field test results and numerical simulation results for (a) Case 2 and (b) Case 4 130

5.1 Receivers used at the Williams Street Park site: (a) Kinemetrics SS-1 Ranger geophone and (b) Mark Products L4-C geophone 137

5.2 Active dispersion curve at Williams Street Park site 139

5.3 Frequency content of the passive energy at Williams Street Park site 140

5.4 Dispersion curves from nine passive tests performed using the circular arrays with radii of (a) 30 m, (b) 40 m, and (c) 50 m 141

5.5 Comparison of average dispersion curves from passive tests with three arrays and an active test over frequencies from (a) 0 to 70 Hz and (b) 1 to 11 Hz 143

5.6 Active and passive dispersion curves for Mud Island B site (Rix et al., 2002) 144

5.7 Two plane waves and a merged wave due to limited wavenumber resolution in 2-D wavenumber space 148

5.8 Ratio of V_{app} to V_{true} as a function of α 149

5.9 16-receiver circular array with a radius of 30 m: (a) geometry, (b) ASF in 2-D space, and (c) ASF in 3-D space 151

5.10 Example of unresolved waves by poor wavenumber resolution 153

5.11 Examples of spurious peaks due to sidelobe leakage for: (1) $\alpha = 43°$ and (2) $\alpha = 87°$ 154

5.12 Example of resolved waves by a given wavenumber resolution 155

5.13 Ratio V_{app}/V_{true} corresponding to limited wavenumber resolution effect as a function of true wavenumber for 16 receiver circular array with 30 m radius 158

5.14 Comparison of ASFs of three circular arrays with different radii of: (a) 30 m, (b) 40 m, and (c) 50 m. Contours are plotted for normalized magnitudes over 0.5 with 0.1 intervals. 161

5.15 Errors due to poor wavenumber resolution in terms of V_{app}/V_{true} and true wavenumber for 16-receiver circular arrays with various spatial extents 163

5.16 Refining process applied to dispersion data from three passive tests using a circular array with 30 m radius: (a) test 1, (b) test 2, and (c) test 3 166

5.17 Refining process applied to dispersion data from three passive tests using a circular array with 40 m radius: (a) test 1, (b) test 2, and (c) test 3 167

5.18 Refining process applied to dispersion data from three passive tests using a circular array with 50 m radius: (a) test 1, (b) test 2, and (c) test 3 168

5.19 Shear wave velocity profile at Williams Street Park site 170

5.20 Comparison of normalized Rayleigh wave velocities associated with field experimental results at Williams Street Park site and numerical results for (a) Case 2 (normally dispersive) and (b) Case 4 (inversely dispersive) 171

5.21 Comparison of experimental and theoretical dispersion curves at Williams Street Park site: (a) Composite 1, (b) Composite 2, and (c) Composite 3 173

5.22 Shear wave velocity profiles at Williams Street Park site from: (a) Composite 1, (b) Composite 2, and (c) Composite 3 174

5.23 Comparison of shear wave velocity profiles at Williams Street Park site 175

6.1 Example of experimental and theoretical attenuation curves (modified from Rix et al., 2000c) 179

6.2 Geometric spreading function for various medium conditions (Lai, 1998) 182

6.3 Comparison of normalized displacement amplitudes and equivalent normalized displacement amplitudes for two attenuation estimation methods at frequencies of (a) 10 Hz and (b) 70 Hz 194

6.4 Comparison of attenuation curves from two attenuation estimation methods and from low-loss material approximation 194

6.5 Comparison of attenuation curves corresponding to three different arrays of 15 receivers with various array centers 197

6.6 Transition frequencies (indicated with black arrows) in attenuation curves associated with three arrays for the Case 2 profile 198

6.7 Near-field effects on attenuation estimates with three 15-receiver arrays for three typical soil profiles 200

6.8 Effect of the number of receivers in each sub-array on equivalent normalized displacement amplitudes for normally dispersive (Case 2, (a) and (b)), inversely dispersive (Case 3, (c) and (d)), and another inversely dispersive (Case 4, (e) and (f)) soil profiles at frequencies of 10 and 70 Hz 203

6.9 Effect of the number of receivers in each sub-array on attenuation estimates for (a) normally dispersive (Case 2), (b) inversely dispersive (Case 3), and (c) another inversely dispersive (Case 4) soil profiles 205

6.10 Noise inclusion effects on attenuation estimates from two methods for (a) normally dispersive (Case 2), (b) inversely dispersive (Case 3), and (c) another inversely dispersive (Case 4) soil profiles 208

6.11 Comparison of attenuation curves corresponding to two arrays consisting of 15 and 30 receivers that are obtained by two estimation methods 211

6.12 Shear wave velocity profiles at Oakridge landfill site 213

6.13 Frequency-dependent normalized calibration factors of 15 receivers used in surface wave field tests 215

6.14 Comparison of attenuation curves obtained from f-k estimation method with three arrays before filtering and after filtering 217

6.15 Effect of the number of receivers in each sub-array in f-k estimation method 219

SUMMARY

Soil properties such as shear modulus and shear damping ratio are important parameters to understand the response of soils to dynamic loads. Surface wave methods have been used to determine dynamic properties of near-surface soils in geotechnical engineering for the past 50 years. Although the capabilities of engineering surface wave methods have improved in recent years due to several advances, including the use of multi-receiver arrays to measure dispersion and attenuation, several issues including (1) near-field effects, (2) combined active and passive measurements, and (3) accurate measurements of surface wave attenuation still require study to further improve the capabilities of modern surface wave methods.

Near-field effects have been studied for traditional surface wave methods with two receivers and several filtering criteria to mitigate the effects have been recommended. However, these filtering criteria are not applicable to surface wave methods with multiple receivers. Moreover, the criteria are not quantitatively based and do not account for different types of soil profiles, which strongly influence near-field effects. A new study of near-field effects on surface wave methods with multiple receivers was conducted with numerical and experimental methods. Two normalized parameters were developed to successfully capture near-field effects for arrays with 10 to 30 receivers. Quantitatively based near-field effect criteria for an ideal homogeneous half-space and three typical soil profiles are presented.

Combining active and passive surface wave measurements allows developing a shear wave velocity profile to greater depth without sacrificing the near-surface resolution

offered by active measurements. Generally, active and passive measurements overlap in the frequency range from approximately 4 to 10 Hz, and there are often systematic differences between the two measurements. The systematic errors in active and passive surface wave methods were explored to explain and resolve the differences, allowing for a more accurate composite dispersion curve.

The accuracy of measured surface wave attenuation is improved by properly accounting for (1) geometric spreading, (2) near-field effects, and (3) ambient noise. In this study, a traditional estimation method and a frequency-wavenumber method utilizing sub-arrays were investigated using displacement data from numerical simulations, focusing on near-field and ambient noise effects. Detailed procedures for the frequency-wavenumber estimation method are developed based on a study of the primary factors affecting attenuation estimates. The two methods are also evaluated using experimental displacement data obtained from surface wave field measurements with three different arrays.

CHAPTER 1

INTRODUCTION

1.1 MOTIVATION

Understanding the behavior of soils subjected to a specific loading condition is a primary goal in geotechnical engineering. The response of soils to dynamic loading is mainly determined by soil properties such as the shear modulus and material damping ratio. Surface wave methods have been used to determine small-strain dynamic properties (G_{max} and D_{Smin}) of near-surface soils in the geotechnical field for the past 50 years (Jones, 1958; Richart et al., 1970; Nazarian, 1984; Stokoe et al., 1994; Tokimatsu, 1995; Rix et al., 2001b; Okada, 2003). The non-invasive nature of surface wave tests allows one to perform tests efficiently, and is especially advantageous for tests on hazardous material such as landfill wastes (Lai, 1998). It is also important to note that the dynamic soil properties are representative of a large volume of the underlying soils, which may be more appropriate for seismic response analysis, compared to other in-situ methods that involve a smaller volume of a soil.

Surface wave tests are usually composed of three steps: field measurement, dispersion (or attenuation) estimation, and inversion. Surface wave methods have been greatly enhanced by recent developments in each step including the use of multi-receiver arrays, active and passive surface wave measurements, robust inversion algorithms, methods to handle multiple modes of Rayleigh wave propagation, Rayleigh wave attenuation and damping measurements, and simultaneous measurement and inversion of dispersion and attenuation curves (Rix et al., 2000). Array-based surface wave methods

have been developed and improved by a group of researchers at the Georgia Institute of Technology (Spang, 1995; Lai, 1998; Zywicki, 1999; Hebeler, 2001; Rix et al., 2002; Orozco, 2004). Despite recent developments, however, several issues remain uncertain or unresolved. These issues include how to properly account for near-field effects, successfully combine active and passive measurements, and successfully estimate attenuation properties of surface waves. The use of array-based surface wave methods without thoughtful consideration of these issues may result in errors in dispersion and attenuation calculations.

1.2 RESEARCH OBJECTIVES

The main focus of research in this study is on the improvement of capabilities of surface wave methods via a better understanding of these issues. Numerical simulations, laboratory simulations, and field tests were selectively used to study each issue. The successful application of the results of the study will consequently allow more accurate and reliable determination of dynamic soil properties. The results of the study will also yield more insight into wave propagation and soil behavior during surface wave testing.

The first objective of this research is to develop guidelines to reduce errors due to near-field effects on surface wave methods with multiple-receiver arrays. Near-field effects have been investigated for traditional surface wave methods with two receivers, and various filtering criteria have been recommended to mitigate the effects. However, the application of these filtering criteria to array-based surface wave methods is uncertain. Moreover, many of the criteria do not have a strong quantitative basis including the level of error involved. A new study about near-field effects on surface

wave methods with multiple-receiver arrays was developed and conducted using normalized parameters to properly capture the effects for arbitrary arrays consisting of 10 to 30 receivers. As a result of the new study, plots of the normalized parameters for an ideal homogeneous half-space and three typical soil profiles are presented as guidelines to quantify and reduce near-field effects for common types of soil profiles.

The second objective of this research is to develop a procedure to combine active and passive surface wave measurements. Surface wave methods can be classified as either active or passive according to the type of source. Combination of active and passive surface wave measurements allows developing a shear wave velocity profile to greater depth without sacrificing the near-surface resolution offered by active measurements (Hebeler, 2001; Rix et al., 2002). Generally, active and passive measurements overlap in the frequency range of approximately 4 to 10 Hz, and there are often systematic differences between the two measurements. Systematic errors in active and passive surface wave methods are explored as possible means to interpret and resolve these differences, leading to more accurate composite dispersion curves.

Finally, the third objective is to develop a robust procedure to correctly measure surface wave attenuation using array-based surface wave methods. Accurate measurements of displacement amplitudes are essential for surface wave attenuation measurements and are improved by properly accounting for three factors: (1) geometric spreading, (2) near-field effects, and (3) ambient noise. Several methods with various geometric spreading models and noise removal techniques have been used to calculate surface wave attenuation coefficients (Rix and Spang, 1995; Spang, 1995; Lai, 1998; Zywicki, 1999; Rix et al., 2000). Frequency-wavenumber (f-k) analysis using sub-arrays

was introduced by Zywicki (1999) for surface wave attenuation measurements. More detailed test and analysis procedures are needed to optimize the number of receivers in each sub-array to reduce near-field effects.

The first two objectives are related to improving dispersion estimates, while the final objective is related to improving attenuation estimates. The achievement of the first two objectives extends capabilities of surface wave methods for more accurate and deeper shear wave velocity profiling based on better understanding of near-field effects on active dispersion estimates and array effects on passive dispersion estimates. The achievement of the final objective extends capabilities of surface wave methods for more accurate shear wave damping ratio profiling based on better understanding of traditional and f-k estimation methods for estimating surface wave attenuation.

1.3 DISSERTATION OUTLINE

Chapter 2 describes the wave propagation theory regarding Rayleigh waves in vertically heterogeneous media that is used in surface wave methods.

Chapter 3 presents an overview of engineering surface wave methods. Following a brief description of traditional surface wave methods with two receivers, detailed procedures for array-based surface wave methods are presented, focusing on field measurements and dispersion calculations. The final section of this chapter is devoted to discussing spatial sampling issues that are essential in subsequent chapters.

Chapter 4 presents the results of the study of near-field effects on array-based surface wave methods. Two normalized parameters to capture near-field effects are proposed. Near-field effects on array-based surface wave methods are investigated for an ideal

homogeneous half-space and three typical soil conditions based on synthetic displacement data from numerical simulations, laboratory simulations, and field tests. These results are used to quantify near-field effects in array-based surface wave methods and develop guidelines to reduce them.

Chapter 5 presents a procedure to combine active and passive surface wave measurements based on the results of a study of the systematic differences between active and passive dispersion curves. Array effects on passive dispersion estimates are investigated using synthetic data from a simple plane wave model. A method to mitigate the array effects on passive estimates is proposed and verified using experimental data from in-situ active and passive tests with various arrays.

Chapter 6 reviews and investigates both traditional and f-k methods used for surface wave attenuation measurements. The f-k estimation method originally introduced by Zywicki (1999) is improved based on a better understanding of factors affecting surface wave attenuation measurements. The f-k estimation method is compared to a method suggested by Lai (1998) and Rix et al. (2000) to identify any advantage from the use of the f-k estimation method.

Finally, Chapter 7 provides the conclusions of this research and recommendations for future work.

CHAPTER 2

RAYLEIGH WAVES IN VERTICALLY HETEROGENEOUS MEDIA

2.1 INTRODUCT ION

Surface waves were first introduced by Lord Rayleigh as the solution of the equation of waves propagating along the free surface of an elastic half-space in 1885 (Rayleigh, 1885). In geotechnical engineering, surface waves have been used to determine the dynamic properties of near-surface soils non-invasively for the past 50 years (Jones, 1958; Richart et al., 1970; Nazarian, 1984; Stokoe et al., 1994; Tokimatsu, 1995; Rix et al., 2001b; Okada, 2003). Surface wave methods are based on measured vertical particle motions of Rayleigh waves at various locations on the ground surface. The measured motions depend on the properties of the medium, frequency of the waves, and distance from a source location. Surface wave methods require more complex data processing and interpretation than other in-situ seismic methods. Therefore, it is important to develop robust procedures for data processing and interpretation of surface wave measurements to characterize soils. Theoretical analyses of the characteristics of Rayleigh waves propagating through various types of media are an essential part of developing robust surface wave methods.

In this chapter, the theoretical study of Rayleigh wave propagation in homogeneous and layered media will be addressed. A layered medium consisting of a stack of homogeneous, isotropic, and elastic layers overlying a homogeneous half-space appears to be an appropriate model for vertically heterogeneous soil profiles. The layered model

is often used in inversion procedures of surface wave methods due to computational efficiency.

2.2 CHARACTERISTICS OF BODY AND SURFACE WAVES

Seismic waves propagating in a medium bounded by a free surface can be categorized into two types: body waves and surface waves. Body waves propagate through the interior of the medium and along the free surface and are of two types: P- and S-waves. P-waves propagate with a compressive disturbance while S-waves induce a shearing deformation. The particle motion associated with P-waves is parallel to the direction of propagation, while the particle motion associated with S-waves is perpendicular to the direction of wave propagation as shown in Figure 2.1 (a) and (b), respectively. According to the plane of the particle motion, S-waves can be subdivided into two types: vertically polarized shear (SV) and horizontally polarized shear (SH) waves.

Surface waves are produced by the interaction between P- and S-waves at the free surface. They travel along the surface of a medium with amplitude exponentially decreasing with depth. They can be divided into two types: Love waves and Rayleigh waves. Love waves are generated only when energy is trapped in a soft surface layer over a stiffer half-space resulting in multiple reflections. Since Love waves result from the interaction of P- and SH-waves, the particle motion has a horizontal component as shown in Figure 2.1 (c). Rayleigh waves, which are generated by the interaction of P- and SV-waves, have both vertical and horizontal particle motion as shown in Figure 2.1 (d).

Most surface wave methods used in geotechnical engineering are based on the velocity and attenuation of Rayleigh waves. In this dissertation, surface waves mean Rayleigh waves unless otherwise stated.

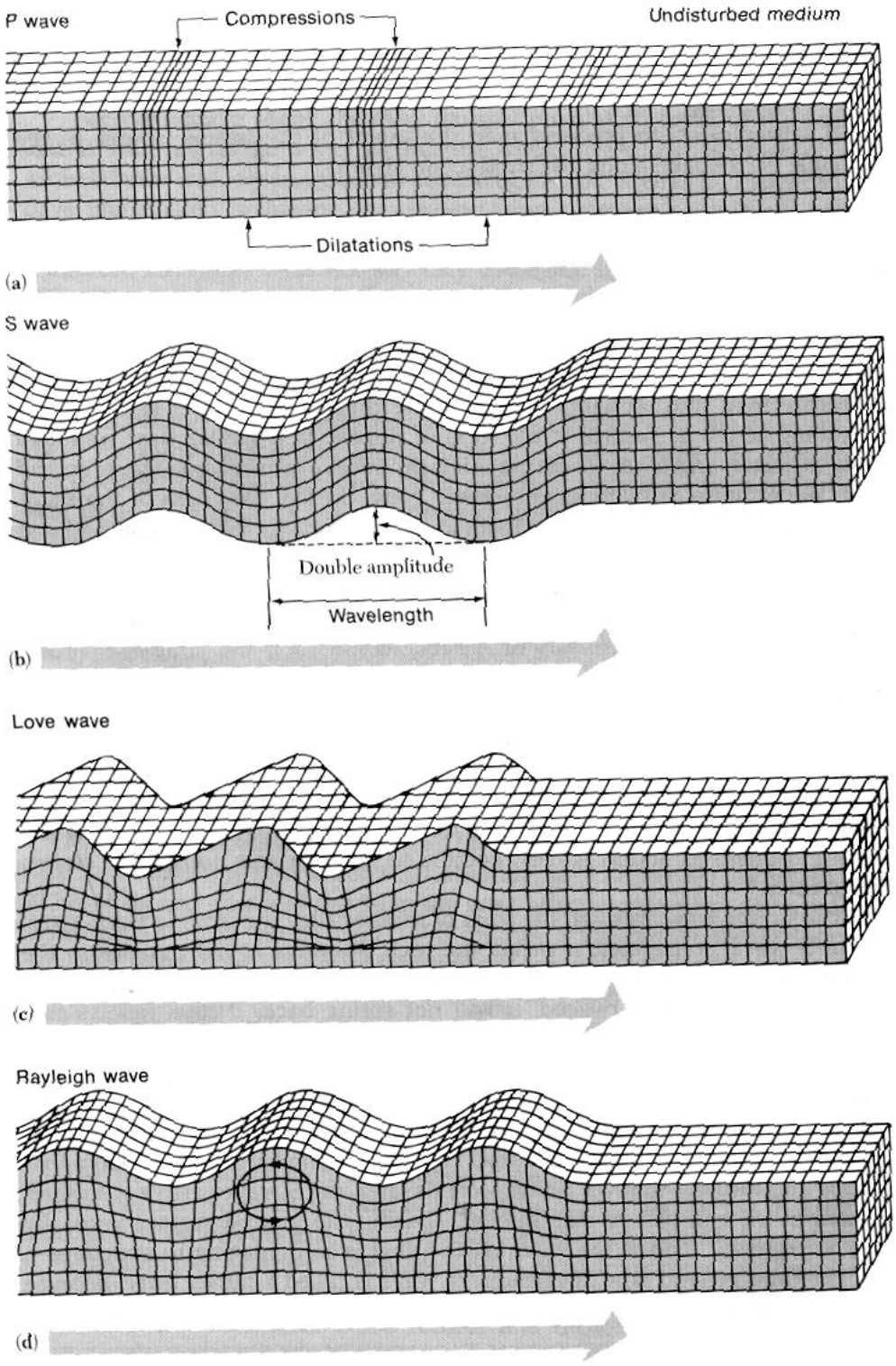

Figure 2.1 Body waves ((a) and (b)) and surface waves ((c) and (d)). The arrows indicate the direction of wave propagation. (Bolt, 1993)

2.3 RAYLEIGH WAVES IN A HOMOGENEOUS HALF-SPACE

2.3.1 Rayleigh Wave Equation

In 1885 Lord Rayleigh published a paper regarding waves propagating along the plane free surface of a homogeneous isotropic elastic half-space and such waves are now called Rayleigh waves. Rayleigh waves propagating through a homogeneous half-space have been theoretically investigated by many researchers, for example, Rayleigh (1885), Viktorov (1967), Richart et al. (1970), Graff (1975), and Achenbach (1973). For the study of Rayleigh wave propagation in elastic media including a homogeneous half-space, a Cartesian coordinate system is defined as shown in Figure 2.2.

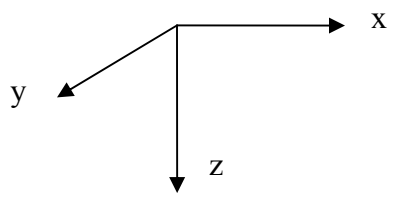

Figure 2.2 Cartesian coordinate system

A set of three basic equations for a homogeneous isotropic elastic medium is summarized using the Cartesian tensor notation as:

$$\sigma_{ij,j} + \rho b_i = \rho \ddot{u}_i \qquad \text{(Equations of Motion)} \tag{2.1}$$

$$\varepsilon_{ij} = \frac{1}{2} \cdot (u_{i,j} + u_{j,i}) \qquad \text{(Kinematical Equations)} \tag{2.2}$$

$$\sigma_{ij} = \lambda \varepsilon_{kk} \delta_{ij} + 2\mu \varepsilon_{ij} \qquad \text{(Constitutive Equations)} \tag{2.3}$$

where i, j = x, y, z directions, σ_{ij} is the stress tensor at a point, u_i is the displacement vector for the i direction, ρ is the mass density, b_i is the body force per unit mass of material, and ε_{ij} is a strain tensor. The terms λ and μ are *Lame parameters*, which are

elastic constants for the medium. Each constant can be expressed in terms of the other elastic constants such as Young's modulus, E, Poisson's ratio, ν, and bulk modulus, B, as summarized in Table 2.1.

Table 2.1 Relationships among elastic constants (modified from Achenbach, 1973)

	$E,\ \nu$	$E,\ G$	$\lambda,\ G$
λ	$\frac{E\nu}{(1+\nu)(1-2\nu)}$	$\frac{\mu(E-2G)}{3G-E}$	λ
μ	$\frac{E}{2(1+\nu)}$	G	G
E	E	E	$\frac{G(3\lambda+2G)}{\lambda+G}$
B	$\frac{E}{3(1-2\nu)}$	$\frac{GE}{3(3G-E)}$	$\lambda+\frac{2}{3}G$
ν	ν	$\frac{E-2G}{2G}$	$\frac{\lambda}{2(\lambda+G)}$

Another expression of Equation 2.1 in terms of displacements is obtained by substituting Equation 2.2 into Equation 2.3 and then substituting the resulting equation into Equation 2.1, yielding *Navier's equation*. In the absence of body forces, Navier's equation is given by:

$$\mu u_{i,jj} + (\lambda + \mu) u_{j,ji} = \rho \ddot{u}_i \tag{2.4}$$

In vector form, it can be expressed by:

$$\mu \nabla^2 \mathbf{u} + (\lambda + \mu) \nabla \nabla \cdot \mathbf{u} = \rho \ddot{\mathbf{u}} \tag{2.5a}$$

where ∇ represents the gradient vector operator, which is expressed by:

$$\nabla = \frac{\partial}{\partial x} i_x + \frac{\partial}{\partial y} i_y + \frac{\partial}{\partial z} i_z \tag{2.5b}$$

And ∇^2 represents the Laplacian operator given by:

$$\nabla^2 = \frac{\partial^2}{\partial x^2} + \frac{\partial^2}{\partial y^2} + \frac{\partial^2}{\partial z^2} \tag{2.5c}$$

Solutions of Navier's equation can be obtained by a method known as *Helmholtz's decomposition*. It is assumed that the particle displacement vectors in the equation can be written by:

$$\mathbf{u} = \nabla\phi + \nabla \times \boldsymbol{\psi} \tag{2.6}$$

where ϕ and $\boldsymbol{\psi}$ are scalar and vector potentials, respectively.

By substituting Equation 2.6 into Navier's equation, we obtain:

$$\nabla^2\phi = \frac{1}{V_P{}^2}\frac{\partial^2\phi}{\partial t^2} \tag{2.7}$$

$$\nabla^2\boldsymbol{\psi} = \frac{1}{V_S{}^2}\frac{\partial^2\boldsymbol{\psi}}{\partial t^2} \tag{2.8}$$

where $V_S = \sqrt{\frac{\mu}{\rho}} = \sqrt{\frac{G}{\rho}}$, $V_P = \sqrt{\frac{\lambda + 2\mu}{\rho}} = \sqrt{\frac{\lambda + 2G}{\rho}}$, and V_P and V_S are P-wave and S-wave velocities, respectively.

Considering waves propagating only in the x-z directions as shown in Figure 2.3, Equations 2.7 and 2.8 can be rewritten as:

$$\left(\frac{\partial^2\phi}{\partial x^2} + \frac{\partial^2\phi}{\partial z^2}\right) = \frac{1}{V_P{}^2}\frac{\partial^2\phi}{\partial t^2} \tag{2.9}$$

$$\left(\frac{\partial^2\boldsymbol{\psi}}{\partial x^2} + \frac{\partial^2\boldsymbol{\psi}}{\partial z^2}\right) = \frac{1}{V_S{}^2}\frac{\partial^2\boldsymbol{\psi}}{\partial t^2} \tag{2.10}$$

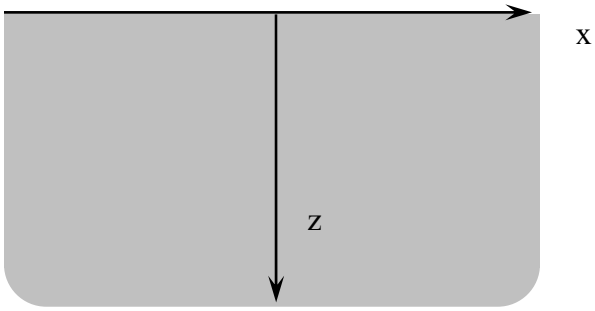

Figure 2.3 Coordinate system in a homogeneous half-space

Assuming time-harmonic, plane waves traveling along the x direction, the displacement potentials are expressed by:

$$\phi(x,z) = F(z) \cdot e^{i(\omega t - kx)} \tag{2.11}$$

$$\psi(x,z) = G(z) \cdot e^{i(\omega t - kx)} \tag{2.12}$$

where $F(z)$ and $G(z)$ are amplitudes that are functions of depth, ω is the circular frequency, and k is the wavenumber. Substituting $\phi(x,z)$ and $\psi(x,z)$ from Equations 2.11 and 2.12 into Equations 2.9 and 2.10, two ordinary differential equations are obtained:

$$\frac{d^2F(z)}{dz^2} + \left(\frac{\omega^2}{V_P{}^2} - k^2\right) \cdot F(z) = 0 \tag{2.13}$$

$$\frac{d^2G(z)}{dz^2} + \left(\frac{\omega^2}{V_S{}^2} - k^2\right) \cdot G(z) = 0 \tag{2.14}$$

Solving Equations 2.13 and 2.14 gives:

$$F(z) = A_1 \cdot e^{-pz} + A_2 \cdot e^{pz} \tag{2.15}$$

$$G(z) = B_1 \cdot e^{-qz} + B_2 \cdot e^{qz} \tag{2.16}$$

where $p = \sqrt{k^2 - \frac{\omega^2}{V_P{}^2}}$ and $q = \sqrt{k^2 - \frac{\omega^2}{V_S{}^2}}$. Equations 2.11 and 2.12 can be rewritten as:

$$\phi(x,z) = \left(A_1 e^{-pz} + A_2 e^{pz}\right) \cdot e^{i(\omega t - kx)} \tag{2.17}$$

$$\boldsymbol{\psi}(x,z) = (B_1 e^{-qz} + B_2 e^{qz}) \cdot e^{i(\omega t - kx)} \tag{2.18}$$

The constants A_1, A_2, B_1, and B_2 are real-valued constants that are determined from the boundary condition for Rayleigh waves, which are zero stresses at free surface and no displacement at infinite depth:

$$\tau_{zx}(x,0) = \tau_{zz}(x,0) = 0 \tag{2.19}$$

$$\mathbf{u}(x,z) = 0 \quad \text{as} \quad z \to \infty \tag{2.20}$$

The constants A_2 and B_2 are, therefore, equal to zero from Equation 2.20. Substituting Equations 2.17 and 2.18 into Equation 2.6, the displacement field $\mathbf{u}(x,z)$ can be obtained. The stress field can also be computed using the computed displacements and Equations 2.2 and 2.3. With the boundary conditions applied, the final result is obtained in matrix form:

$$\begin{bmatrix} 2p & \frac{k^2}{q} \cdot \left(2 - \frac{V_R^{\,2}}{V_S^{\,2}}\right) \\ \left(2 - \frac{V_R^{\,2}}{V_S^{\,2}}\right) & 2 \end{bmatrix} \cdot \begin{bmatrix} A_1 \\ B_1 \end{bmatrix} = \begin{bmatrix} 0 \\ 0 \end{bmatrix} \tag{2.21}$$

where V_R is the Rayleigh wave phase velocity

A non-trivial solution of Equation 2.21 can be computed by:

$$\det \begin{bmatrix} 2p & \frac{k^2}{q} \cdot \left(2 - \frac{V_R^{\,2}}{V_S^{\,2}}\right) \\ \left(2 - \frac{V_R^{\,2}}{V_S^{\,2}}\right) & 2 \end{bmatrix} = 0 \tag{2.22}$$

from which final equation is derived as follows:

$$\left(2 - \frac{V_R^{\,2}}{V_S^{\,2}}\right)^2 - 4\left(1 - \frac{V_R^{\,2}}{V_P^{\,2}}\right)^{0.5} \cdot \left(1 - \frac{V_R^{\,2}}{V_S^{\,2}}\right)^{0.5} = 0 \tag{2.23}$$

Equation 2.23 is called the c*haracteristic equation of Rayleigh waves* or simply the *Rayleigh wave equation*. From this equation, it is apparent that the Rayleigh wave phase velocity V_R in a homogeneous half-space is only a function of the P- and S-wave velocities. It is important to note that it is independent of frequency, which means that Rayleigh waves in a homogeneous half-space are non-dispersive.

In addition to Equation 2.23, a simple estimate for V_R in terms of V_S and Poisson's ratio is (Stokoe and Santamarina, 2000: modified from Achenbach, 1973):

$$V_R = \frac{0.874 + 1.117\nu}{1+\nu} V_S \tag{2.24}$$

Figure 2.4 compares the estimated values of V_R to values from the Rayleigh wave equation.

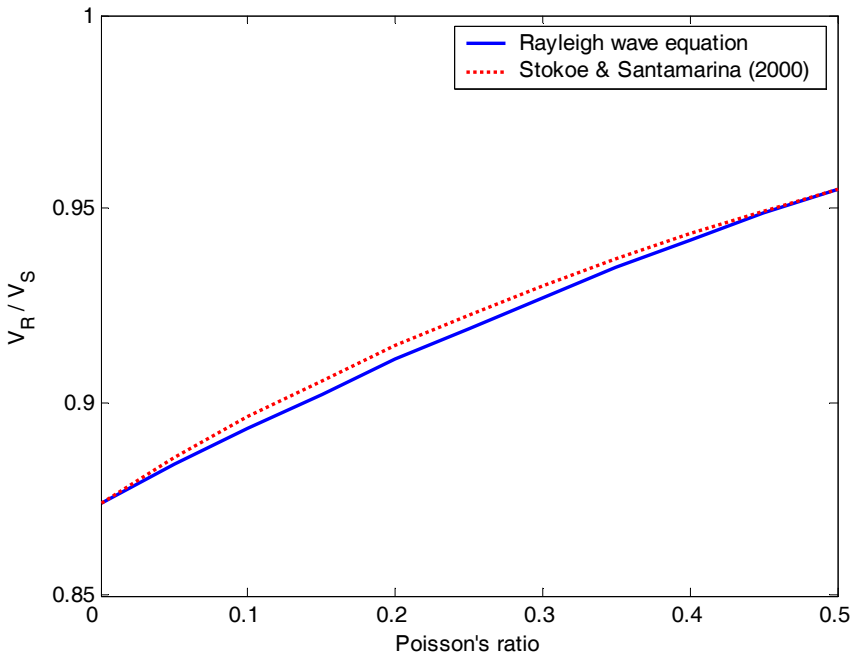

Figure 2.4 Ratio of V_R to V_S with Poisson's ratio

2.3.2 Displacements Due to Rayleigh Waves

In addition to the Rayleigh wave phase velocity, it is also of interest to calculate displacements caused by Rayleigh waves propagating in a homogeneous half-space. Since the Rayleigh wave equation was derived using Helmholtz's decomposition, Rayleigh waves are composed of the superposition of longitudinal and transverse components. It is possible to derive the vertical and horizontal components of the displacements associated with Rayleigh waves propagating through a homogenous half-space medium. Equation 2.6 can be rewritten as:

$$u_x = \frac{\partial \phi}{\partial x} + \frac{\partial \psi}{\partial z} \tag{2.25}$$

$$u_z = \frac{\partial \phi}{\partial z} - \frac{\partial \psi}{\partial x} \tag{2.26}$$

Substituting the solutions for the two potential functions, ϕ and ψ, into Equations 2.25 and 2.26 leads to vertical and horizontal displacements of Rayleigh waves in a homogeneous medium:

$$u_x(x,z) = ikA_1(-e^{-pz} + \frac{2pq}{q^2+k^2}e^{-qz})e^{i(\omega t - kx)} \tag{2.27}$$

$$u_z(x,z) = kA_1(-\frac{p}{k}e^{-pz} + \frac{2pk}{q^2+k^2}e^{-qz})e^{i(\omega t - kx)} \tag{2.28}$$

At t = 0 and x = 0, normalized vertical and horizontal displacements can be plotted as a function of normalized depth as shown in Figure 2.5.

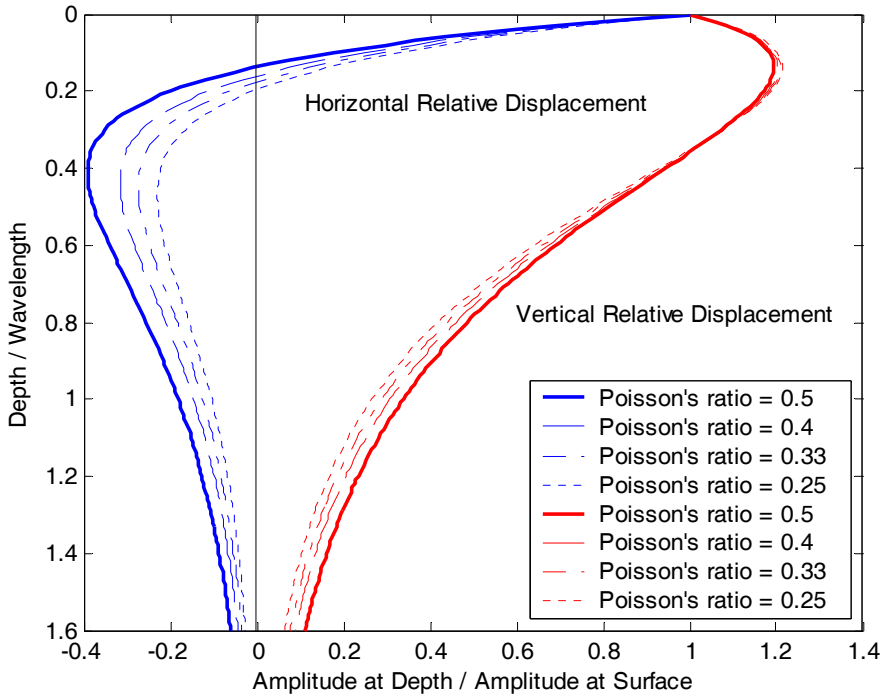

Figure 2.5 Vertical and horizontal displacements of Rayleigh waves in homogeneous half-space media (after Richart et al., 1970)

2.4 RAYLEIGH WAVES IN LAYERED MEDIA

2.4.1 Rayleigh Dispersion Equation

Although a homogeneous half-space is useful to introduce basic aspects of Rayleigh wave propagation, it is too simple to model real soil conditions. Soil profiles with depth-dependent properties may be idealized using a simplified layered model shown in Figure 2.6. Soils have been frequently modeled as layered media in many geotechnical problems due to computational efficiency. The layered medium consists of a stack of N homogeneous, isotropic, elastic layers described with properties shear wave velocity (V_S), mass density (ρ), Poisson's ratio (ν), and thickness (h).

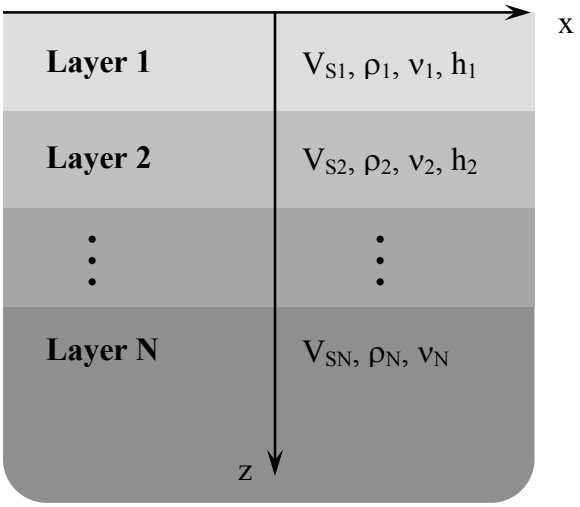

Figure 2.6 Elastic layered media model

Recall that the boundary conditions of Rayleigh waves in a homogeneous half-space are no stresses at the surface and zero amplitude at infinite depth. These boundary conditions descried in Equations 2.19 and 2.20 are still valid for the case of Rayleigh waves in a layered medium. Continuity in stresses and displacements at each layer interface results in additional boundary conditions expressed by:

$$\tau_{zx}(x,z_n) = \tau_{zx}(x,z_{n+1}) \tag{2.29}$$

$$\tau_{zz}(x,z_n) = \tau_{zx}(x,z_{n+1}) \tag{2.30}$$

$$\mathbf{u}(x,z_n) = \mathbf{u}(x,z_{n+1}) \tag{2.31}$$

where $n = 1,\ldots, N$.

By employing the same procedure as used for the study of Rayleigh wave propagation in a homogeneous half-space, displacements $\mathbf{u}_n(x,z)$ in each layer are obtained by:

$$\mathbf{u}_n(x,z) = \nabla\phi_n + \nabla\times\boldsymbol{\psi}_n \tag{2.32}$$

Application of the boundary conditions in Equations 2.19, 2.20, 2.29, 2.30, and 2.31 leads to a homogeneous system of 4N-2 linear equations, denoted by **S**. Non-trivial solutions can be obtained by setting det[**S**] = 0, and this final product is called the *Rayleigh dispersion equation* for a layered half-space. This equation provides an implicit relationship between the phase velocity of Rayleigh waves, frequency and the properties of the layers and can be written (Lai, 1998):

$$f_R(V_{S,n}, \nu_n, \rho_n, h_n, k_j, \omega) = 0 \tag{2.33}$$

It is important to note the main features of this equation. First, the phase velocity of Rayleigh waves in a vertically heterogeneous medium is dependent on frequency. This phenomenon is called *geometric dispersion* since it is related to the geometrical variations of properties with depth. Figure 2.7 illustrates the cause of geometric dispersion of Rayleigh waves. As shown in Figure 2.7, a Rayleigh wave with a short wavelength is confined within only the upper layer, while a longer wavelength Rayleigh wave has particle motion in all three layers. As such, the velocity of the short wavelength Rayleigh wave is controlled by the material properties of Layer 1, while the combined material properties of all three layers control the velocity of the longer wavelength Rayleigh wave. It is a key element in surface wave methods that Rayleigh waves with different wavelengths (or frequencies) sample different parts of the layered medium (Stokoe et al., 1994), allowing them to be used to determine the variation of material properties with depth. Secondly, for a given frequency, multiple solutions of the Rayleigh dispersion equation exist. This means that for a given frequency, there are multiple modes of Rayleigh waves traveling at different phase velocities. Multiple modes of Rayleigh wave propagation at a certain frequency can be physically explained by the

constructive interference occurring among waves undergoing multiple reflections at the layer interfaces (Lai, 1998).

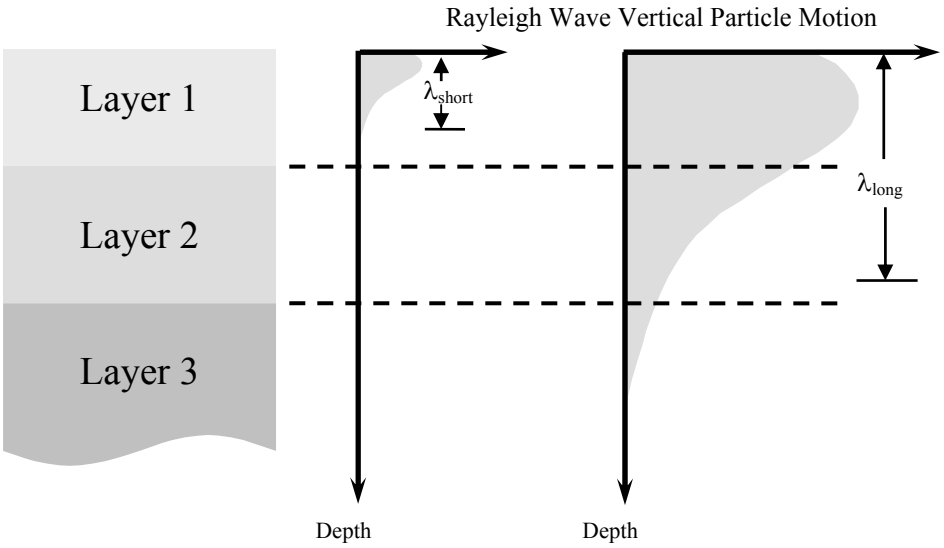

Figure 2.7 Vertical particle motions of two Rayleigh waves with different wavelengths (Rix, 2000)

For many applications, it is desirable to avoid the use of potentials (Equation 2.6) and to use an alternative formulation of the Rayleigh dispersion equation in terms of a *differential eigenvalue problem* (Aki and Richards, 1980). A linear differential eigenvalue problem with displacement eigenfunctions $r_1(z,k,\omega)$ and $r_2(z,k,\omega)$ and stress eigenfunctions $r_3(z,k,\omega)$ and $r_4(z,k,\omega)$ in a layered medium is defined by:

$$\frac{df(z)}{dz} = A(z) \cdot f(z) \tag{2.34}$$

where $f(z) = [r_1\ r_2\ r_3\ r_4]^T$ and a 4-by-4 matrix $A(z)$ are composed of elements which are functions of $\lambda(z)$, $G(z)$, $\rho(z)$, k, and ω. The eigenfunctions r_1 through r_4 are defined by:

$$u_x = r_1(z,k,\omega) \cdot e^{i(\omega t - kx)} \tag{2.35a}$$

$$u_z = i \cdot r_2(z,k,\omega) \cdot e^{i(\omega t - kx)} \tag{2.35b}$$

$$\tau_{zx} = \mu\left(\frac{dr_1}{dz} - kr_2\right) \cdot e^{i(\omega t - kx)} = r_3(z,k,\omega) \cdot e^{i(\omega t - kx)} \tag{2.36a}$$

$$\tau_{zz} = i\left[(\lambda + 2\mu)\frac{dr_2}{dz} + k\lambda r_1\right] \cdot e^{i(\omega t - kx)} = ir_4(z,k,\omega) \cdot e^{i(\omega t - kx)} \tag{2.36b}$$

The boundary conditions described in Equations 2.19 and 2.20 can be rewritten in terms of the displacement and stress eigenfuctions:

$$r_3(z,k,\omega) = r_4(z,k,\omega) = 0 \qquad \text{at} \qquad z = 0 \tag{2.37}$$

$$r_1(z,k,\omega) = r_2(z,k,\omega) = 0 \qquad \text{as} \qquad z \to \infty \tag{2.38}$$

For a given frequency, non-trivial solutions of Equation 2.34 with the boundary conditions in Equations 2.37 and 2.38 exist only for special values of the wavenumber $k_j(\omega)$, (j=1,…,M) where M is the total number of modes at a certain frequency ω (Lai, 1998). The values of k_j and the corresponding solutions $r_i(z,k_j,\omega)$, (i=1,…,4) are the eigenvalues and the eigenfunctions of the eigenvalue problem described in Equation 2.34, respectively (Lai, 1998).

The values of k_j for Rayleigh waves in the layered medium can be obtained by solving the Rayleigh dispersion equation in Equation 2.33 via one of solution techniques that will be discussed in the next section. The eigenfuctions $r_i(z,k_j,\omega)$ satisfying Equation 2.34 can be easily calculated once the roots of the Rayleigh dispersion equation, i.e., the values of k_j, are obtained. Each pair of k_j and corresponding $r_i(z,k_j,\omega)$ defines a specific mode of Rayleigh wave propagation. In a medium consisting of a finite number of homogeneous layers overlying a homogeneous half-space, the total number of modes of Rayleigh wave propagation is always finite (Ewing et al., 1957).

2.4.2 Techniques to Solve the Rayleigh Dispersion Equation

The implicit Rayleigh dispersion equation described in Equation 2.33 can be solved only numerically. Several techniques are available to construct and solve the Rayleigh dispersion equation for layered media.

The *transfer matrix method* belonging to the class of propagator-matrix methods is the oldest and best known technique among this class. It was originally developed by Thomson (1950) and subsequently improved by Haskell (1953). In the method, the dispersion equation is constructed by a series of matrix multiplications involving functions of material properties of the layers in the stratified medium. This method has been modified and improved by many other researchers (Schwab and Knopoff, 1970; Abo-Zena, 1979; Harvey, 1981) because the original formulation has been shown to have numerical instability problems at high frequencies (Knopoff, 1964).

The *stiffness matrix method* was suggested by Kausel and Roesset (1981). This method is the reformulation of the transfer matrix method, and it replaces the Thomson-Haskell transfer matrices with layer stiffness matrices obtained by using concepts used in classical structural analysis.

Another important class of solution techniques for the Rayleigh dispersion equation is the *reflection and transmission coefficients method*. The method originally developed by Kennett (1974) has been modified and improved by others (Kennett and Kerry, 1979; Luco and Aspel, 1983; Hisada, 1994; Hisada, 1995).

Once the Rayleigh dispersion equation is formulated using one of the above methods, a root finding technique is applied to obtain the roots of the Rayleigh dispersion equation. The solutions of the dispersion equation are the frequency-dependent

wavenumbers $k_j(\omega)$, (j=1,…,M) corresponding to modes of Rayleigh wave propagation in a layered medium. Since the Rayleigh dispersion equation can be solved only numerically, great attention should be paid in the root finding process due to the behavior of the dispersion equation. The dispersion equation may not be properly solved by some root finding techniques due to the strong oscillation of the dispersion equation especially at high frequencies (Hisada, 1994; 1995).

2.4.3 Green's Function for Plane Rayleigh Waves

Solutions of the Rayleigh dispersion equation in Equation 2.33 yield modal Rayleigh dispersion curves corresponding to natural modes of Rayleigh wave propagation in vertically heterogeneous media. The modal Rayleigh dispersion curves are used as reference dispersion curves in the media for the case of modal isolation. In many cases, it is useful to calculate surface displacements associated with the propagation of Rayleigh waves from a source to more closely simulate a surface wave test. This is especially useful at sites where multiple modes contribute to the displacement field. From a practical point of view, it is required to calculate theoretical Rayleigh dispersion curves to be compared with the dispersion curves from field testing data measured at spatially spaced receivers.

In engineering, Green's functions have often been used to calculate the response of a linear system to an arbitrary source. Lai (1998) used the displacement Green's functions for plane Rayleigh waves to derive the explicit equation for the response of a layered, linear elastic half-space to a harmonic unit source. The displacement Green's functions for plane Rayleigh waves allow one to calculate theoretical dispersion curves with the same procedure used for experimental dispersion curves. Solutions of the Green's

functions for plane Rayleigh waves are the surface displacements of a layered medium that may be considered as linear at very low strain levels to an arbitrary point source at specific locations. The next step is to transform the displacements to a dispersion curve through the application of the same signal processing technique used to calculate the experimental dispersion curve. It may be concluded that the solutions of the Green's functions of plane Rayleigh waves and an associated signal processing technique provide an opportunity to obtain a theoretical dispersion curve in a manner that closely simulates the experimental procedure.

For a vertical harmonic point source $1 \cdot e^{i\omega t}$ located at x = 0 and z = 0, the vertical particle displacement at the ground surface (z = 0) resulting from the superposition of the modes of Rayleigh wave propagation is calculated by:

$$u_z(x,\omega) = |u_z(x,\omega)|\, e^{i[\omega \cdot t - \Psi_z(x,\omega)]} \tag{2.39a}$$

where:

$$|u_z(x,\omega)| = \frac{1}{4\sqrt{2\pi x}} \left\{ \sum_{i=1}^{M} \sum_{j=1}^{M} \frac{r_1(k_i,\omega) r_1(k_j,\omega) r_2(k_i,\omega) r_2(k_j,\omega) cos\left[x(k_i - k_j)\right]}{\sqrt{k_i k_j}\,(V_i U_i I_i)(V_j U_j I_j)} \right\}^{0.5} \tag{2.39b}$$

and

$$\Psi_z(x,\omega) = \tan^{-1}\left[\frac{\sum_{i=1}^{M} \frac{r_2^2(k_i,\omega)}{\sqrt{k_i}\,(V_i U_i I_i)} \sin\left(k_i x + \frac{\pi}{4}\right)}{\sum_{j=1}^{M} \frac{r_2^2(k_j,\omega)}{\sqrt{k_j}\,(V_j U_j I_j)} \cos\left(k_j x + \frac{\pi}{4}\right)} \right] \tag{2.39c}$$

where $V_j = \omega/k_j$ is the phase velocity, $U_j = d\omega/dk_j$ is the group velocity (j = 1,…,M), and $k_j(\omega)$ is the wavenumber of the j^{th} mode plane Rayleigh wave. The term I_j is the first

Rayleigh energy integral associated with the j^{th} mode of propagation and is defined by (Aki and Richards, 1980):

$$I_j(z,k_j,\omega) = \frac{1}{2}\int_0^{\infty} \rho(z)\left[r_1^{\,2}(z,k_j,\omega) + r_2^{\,2}(z,k_j,\omega)\right]dz \tag{2.40}$$

Figures 2.8(a) and 2.8(b) show the magnitude of the vertical displacements of Rayleigh waves in a regular medium, where the stiffness of layers increases with increasing depth, and an irregular medium, where a soft layer is trapped between two stiffer layers, respectively, for a frequency of 20 Hz. The former is designated as a normally dispersive medium and the latter is designated as an inversely dispersive medium. Properties of these media are tabulated in Tables 2.2 and 2.3, respectively.

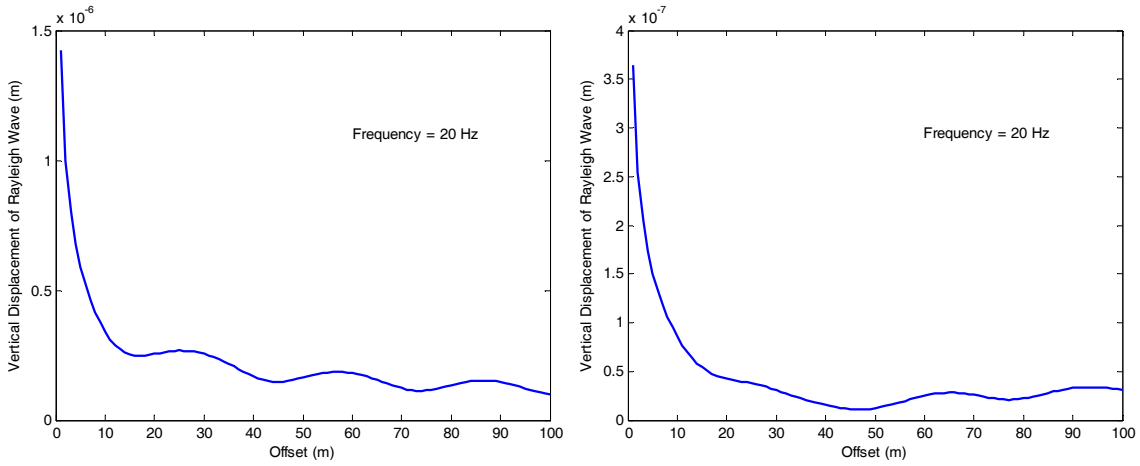

(a) (b)

Figure 2.8 Vertical displacement of Rayleigh waves at various offsets: (a) normally dispersive medium and (b) inversely dispersive medium

Table 2.2 Properties of a normally dispersive medium

Layer No.	Thickness (m)	V_S (m/sec)	Poisson's ratio, ν	Damping ratio, D (%)	Mass density, ρ (t/m^3)
1	5	200	0.3	0	1.8
2	10	300	0.3	0	1.8
3	10	400	0.3	0	1.8
Half-Space	∞	500	0.3	0	1.8

Table 2.3 Properties of an inversely dispersive medium

Layer No.	Thickness (m)	V_S (m/sec)	Poisson's ratio, ν	Damping ratio, D (%)	Mass density, ρ (t/m^3)
1	5	300	0.3	0	1.8
2	10	200	0.3	0	1.8
3	10	400	0.3	0	1.8
Half-Space	∞	500	0.3	0	1.8

2.4.4 Green's Function for Full Wavefield (PUNCH)

In practice, an active source vertically applied on the surface generates a wavefield composed of spherically spreading body waves (P- and S-waves) and cylindrically spreading Rayleigh waves. To simulate a real active surface wave test, a way to calculate this full wavefield is required. Solutions of the Green's function for full wavefield corresponding to dynamic loads acting on a horizontally layered medium provide its responses against the loads, introducing a way to mathematically simulate a real active surface wave test. For each frequency, the solutions of the Green's function can be determined in terms of displacements by using Fourier transformed load vector and the global stiffness matrix corresponding to a specific layered medium. The global stiffness matrix can be obtained by the approach suggested by Kausel and Roesset (1981). For computational efficiency, the solutions are often Fourier transformed displacements in temporal frequency domain.

The formulation of explicit solutions for the Green's function for arbitrary dynamic loads in layered media was developed by Kausel (1981) and implemented in the computer program PUNCH (Kausel, 1981). The program provides the solutions of the vertical and horizontal displacement Green's function for body and Rayleigh waves for various types of sources such as line, disk, ring, and point loads at arbitrary locations in the medium. For a vertical harmonic point load of amplitude p, a vertical particle displacement u_z from the Green's function is calculated by (Kausel, 1981):

$$u_z = \frac{p}{4i} \sum_{l=1}^{2N} \phi_z^{ml} \phi_z^{nl} H_0^{(2)}(k_l x) \tag{2.41}$$

where ϕ_z^l and k_l are a vertical component of the l eigenvector and the l eigenvalue, respectively, of the eigenvalue problem associated with the natural modes of wave propagation in a layered medium, the indexes m and n indicate the node or interface where the load is applied and the displacement is calculated, respectively, N is a total number of layers, and $H_0^{(2)}(\cdot)$ is the second kind Hankel function of zero order.

Since a linearization technique was adopted in the program PUNCH to express the solutions in terms of algebraic functions for computational efficiency, it was recommended that the layers be sufficiently thin to accurately reproduce the variation in the displacements with depth (Sanchez-Salinero, 1987). A layering for numerical simulations with the program PUNCH was determined based on the layering criteria suggested by Sanchez-Salinero (1987). Before using the program PUNCH with a specific layering, it is required to validate if it provides reliable solutions. In this study, the validation was performed by comparing the solutions of the Rayleigh boundary value

problem in homogeneous elastic and viscoelastic media using the program PUNCH with analytical solutions that were presented by Lamb (1904).

The problem of calculating the displacement field induced by a vertical harmonic source on the surface of a homogeneous, isotropic, linear elastic half-space was first solved by Lamb (1904). Today, the problem is known as Lamb's problem and Lamb used the means of complex variable theory to find the explicit solution which is known as Lamb's solution today. Lamb's solution providing exact response of the simplest medium corresponding to the vertical harmonic source without any error in numerical procedure may be used as a reference to verify the numerical procedure using the program PUNCH. Lamb's solution for a vertical harmonic source $Fe^{i\omega t}$ can be given by:

$$w_R(x,\omega) = \frac{Fe^{i\omega t}}{2iG} \cdot k_R \cdot \Phi(k_R) \cdot H_0^{(2)}(k_R x) \tag{2.42}$$

where $w_R(x,\omega)$ is the vertical displacement of Rayleigh wave at the free surface of a homogeneous elastic half-space medium at a distance x from the source. G is the shear modulus of the medium, k_R is the wavenumber of Rayleigh wave, and $H_0^{(2)}$ denotes the Hankel function of the second kind of zero order. The symbol $\Phi(k_R)$ is defined by:

$$\Phi(k_R) = -\frac{k_S^2\sqrt{k_R^2 - k_P^2}}{R'(k_R)} \tag{2.43}$$

where k_P and k_S are the wavenumbers of P-wave and S-wave, respectively. The function $R(k_R)$ is expressed by:

$$R(k_R) = (2k_R^2 - k_S^2)^2 - 4k_R^2\sqrt{(k_R^2 - k_P^2)(k_R^2 - k_S^2)} \tag{2.44}$$

where $k_R = \omega/V_R$ and V_R is the non-dispersive Rayleigh wave phase velocity that can be obtained by solving the Rayleigh wave equation in Equation 2.23.

Elastic and viscoelastic homogeneous media with material properties tabulated in Tables 2.4 and 2.5 are selected to validate the program PUNCH.

Table 2.4 Properties of an elastic homogeneous medium used for validation of PUNCH

Layer No.	Thickness (m)	V_S (m/sec)	Poisson's ratio, ν	Damping ratio, D (%)	Mass density, ρ (t/m^3)
Half-Space	∞	200	0.3	0	1.8

Table 2.5 Properties of a viscoelastic homogeneous medium used for validation of PUNCH

Layer No.	Thickness (m)	V_S (m/sec)	Poisson's ratio, ν	Damping ratio, D (%)	Mass density, ρ (t/m^3)
Half-Space	∞	200	0.3	2	1.8

For the validation, vertical displacement amplitudes and phases from the Lamb's solutions and the program PUNCH are plotted as functions of the distance from the source for a specific frequency. Figures 2.9(a) and 2.9(b) shows the validation results for the elastic homogeneous medium at a frequency of 5 Hz and Figures 2.9(c) and 2.9(d) shows those for the viscoelastic homogeneous medium at the same frequency. For both medium conditions, the agreement between the analytical solutions given by Lamb (1904) and those from the program PUNCH is excellent.

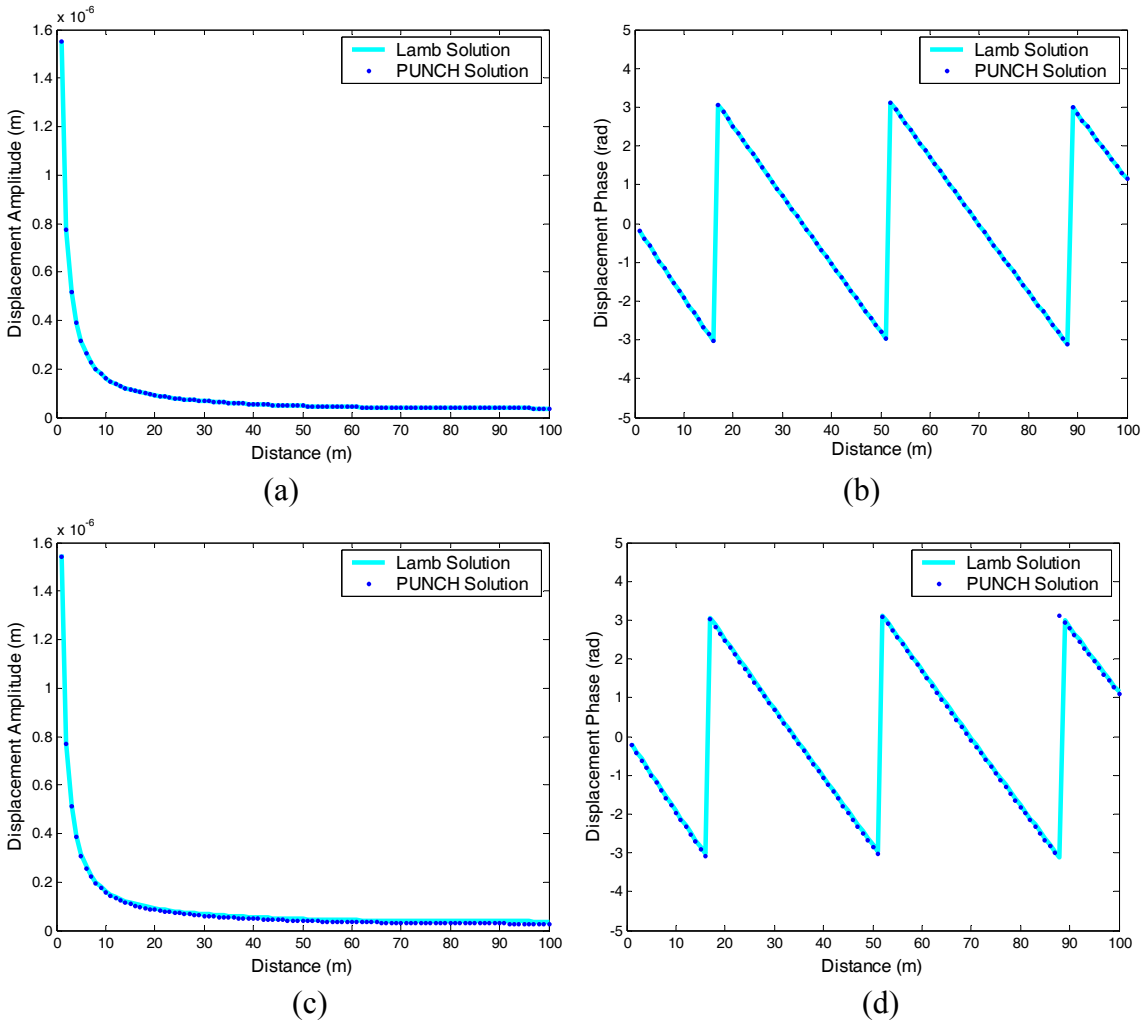

Figure 2.9 Comparison of solutions from Lamb (1904) and PUNCH for vertical displacement amplitudes and phases in elastic ((a) and (b)) and viscoelastic ((c) and (d)) homogeneous media for a frequency of 5 Hz

CHAPTER 3

OVERVIEW OF SURFACE WAVE METHODS

3.1 SPECTRAL ANALYSIS OF SURFACE WAVE (SASW) METHOD

The spectral analysis of surface waves (SASW) method was developed in the early 1980s by a group of researchers at the University of Texas of Austin (Heisey et al., 1982; Nazarian and Stokoe, 1984). Since its initial development, the experimental, data processing, and inversion procedures have been improved through continuous studies by many researchers (Al-Hunaidi, 1993; Gucunski and Woods, 1992; Heisey *et al*., 1982; Hiltunen and Woods, 1990; Sanchez-Salinero *el al*., 1987; Stokoe *et al*., 1994). Well-established inversion procedures based on wave propagation theory have enabled the use of the method for a variety of site conditions.

However, the traditional SASW method using only two receivers and the associated signal processing technique are limited by: inability to separate individual modes, limited noise removal capability, limited attenuation estimation capability, inability to measure a broad range of frequencies simultaneously, limited low-frequency resolution, substantial near-field interference, and the possible need for manual phase interpretation (Zywicki, 1999).

3.2 ARRAY- BASED SURFACE WAVE METHOD

With the availability of multi-channel data acquisition systems, most modern surface wave test procedures utilize a spatial array of multiple receivers. Increasing the number of receivers allows measurements at all spatial lags to be made simultaneously and more efficiently. Consequently, measurements using spatial arrays not only allow a much

greater range of spatial lags to be sampled in less time, but also provide the possibility of separating multiple modes of propagation. Moreover, the use of a spatial array and spatial array processing techniques allow testing with passive surface waves whose propagating direction is not known prior to the test. Typically, passive surface waves contain more low-frequency energy and can be used to develop soil profiles to much greater depth than active surface waves.

Like the traditional SASW method, array-based surface wave methods are performed in three steps: (1) field measurements, (2) dispersion (or attenuation) calculations, and (3) inversion. In this section, each step will be discussed in detail with some examples of array-based surface wave tests performed at several sites.

3.2.1 Field Measurements

Field measurement is the first step in a surface wave test and is performed using (1) a source, (2) an array of multiple receivers, and (3) data acquisition and processing system.

3.2.1.1 Sources

As shown in Figure 3.1, a vertical point source acting on the surface of a homogeneous, isotropic, and elastic half-space generates body waves propagating with a spherical wave front as well as Rayleigh waves propagating with a cylindrical wave front. However, at large distances from the source, Rayleigh waves dominate because of two factors: (1) Most of the energy, about two-thirds for a homogeneous and elastic half-space, is transmitted via Rayleigh waves (Miller and Pursey, 1955), and (2) Rayleigh waves attenuate geometrically much less than body waves because Rayleigh waves propagate radially outward along a cylindrical wave front having a geometrical

attenuation proportional to $1/r^{1/2}$, while body waves propagate radially outward along a hemispherical wave front having a geometrical attenuation proportional to $1/r^2$.

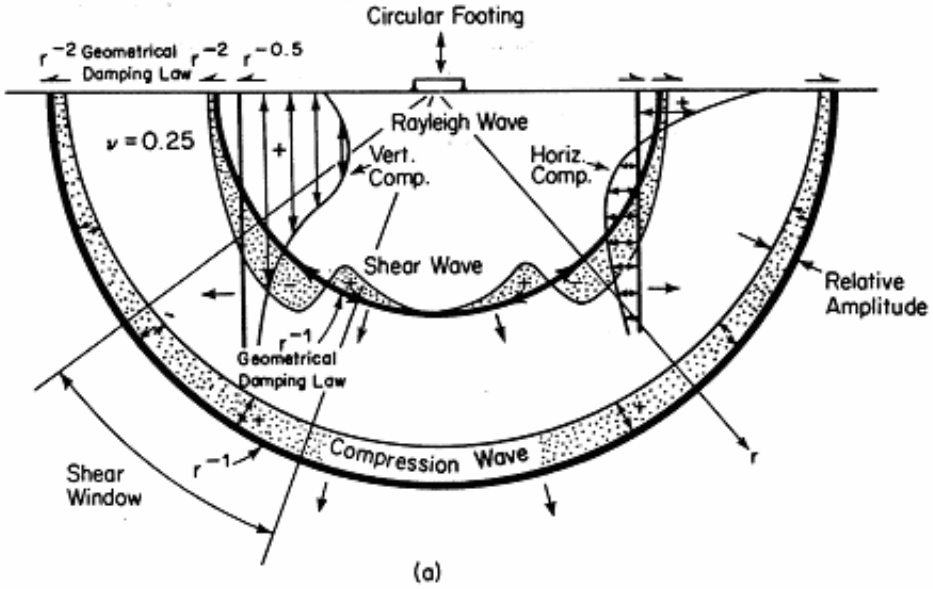

Wave Type	Per Cent of Total Energy
Rayleigh	67
Shear	26
Compression	7

(b)

Figure 3.1 Vertically-oscillating harmonic point source acting on a homogeneous, isotropic, and elastic half-space: (a) complete wavefield generated by the source and (b) energy portion associated with different types of waves (Woods, 1968)

Generally, three types of sources, (1) active-transient, (2) active- harmonic, and (3) passive, are used in surface wave methods. Typical examples of active-transient sources include hammers, buckets, and dropped weights. A transient source allows a test to be performed relatively quickly because a broad range of frequencies is generated and measured simultaneously. However, the frequency content is often limited and poorly

controlled. It is also important to realize that different transient sources generate energy over different frequency ranges as shown in Figure 3.2.

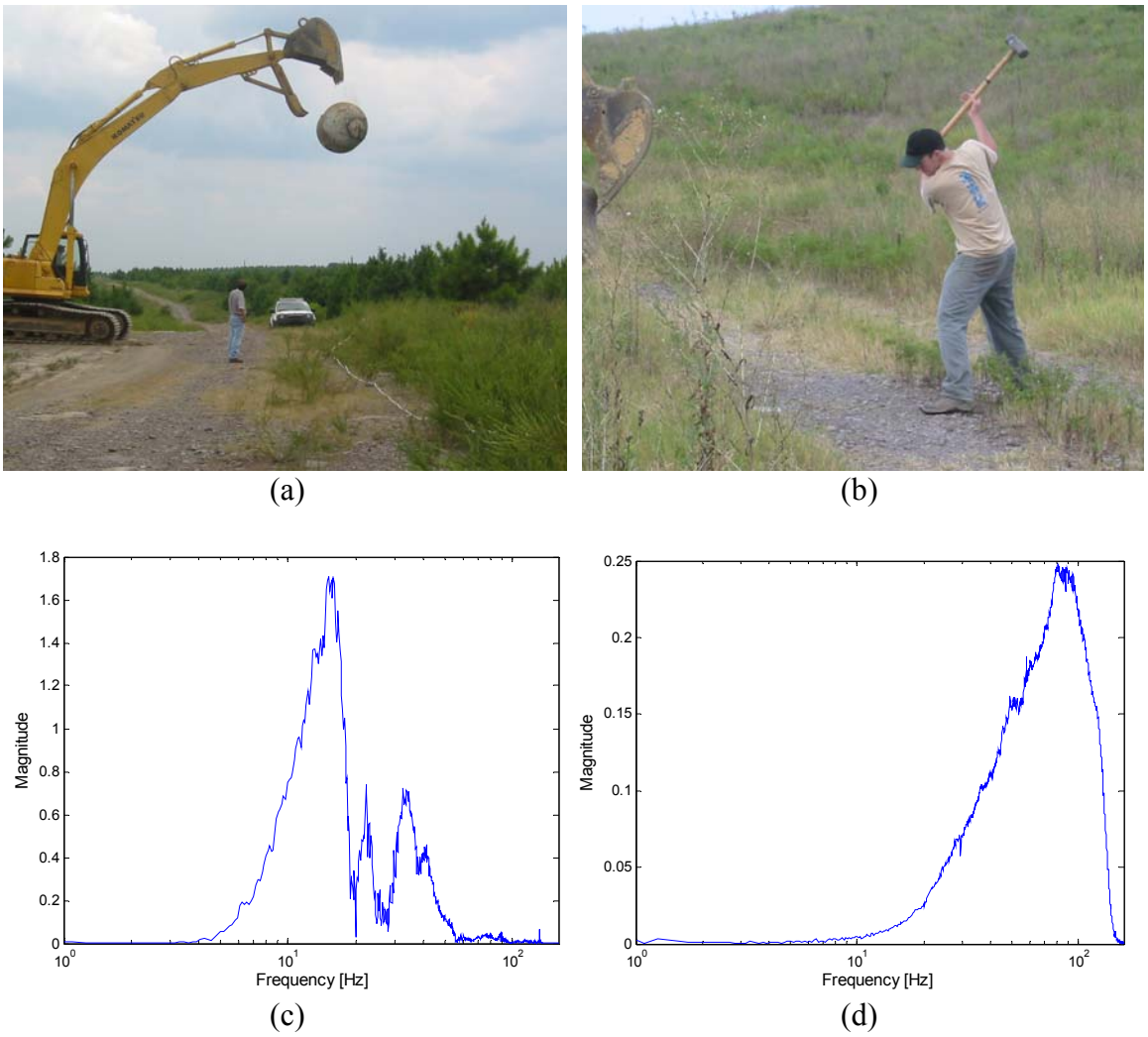

Figure 3.2 Examples of two different transient sources and their frequency contents: (a) dropped heavy weight, (b) sledge hammer, (c) frequency content for the dropped heavy weight, and (d) frequency content for the sledge hammer.

A test with an active-harmonic source such as a vertically oscillating shaker requires a longer testing time to perform because the test is conducted at individual frequencies in sequence, but the user has much greater control over the frequency content. Moreover,

harmonic sources can often generate measurable energy at lower frequencies than transient sources (Spang, 1995). These advantages of the harmonic source over the transient source often provide significant improvements in the estimation of dispersion (or attenuation) data.

The active source, however, is limited in its ability to sample deep soils due to the difficulty of generating very low-frequency energy with a reasonably portable source. Passive sources such as microtremors and cultural noise may be utilized as an alternative to overcome this limitation because passive waves typically contain sufficient energy at lower frequencies than most active sources. However, passive tests may be impractical at some sites where such sources are absent. An important assumption associated with passive surface wave tests is that the measured vertical particle motions are those of Rayleigh waves (Tokimatsu, 1995).

In the array-based surface wave methods used in this study, a harmonic source was used to control the frequency content. An APS Dynamics, Inc. Model 400 Electro-Seis electromechanical shaker shown in Figure 3.3 was selected as the harmonic source to generate the active Rayleigh wavefield. Power for the shaker is provided by an APS Model 144 DUAL-MODE power amplifier. Typical measurements span from about 4 Hz to 100 Hz, while the shaker can be operated with frequencies ranging from about 2 Hz to 200 Hz. There are often minor variations in the lowest frequency that is obtained due to site-specific conditions.

Figure 3.3 Active harmonic source (electromechanical shaker)

3.2.1.2 Array Selection

Rayleigh waves are monitored by a spatial array of receivers whose arrangement depends on a priori knowledge of a direction of wave propagation. For a given equipment configuration including the number of receivers, cable length, and source capability, it is very important to select an array with an appropriate combination of wavenumber resolution, spatial aliasing, and sidelobe height for accurate measurements of propagating Rayleigh waves.

For active tests in this study, a non-uniform linear array of 15 receivers spaced at 2.4, 3, 3.7, 4.6, 5.5, 6.7, 8.5, 10.4, 12.8, 15.2, 18.3, 21.3, 24.4, 29, and 33.5 m was selected (Hebeler, 2001) and referred to as the standard array. Figure 3.4a shows a schematic diagram of an active test performed with a non-uniform array.

Zywicki (1999) conducted experimental measurements of passive waves with several different array geometries. From the comparison of the several array geometries, a circular array of 16 equally-spaced receivers along the circumference without a center receiver was selected for the following reasons (Zywicki, 1999): (1) the array appears to be nearly identical for a plane wave coming from any direction yielding almost constant azimuthal resolution, (2) the symmetry of its array smoothing function allows one to identify a maximum wavenumber before encountering large sidelobes, and (3) the array shows good resolution characteristics. Figure 3.4b shows the spatial array and passive energy coming from main and minor energy sources for a passive test.

(a)

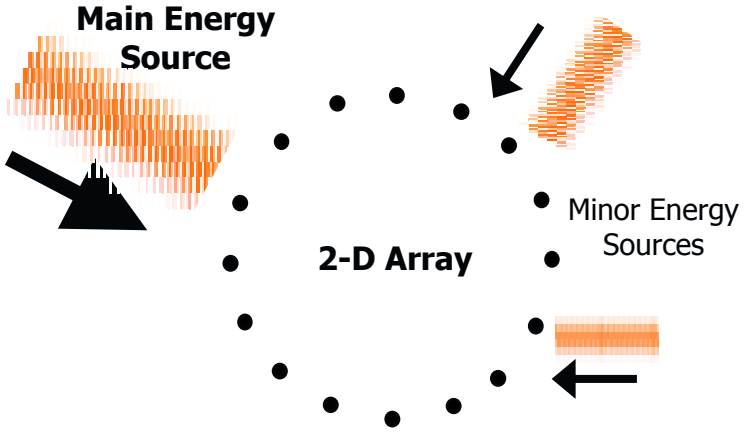

(b)

Figure 3.4 Array and wave: (a) active tests, and (b) passive tests. Note that the square and the circles indicate an active source and receivers, respectively, and the arrows indicate directions of wave propagation.

In passive surface wave tests requiring a two-dimensional array, the focus is placed on the measurement of low frequencies. Considering a given cable length and available area at a site, it may be desirable to select a circular array with the largest possible radius so that the resulting wavenumber resolution allows reliable measurements of low-frequency Rayleigh waves. Frequently, spatial aliasing of high-frequency waves is not of concern in passive tests.

3.2.1.3 Data acquisition system

The data acquisition system used in this study is shown in Figure 3.5 and consists of a modular VXI multi-channel system, up to 16 receivers, a signal conditioner, and a laptop computer.

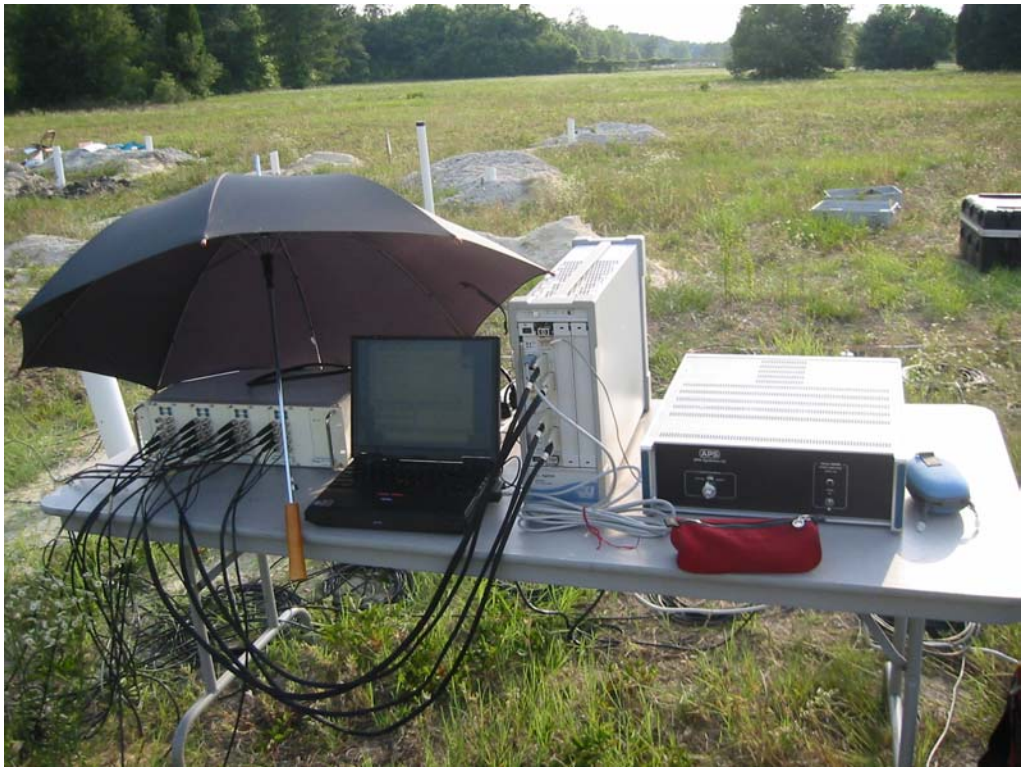

Figure 3.5 Data acquisition system used for array-based surface wave measurements

A Hewlett-Packard VXI digital signal analyzer with 16 channels was used as the data recording device. Its mainframe contains an analog-to-digital converter, dynamic signal analysis module, and an IEEE 1394 interface module. A laptop computer featuring a 366 MHz Pentium II controller and 128 MB DRAM is connected to the signal analyzer via the IEEE 1394 interface to allow data to be transferred to the computer. A 16-channel, 16-bit HP E1342A digitizer plus dynamic signal processor enables sampling at up to 51.2

kSamples/sec. A PCB Piezotronics 440 module containing four, 4-channel PCB 442A 104 signal conditioners provides signal conditioning and selectable amplification of 1, 10, and 100.

The frequencies of interest for near-surface soil characterization range from about 2 Hz to 100 Hz for soils from 0 to about 200 m in depth. Receivers must be selected with this range of frequencies in mind. Other characteristics include high sensitivity and adequate resolution. Based on such criteria, Wilcoxon Research 731A Ultra-Quiet, Ultra-Low-Frequency seismic accelerometers providing a flat response between 0.2 Hz and 100 Hz with a resonant frequency near 950 Hz and sensitivity of 10 V/g were used during all surface wave field tests in this study. The receiver is shown in Figure 3.6. A single Wilcoxon Research 728T High-Sensitivity, Low-Noise accelerometer responding linearly at higher frequencies up to 20 kHz with a resonant frequency near 23 kHz and sensitivity of 0.5 V/g was used to monitor the shaker motion during testing.

Figure 3.6 Receiver used for array-based surface wave measurements

The Wilcoxon Research 731A receivers were coupled to the ground surface by hand after removing surface vegetation, while the Wilcoxon Research 728T was coupled to the shaker armature via a threaded mounting stud. Wilcoxon Research low-noise coaxial cables were used with the receivers. For the typical frequencies of seismic interest, the loss of signal quality caused by driving long cables can be ignored (Zywicki, 1999).

Programming scripts written in Matlab were used to control test sequences including source generation and data collection for all measurements in this study. System control software written in Matlab enables one to input spatial array and digital signal processing parameters including sampling frequency, number of blocks of data to be averaged, block length, and receiver locations. The frequency generated by the harmonic active source and the receiver geometry can be specified by modifying relevant commands in the scripts. During measurements, time history data from an array of receivers are displayed to check and monitor the raw data. Figure 3.7 shows a schematic diagram of the harmonic source and the data acquisition system for the active array-based surface wave method.

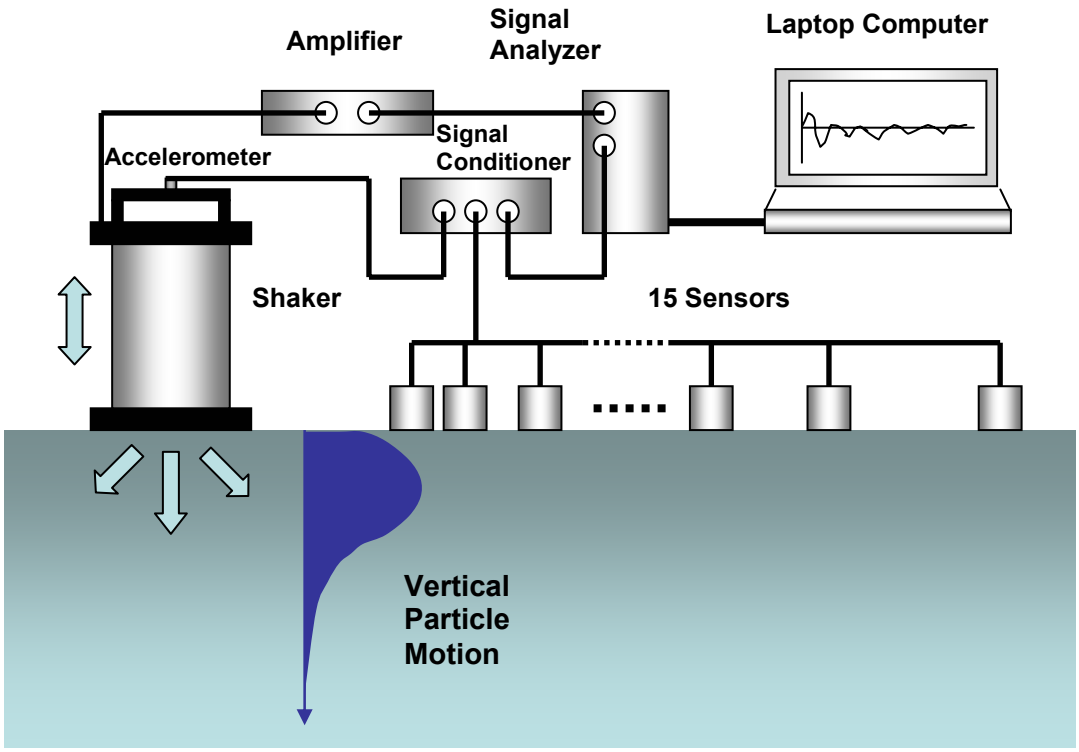

Figure 3.7 Source and data acquisition system for array-based surface wave measurements

3.2.2 Dispersion Calculations

Many techniques are available to calculate Rayleigh phase velocity from multiple receiver measurements. Among them, frequency-wavenumber (f-k) analysis has been widely used in geotechnical and geophysical fields by various researchers (Horike, 1985; Tokimatsu et al., 1992a, 1992b; Tokimatsu, 1995; Zywicki, 1999; Foti, 2000; Liu et al., 2000; Hebeler, 2001; Roma, 2001; Okada, 1993; Yoon and Rix, 2004). Frequency-wavenumber analysis is divided into two subtypes: (1) the *high-resolution f-k* method, also called *maximum-likelihood method*, proposed by Capon (1969) and (2) *frequency domain beamforming* (FDBF) method originally proposed by Lacoss et al. (1969).

Zywicki (1999) compared these f-k spectrum estimators and suggested FDBF method for the following reasons: (1) FDBF method is the most computationally efficient

method, (2) FDBF method is easiest to understand and implement due to the constant structure of the array smoothing function, and (3) FDBF offers the most tractable method for extracting multiple modes. For a more comprehensive discussion of this, see Zywicki (1999).

The FDBF method utilizes multiple receivers arranged in a one-dimensional array for active measurements or a two-dimensional array for passive measurements. The time history, $s(\mathbf{x}_m,t)$ is observed at the m^{th} receiver (m = 1,…,M), which is located at position $\mathbf{x}_m = (x_m,y_m)$. The f-k spectrum is estimated via a process called *beamforming*. $S(\omega_0) = [S(\mathbf{x}_1,\omega_0), \ldots, S(\mathbf{x}_M,\omega_0)]^T$ denotes a column vector containing the Fourier transform of the time history at $\omega = \omega_0$ for each receiver. A *steering vector* is defined by:

$$\mathbf{e}(\mathbf{k}) = [\exp(-i\mathbf{k}\cdot\mathbf{x}_1),\ldots, \exp(-i\mathbf{k}\cdot\mathbf{x}_M)]^T \tag{3.1}$$

where $\mathbf{k} = (k_x,k_y)$ is the vector wavenumber and *T* denotes the transpose of the vector. If the signals are weighted by a diagonal matrix $\mathbf{W} = \text{diag}[w_1,\ldots,w_M]$ that contains the *shading weight* w_m for the m^{th} receiver, the *steered response power spectrum* (Johnson and Dudgeon, 1993) is given by:

$$P(\mathbf{k},\omega_0) = \mathbf{e}^H\mathbf{W}\mathbf{S}\mathbf{S}^H\mathbf{W}^H\mathbf{e} = \mathbf{e}^H\mathbf{W}\mathbf{R}\mathbf{W}^H\mathbf{e} \tag{3.2}$$

where *H* denotes the Hermitian transpose of the vector and **R** is the *spatiospectral correlation matrix* expressed as follows:

$$\mathbf{R}(\omega_0) = \mathbf{S}\mathbf{S}^H = \begin{bmatrix} G_{11}(\omega_0) & G_{12}(\omega_0) & \cdots & G_{1M}(\omega_0) \\ G_{21}(\omega_0) & G_{22}(\omega_0) & \cdots & G_{2M}(\omega_0) \\ \vdots & \vdots & \ddots & \vdots \\ G_{M1}(\omega_0) & G_{M2}(\omega_0) & \cdots & G_{MM}(\omega_0) \end{bmatrix} \tag{3.3}$$

Each term $G_{ij}(\omega_0)$ in the spatiospectral matrix **R** is the *cross-power spectrum* between receivers *i* and *j*:

$$G_{ij}(\omega_0) = S^*(\mathbf{x}_i, \omega_0) S(\mathbf{x}_j, \omega_0) \tag{3.4}$$

where * denotes the complex conjugate.

In practice, it is desirable to use ensemble averaging to reduce the variance of the measured cross-power spectra (Bendat and Piersol, 1986):

$$\hat{G}_{ij}(\omega_0) = \frac{1}{n_d} \sum_{k=1}^{n_d} S_k^*(\mathbf{x}_i, \omega_0) S_k(\mathbf{x}_j, \omega_0) \tag{3.5}$$

where n_d is the number of data blocks for averaging. Consequently, Equation 3.2 becomes:

$$P(\mathbf{k}, \omega_0) = \mathbf{e}^H \mathbf{W} \hat{\mathbf{R}} \mathbf{W}^H \mathbf{e} \tag{3.6}$$

where $\hat{\mathbf{R}}$ denotes a spaciospectral correlation matrix whose elements are the average cross-power spectra between pairs of receivers.

Peaks in the steered response power spectrum for a given frequency ω_0 correspond to the wavenumbers of dominant modes of Rayleigh waves propagating across the array of receivers. These Rayleigh wave phase velocities are calculated using:

$$V_R(\omega_0) = \frac{\omega_0}{|\mathbf{k}_{peak}|} = \frac{2\pi f_0}{|\mathbf{k}_{peak}|} \tag{3.7}$$

where $\mathbf{k}_{peak}$ is a vector quantity in passive tests and a scalar value in active tests.

3.2.2.1 Beamforming for active tests

Beamforming is a powerful tool that can be used for both active and passive surface wave tests. As a first example, consider an active surface wave test performed using a harmonic source. The standard array was used to record vertical particle motion associated with propagating Rayleigh waves. Because the direction of wave propagation is known prior to the test, the wavenumber and receiver locations are scalar values k and

x_m. Figure 3.8 shows an example of the harmonic waves measured at each receiver location for a source frequency of 5.1563 Hz.

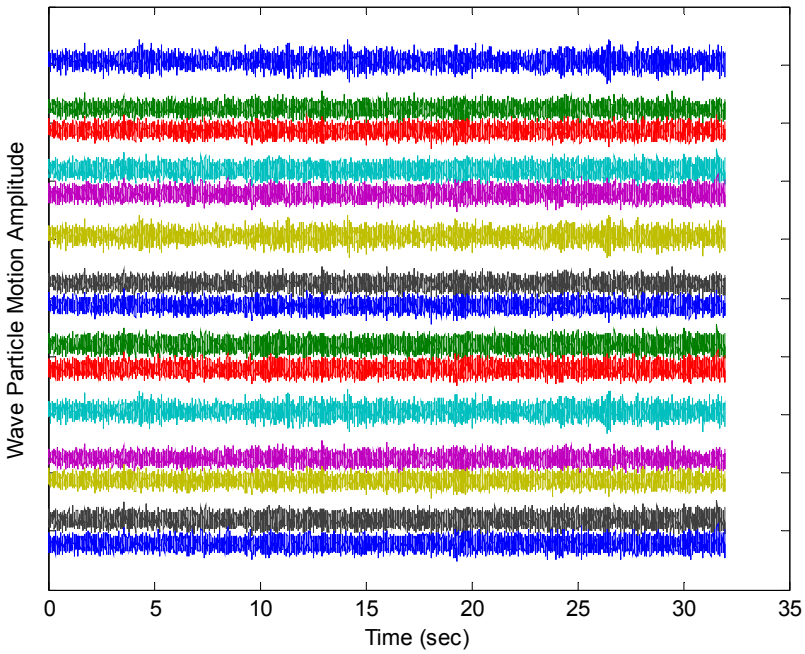

Figure 3.8 Example of time history plots from a harmonic active test

The phase information of the spaciospectral correlation matrix $\hat{\mathbf{R}}$ is illustrated in Figure 3.9. It is important to note that the diagonal elements of the matrix are the autopower spectra of the receivers, and therefore, the phase spectrum is equal to zero at all frequencies.

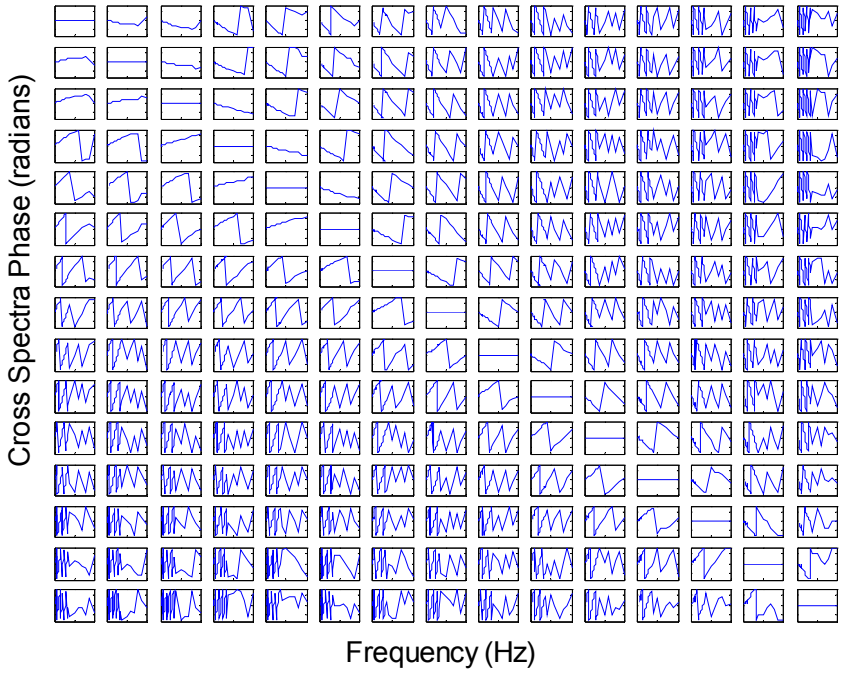

Figure 3.9 Example of graphical representation of a spaciospectral correlation matrix

Once the spatiospectral correlation matrix is obtained, the steered response power spectrum $P(\mathbf{k},\omega)$ is calculated using Equation 3.6. Figure 3.10 shows an example of a steered response power spectrum obtained using the FDBF method.

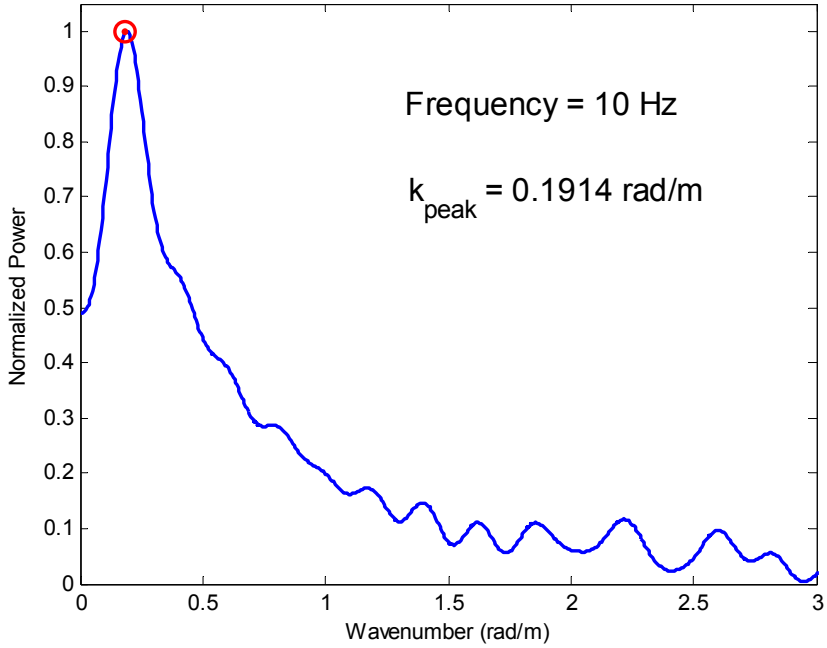

Figure 3.10 Example of a steered response power spectrum at a frequency of 10 Hz. A circle indicates the largest peak.

The largest peak in the steered response power spectrum is the wavenumber of the dominant mode (or combined modes if there is poor wavenumber resolution) at the given frequency. The wavenumber corresponding to the peak (k_{peak}) is used to yield a phase velocity using Equation 3.7. Repeating the procedure for other frequencies leads to a frequency-wavenumber spectrum as shown in Figure 3.11. In addition to choosing the dominant mode, multiple modes may be selected by identifying secondary peaks in the steered response power spectrum at each frequency. Figure 3.12 shows the dispersion curve resulting from selecting only the largest peaks in the steered response power spectrum.

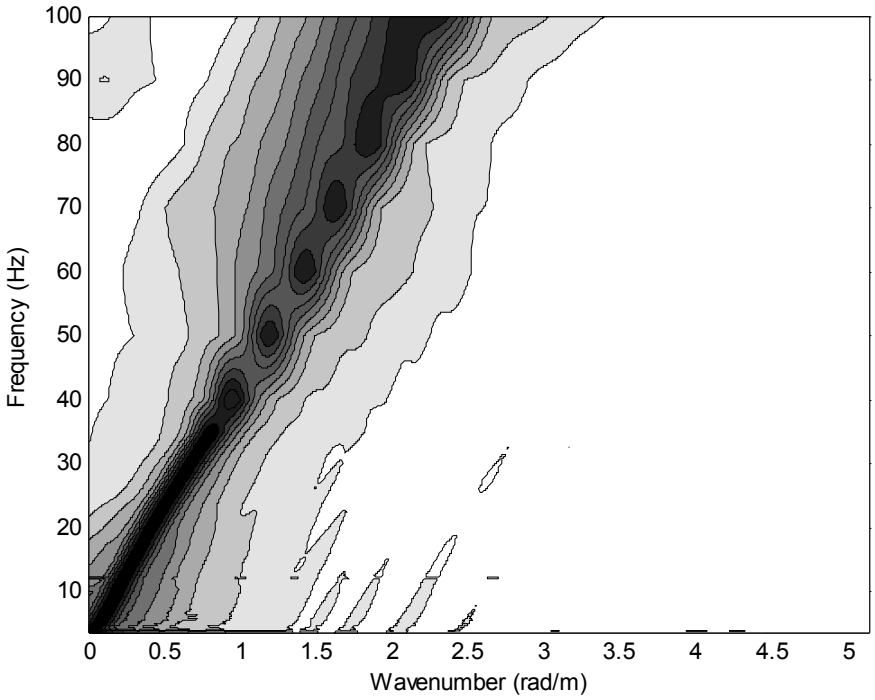

Figure 3.11 Example of a frequency-wavenumber spectrum

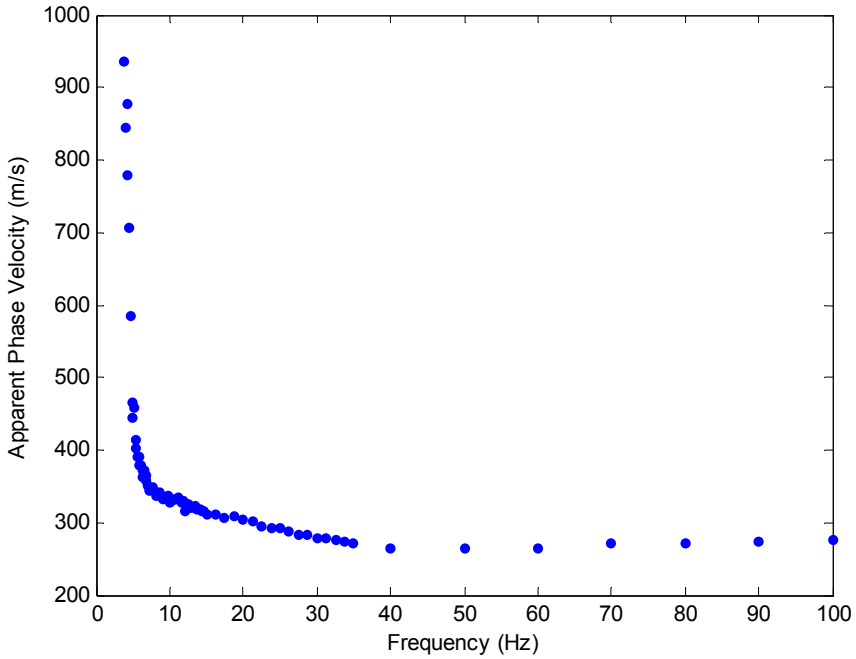

Figure 3.12 Example of a dispersion curve from a harmonic active test

3.2.2.2 Beamforming for passive tests

Beamforming may also be used with passive sources to obtain dispersion data, especially at low frequencies. Unlike an active surface wave test, source location in a passive surface wave test is often not known prior to testing. A two-dimensional array of receivers is required to identify the wavenumber vector **k** at each frequency. Figure 3.13 shows an example of the 2-D steered response power spectrum at the frequency of 5.8594 Hz. Figure 3.14 shows an example of a dispersion curve from a passive test. Note that dispersion data are limited to frequencies less than about 10 Hz.

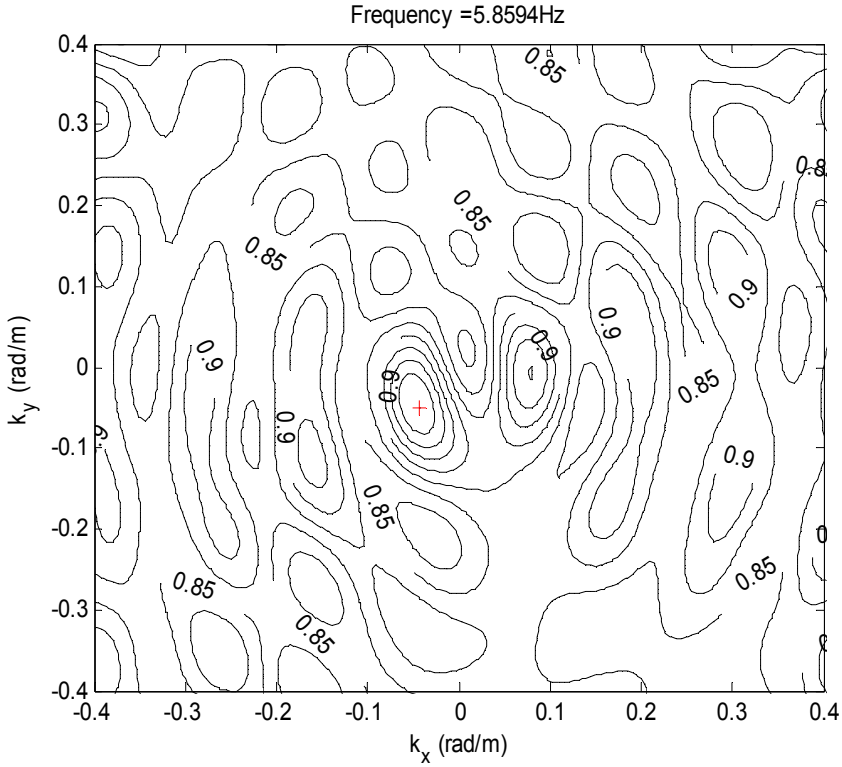

Figure 3.13 Example of a 2-D wavenumber spectrum at frequency of 5.9584 Hz. The + symbol indicates the largest peak.

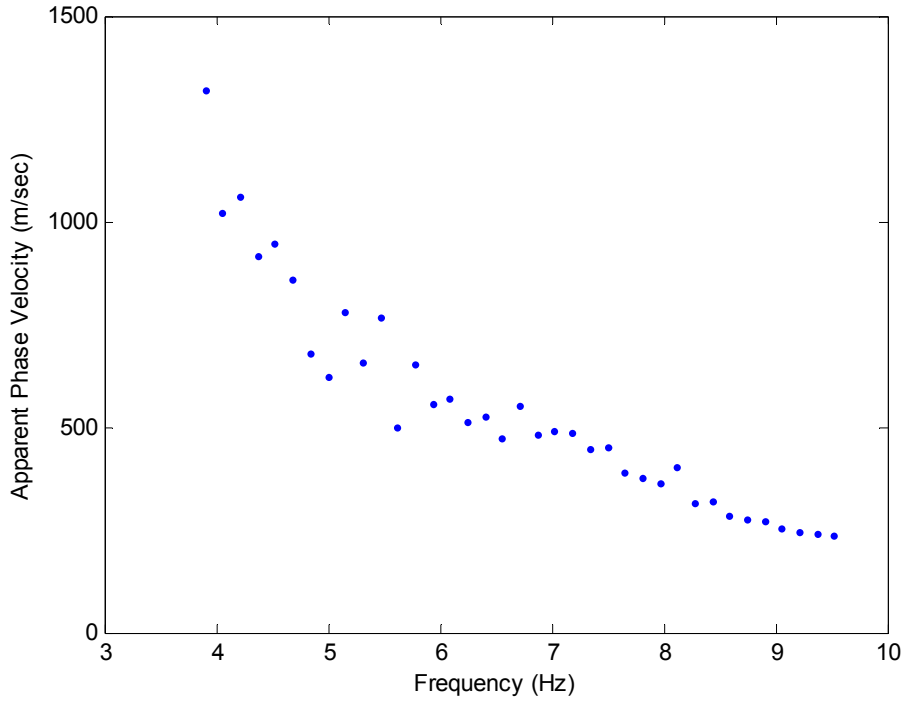

Figure 3.14 Example of a dispersion curve from a passive test

3.2.3 Inversion

The measured dispersion curves are used to determine the shear wave velocity profile via a process called *inversion*. Figure 3.15 shows a flow diagram of the inversion algorithm.

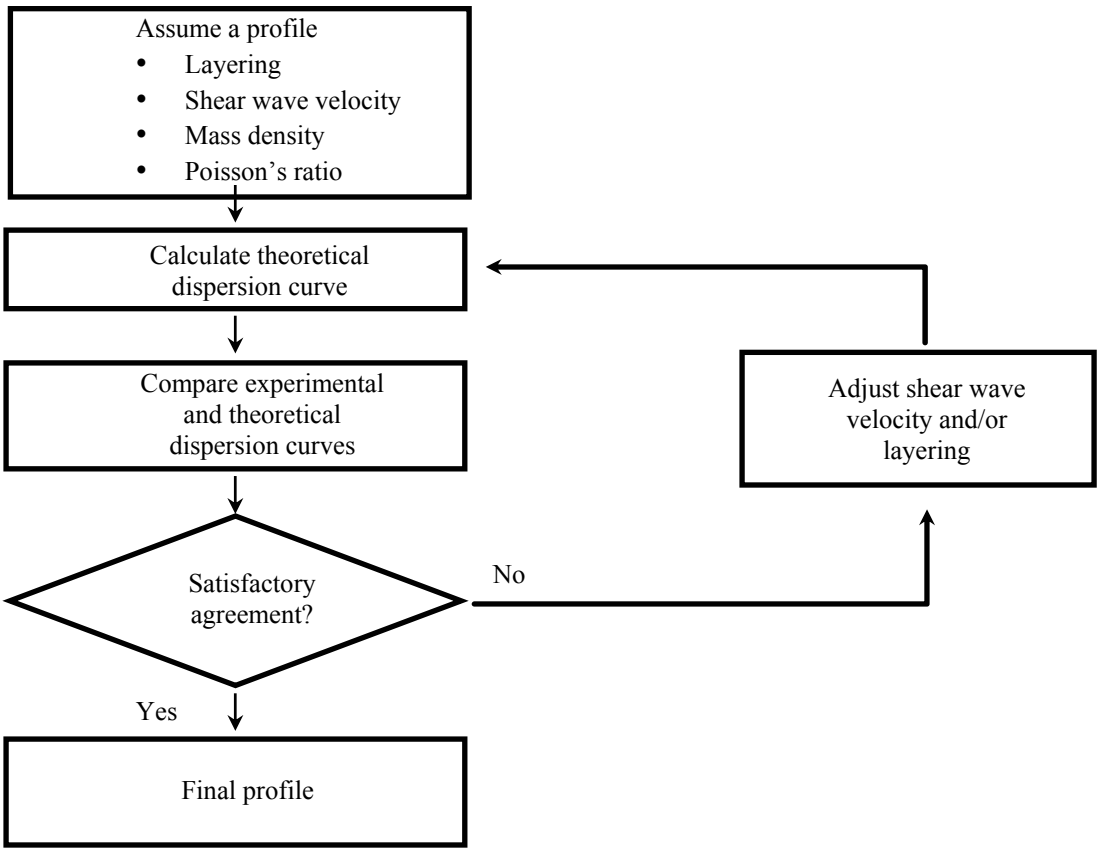

Figure 3.15 Flow chart of inversion algorithm (Rix, 2000)

The inverse problem in surface wave methods is ill-posed due to limited, uncertain experimental data and modeling errors. To solve this ill-posed inverse problem, it is necessary to introduce additional information about the solution (i.e.,V_S profile) into the inversion algorithm. A constrained least-squares inversion algorithm originally proposed by Constable et al. (1987) and implemented by Rix and Lai (1998) and Lai (1998) was employed in the inversion process in this study. The inversion algorithm is an iterative process to find the smoothest shear wave velocity profile yielding a theoretical dispersion curve fitting an experimental dispersion curve with a specified tolerance. In the algorithm, the roughness (the inverse of smoothness) is calculated for a candidate profile using:

$$R_1 = \left\| \delta V_S \right\|^2 \tag{3.8}$$

where δ is the two-point, backward difference operator and is expressed by:

$$\delta = \begin{bmatrix} 0 & \cdots & & & \\ -1 & 1 & & 0 & \\ \cdots & -1 & 1 & & \\ & & \cdots & & \\ & 0 & & -1 & 1 \end{bmatrix}$$

V_S is an $N \times 1$ vector of shear wave velocities, N is the number of layers including the half-space, and $\|\cdot\|$ is the Euclidian norm. Roughness R_1 obtained from Equation 3.8 is the sum of squared differences between V_S values of adjacent layers in the selected profile.

The root-mean-square (*rms*) error between the experimental and theoretical dispersion curves is given by:

$$rms \text{ error} = \left(\frac{\left\| \tilde{\mathbf{W}} \mathbf{V}_R^{exp} - \tilde{\mathbf{W}} \mathbf{V}_R^{theo} \right\|^2}{nf} \right)^{1/2} \tag{3.9}$$

where $\mathbf{V}_R^{\exp}$ is an $nf \times 1$ vector of experimentally measured Rayleigh phase velocities, $\mathbf{V}_R^{theo}$ is an $nf \times 1$ vector of theoretical Rayleigh phase velocities obtained by solving the forward problem associated with a trial shear wave velocity profile, and nf is the number of frequencies. The term $\tilde{\mathbf{W}}$ is an $nf \times nf$ diagonal matrix containing elements reflecting the uncertainty due to errors associated with the measurement of experimental phase velocities and the use of a specific forward model:

$$\tilde{\mathbf{W}} = dia(1/\sigma_1, 1/\sigma_2, \ldots, 1/\sigma_{nf}) \tag{3.10}$$

where σ_j is the total uncertainty associated with $\mathbf{V}_{Rj}^{exp}$ (j=1,…,nf). In practice, the uncertainty is primarily contributed by the modeling error because the layered soil model

consisting of a stack of homogeneous elastic layers overlying a half-space is an idealized representation of actual soil conditions. In this study, it is assumed that σ_j is equal to $0.05 \cdot \mathbf{V}_{Rj}^{exp}$. The uncertainties in surface wave methods require further study.

The solution of the non-linear inverse problem may be obtained by finding a V_S profile minimizing the roughness R_1 with the *rms* error satisfying a specified threshold. The method of Lagrange multipliers is employed to solve this constrained minimization problem as given by:

$$\mathbf{V}_{S(i+1)}(\mu) = \left[\mu\delta^T\delta + (\tilde{\mathbf{W}}\mathbf{J}_i)^T\tilde{\mathbf{W}}\mathbf{J}_i\right]^{-1}(\tilde{\mathbf{W}}\mathbf{J}_i)^T\tilde{\mathbf{W}}\left[\mathbf{J}_i\mathbf{V}_{Si} + \mathbf{V}_R^{exp} - \mathbf{V}_{Ri}^{theo}\right] \tag{3.11}$$

where μ is the Lagrange multiplier, which may be interpreted as a smoothing parameter. The term $\mathbf{J}_i$ is an $nf \times n$ Jacobian matrix whose elements are the partial derivatives of the Rayleigh phase velocities with respect to the shear wave velocities of the layers $\partial V_{Rj}/\partial V_{Sk}$ (j=1,…,nf, k=1,…,N) evaluated at $\mathbf{V}_{Si}$. The partial derivatives are obtained using the variational principle of Rayleigh waves (Aki and Richards, 1980; Lai, 1998), leading to closed-form expressions.

For this non-linear, constrained least-squares inversion algorithm, the uncertainty associated with an estimated shear wave velocity profile is calculated using the following relationship (Lai et al., 2005):

$$\begin{aligned}\mathrm{Cov}[\mathbf{V}_S] \approx &\left[\left(\mu\delta^T\delta + \left(\tilde{\mathbf{W}}\mathbf{J}\right)^T\tilde{\mathbf{W}}\mathbf{J}\right)^{-1}\left(\tilde{\mathbf{W}}\mathbf{J}\right)^T\tilde{\mathbf{W}}\right]\cdot \\ &\cdot \mathrm{Cov}[\mathbf{V}_R]\left[\left(\mu\delta^T\delta + \left(\tilde{\mathbf{W}}\mathbf{J}\right)^T\tilde{\mathbf{W}}\mathbf{J}\right)^{-1}\left(\tilde{\mathbf{W}}\mathbf{J}\right)^T\tilde{\mathbf{W}}\right]^T\end{aligned} \tag{3.12}$$

where $\mathrm{Cov}[\mathbf{V}_R]$ is an $nf \times nf$ matrix of covariances of the experimental Rayleigh phase velocities. Assuming that $\mathbf{V}_R(\omega)$ are uncorrelated, the matrix $\mathrm{Cov}[\mathbf{V}_R]$ is diagonal with

the non-zero elements equal to the variances of $\mathbf{V}_R(\omega)$. Cov$[\mathbf{V}_S]$ is an N$\times$N diagonal matrix whose elements are the variances of the estimated shear wave velocities $\mathbf{V}_{Si}$ with $i = 1,..., \mathrm{N}$.

As discussed earlier, a dispersion curve may represent only the fundamental Rayleigh mode or a combination of multiple Rayleigh modes depending on specific site conditions. For a normally dispersive site, the theoretical dispersion curve corresponding to the fundamental Rayleigh mode is compared to the experimental dispersion curve for the inversion process. For an inversely dispersive site, the inversion process can be performed using an effective dispersion curve as a theoretical dispersion curve or a dispersion curve corresponding to multiple Rayleigh modes as a theoretical dispersion curve. The former method can be used with any experimental dispersion curve showing either modal transition or modal separation, while the latter can be applied to only the curve with sufficient modal separation.

3.3 SPATIAL SAMPLING ISSUES

3.3.1 Array Characteristics

3.3.1.1 Notation for uniform arrays

In this study, a variety of uniform arrays with various numbers of receivers were used for numerical simulations and laboratory simulations. Instead of describing an entire geometry of each array, it would be desirable to develop a way to express it in an abbreviated form.

The notation 1SR1RR-5 is one example of uniform linear arrays expressed in the abbreviated form developed in this study. The array of 1SR1RR-5 denotes a uniform

array of 5 receivers with source-to-first receiver (SR) distance of 1 m and receiver-to-receiver (RR) distance of 1 m. For laboratory simulations described in Chapter 4, the units change from m to cm. The main characteristics of a specific array are determined by SR and RR distances as well as total sampling distance dictated by the total number of receivers. Therefore, the above notation describes all information about a uniform linear array of multiple receivers. The notation is used through the remainder of this dissertation unless otherwise stated. Non-uniform arrays and two-dimensional arrays are described using other means.

3.3.1.2 Source-to-first receiver (SR) distance vs. array center (AC)

The SR distance has been widely used to represent an array of two receivers in traditional SASW methods, especially for the study of near-field effects. Since most SASW methods have used a simple array configuration with the same SR and RR distances, the SR distance is a good parameter representing the array configuration. However, the SR distance alone incompletely describes arrays of arbitrarily placed, multiple receivers. The array center (AC) that is the average distance of all receivers from a source was suggested as a more representative distance for an array of arbitrarily placed multiple receivers (Yoon and Rix, 2004).

3.3.2 Effects of Finite Sampling in Space

Perfect spatial sampling of a signal requires measurements at all possible locations. In practice, however, the signal is sampled only at a finite number of receiver locations. This limitation influences our ability to determine a wavenumber associated with the signal from a steered response power spectrum.

For simplicity, consider a one-dimensional signal propagating along the x direction. The signal *s(x,t)* may be sampled for a finite sampling distance *D* yielding:

$$z(x,t) = w(x)s(x,t) \tag{3.13}$$

where *w(x)* is a spatial array in the x direction defined by:

$$w(x) = \begin{cases} 1 & 0 \le x \le D \\ 0 & otherwise \end{cases} \tag{3.14}$$

The Fourier transform of *z(x,t)* can be expressed as the convolution of the spatial Fourier transforms of *w(x)* and *s(x,t)*:

$$Z(k,t) = \int_{-\infty}^{\infty} W(k-\zeta)S(\zeta,t)d\zeta \tag{3.15}$$

where ζ is a dummy variable. Equation 3.15 can be rewritten by:

$$Z(k,t) = W(k) * S(k,t) \tag{3.16}$$

where *W(k)* is the Fourier transform of the spatial array *w(x)* in Equation 3.14, which can be calculated using:

$$W(k) = \int_{-\infty}^{\infty} w(x)e^{-ik\cdot x}dx = D\cdot e^{-i\frac{kD}{2}} \cdot \left(\frac{\sin\frac{kD}{2}}{\frac{kD}{2}} \right) \tag{3.17}$$

The magnitude of *W(k)* is given by:

$$|W(k)| = D\left| \frac{\sin\frac{kD}{2}}{\frac{kD}{2}} \right| \tag{3.18}$$

Equation 3.18 is plotted as shown in Figure 3.16. The effects of finite sampling in space are apparent; as the total sampling distance *D* increases, *W(k)* becomes closer in shape to the impulse $\delta(k)$ and *Z(k,t)* approximates the transformed original signal *S(k,t)*

more closely. According to the Rayleigh criterion, the wavenumber resolution is defined one half of the mainlobe width of *W(k)*:

$$\Delta k_{Rayleigh} = \frac{2\pi}{D} \tag{3.19}$$

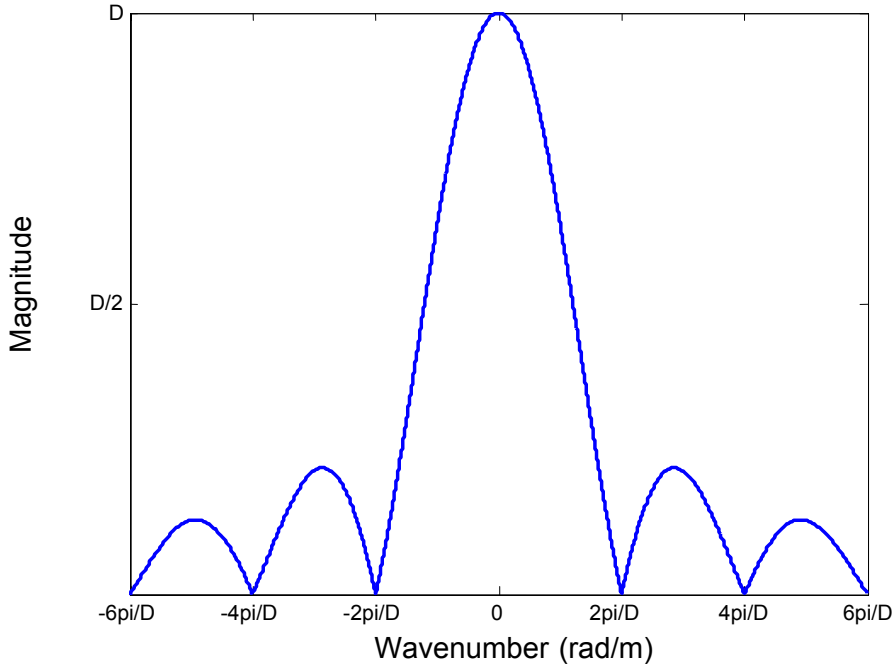

Figure 3.16 Fourier transform of the spatial window *w(x)*

The signal is sampled at discrete spatial locations in practice rather than continously. Consider a one-dimensionally propagating signal that is sampled through an array of receivers placed at various spatial locations x_m. For this case, the discrete spatial window and its Fourier transform are newly defined as:

$$w(x) = \sum_{m=1}^{M} w_m \delta(x - x_m) \tag{3.20}$$

$$W(k) = \sum_{m=1}^{M} w_m e^{ik \cdot x_m} \tag{3.21}$$

where M is the number of receivers in the array and w_m is a *shading weight* for the m^{th} receiver.

Like other filters, the signal is smoothed by the kernel *W(k)* once it is measured by an array of receivers. Assuming perfect sampling, the ideal array smoothing kernel would be an impulse function in the x direction. However, realistic spatial data collection is performed in a finite, discrete manner governed by the number of available receivers and capability of the data acquisition system. To maximize the filter performance to accurately measure the wavenumber components of a signal, the effects of finite spatial sampling must be taken into consideration with special care. From a spatial signal processing point of view, Equation 3.21 is especially called the *array pattern* or *array smoothing function* (ASF) (Johnson and Dudgeon, 1993), and it can be utilized to characterize a given array geometry.

Another consequence of the finite spatial sampling is *spatial aliasing*. To avoid aliasing in wavenumber, the minimum spatial lag d_{min} in the array must be smaller than a half of the smallest wavelength λ_{min} of measured waves. The largest wavenumber that can be measured without spatial aliasing is called the *Nyquist wavenumber* ($k_{Nyquist}$) and is related to the minimum spatial lag in the array as follows:

$$k_{Nyquist} = \frac{2\pi}{\lambda_{min}} = \frac{\pi}{d_{min}} \tag{3.22}$$

As described in Equation 3.19 and 3.22, two important array characteristics, wavenumber resolution and spatial aliasing, are related to the maximum spatial lag D and the minimum spatial lag d_{min} in the array, respectively.

In addition to the wavenumber resolution and spatial aliasing, another important array characteristic is associated with sidelobes. As shown in Figure 3.16, there are

sidelobes adjacent to the mainlobe in the ASF. The heights and locations of sidelobes are associated with energy leakage. Energy leakage resulting from large sidelobe heights may yield spurious peaks in wavenumber spectra of the filtered wavefield, leading to incorrectly-estimated dispersion data.

For a fixed number of receivers, there is a trade off between spatial aliasing and wavenumber resolution. The use of a linear array with irregularly-spaced receivers is one means of achieving a good balance between these competing objectives. Figure 3.17 shows the geometries of three different linear arrays having the same number of receivers. Array 1 is the standard array (i.e., non-uniform spacing). Array 2 and Array 3 are linear arrays of uniformly-spaced 15 receivers with the same maximum spatial lag (31.1 m) and the same minimum spatial lag (0.6 m) as Array 1, respectively. The characteristics of three arrays are tabulated in Table 3.1, and array smoothing functions of these arrays are compared in Figure 3.18.

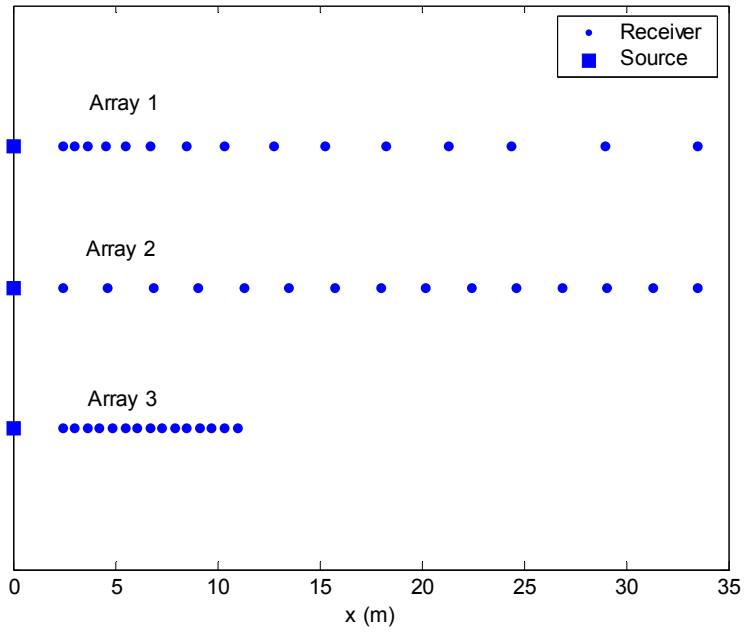

Figure 3.17 Geometries of three linear arrays with 15 receivers

Table 3.1 Comparison of characteristics of three linear arrays with 15 receivers

	Max. spatial lag, D (m)	Min. spatial lag, d_{min} (m)	Wavenumber resolution, Δk (rad/m)	Nyquist wavenumber, $k_{Nyquist}$ (rad/m)
Array 1	31.1	0.6	0.202	5.152
Array 2	31.1	2.2	0.202	1.414
Array 3	8.5	0.6	0.739	5.152

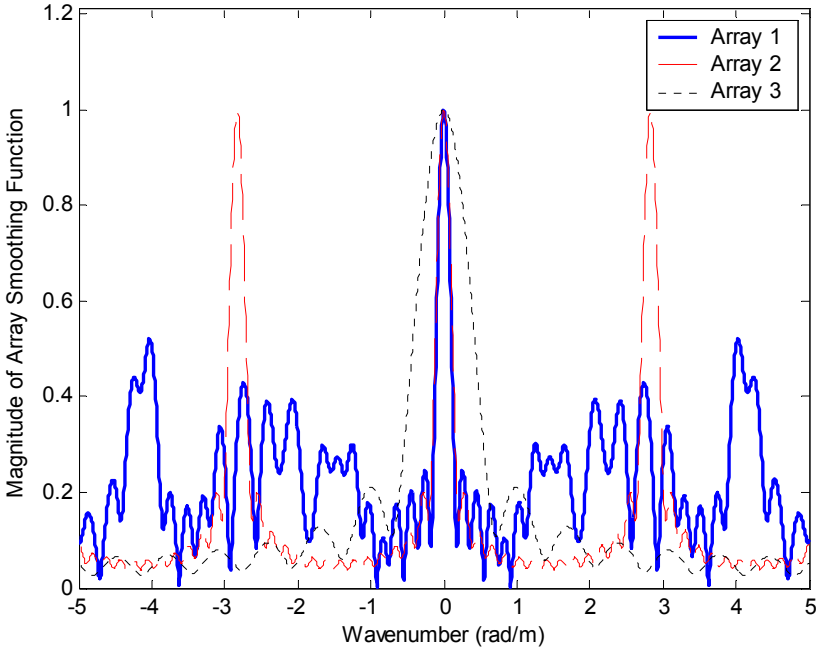

Figure 3.18 Comparison of ASFs of three linear arrays with 15 receivers

When calculating the array smoothing function in Equation 3.21, the shading weight was selected as:

$$w_m = \sqrt{x_m} \tag{3.23}$$

to approximately account for the geometric spreading of Rayleigh waves. Zywicki (1999) demonstrated that better wavenumber resolution was obtained by using Equation 3.23 than other normalization techniques.

Two important features of the ASF are mainlobe width and sidelobe height, which control wavenumber resolution and energy leakage, respectively. As shown in Figure 3.18, Arrays 1 and 2 with the larger maximum spatial lag D (31.1 m) have narrower mainlobe widths in their array smoothing functions, representing better spatial resolution, compared to that of Array 3 with the smaller D (8.4 m). Arrays 1 and 3 with the smaller minimum spatial lag d_{min} (0.6 m) have a larger distance between adjacent primary peaks in wavenumber, while Array 2 with the larger d_{min} (2.2 m) has a large peak at a smaller wavenumber interval, yielding a smaller $k_{Nyquist}$. It is also important to note that the sidelobes of Array 1 are larger in magnitude than those associated with other two arrays, leading to poorer control in energy leakage. A sidelobe height becomes important in multiple signals having similar magnitudes at the same frequency because it may reinforce signals with smaller magnitudes yielding spurious peaks (Zwyicki, 1999).

It is also instructive to examine the characteristics of these arrays using a multi-modal signal composed of two ideal plane waves having different phase velocities:

$$s(x,t) = s_1(x,t) + s_2(x,t) \tag{3.24a}$$

$$s_1(x,t) = e^{i(\omega_0 t - \frac{\omega_0}{V_1}x)} \tag{3.24b}$$

$$s_2(x,t) = e^{i(\omega_0 t - \frac{\omega_0}{V_2}x)} \tag{3.24c}$$

where, V_1 and V_2 are phase velocities of the two waves.

The signal in Equation 3.24a is measured by the three different arrays in Figure 3.17. A signal composed of two waves with V_1 of 200 m/sec and V_2 of 160 m/sec was generated at a frequency of 40 Hz. Figure 3.19 shows the normalized power spectra of the measurements using these arrays over a wide range of wavenumbers. The

wavenumbers corresponding to these velocities at the frequency are 1.257 rad/m and 1.571 rad/m, and the difference between the wavenumbers is 0.314 rad/m. In order to successfully separate the two wavenumbers, a wavenumber resolution of an array must be sufficiently small compared to the wavenumber difference. As seen in Figure 3.19, Array 3 is unable to isolate the two waves due to its poor wavenumber resolution, while Arrays 1 and 2 with wavenumber resolutions smaller than the wavenumber difference are able to do so.

Another important consequence of the finite spatial sampling, i.e. spatial aliasing, can be observed by comparing the wavenumber spectra of Array 2 with the others. As discussed, Array 2 with the larger d_{min} has a smaller $k_{Nyquist}$ than other arrays, making it incapable of measuring a wavenumber greater the $k_{Nyquist}$ as shown in Figure 3.19. It can be concluded that Array 1 appears to be a good choice to balance between wavenumber resolution and spatial aliasing.

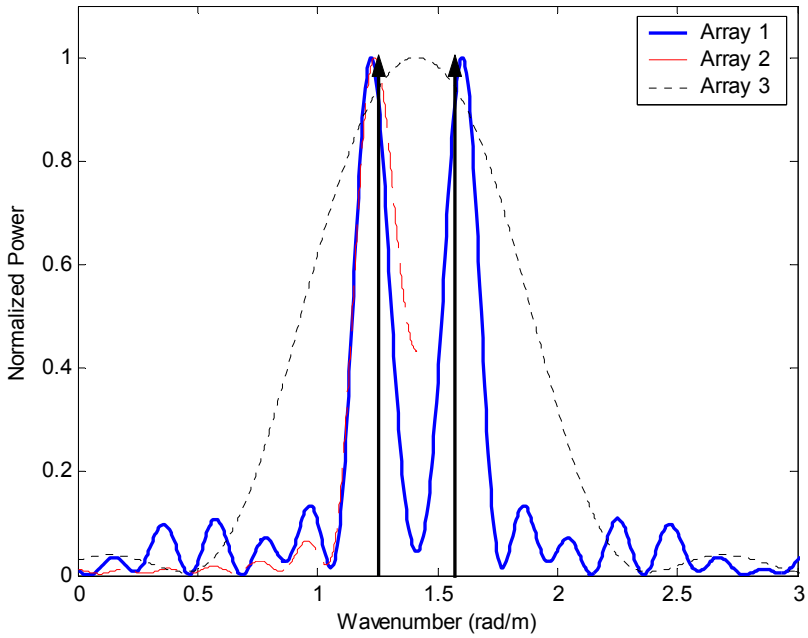

Figure 3.19 Comparison of wavenumber spectra using the three different linear arrays

The concept may be easily extended to determine the array smoothing function associated with two-dimensional arrays of discrete receivers. The spatial window and the ASF associated with a two-dimensional array are derived easily from those of a linear array (Equations 3.20 and 3.21) and are given by:

$$w(\mathbf{x}) = \sum_{m=1}^{M} w_m \delta(\mathbf{x} - \mathbf{x}_m) \tag{3.25}$$

$$W(\mathbf{k}) = \sum_{m=1}^{M} w_m e^{i\mathbf{k}\cdot\mathbf{x}_m} \tag{3.26}$$

Figure 3.20 shows a contour plot of the ASF of a 16-receiver circular array with a radius of 30 m. The receivers are equally spaced along the circumference of the circular array. For active tests, the sidelobes are smaller because we only have to sample one direction with a given number of receivers. For passive tests, we use the same number of receivers to sample two directions (x and y). Thus, we cannot sample the 2-D space as well as the 1-D space, leading to higher sidelobes for 2-D spacing. Sidelobes become more important in passive tests than active tests.

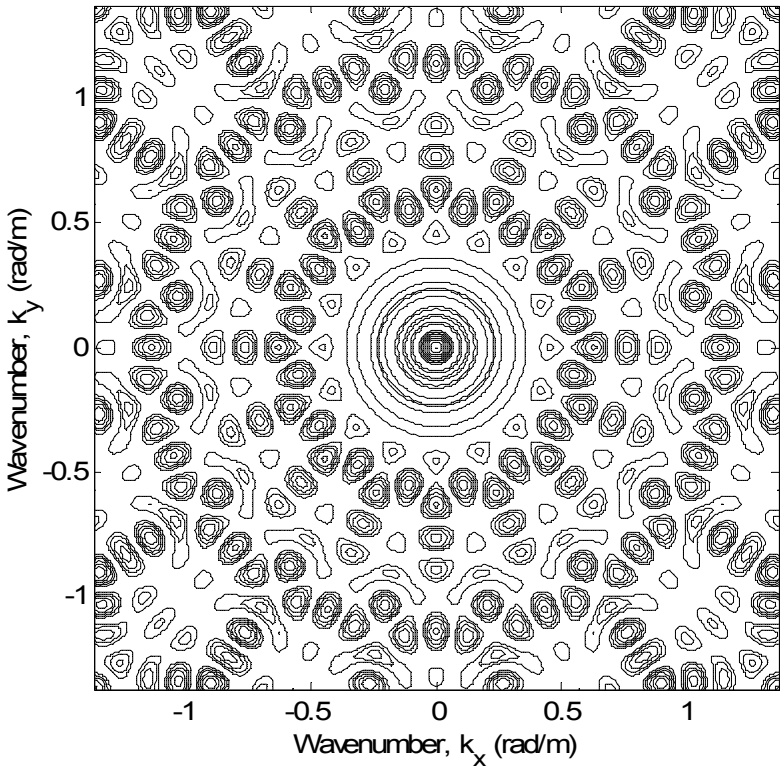

Figure 3.20 Array smoothing function of a 16-receiver circular array with a radius of 30 m

3.3.3. Examples of Array Effects

To further illustrate the limitations of finite spatial sampling, Figure 3.21 shows the comparison of dispersion curves from the Green's function solutions of plane Rayleigh waves with three different arrays to modal dispersion curves of Rayleigh waves from the Rayleigh dispersion equation in the normally and inversely dispersive soil profiles in Tables 2.2 and 2.3, respectively. For the normally dispersive soil profile as shown in Figure 3.21(a), all of three dispersion curves agree reasonably well with the fundamental mode dispersion curve as expected. However, it is important to note that dispersion curves associated with arrays of 1SR1RR-5 and 1SR1RR-15 differs slightly from the dispersion curve of the fundamental Rayleigh mode due to array effects. Increasing the number of receivers to 100 (with the same SR and RR distances) improves the match

between the dispersion curve of Green's functions of plane Rayleigh waves and the fundamental dispersion curve significantly.

For the inversely dispersive soil profile as shown in Figure 3.21(b), higher modes of propagation become dominant as the frequency increases. While the dispersion curves from Green's function solutions of plane Rayleigh waves are primarily controlled by only the fundamental mode at frequencies below about 10 Hz, they are controlled by higher modes at frequencies greater than about 10 Hz. Note that the uniform arrays of 5 and 15 receivers are unable to separate the individual modes in the dispersion curves, while a uniform array of 100 receivers succeeds in isolating individual modes over the frequency range up to 100 Hz. From Figure 3.21, it is concluded that the use of the array of 100 receivers leads to dispersion curves with negligible array effects.

Array effects also become more important for passive methods where a limited number of receivers must sample two spatial dimensions. Array effects on passive methods will be discussed in more detail in Chapter 5.

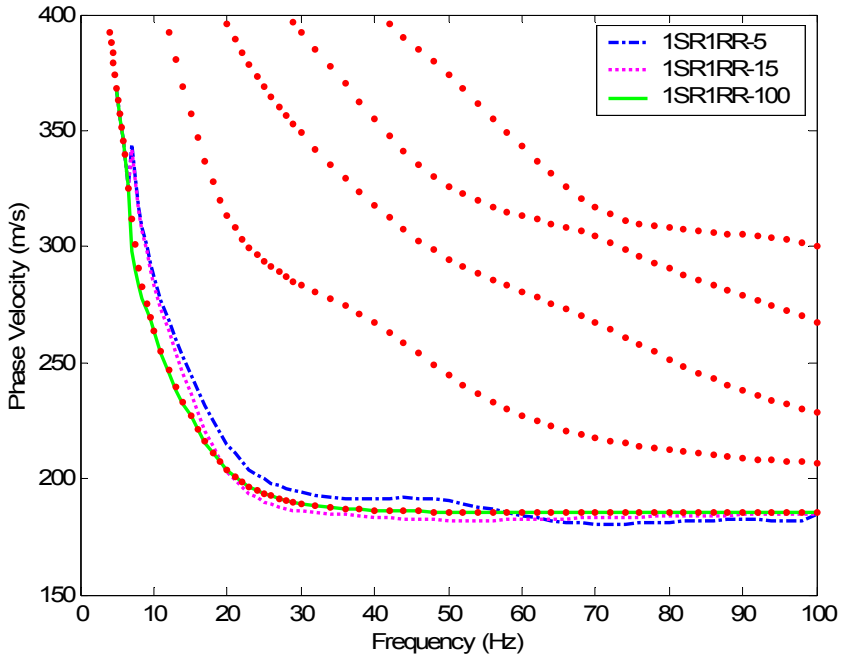

(a)

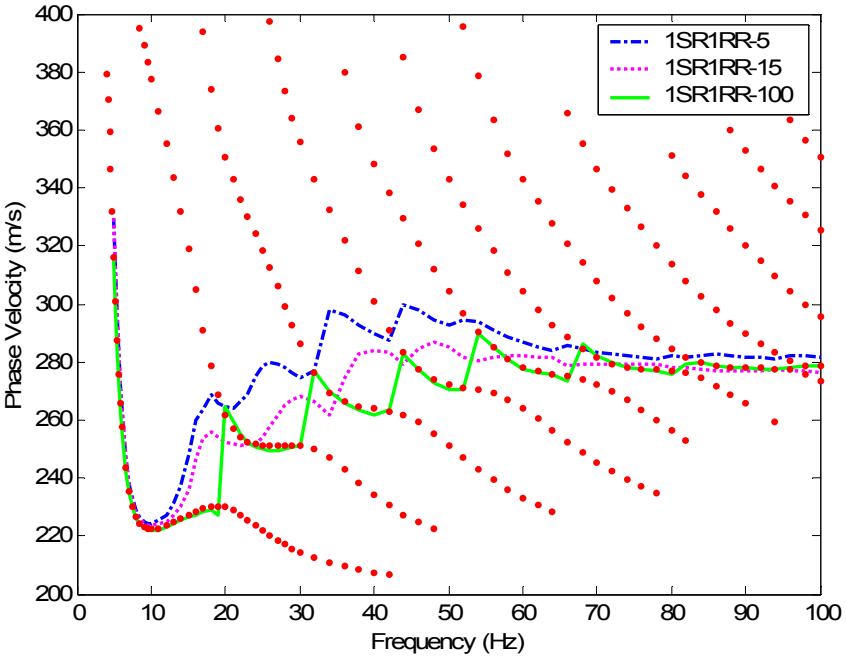

(b)

Figure 3.21 Array effects on array-based surface wave methods in (a) normally, and (b) inversely dispersive soil profiles. Dots represent modal dispersion curves in an increasing order from left to right

CHAPTER 4

NEAR-FIELD EFFECTS ON ARRAY-BASED SURFACE WAVE METHOD

4.1 INTRODUCTION AND STATEMENT OF THE PROBLEM

In most surface wave methods, dispersion estimates and inversion procedures are based on the assumption that the wavefield consists only of plane Rayleigh waves. This is likely true when passive surface wave tests are performed because passive waves are typically generated by distant sources and body wave components are negligible. However, active sources are often placed relatively close to the receiver array, leading to cylindrically propagating Rayleigh waves and significant body waves. The region where the assumption of plane Rayleigh waves is not valid is called the *near-field*, and any adverse effect resulting from the invalid assumption is called a *near-field effect*.

It is important to distinguish this definition of a near-field effect from others found in the literature. Strong coupling between the P- and S-waves is present close to the source and the coupling becomes negligible far from the source, leading to the separate P- and S-wave components (Tang, Toksöz, and Chen, 1997). Two types of body waves appear in a wavefield; one propagating at the P-wave velocity and the other propagating at the S-wave velocity. When attempting to monitor particle motions associated with the P-waves, the motions associated with the S-waves represent a near-field effect, which decreases with increasing a distance from the source. When exciting pure S-wave motions, the P-wave motions result in a near-field effect.

For a point load X_0(t) in the x_j-direction at the origin applied to a homogeneous and isotropic medium, the displacement from Green's function is calculated by (Aki and Richards, 1980):

$$\begin{aligned} u_i(\mathbf{x},t) = & \frac{1}{4\pi\rho}(3\gamma_i\gamma_j - \delta_{ij})\frac{1}{r^3}\int_{r/\alpha}^{r/\beta} \tau X_0(t-\tau)d\tau \\ & + \frac{1}{4\pi\rho\alpha^2}\gamma_i\gamma_j\frac{1}{r}X_0(t-\frac{r}{\alpha}) \\ & - \frac{1}{4\pi\rho\beta^2}(\gamma_i\gamma_j - \delta_{ij})\frac{1}{r}X_0(t-\frac{r}{\beta}) \end{aligned} \tag{4.1}$$

where r is the source-to-receiver distance, $\gamma_i = x_i/r$ is the direction cosine, δ_{ij} is the Kronecker delta ($\delta_{ij} = 0$ for $i \neq j$ and $\delta_{ij} = 1$ for $i = j$), α is the P-wave phase velocity, V_P, and β is the S-wave phase velocity, V_S.

The first term of Equation 4.1 behaves like r^{-2}, while the remaining terms in the equation behave like r^{-1}. The terms including $r^{-1}X_0(t\text{-}r/\alpha)$ and $r^{-1}X_0(t\text{-}r/\beta)$ are dominant over the first term including as $r \rightarrow \infty$ and are therefore called far-field terms(Aki and Richards, 1980). Since r^{-2} is dominant over r^{-1} as $r \rightarrow 0$, the term including $r^{-3}\int \tau X_0(t-\tau)d\tau$ is called a near-field term (Aki and Richards, 1980). Since the near-field term is attenuated more rapidly compared to the far-field terms, each body wave is composed only of its far-field term at a distance relatively far from the source, indicating an insignificant near-field effect. In this study, body waves (P- and S-waves) are composed only of the far-field terms in Equation 4.1.

There are two main causes of near-field effects on surface wave methods (Zywicki, 1999): (1) model incompatibility between plane and cylindrical Rayleigh waves and (2) body wave interference. Both effects diminish with increasing distance between the source and a given receiver. As the distance increases, the Rayleigh wave front from a

point source will more closely approximate a plane wave. Also, since the amplitude of body waves decreases more rapidly with distance than Rayleigh waves, the interference from body waves will decrease with increasing distance. Frequency (or wavelength) is another important factor influencing near-field effects because high-frequency body waves will attenuate more rapidly with distance due to material damping.

Near-field effects have been studied and discussed in the traditional two-receiver surface wave method, i.e., SASW method (Heisey *et al*., 1982; Sanchez-Salinero *et al*., 1987; Hiltunen and Woods, 1990; Gucunski and Woods, 1992; Al-Hunaidi, 1993). Most SASW tests using two receivers are performed with the source-to-first receiver (SR) distance identical to the receiver-to-receiver (RR) distance. Most filtering criteria for near-field effects on the traditional SASW method have been expressed as functions of the ratio between the wavelength of a Rayleigh wave and a SR distance. For consistency with the notation used in previous studies, the wavelength of a Rayleigh wave, the SR distance, and the RR distance for the array of two receivers are denoted by λ_R, d_1, and Δd, respectively. The filtering criteria for near-field effects on the traditional SASW method suggested in these previous studies are summarized in Table 4.1.

Table 4.1 Summary of filtering criteria for near-field effects on SASW tests

Reference	Filtering criterion	Receiver configuration	Method of study
Heisey et al. (1982)	$\lambda_R < 3d_1$	$\Delta d/d_1 = 1$	Numerical
Sanchez-Salinero et al. (1987)	$\lambda_R < 0.5d_1$*	$\Delta d/d_1 = 1$	Numerical
Roesset et al. (1990)	$\lambda_R < 2d_1$	$\Delta d/d_1 = 0.2$, 0.5, 1, and 2	Numerical
Hiltunen & Woods (1990)	$\lambda_R < 2\Delta d$ and $d_1/\Delta d \leq 2$	$\Delta d/d_1 = 0.33 \sim 2$	Experimental
Gucunski & Woods (1992)	$\lambda_R < d_1$	$\Delta d/d_1 = 1$	Numerical
Al-Hunaidi (1993)	N/A	$\Delta d/d_1 = 1$	Numerical

* It was also recommended that the criterion of $\lambda_R < d_1$ could be used if more data were required in the low-frequency range.

The criteria shown in Table 4.1 differ significantly, which may result from: (1) the poor dispersion estimation capability of the traditional SASW methods (Zywicki, 1999), (2) inconsistent site conditions (Al-Hunaidi, 1993), and (3) different receiver configurations in some studies. As indicated by many researchers (Sanchez-Salinero, 1987; Al-Hunaidi, 1993; Tokimatsu, 1995), the severity of near-field effects is dependent on site conditions. It was reported that near-field effects resulted in larger errors in dispersion estimates for inversely dispersive site conditions (Sanchez-Salinero, 1987; Tokimatsu, 1995). In addition, it is important to note that most of the criteria are based on numerical simulations with only limited experimental validation. It is desirable to complement the results of numerical simulations with laboratory and field testing. Finally, few of the previous studies have quantified the magnitude of the errors associated with near-field effects. It is desirable to present near-field criteria that are more quantitatively based.

It has been stated that array-based active surface wave tests employing f-k analysis are less prone to the near-field effects than the traditional SASW method (Tokimastu, 1995; Foti, 2000; Hebeler, 2001). However, the phenomenon has not been widely studied and no specific criterion to mitigate and identify the level of near-field effects has been suggested. In this study, three methods are used to investigate near-field effects on array-based surface wave methods: (1) numerical simulations using Green's functions, (2) laboratory simulations using a two-dimensional experimental model, and (3) field tests.

4.2 NUMERICAL SIMULATIONS

As discussed in Chapter 2, Green's functions provide mathematical means to simulate a real active surface wave test. In this study, numerical simulations of active surface wave tests are performed with the program PUNCH (Kausel, 1981).

4.2.1 Typical Soil Profiles

An ideal homogeneous half-space and three other soil profiles representing actual soil deposits are chosen for numerical simulation. Material properties including layer thickness, shear wave velocity (V_S), Poisson's ratio (ν), damping ratio (D), and mass density (ρ) for the four cases are described in Tables 4.2 through 4.5, respectively. The Case 1 soil profile is a simple homogeneous half-space that severs as an important point of reference for the parametric study. A regular soil profile where the stiffness of layers increases with increasing depth is represented by Case 2. This type of soil profile is often encountered in real situations and is designated as a normally dispersive soil profile (Tokimatsu, 1995). The two soil profiles in Case 3 and Case 4 represent two typical types in irregular soil profiles where a soft layer is trapped between two stiffer layers and a stiff

layer is trapped between two softer layers, respectively. These profiles are designated as inversely dispersive soil profiles. Figure 4.1 shows the shear wave velocity profiles of these four soil conditions.

Table 4.2 Medium properties of a soil profile (Case 1)

Layer No.	Thickness (m)	V_S (m/sec)	Poisson's ratio, ν	Damping ratio, D (%)	Mass density, ρ (t/m^3)
Half-Space	∞	200	0.3	0	1.8

Table 4.3 Medium properties of a soil profile (Case 2)

Layer No.	Thickness (m)	V_S (m/sec)	Poisson's ratio, ν	Damping ratio, D (%)	Mass density, ρ (t/m^3)
1	5	200	0.3	0	1.8
2	10	300	0.3	0	1.8
3	10	400	0.3	0	1.8
Half-Space	∞	500	0.3	0	1.8

Table 4.4 Medium properties of a soil profile (Case 3)

Layer No.	Thickness (m)	V_S (m/sec)	Poisson's ratio, ν	Damping ratio, D (%)	Mass density, ρ (t/m^3)
1	5	300	0.3	0	1.8
2	10	200	0.3	0	1.8
3	10	400	0.3	0	1.8
Half-Space	∞	500	0.3	0	1.8

Table 4.5 Medium properties of a soil profile (Case 4)

Layer No.	Thickness (m)	V_S (m/sec)	Poisson's ratio, ν	Damping ratio, D (%)	Mass density, ρ (t/m^3)
1	5	200	0.3	0	1.8
2	10	400	0.3	0	1.8
3	10	300	0.3	0	1.8
Half-Space	∞	500	0.3	0	1.8

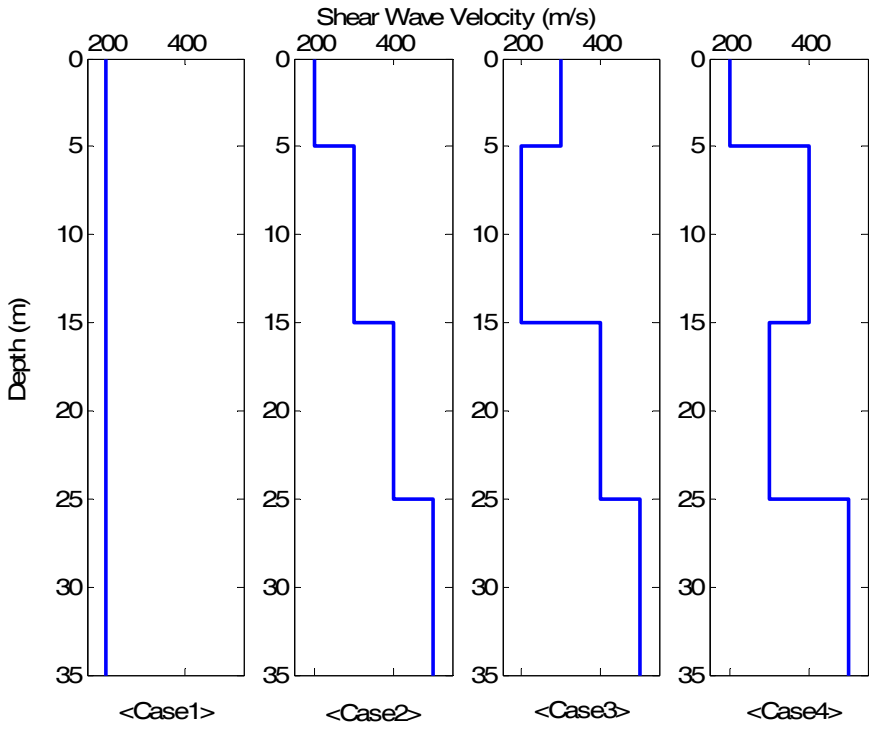

Figure 4.1 Shear wave velocity profiles of four typical soil profiles

4.2.2 Two Normalized Parameters to Evaluate Near-Field Effects

In this study, two dimensionless parameters are suggested for the study of near-field effects in array-based surface wave methods:

$$Normalized\ \ Array\ Center = \frac{AC}{\lambda_R} = \frac{AC \cdot f_0}{V_R} \tag{4.2}$$

$$Normalized\ \ Rayleigh\ Wave\ Velocity = \frac{V_R}{V_{R,plane}} \tag{4.3}$$

where AC is the array center that is the average distance of all receivers in an array relative to the source, V_R is the measured Rayleigh wave velocity at frequency f_0 and $V_{R,plane}$ is the plane Rayleigh wave velocity at the same frequency.

The normalized AC is a function of two important factors (distance from the source and wavelength) associated with errors due to near-field effects. The normalized

Rayleigh wave velocity is composed of the measured Rayleigh wave velocity including near-field effects (V_R) and the reference Rayleigh wave velocity free from near-field effects ($V_{R,plane}$) and represents the relative error due to near-field effects. The reference Rayleigh wave velocity $V_{R,plane}$ is calculated from the solutions of the plane Rayleigh Green's functions associated with the array configuration used for the calculation of V_R. Calculating $V_{R,plane}$ in this manner includes array effects due to limited spatial sampling. Therefore, array effects cancel in the normalized Rayleigh wave velocity, leading to relative errors associated only with near-field effects.

4.2.3 Array Center as an Indicator of Near-Field Effects

The advantages of using the array center (AC) compared to the source-to-first receiver (SR) distance as a representative distance for a multiple-receiver array are demonstrated with numerical results in a homogeneous half-space. Numerical simulations with two sets of uniform arrays were carried out for the Case 1 soil profile. The numerical simulations were performed using the Green function program PUNCH for a set of 69 frequencies ranging from 5 to 100 Hz. Figure 4.2 shows a comparison of dispersion curves associated with two sets of arrays: the first set is composed of five, 15-receiver arrays with various SR distances and the second set is composed of five arrays with different numbers of receivers. The fact that near-field effects become more significant with decreasing frequency and with decreasing distance from the source are well illustrated in Figure 4.2.

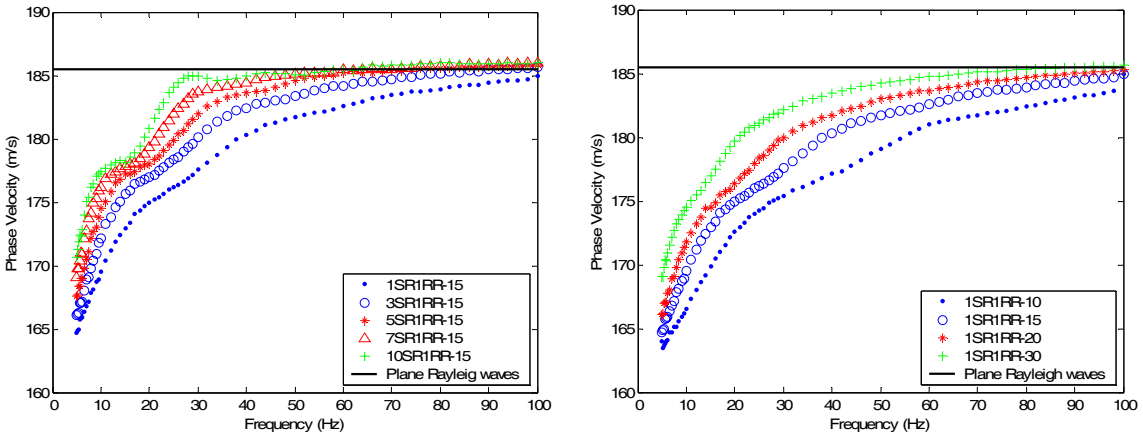

(a) (b)

Figure 4.2 Comparison of dispersion curves associated with various arrays in a homogeneous half-space

With the dispersion curves from Figure 4.2(a), normalized Rayleigh wave velocities are plotted as functions of normalized AC (Figure 4.3(a)) and normalized SR distance (Figure 4.3(b)). With the dispersion curves from Figure 4.2(b), plots of normalized Rayleigh wave velocities are made as functions of normalized AC (Figure 4.4(a)) and normalized SR distance (Figure 4.4(b)). As shown in Figures 4.3 and 4.4, the normalized AC successfully captures the trend of the near-field effects on array-based surface wave tests with various arrays, whereas the normalized SR distance does not. In this study, the normalized AC is subsequently used as an indicator of near-field effects.

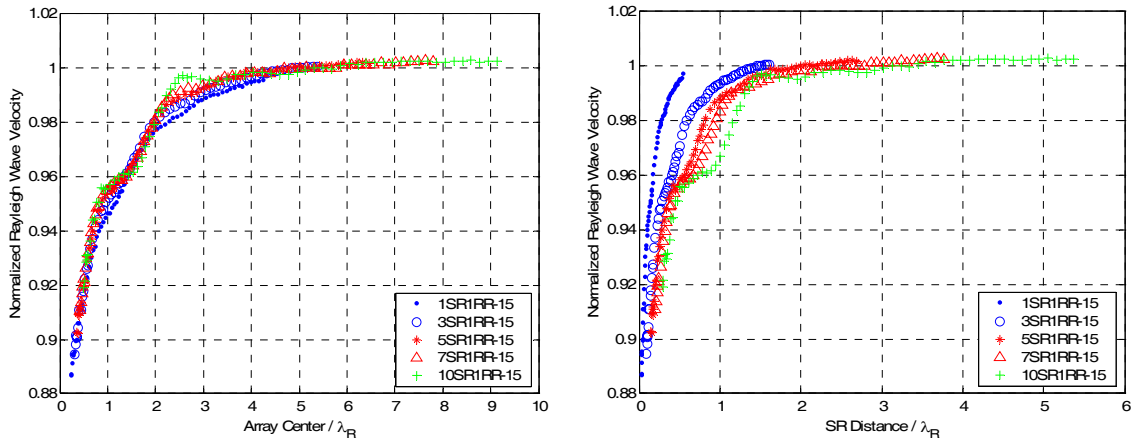

(a) (b)

Figure 4.3 Near-field effects on array-based surface wave tests with the first array set in a homogeneous half-space captured by: (a) normalized AC and (b) normalized SR distance

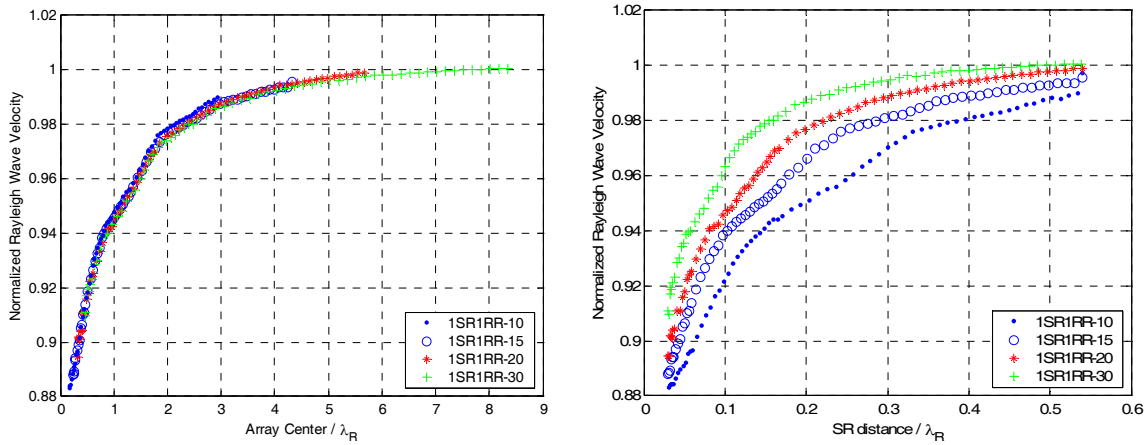

(a) (b)

Figure 4.4 Near-field effects on array-based surface wave tests with the second array set in a homogeneous half-space captured by: (a) normalized AC and (b) normalized SR distance

4.2.4 Influence of Medium Properties on Near-Field Effects

Dividing soil conditions into simplified categories such as normally or inversely dispersive condition is useful to investigate topics associated with wave propagation characteristics. A homogeneous half-space and three typical soil profiles were suggested to investigate near-field effects depending on soil conditions as tabulated in Tables 4.2 through 4.5. The profiles are constructed with four medium properties (shear wave

velocity, Poisson's ratio, damping ratio, and mass density) and layer thickness. To derive a more general conclusion, it is desirable to investigate the influence of individual medium properties on near-field effects.

For the investigation, numerical simulations with the array of 1SR1RR-15 were performed for homogeneous half-spaces with ten different sets of the four medium properties as listed in Table 4.6. To evaluate near-field effects for each case, plots of the normalized parameters were derived from dispersion curves from the numerical simulations. With case No.1 as a reference profile, the influence of the four individual medium properties on near-field effects is investigated as shown in Figure 4.5. The influence of shear wave velocity, damping ratio, and mass density on near-field effects was negligible. However, the influence of Poisson's ratio on near-field effects was significant at normalized AC values less than 1, as shown in Figure 4.5(b). Based on the result of the investigation, it is concluded that the result of the near-field effect study using numerical simulations with a specific typical soil profile can be used to estimate near-field effects on active tests for various soil profiles belonging to this category.

Table 4.6 Soil profiles for investigating medium property effect on near-field effects

Case No.	V_S (m/sec)	Poisson's ratio, ν	Damping ratio, D (%)	Mass density, ρ (t/m^3)	Remarks
1	200	0.3	0	1.8	Reference
2	300	0.3	0	1.8	V_S effect
3	400	0.3	0	1.8	
4	200	0.2	0	1.8	ν effect
5	200	0.4	0	1.8	
6	200	0.5	0	1.8	
7	200	0.3	2	1.8	D effect
8	200	0.3	5	1.8	
9	200	0.3	0	1.7	ρ effect
10	200	0.3	0	1.9	

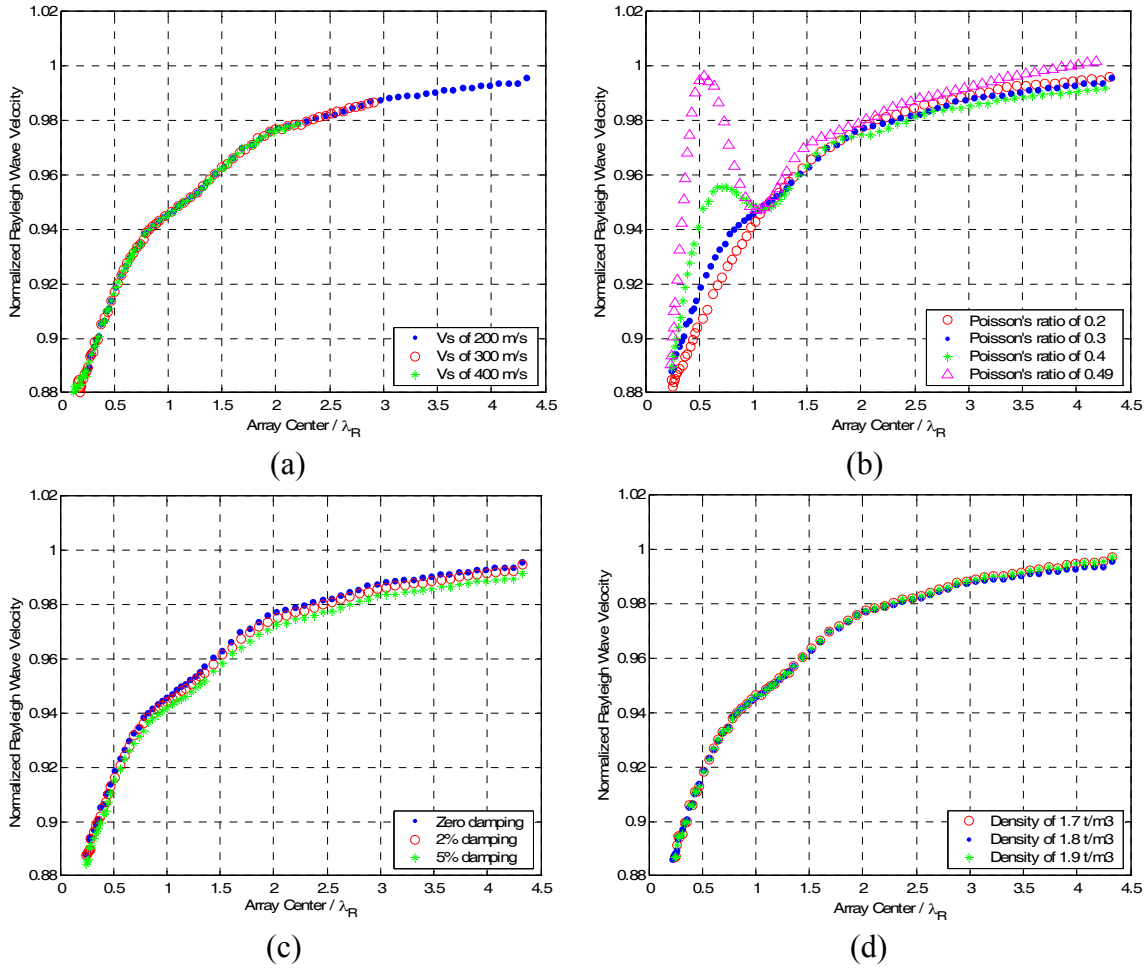

Figure 4.5 Influence of medium properties on near-field effects: (a) V_S effect, (b) Poisson's ratio effect, (c) damping ratio effect, and (d) mass density effect

4.2.5 Array Configurations

The numerical simulations were performed using the Green function program PUNCH for a set of 69 frequencies ranging from 5 to 100 Hz that is a frequency range typically used in the array-based active surface wave tests for near-surface site characterization. Since focus should be paid more to data at lower frequencies for the study of near-field effects, simulation frequencies were set up having the frequencies concentrated at lower frequencies.

Most modern active surface wave tests use less than 30 receivers due to limited testing time, cost, and data acquisition device capability. Numerical simulations with arrays of 10, 15, 20, and 30 receivers were performed to investigate the influence of the total number of receivers on near-field effects in array-based active surface wave methods. For each total number of receivers, five uniform linear arrays having different SR distances were used as listed in Table 4.7.

Table 4.7 Array sets used for numerical simulation to investigate near-field effects

Array set No.	Array	Array parameter		
		Array center (m)	Number of receivers	Maximum spatial lag (m)
1	1SR1RR-10	5.5	10	9
	3SR1RR-10	7.5		
	5SR1RR-10	9.5		
	7SR1RR-10	11.5		
	10SR1RR-10	14.5		
2	1SR1RR-15	8	15	14
	3SR1RR-15	10		
	5SR1RR-15	12		
	7SR1RR-15	14		
	10SR1RR-15	17		
3	1SR1RR-20	10.5	20	19
	3SR1RR-20	12.5		
	5SR1RR-20	14.5		
	7SR1RR-20	16.5		
	10SR1RR-20	19.5		
4	1SR1RR-30	15.5	30	29
	3SR1RR-30	17.5		
	5SR1RR-30	19.5		
	7SR1RR-30	21.5		
	10SR1RR-30	24.5		

4.2.6 Results of Numerical Simulations

Near-field effects are investigated by comparing dispersion curves of full wavefield to dispersion curves of plane Rayleigh waves for the arrays in Table 4.7 for the four soil profiles. In addition, near-field effect criteria in terms of normalized parameters are calculated with the data from these dispersion curves. As discussed in the section 4.2.2, the reference Rayleigh wave velocity free from near-field effects ($V_{R,plane}$) is calculated from the solutions of the plane Rayleigh Green's functions associated with the array configuration used for the calculation of the Rayleigh wave velocity of full wavefield to cancel array effects. In addition, the dispersion curves of plane Rayleigh waves associated with the array of 1SR1RR-100 are calculated and compared to the other dispersion curves as reference curves free from near-field and array effects. As discussed in Chapter 3, the use of the array of 100 receivers leads to dispersion curves with negligible array effects.

4.2.6.1 Dispersion curves of full wavefield

Figure 4.6 shows the comparison of dispersion curves of full wavefield for the arrays in Table 4.7 for the Case 1 soil profile. As a reference dispersion curve free from near-field and array effects, the dispersion curves of plane Rayleigh waves were calculated from plane Rayleigh Green's function solutions associated with the array of 1SR1RR-100. Note that the dispersion curves of full wavefield include both near-field and array effects. Based on the knowledge of near-field effects, it could be hypothesized that near-field effects decrease with increasing distance from the source and with increasing frequency. For this simple soil profile, the hypothesis is satisfied as shown in Figure 4.6. Note that

estimated phase velocities in dispersion curves are underestimated due to near-field effects.

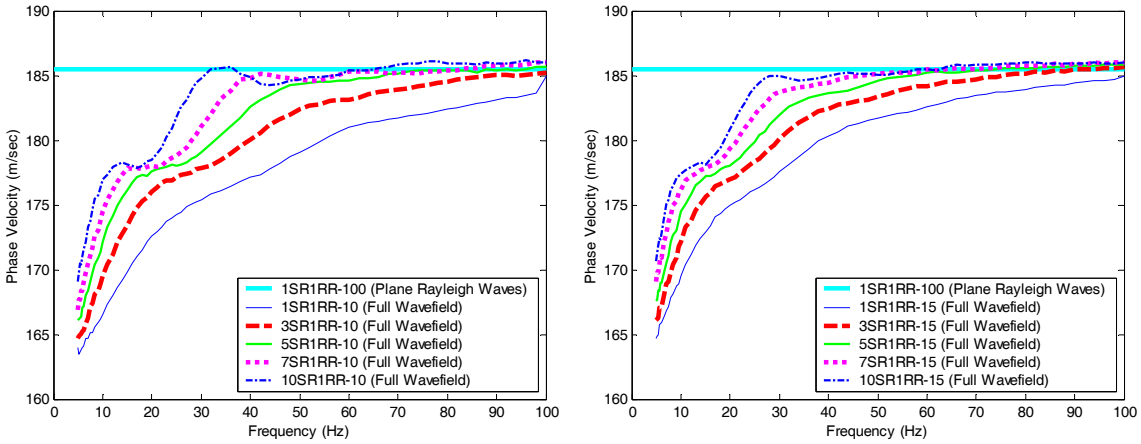

(a) 10 receivers

(b) 15 receivers

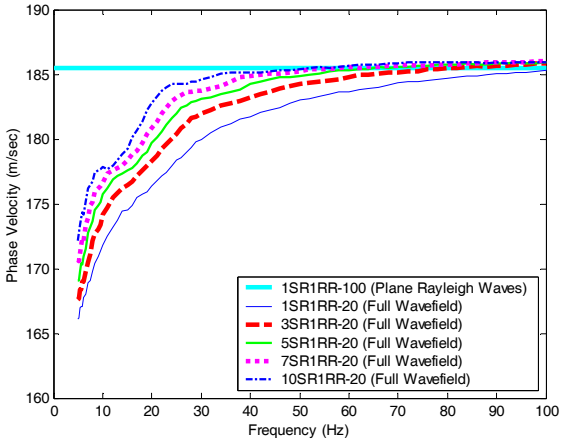

(c) 20 receivers

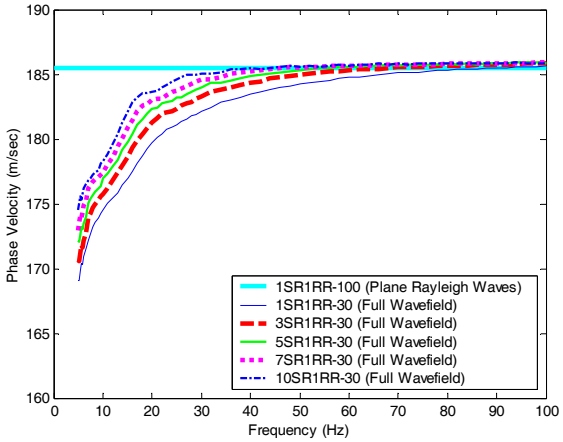

(d) 30 receivers

Figure 4.6 Comparison of dispersion curves of full wavefield for the Case 1 soil profile

Figure 4.7 shows the comparison of dispersion curves of full wavefield for the arrays in Table 4.7 and a dispersion curve of plane Rayleigh waves with an array of 1SR1RR-100 for the Case 2 soil profile. For this normally dispersive site condition, the hypothesis regarding near-field effects is also satisfied. Phase velocities are underestimated due to near-field effects over almost the entire frequency range.

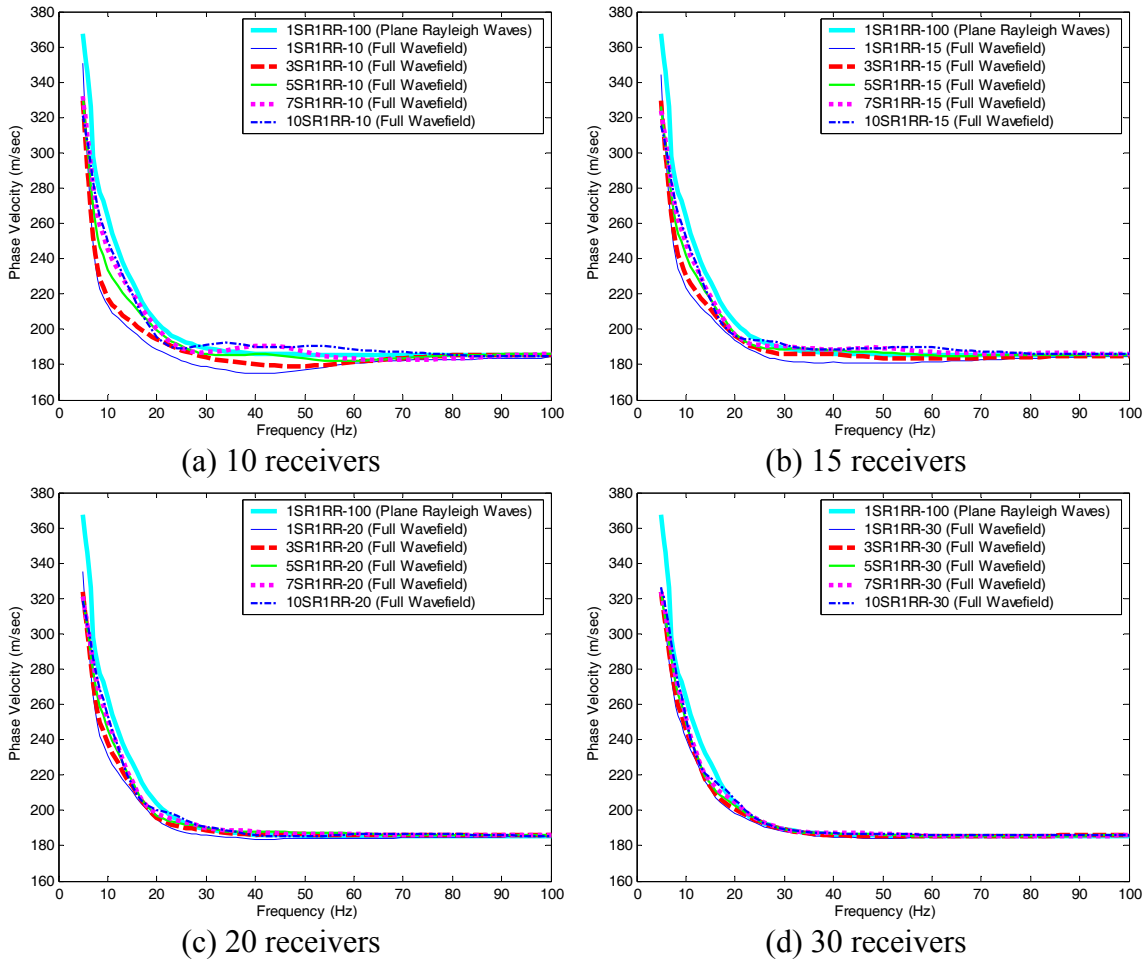

Figure 4.7 Comparison of dispersion curves of full wavefield for the Case 2 soil profile

Figure 4.8 shows the comparison of dispersion curves of full wavefield corresponding to the arrays in Table 4.7 and a dispersion curve of plane Rayleigh waves with an array of 1SR1RR-100 for the Case 3 soil profile. For this inversely dispersive soil profile, the hypothesis appears to be generally satisfied. As shown in Figure 4.8, dispersion curves become closer to the plane Rayleigh dispersion curve with successful modal separation as the number of receivers and/or AC increases. Since the wavefield is

much more complicated for this soil condition, the use of an optimized array is more essential for reliable measurements of dispersion curves.

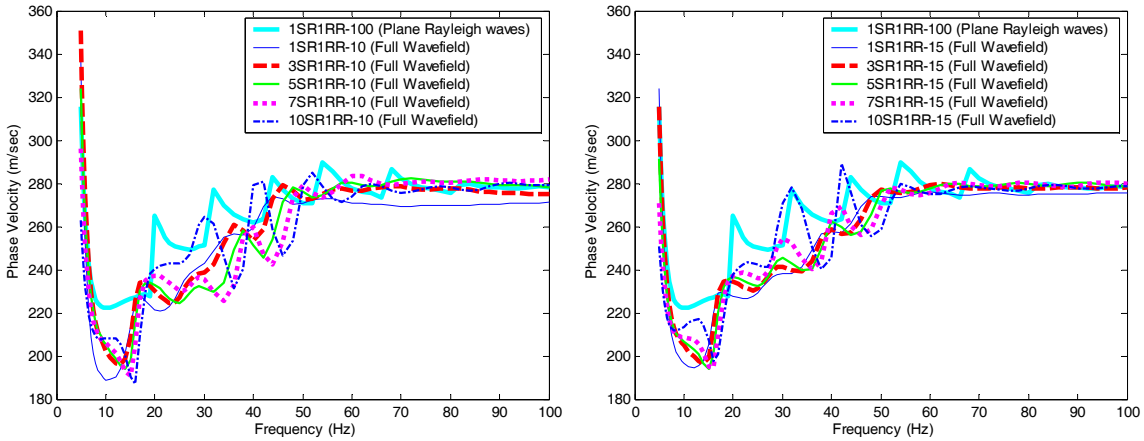

(a) 10 receivers

(b) 15 receivers

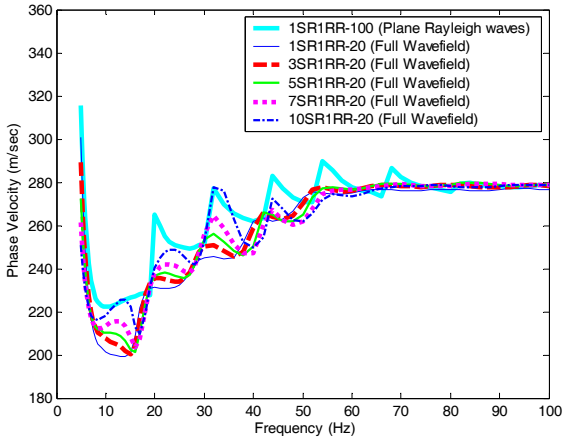

(c) 20 receivers

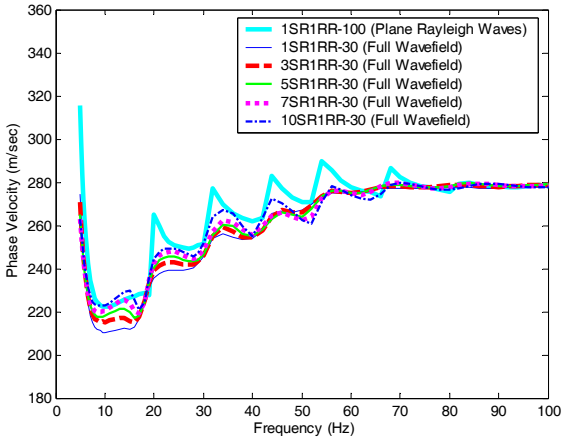

(d) 30 receivers

Figure 4.8 Comparison of dispersion curves of full wavefield for the Case 3 soil profile

Figure 4.9 shows the comparison of dispersion curves of full wavefield corresponding to the various arrays in Table 4.7 and a dispersion curve of plane Rayleigh waves with an array of 1SR1RR-100 for the Case 4 soil profile. A reduction in near-field effects was achieved by increasing the number of receivers and/or increasing the AC as shown in Figure 4.9.

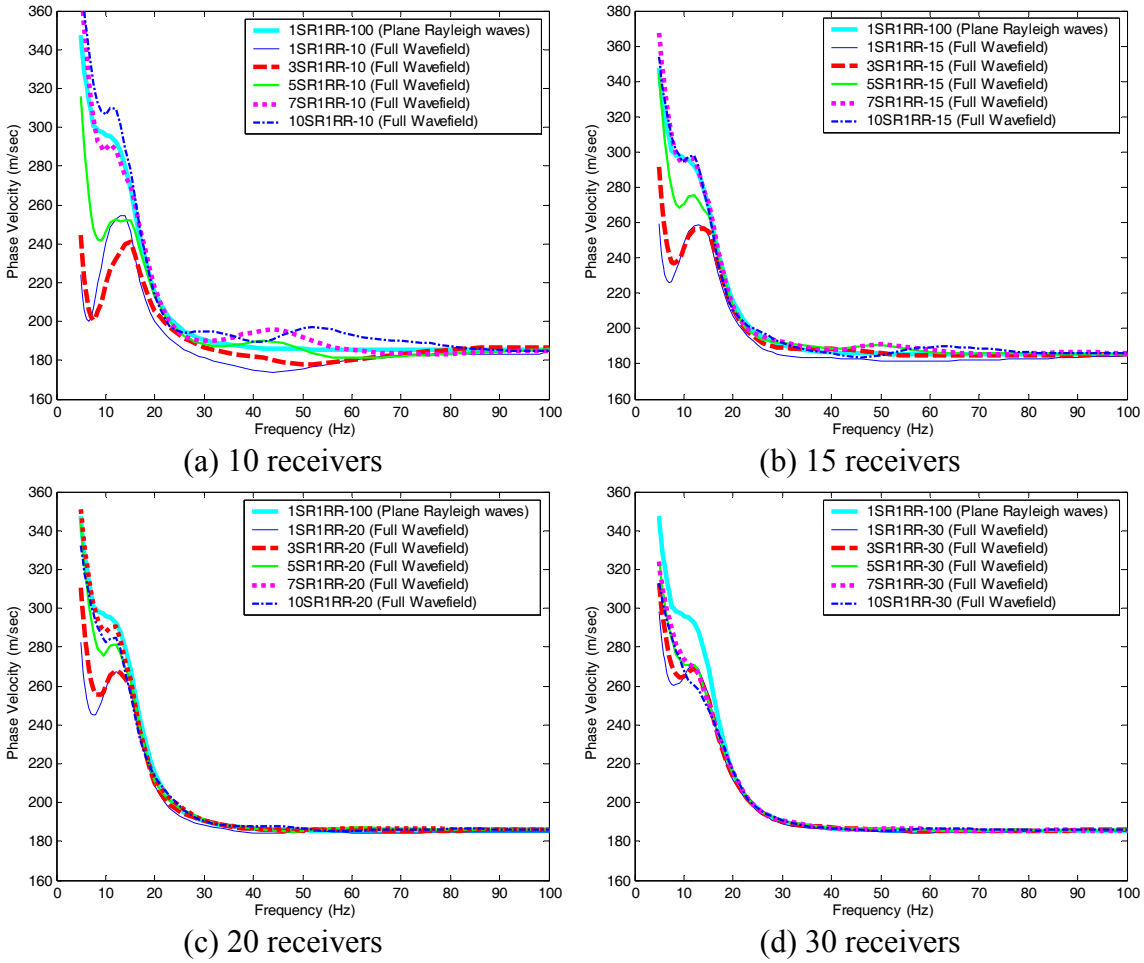

Figure 4.9 Comparison of dispersion curves of full wavefield for the Case 4 soil profile

4.2.6.2 Dispersion curves of plane Rayleigh waves

In the previous section, dispersion curves contaminated by near-field effects have been presented in Figures 4.6 through 4.9. To evaluate near-field effects with consideration of array effects, dispersion curves of plane Rayleigh waves associated with the arrays in Table 4.7 need to be presented as reference dispersion curves associated with the arrays as well. For Cases 2 through 4, dispersion curves of plane Rayleigh waves associated with the arrays are presented in Figures 4.10 through 4.12. To evaluate array effects, dispersion curves of plane Rayleigh waves with an array of 1SR1RR-100 are also

presented in Figures 4.10 through 4.12. As shown in Figures 4.10 through 4.12, the dispersion curves of plane Rayleigh waves agree more with those associated with an array of 1SR1RR-100 as the number of receivers increases, indicating reduced array effects.

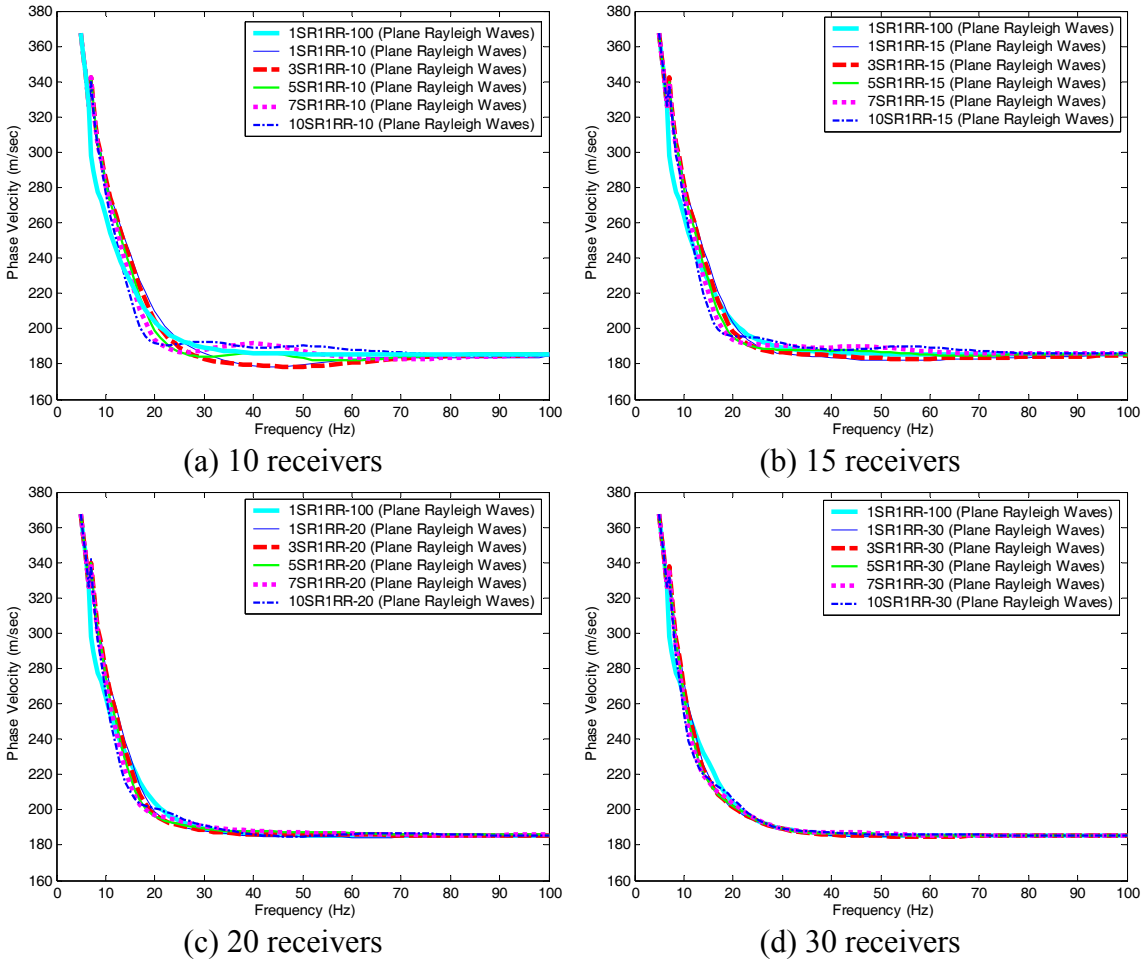

Figure 4.10 Comparison of dispersion curves of plane Rayleigh Green's function for the Case 2 soil profile

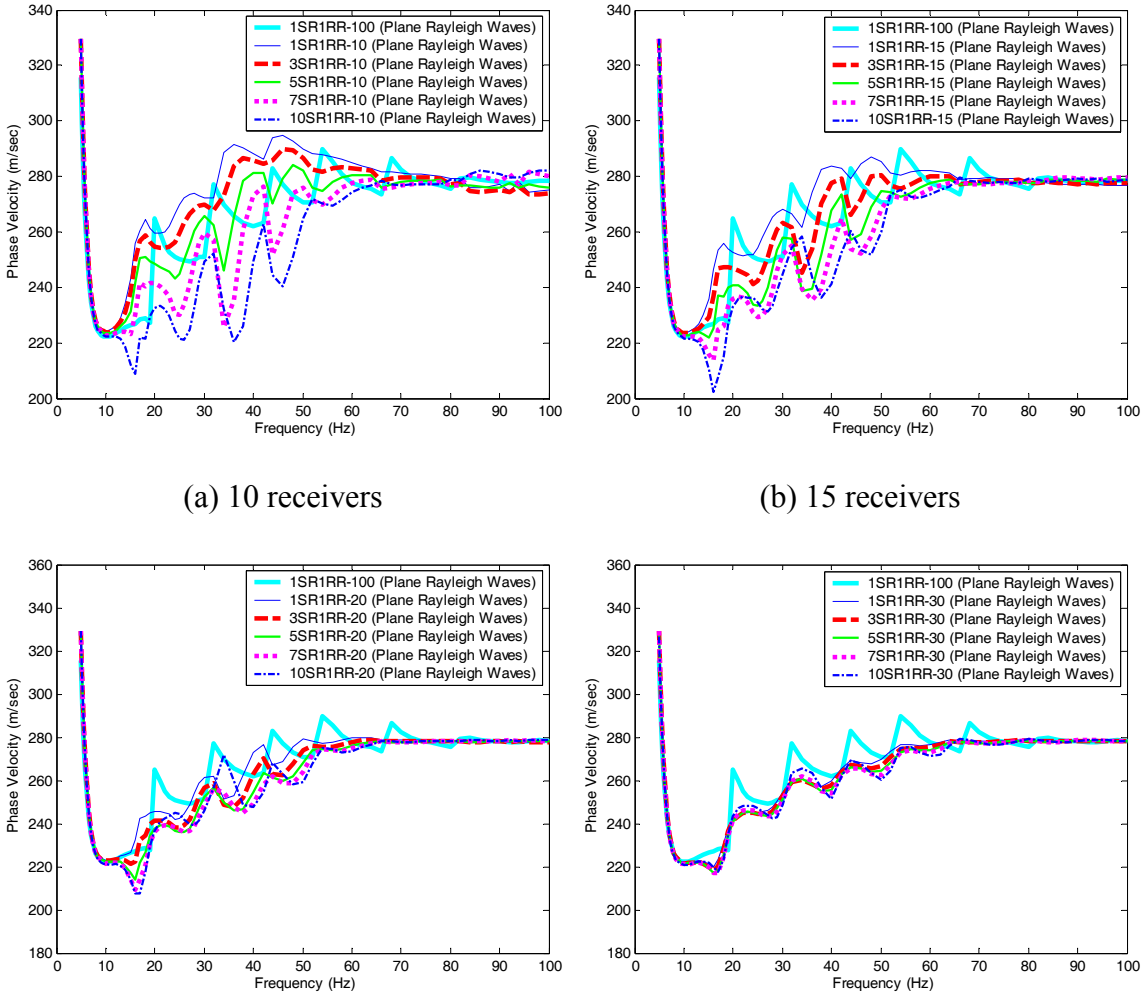

(a) 10 receivers

(b) 15 receivers

(c) 20 receivers

(d) 30 receivers

Figure 4.11 Comparison of dispersion curves of plane Rayleigh Green's function for the Case 3 soil profile

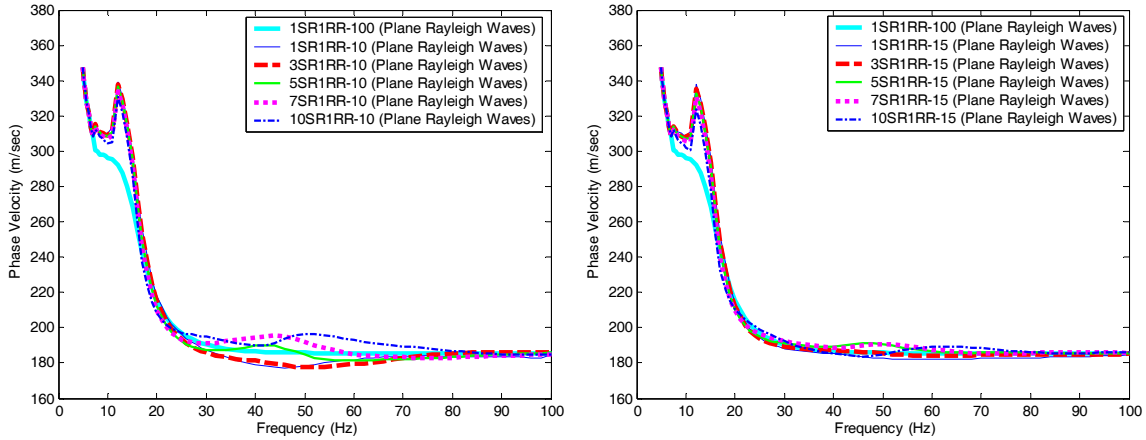

(a) 10 receivers

(b) 15 receivers

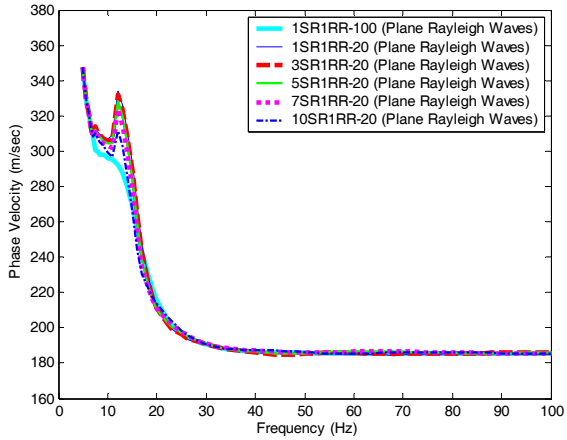

(c) 20 receivers

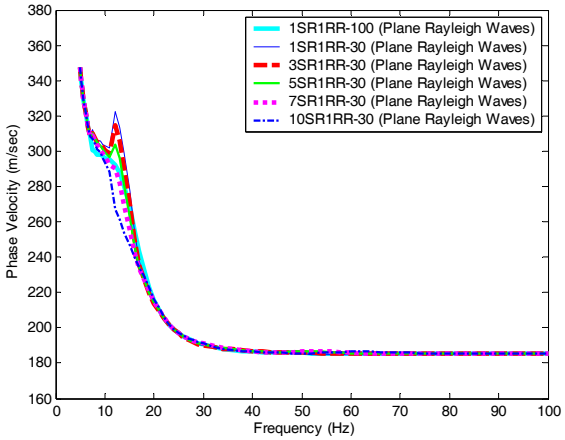

(d) 30 receivers

Figure 4.12 Comparison of dispersion curves of plane Rayleigh Green's function for the Case 4 soil profile

4.2.6.3 Near-field effect criteria in terms of normalized parameters

Near-field effects are captured using normalized parameters with the dispersion curves of full wavefield in Figures 4.6 through 4.9 and dispersion curves of plane Rayleigh waves in Figures 4.10 through 4.12 for the four soil profiles. For Case 1, a reference dispersion curve is a dispersion curve of plane Rayleigh waves with an array of 1SR1RR-100 because no array effect was observed for this simple medium condition. For Cases 2 through 4, a reference dispersion curve is a dispersion curve of plane

Rayleigh waves associated with the array configuration used for a dispersion of full wavefield as discussed in the section 4.2.2.

As previously observed through the comparison of the dispersion curves, the hypothesis regarding near-field effects is satisfied for the homogeneous half-space (Case 1). It is expected that plots of the results in terms of normalized parameters will capture this behavior with a more unique trend. Figure 4.13 shows near-field effects on array-based active tests for the Case 1 soil profile captured by the normalized parameters. As expected, near-field effects are reasonably captured by the normalized parameters. It is observed that near-field effects cause the measured phase velocities to underestimate the true values. Therefore, lower-bound normalized Rayleigh wave velocities as a function of normalized AC can be used to estimate the maximum errors due to near-field effects for this type of profile. At a normalized AC of 2, the lower-bound normalized Rayleigh wave velocity is about 0.97. At a normalized AC of 1, the lower-bound normalized Rayleigh wave velocity is about 0.94. At a normalized AC of 0.5, the lower-bound normalized Rayleigh wave velocity is about 0.91.

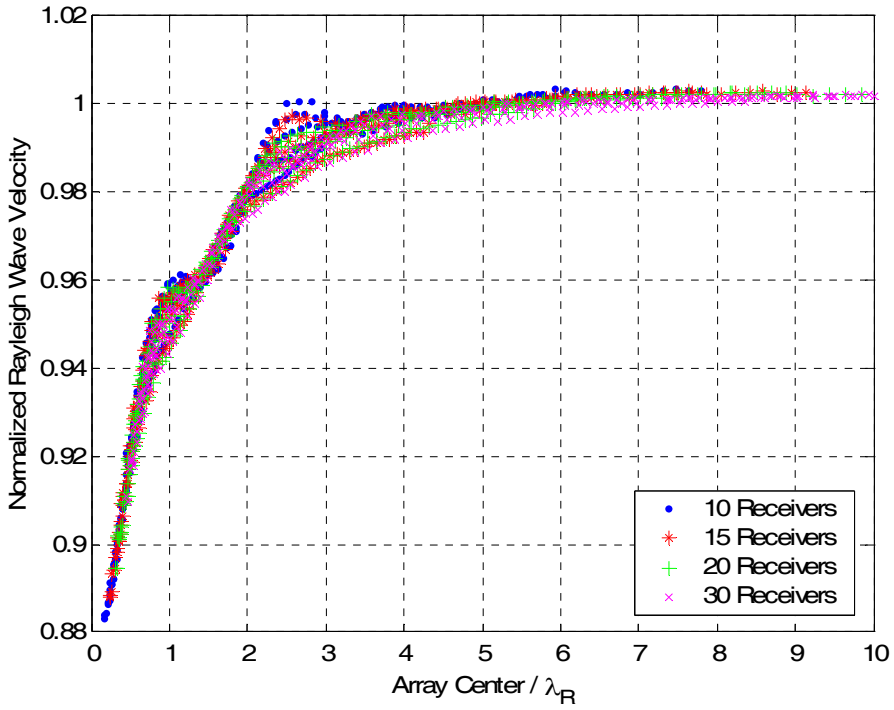

Figure 4.13 Near-field effects on array-based active methods in homogeneous half-spaces (Case1)

In addition to the ideal homogeneous half-space, near-field effects are captured by normalized parameters for the three typical soil profiles (Case 2, Case 3, and Case 4). Figure 4.14 shows the near-field effects for the Case 2 soil profile. As noted previously, the normalized parameters offer a useful lower-bound to capture the magnitude of the error for this type of soil profile. At a normalized AC of 2, the lower-bound normalized Rayleigh wave velocity is about 0.98. At normalized Array centers of 1 and 0.5, the lower-bound normalized Rayleigh wave velocities are about 0.95 and 0.83, respectively. Although near-field effects cause the phase velocity to be overestimated for some cases, most errors result in underestimation as shown in Figure 4.14. For normalized AC values greater than 0.5, near-field effects diminish with increasing normalized AC. However, for normalized AC values less than 0.5, near-field effects do not appear to decrease

monotonically with increasing normalized AC. Fortunately, the lower-bound can still serve as a means to estimate the maximum error for this range of normalized AC.

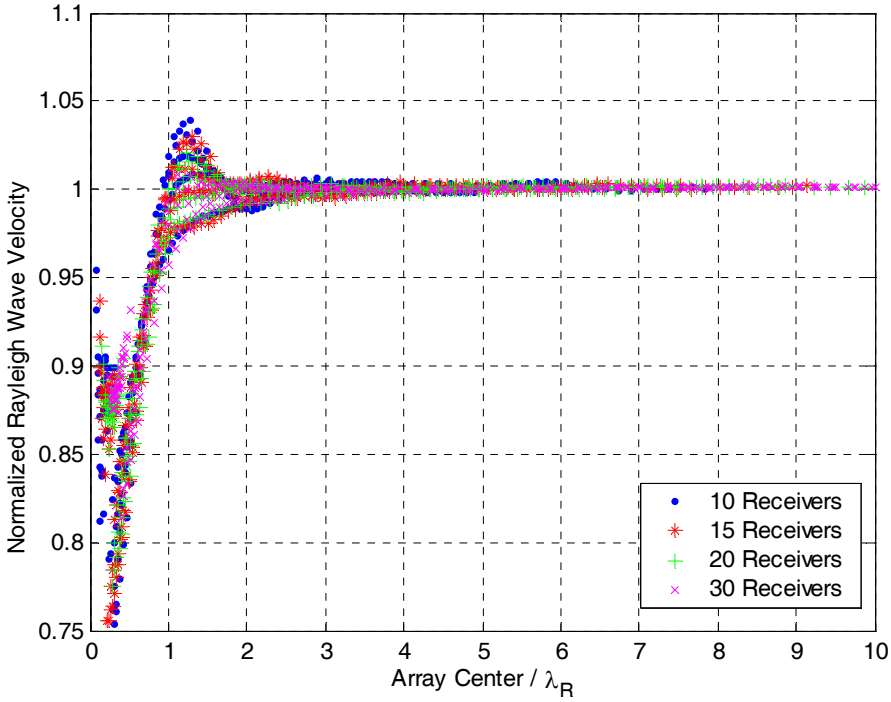

Figure 4.14 Near-field effects on the array-based active methods in normally dispersive soil profiles (Case2)

Figure 4.15 shows near-field effects for the Case 3 soil profile captured by normalized parameters. It may be noted that errors due to near-field effects result in underestimation of the Rayleigh phase velocity as in the previous two cases. However, overestimated values of Rayleigh phase velocity are much more frequently found. At a normalized AC of 2, the lower-bound normalized Rayleigh wave velocity is about 0.95. At normalized array centers of 1 and 0.5, the lower-bound normalized Rayleigh wave velocities are about 0.85 and 0.8, respectively. The statement that near-field effects lead to more significant errors in dispersion estimates for inversely dispersive site conditions (Sanchez-Salinero, 1987; Tokimatsu, 1995) can be verified by comparing these lower-

bound normalized Rayleigh wave velocities for Case 3 to those for Case 2. The more scattered distribution of normalized Rayleigh wave velocities at low normalized AC indicates more dependency of near-field effects on array configuration. Selecting an array configuration becomes more critical for accurate measurements of Rayleigh wave velocities for inversely dispersive soil profiles.

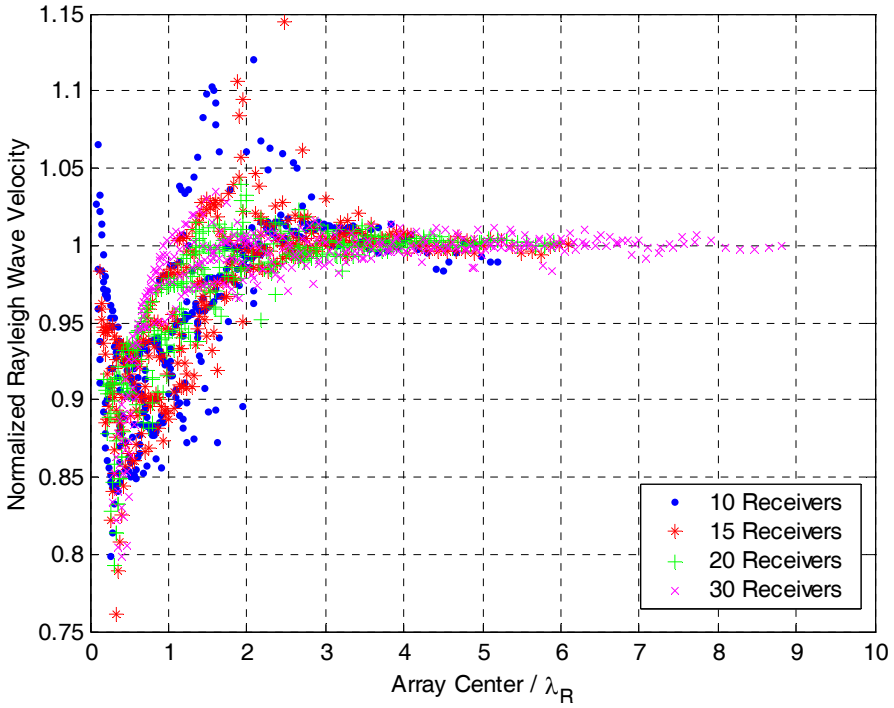

Figure 4.15 Near-field effects on the array-based active methods in inversely dispersive soil profiles (Case 3)

Figure 4.16 shows the near-field effects for another type of inversely dispersive soil profile (Case 4). Like the previous soil profiles, most measured values of Rayleigh phase velocity are less than the true values. At a normalized AC of 2, the lower-bound normalized Rayleigh wave velocity is about 0.98. At normalized array centers of 1 and 0.5, the lower-bound normalized Rayleigh wave velocities are about 0.9 and 0.75, respectively.

For normalized values of AC greater than 1, near-field effects for this soil profiles are slightly more severe than those for normally dispersive soil profiles (Case 2) and are less severe than those of the other inversely dispersive soil profiles (Case 3). However, for normalized values of AC less than 1, near-field effects for this soil profiles are more significant than those for any other soil profile. For this low normalized AC, calculated normalized Rayleigh wave velocities are very scattered indicating high dependency of near-field effects on array configuration.

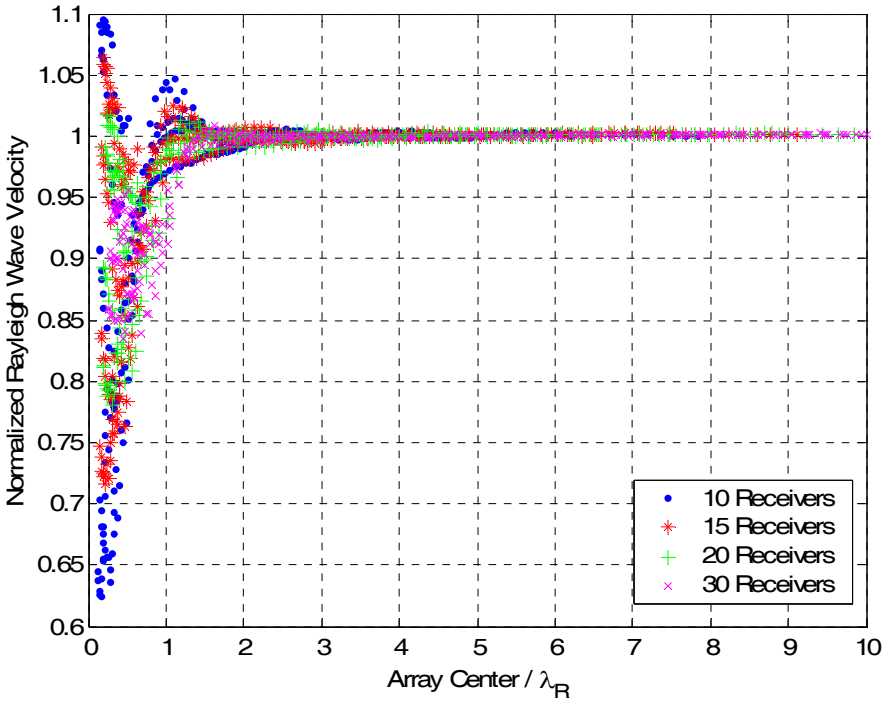

Figure 4.16 Near-field effects on the array-based active methods in inversely dispersive soil profiles (Case 4)

Assuming that the results regarding near-field effects on array-based active tests can be used to estimate near-field effects on traditional SASW tests, the maximum errors associated with the previous near-field criteria in Table 4.1 may be approximated using Figures 4.13 through 4.16 with consideration of site conditions. For example, Heisey et al.

(1982) suggested that measured signals whose wavelength is 3 times greater than the value of d_1 should be eliminated to mitigate near-field effects. Since the typical receiver configuration (i.e., $d_1 = \Delta d$) of SASW tests was used, the AC of the two-receiver array is 1.5 times d_1. Therefore, a longest acceptable wavelength associated with the criterion is 2 times the value of the AC (i.e, $AC/\lambda_R = 0.5$). At a normalized AC of 0.5, the maximum probable errors due to near-field effects are about 17 %, 20 %, and 25 % for the Case 2, Case 3, and Case 4 soil profiles, respectively. It is also important to note that the traditional SASW tests have been known to be more vulnerable to near-field effects than array-based surface wave tests. Actual maximum errors associated with near-field effects on SASW tests could be larger than these estimated values.

Because near-field effects are more severe for small values of normalized array centers, Figures 4.13 through 4.16 are re-plotted with emphasis on small-valued normalized values of AC as shown in Figure 4.17. To easily compare figures, they were plotted with the same scale for both normalized parameter axes.

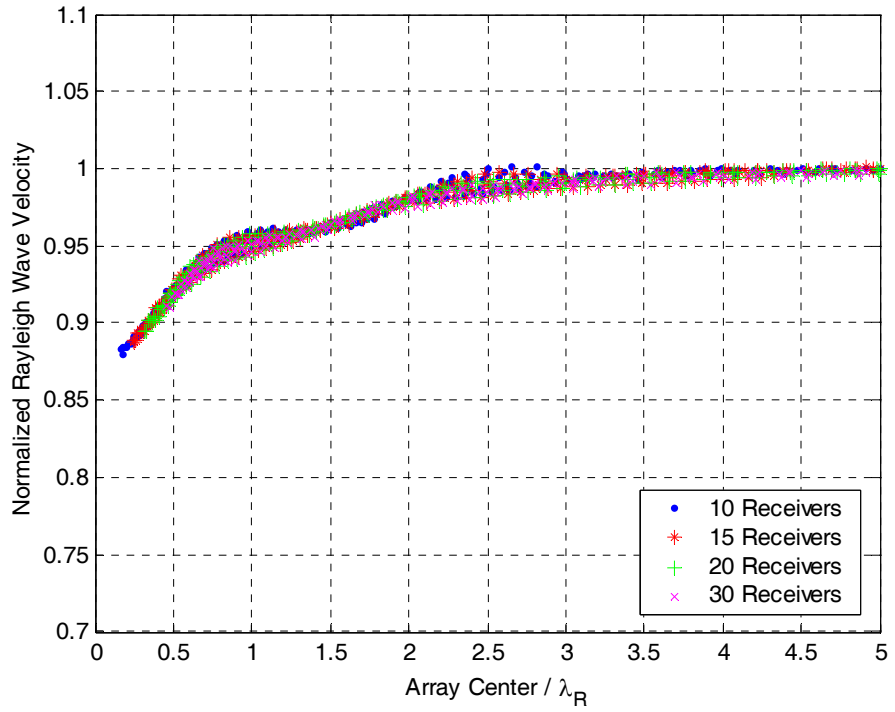

(a)

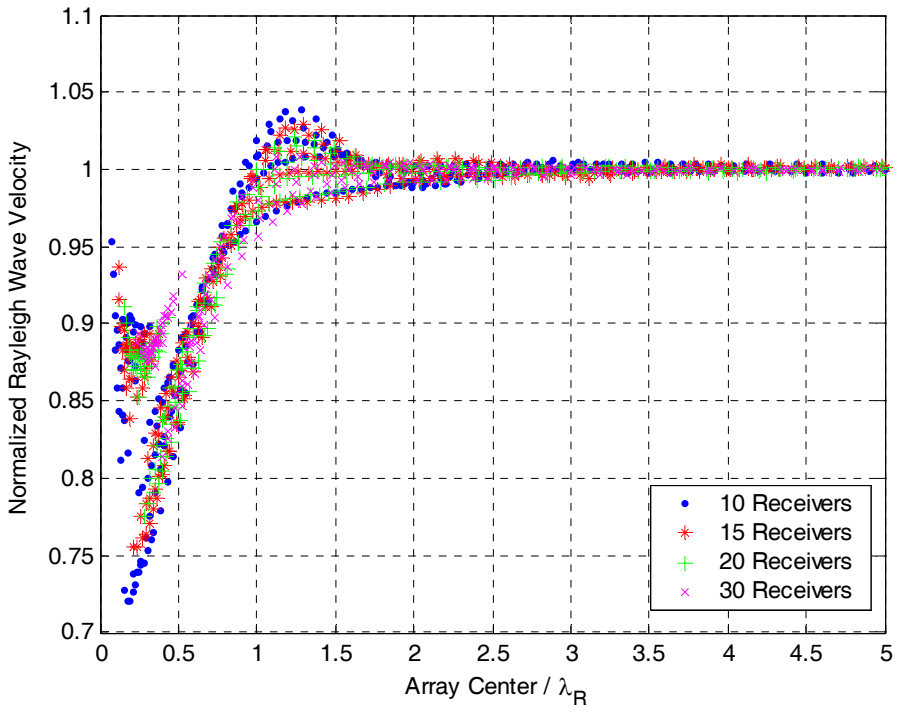

(b)

Figure 4.17 Near-field effects on the array-based active methods in various soil profiles with emphasis on small normalized array centers: (a) homogeneous half-space (Case 1), (b) normally dispersive (Case 2)

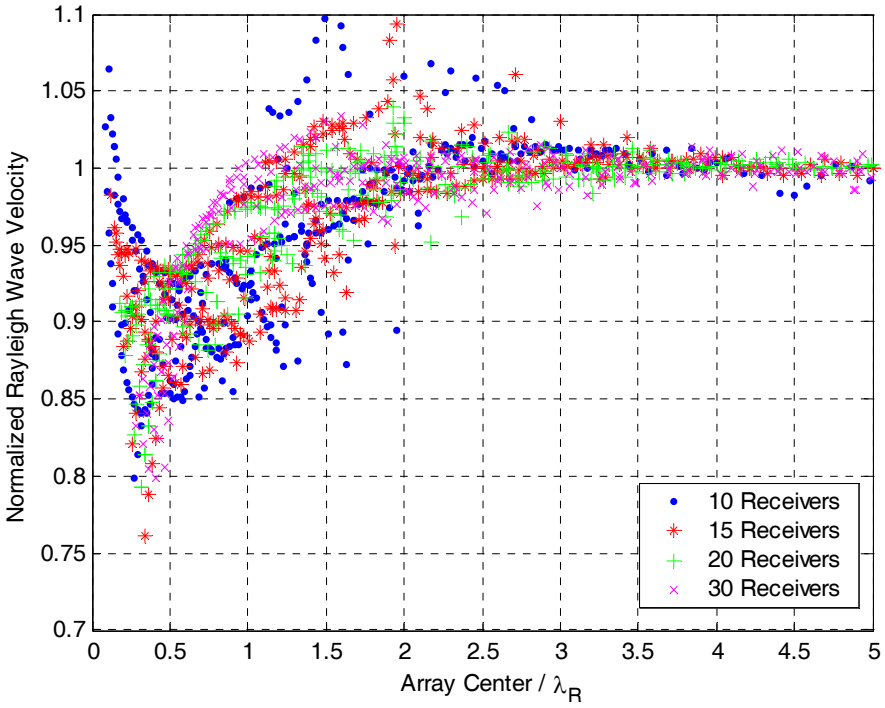

(c)

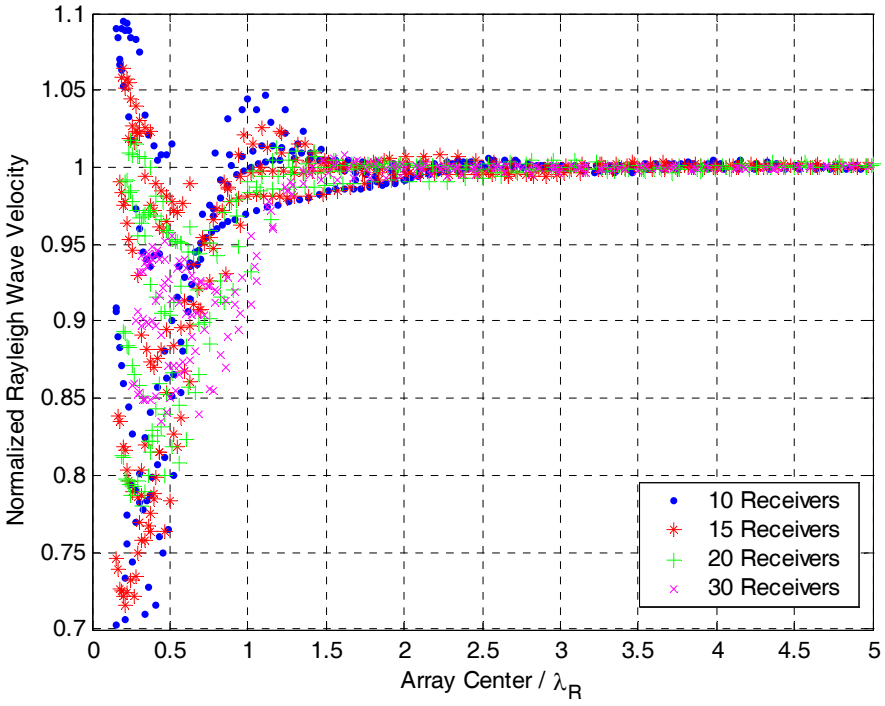

(d)

Figure 4.17 (continued) (c) inversely dispersive (Case 3), and (d) inversely dispersive (Case 4)

4.3 LABORATORY SIMULATIONS

Laboratory tests provide several advantages including better-controlled conditions, ease of repeatability, and more accurate measurements than field tests. These advantages allow performing parametric studies with better-controlled conditions, reduced time and available reference values from known material properties.

To perform parametric studies of factors affecting results of surface wave methods, a method to simulate surface wave field measurement procedure in the laboratory is developed. A thin polymethylmethacrylate (PMMA) plate in an upright position was selected as a propagating medium for the laboratory simulations. To perform the theoretical study regarding wave propagation in the thin plate in upright position, the concept of generalized plane stress (Love, 1944) accounting for waves in a two-dimensional (2-D) medium and the Rayleigh-Lamb frequency equation (Rayleigh, 1888; Lamb, 1889) accounting for waves in a plate need to be combined. The appropriate frequency range was determined based on a theoretical study of wave propagation in the PMMA plate, followed by selection of a source type and PMMA material properties for the frequency range. A preliminary study was performed to identify the source and system selected for the laboratory simulation. Laboratory simulations were then performed to investigate near-field effects based on these studies of Rayleigh wave propagation in the plate, the frequency range of interest, the medium properties for the frequency range, and source and system identification.

4.3.1 Waves in a Thin PMMA Plate

A thin PMMA plate in an upright position as shown in Figure 4.18 was selected as a propagating medium for laboratory simulations. The medium with a small thickness, 2h,

can be considered a 2-D medium. The medium with a limited height, 2b, can be also considered as a plate with two free boundaries. The Rayleigh-Lamb frequency equation can be used to identify wavefields in a plate with two free boundaries. The concept of generalized plane stress can be applied to understand wavefields in a 2-D medium. The Rayleigh-Lamb frequency equation and the generalized plane stress concept are combined to identify wavefields in a thin PMMA plate in Figure 4.18. This section starts with introduction of the Rayleigh-Lamb frequency equation. The equation is slightly modified based on the concept of generalized plane stress in the y direction, leading to a final equation describing wavefields in a thin PMMA plate.

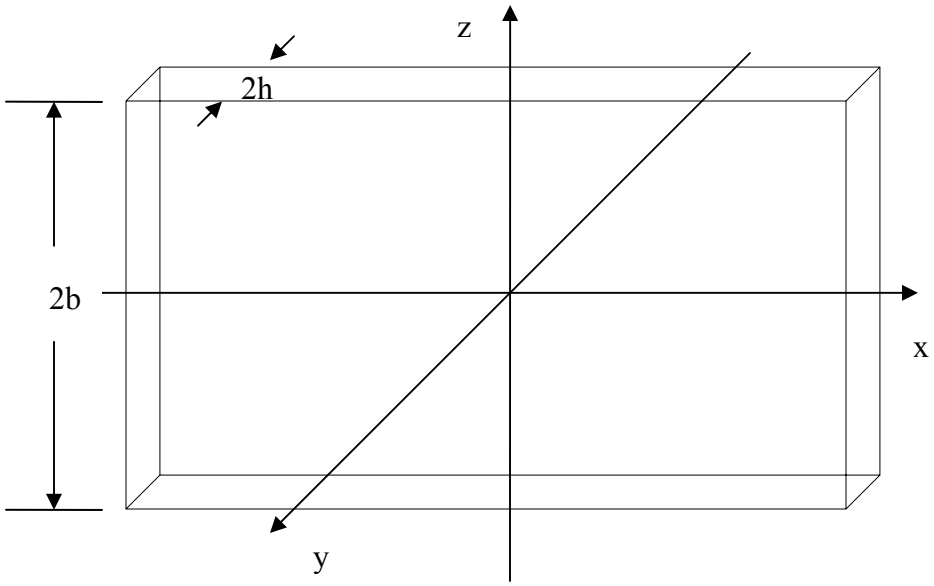

Figure 4.18 Coordinate system for a thin plate in an upright position

A plate having finite dimension in height is often selected for laboratory tests. To successfully interpret results of laboratory tests with a plate, wave propagation in a plate-type medium must be fully understood. It is known that waves in a plate are guided by two traction-free surfaces at the top and bottom of the plate.

Wave propagation equation in an elastic plate was first investigated by Rayleigh (1888) and Lamb (1889). The final equation completely describing wave motions in their study is called the *Rayleigh-Lamb frequency equation*. A Detailed derivation of the Rayleigh-Lamb frequency equation can be found in Mindlin (1960), Victorov (1967), and Graff (1975). The Rayleigh-Lamb frequency equation in a plate with free boundaries at top and bottom is given by:

$$\frac{\tan qb}{\tan pb} + \left[\frac{4k^2 pq}{(k^2 - q^2)^2} \right]^{\pm 1} = 0 \tag{4.4}$$

where $p^2 = \frac{\omega^2}{V_P^{\,2}} - k^2$, $q^2 = \frac{\omega^2}{V_S^{\,2}} - k^2$, b = half thickness of a plate, and k = wavenumber. The exponent +1 and –1 represent symmetric and anti-symmetric modes, respectively.

Victorov (1967) and Zerwer (1999) observed the creation of Rayleigh waves in a plate by superimposed fundamental (both symmetric and asymmetric) Lamb modes at high frequency. Zerwer (1999) performed 2-D model tests using a small size PMMA plate with dimensions of 122 cm × 30 cm × 0.6 cm (width × height × thickness) to investigate the application of Rayleigh waves to the detection of near-surface fractures in typical structural elements such as a concrete beam. The generalized plane stress concept suggested by Love (1944) and the Rayleigh-Lamb frequency equation were employed to identify wavefields in the plate. Zerwer (1999) reported that Rayleigh waves were successfully detected and matched well with the theoretical results at frequencies greater

than 8.4 KHz. From the results of his experimental study, the use of 2-D model tests with a thin PMMA plate was validated as a propagating medium for laboratory simulations of surface wave methods. In this study, a larger PMMA plate with dimensions of 251 cm × 127 cm × 1.2 cm (width × height × thickness) was selected as a 2-D medium because there is less interference from edge reflections and Rayleigh waves may be generated at lower frequency compared to a small plate[1].

Wave propagation in a thin plate held in an upright position as shown in Figure 4.18 can be explained using wave propagation in a 2-D medium if wavelength is much longer than the plate thickness, 2h (Oliver et al., 1954). Parham and Sutton (1971) reported that if a wavelength was longer than 5 times the plate thickness, the concept of the 2-D wave propagation was valid. If the condition for the 2-D wave propagation is satisfied, the generalized plane stress concept can be applied to obtain simplified mathematical derivation of wave velocities through the medium (Oliver et al., 1954). The P-wave velocity in a homogeneous and elastic medium under 3-D condition can be expressed as:

$$V_P^{3D} = \sqrt{\frac{M}{\rho}} = \sqrt{\frac{E(1-\nu)}{\rho(1+\nu)(1-2\nu)}} \tag{4.5}$$

where M, E, ρ, and ν are the constrained modulus, elastic modulus, mass density, and Poisson's ratio of a medium, respectively.

For a 2-D medium, plane stress condition in which stress is equal to zero in the y direction is present and the P-wave velocity in a 2-D medium is given by:

$$V_P^{2D} = \sqrt{\frac{E}{\rho(1-\nu^2)}} \tag{4.6}$$

[1] Successful measurements of low-frequency Rayleigh waves are essential for studying important issues like near-field effects on array-based surface wave method.

In order to calculate the Rayleigh wave velocity in the plate, the vertically polarized shear (SV) wave velocity is necessary as well as the P-wave velocity because Rayleigh waves are generated by the combination of P- and SV-waves. The SV-wave velocity remains the same between the 3-D and the 2-D conditions and is calculated by:

$$V_{SV} = \sqrt{\frac{G}{\rho}} = V_P^{3D}\sqrt{\frac{(1-2\nu)}{2(1-\nu)}} = V_P^{2D}\sqrt{\frac{1-\nu}{2}} \tag{4.7}$$

where G is the shear modulus.

The final equation regarding wave propagation in the 2-D PMMA plate can be obtained by combining the Rayleigh-Lamb frequency equation with the generalized plane stress concept. As a consequence, V_P (i.e., V_P^{3D}) and V_S in Equation 4.3 are replaced with V_P^{2D} and V_{SV}, leading to:

$$\frac{\tan(b\sqrt{\frac{\omega^2}{(V_{SV})^2}-k^2})}{\tan(b\sqrt{\frac{\omega^2}{(V_P^{2D})^2}-k^2})} + \left[\frac{4k^2\sqrt{(\frac{\omega^2}{(V_{SV})^2}-k^2)(\frac{\omega^2}{(V_P^{2D})^2}-k^2)}}{\frac{\omega^4}{(V_{SV})^4}}\right]^{\pm 1} = 0 \tag{4.8}$$

Given material properties, Equation 4.8 is a function of circular frequency ω and wavenumber k. Therefore, Equation 4.8 can be used to obtain a frequency-wavenumber (f-k) spectrum for the thin PMMA plate. Consequently, the f-k spectrum with given material properties is expected to show a frequency at which Rayleigh waves are created.

4.3.2 System and Source Identification

It is important to choose the equipment and signal processing techniques to optimize measurements in the desired range of frequency. In order to do this, the range of frequency needs to be selected based on understanding of wave propagation in a

propagating medium. In this section, the system and source identification for laboratory simulations with a thin PMMA plate will be discussed.

4.3.2.1 Properties of PMMA

PMMA is the medium material that was selected for the laboratory simulation. PMMA has been also widely known as its commercial name *Plexiglas*. PMMA was selected as the medium material due to following reasons: (1) the properties of the material are well known, (2) plates of various sizes are available in the marketplace and inexpensive, and (3) it may be easily machined.

PMMA is a viscoelastic material, and its stiffness and damping ratio are dependent on frequency as shown in Figure 4.19. Considering the variation in the material properties with respect to frequency allows more accurate calculation of wavefields in the material, but requires complexity in the calculation. The complexity can be significantly reduced by choosing constant property values independent of frequency, which is reasonable for a limited frequency range. From Figure 4.19, Young's modulus E ranges from 5.1 GPa to 5.3 GPa for frequencies ranging from 3 kHz to 20 kHz[2]. The range of V_R in a 2-D medium calculated using the range of the Young's modulus, mass density of 1.19 (t/m^3), and Poisson's ratio of 0.33 is from 1166 (m/sec) to 1189 (m/sec). The variation in V_R for this frequency range is about 1.9% of the largest V_R and therefore, the assumption of constant stiffness of PMMA for the frequency range appears to be reasonable. Poisson's ratio is also assumed constant through the frequency range, while it actually varies slightly with frequency. A Poisson's ratio of 0.33 is selected for the frequency range. The assumption of constant stiffness offers a convenient means to extract the f-k spectrum from a theoretical study of wave propagation in the PMMA plate.

[2] Rayleigh waves are present in the PMMA plate for this frequency range. See the next section for details. `

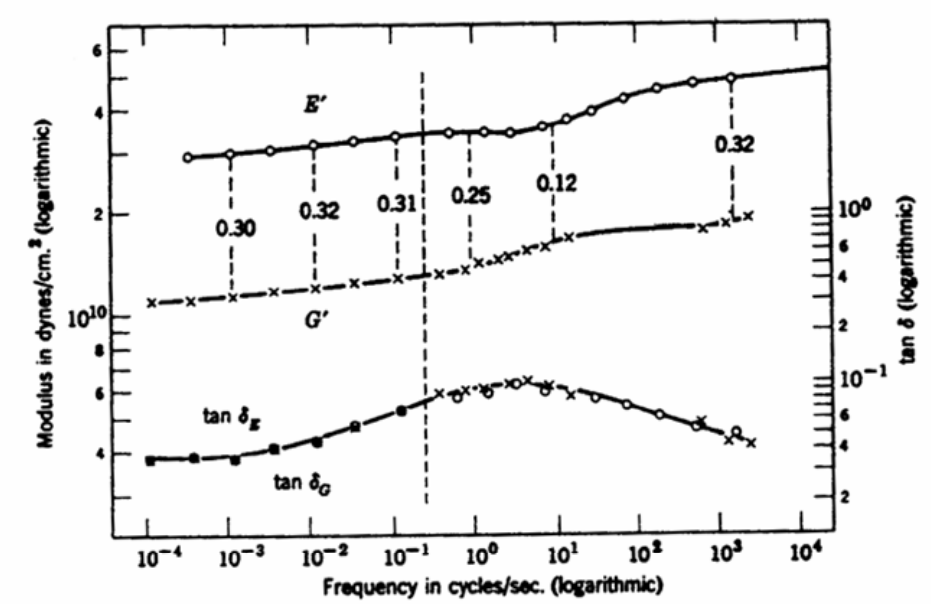

Figure 4.19 Viscoelastic properties of PMMA (modified from Kopplemann (1958), Ferry, 1980)

Wave velocities in PMMA at various frequencies were reported by several researchers (Oliver et al., 1954; Press et al, 1954; Koppelmann, 1958) and tabulated in Table 4.8. It can be observed that the wave velocities are slightly different depending on investigator and operating frequency. In this study, the measurement of the P-wave in the PMMA medium was conducted using two 50 kHz transducers. From the measurement, V_p^{3D} of 2581 (m/sec) was obtained and it was used to calculate other wave velocities such as V_P^{2D}, V_S, V_R^{3D}, and V_R^{2D}. The value of V_R^{2D} of 1195 (m/sec) from the measurement is selected as a reference Rayleigh wave velocity in this 2-D PMMA medium for laboratory simulations.

Table 4.8 Wave velocities in PMMA

Reference	V_P^{3D} (m/s)	V_P^{2D} (m/s)	V_S (m/s)	V_R^{3D} (m/s)	V_R^{2D} (m/s)	Frequency (kHz)	Medium condition for measurement
Oliver et al. (1954)	2724	2362	1372	1279	1261	67	2-D
Press et al. (1954)	2644	2302	1332	1241	1224	67	2-D
Koppelmann* (1958)	2544	2214	1282	1195	1178	10	N/A
This study	2581	2246	1300	1212	1195	50	3-D

* Velocities are back-calculated using the given properties.

4.3.2.2 Rayleigh-Lamb waves in a thin PMMA plate

Using these material properties, the complete spectrum of all the wavefields in the thin PMMA plate may be calculated using the Rayleigh-Lamb frequency equation for 2-D condition as described in Equation 4.7. Since Equation 4.7 describes relationship between frequency and wavenumber of multiple mode Lamb waves, frequency-wavenumber spectra and dispersion curves can be obtained. The complex, transcendental Rayleigh-Lamb frequency equation can be solved only numerically (Rose, 1999). With consideration of only real solutions of the Rayleigh-Lamb frequency equation, the numerical solutions of the equation were obtained by a root finding process called the *scanning approach*. Refer to Rose (1999) for details of the scanning approach.

Frequencies ranging from 0 to 20 kHz and wavenumbers ranging from 0 to 100 rad/m were scanned with a frequency scanning step size of 0.5 Hz and a wavenumber step size of 5 rad/m. Frequency-wavenumber spectra and dispersion curves associated with the first four modes of Lamb waves in the thin PMMA plate are shown in Figures 4.20 and 4.21, respectively.

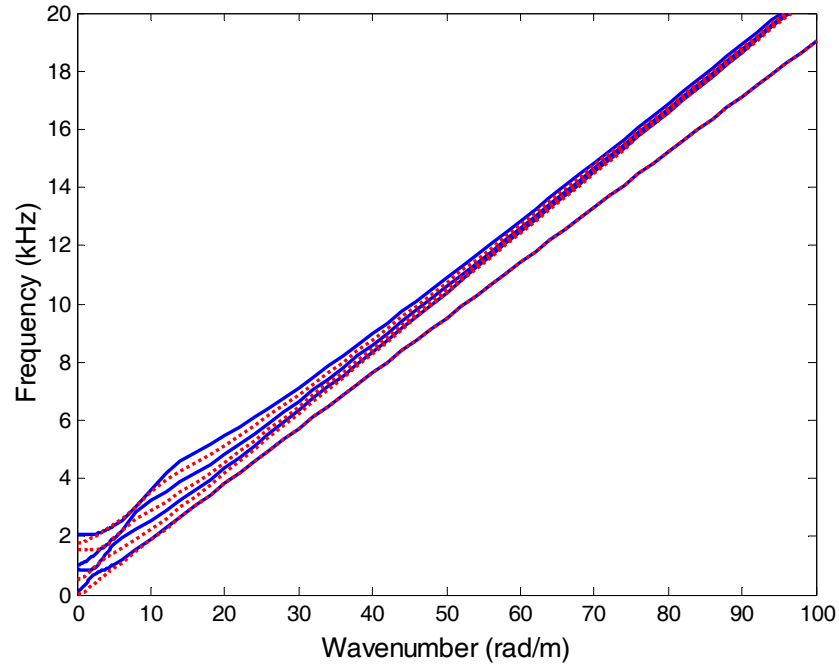

(a)

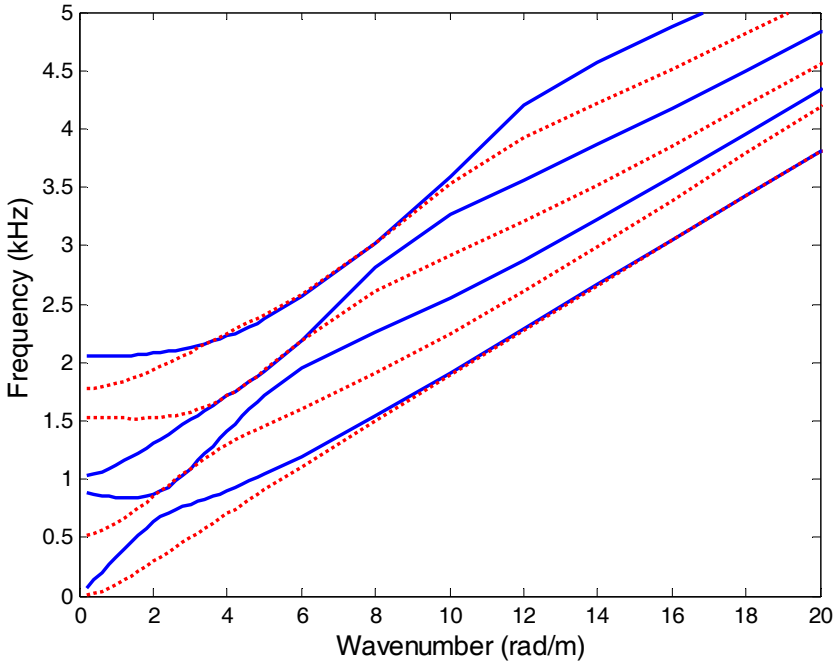

(b)

Figure 4.20 Frequency-wavenumber spectra of Lamb waves in a thin PMMA plate for (a) frequencies up to 20 kHz and (b) frequencies up to 5 kHz. Solid and dotted lines denote symmetric and anti-symmetric modes, respectively. The order of mode increases from bottom to top.

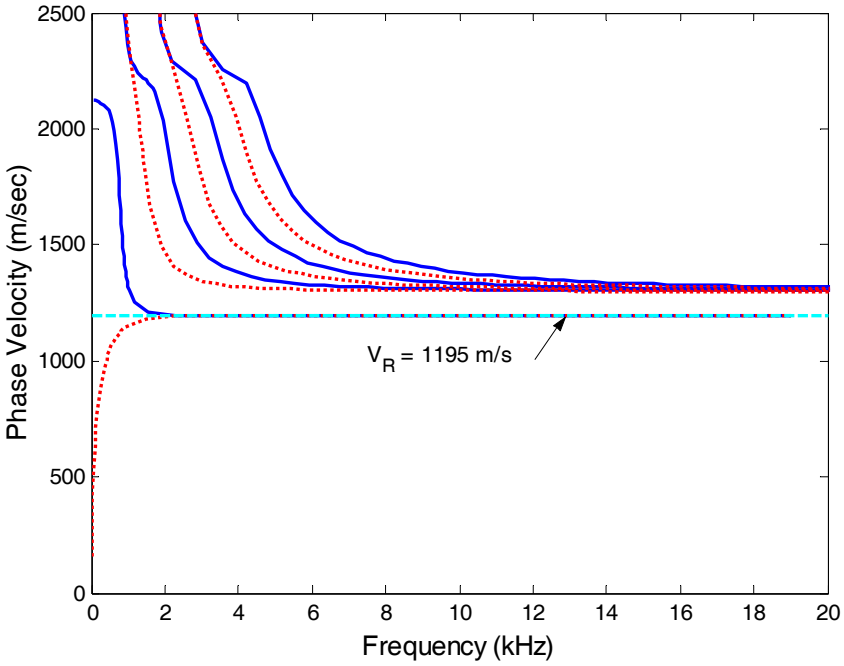

(a)

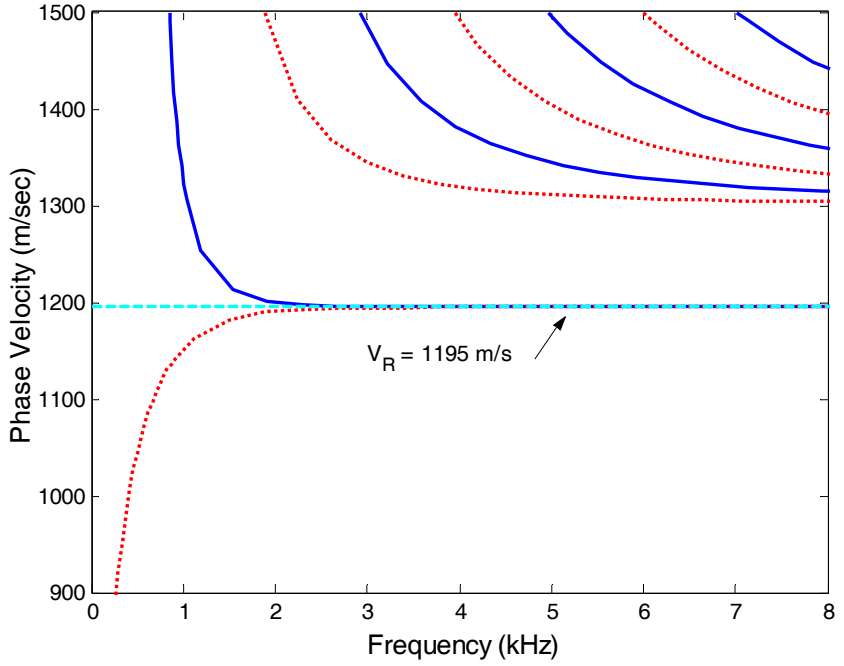

(b)

Figure 4.21 Dispersion curves of Lamb waves in a thin PMMA plate for (a) frequencies up to 20 kHz and (b) frequencies up to 8 kHz. Solid and dotted lines denote symmetric and anti-symmetric modes, respectively. The order of mode increases from left to right.

As shown in Figure 4.21(b), the fundamental symmetric and anti-symmetric Lamb modes appear to create Rayleigh waves in the thin PMMA plate at frequencies greater than approximately 3 kHz. Considering a largest acceptable wavelength to satisfy the assumption that the PMMA plate is a 2-D medium, frequencies ranging 3 kHz to 20 kHz are selected as operating frequency range for laboratory simulations with the plate. A theoretical Rayleigh wave velocity of 1195 (m/sec) is selected as a reference Rayleigh wave velocity of the PMMA plate for this range of frequency.

4.3.2.3 Equipment configuration

The PMMA plate used for laboratory simulations is shown in Figure 4.22. Holes with inner threads were drilled in inter-hole spacing of 3 cm at the top edge as shown in Figure 4.22 so that a variety of arrays of receivers mounted at arbitrary positions could be selected. The first hole is located at a position 80 cm away from the one end of the plate edge.

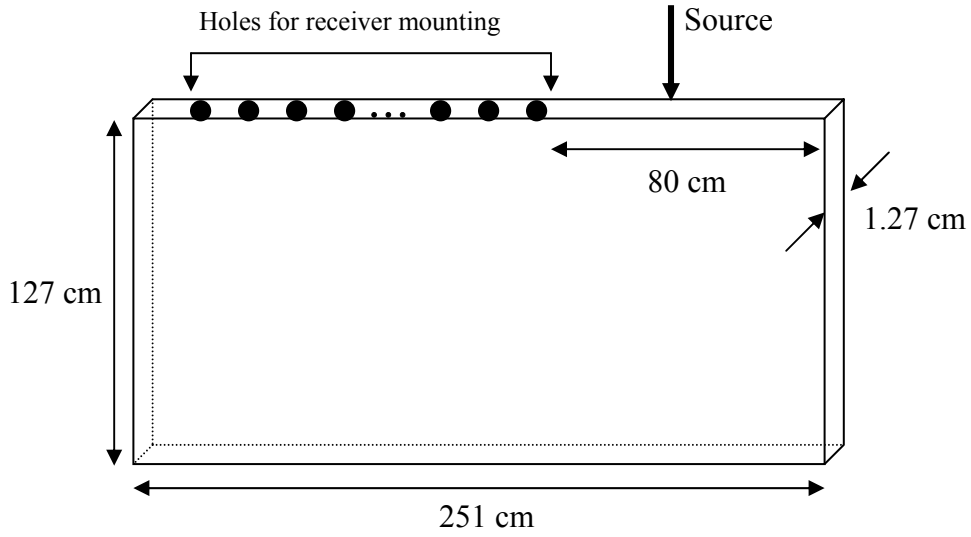

Figure 4.22 PMMA plate used for laboratory simulations

Model WR 728T high frequency accelerometers manufactured by Wilcoxon Research Inc. are used as receivers. A VXI mainframe system with a 16 channel HP E1432A and a PCB 442A104 signal conditioner are used as recording units. A WR F7 piezoelectric vibration generator as shown in Figure 4.23 is selected as a harmonic source. WR N7L matching network and WR PA7E are also required for use of the harmonic source. Figure 4.24 illustrates the equipment configuration for laboratory simulations with a harmonic source.

Figure 4.23 WR F7 piezoelectric vibrator

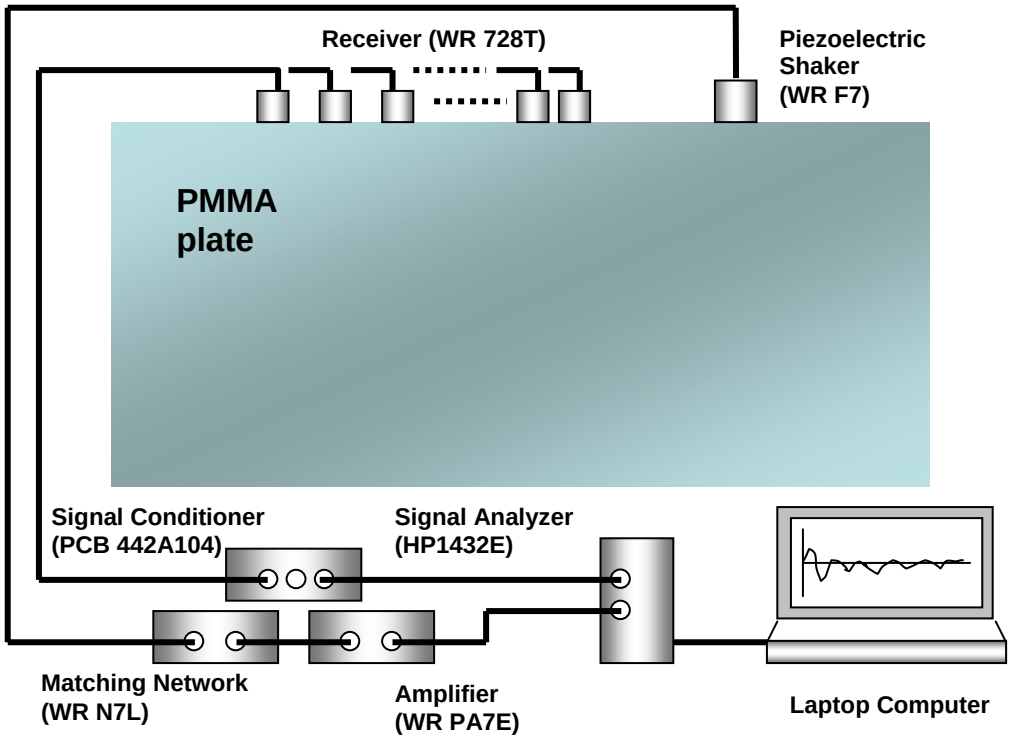

Figure 4.24 Equipment configuration for laboratory simulations

4.3.2.4 Mass loading by receivers

Array-based surface wave tests are preferably performed with multiple receivers placed simultaneously. Laboratory simulation with a thin PMMA plate was initially designed to perform simulated laboratory surface wave tests with multiple receivers placed simultaneously. Figure 4.25 shows frequency-wavenumber spectrum and dispersion curve from the initial laboratory simulation with receivers placed simultaneously.

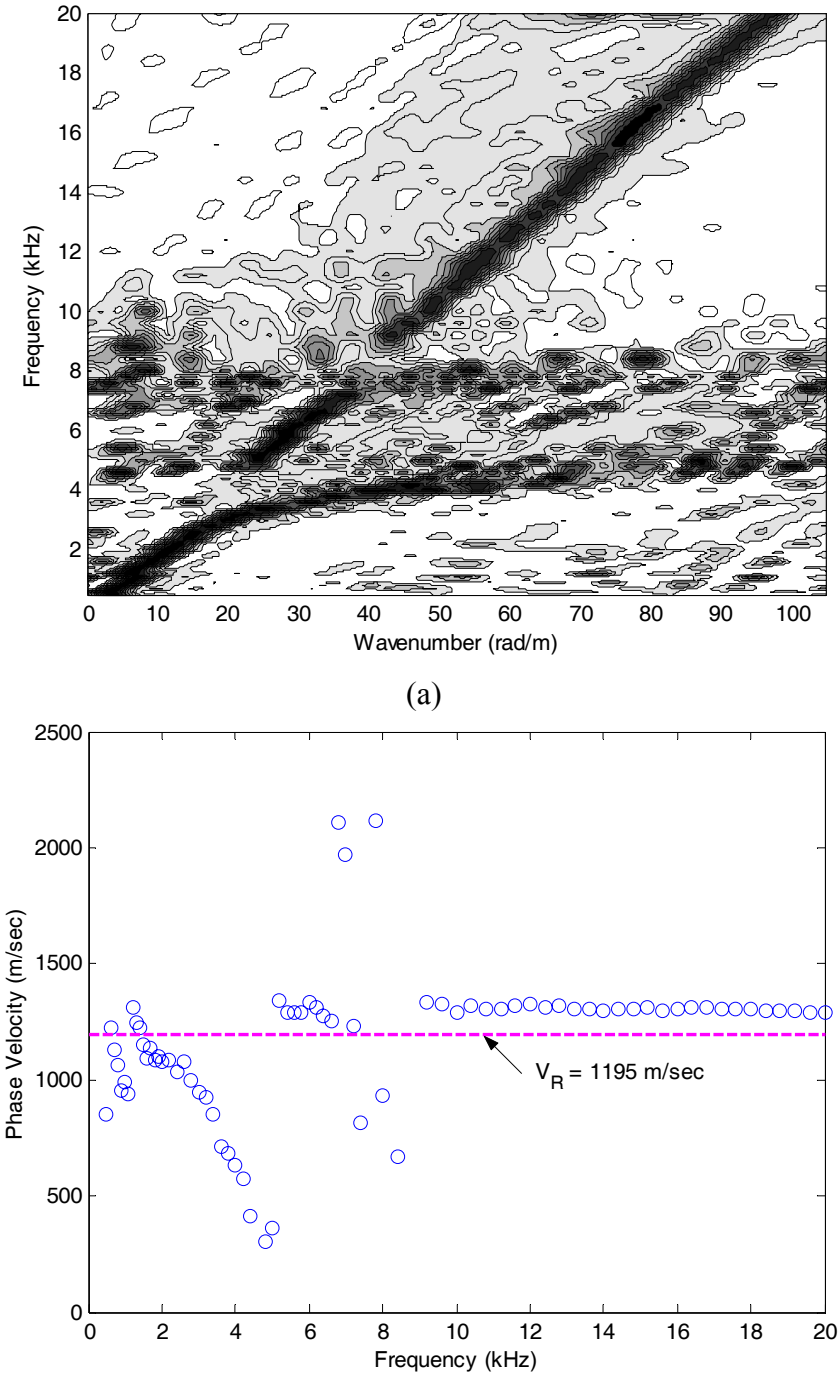

Figure 4.25 Test results of laboratory simulation with 15 receivers placed simultaneously: (a) f-k spectrum and (b) dispersion curve

Two important features are observed in Figures 4.25: (1) complicated wavefields at frequencies lower than about 10 kHz, and (2) measured phase velocities higher than the reference Rayleigh wave phase velocity at frequencies greater than 10 kHz. Mass loading by simultaneously placed receivers was suspected of a main cause of these unexpected features. To minimize the effect of receiver mass, a test was performed with only one receiver by moving it from position to position and repeating the source excitation. Finally, the individual tests were combined to calculate f-k spectra and dispersion curves. If each test is repeatable, this procedure provides experimental measurements of propagating waves at various locations with the minimized effect of receiver mass. The harmonic source is a good choice to satisfy the requirement of repeatability in measurements.

Figure 4.26 shows frequency-wavenumber spectrum and dispersion curve from laboratory simulations performed in this manner. As shown in Figure 4.26, the complicated wavefields observed in Figure 4.25 at the frequencies lower than 10 kHz are no longer observed. Note that the measured phase velocities from the simulations with the minimized receiver mass effect are much closer to the reference Rayleigh wave velocity of 1195 (m/sec) compared to those from the simulations with the receiver mass effect.

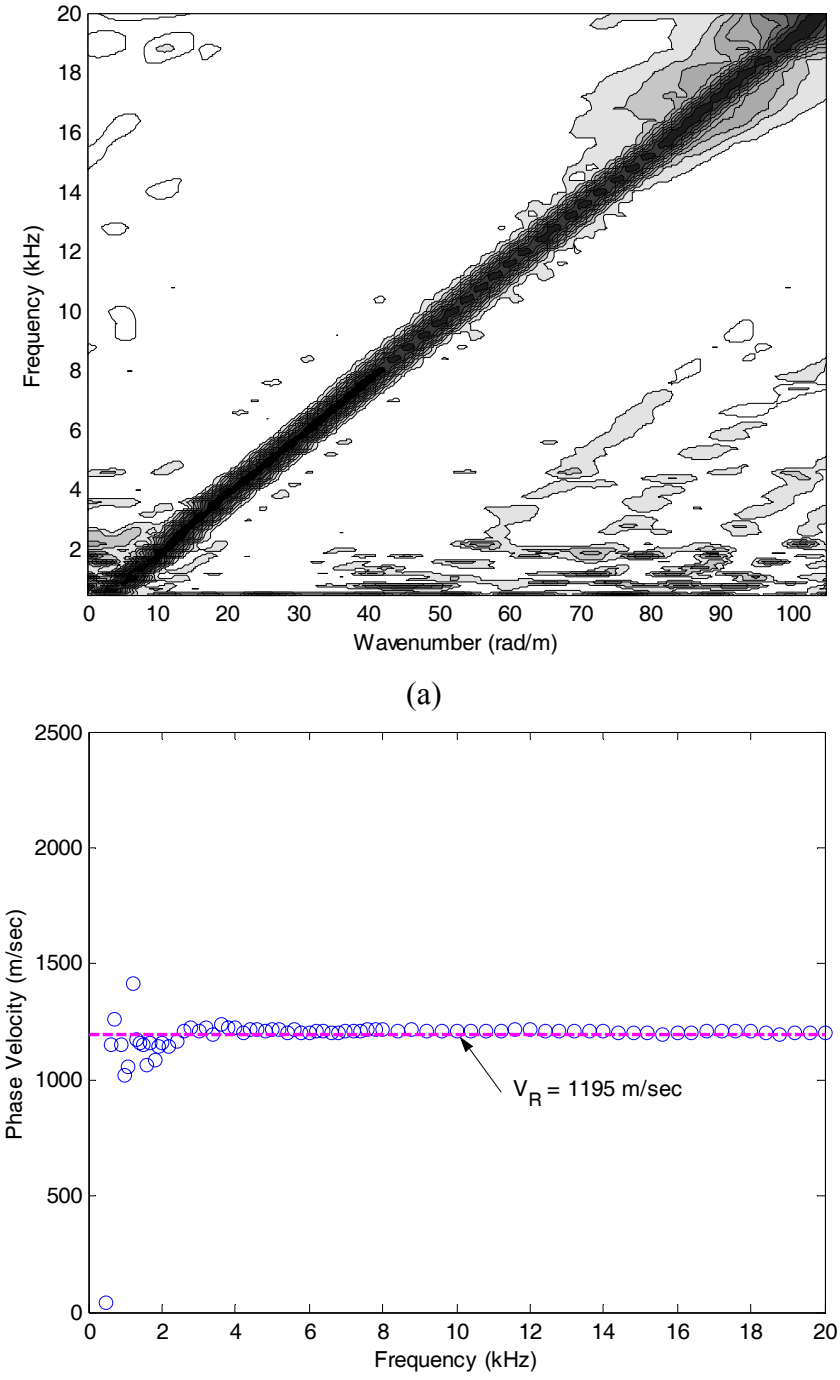

Figure 4.26 Test results with the minimized receiver mass effect: (a) f-k spectrum and (b) dispersion curve

4.3.3 Laboratory Simulation Procedure to Investigate Near-Field Effects

Based on the results of the study of system and source identification, a detailed procedure for laboratory simulation was developed to investigate near-field effects on array-based active methods. Laboratory simulations were performed for a set of 56 frequencies ranging from 3 to 20 kHz. Since focus is on data at lower frequencies for the study of near-field effects, the frequencies were concentrated at lower values. Ten blocks of time-domain recordings with sampling frequency of 51.2 kHz were collected for a time period of 0.02 sec per each recording and averaged in frequency domain to reduce the variance of the signal.

Laboratory simulations with arrays having 10, 15, and 20 receivers were performed. For each number of receivers, three uniform linear arrays with different SR distances were used for laboratory simulations as listed in Table 4.9.

Table 4.9 Array sets used for laboratory simulation to investigate near-field effects

Array set No.	Array*	Array parameter		
		Array center (cm)	Number of receivers	Total sampling distance (cm)
1	5SR3RR-10	18.5	10	27
	8SR3RR-10	21.5		
	11SR3RR-10	24.5		
2	5SR3RR-15	26	15	42
	8SR3RR-15	29		
	11SR3RR-15	32		
3	5SR3RR-20	33.5	20	57
	8SR3RR-20	36.5		
	11SR3RR-20	39.5		

* Unit in the notation is cm. For example, 5SR3RR-10 denotes a uniform array of 10 receivers with SR distance of 5 cm and RR distance of 3 cm.

4.3.4 Results of Laboratory Simulations

4.3.4.1 Dispersion curves

Figure 4.27 shows comparisons of the dispersion curves from the laboratory simulations. Dispersion curves were plotted over the operating frequencies ranging 3 to 20 kHz and V_R of 1195 m/sec is also shown as a reference Rayleigh wave velocity. The deviations in dispersion curves from the reference wave velocity represent errors due to near-field effect. As shown in Figure 4.27, the hypothesis regarding near-field effects (i.e. near-field effects decrease with increasing frequency and with increasing array distance from the source) is satisfied. Note that errors due to near-field effects is much more significant for dispersion curves associated with the 10 receiver arrays compared to those associated with the arrays of 15 or 20 receivers.

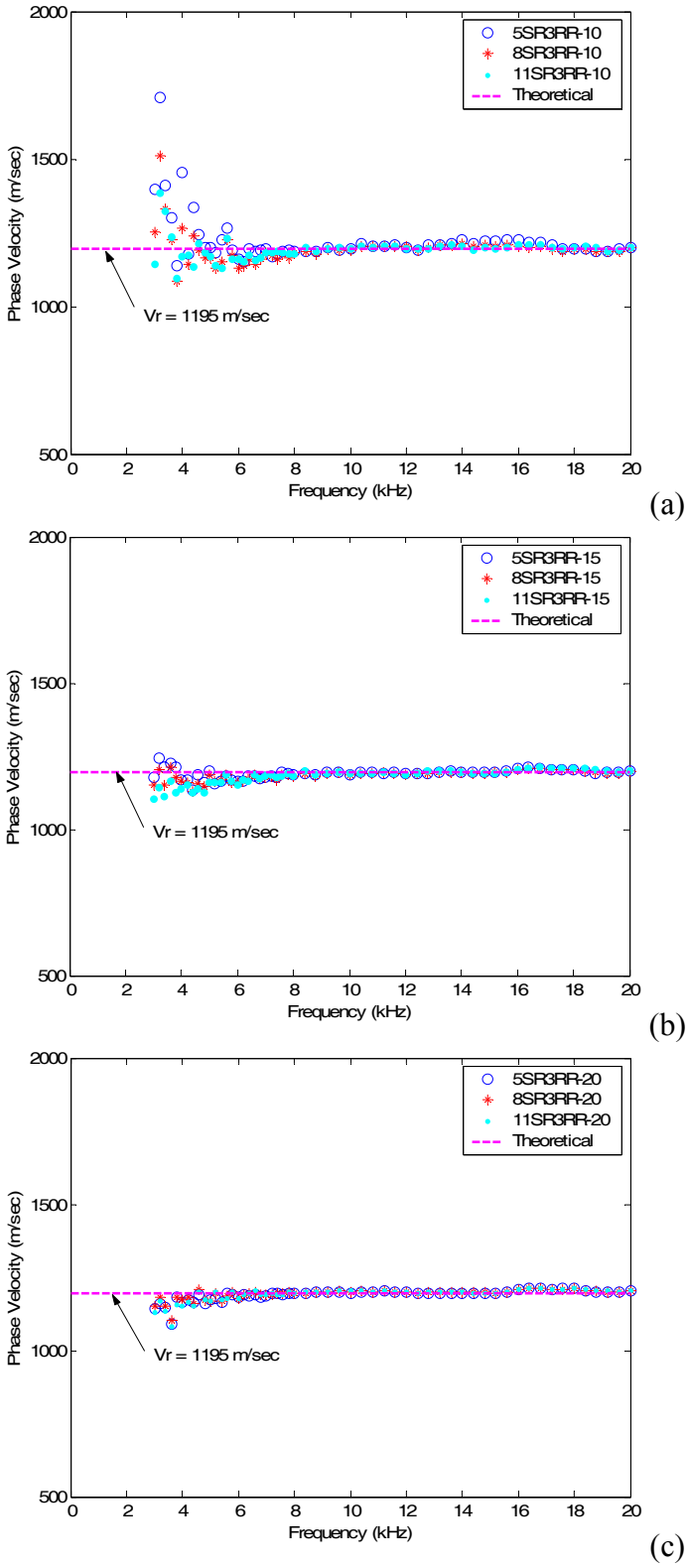

Figure 4.27 Comparison of dispersion curves from laboratory simulations with various arrays of (a) 10 receivers, (b) 15 receivers, and (c) 20 receivers

4.3.4.2 Near-field effect criteria in terms of normalized parameters

Figure 4.28 presents near-field effects captured by two normalized parameters with the dispersion data from laboratory simulations with arrays in Table 4.9. As shown in Figure 4.28, most errors due to near-field effects contribute to underestimation of the Rayleigh wave velocity. Most of the overestimated Rayleigh wave velocities occur with 10-receiver arrays. Poor wavenumber resolution of the 10 receiver arrays may not be able to correctly identify wavenumbers.

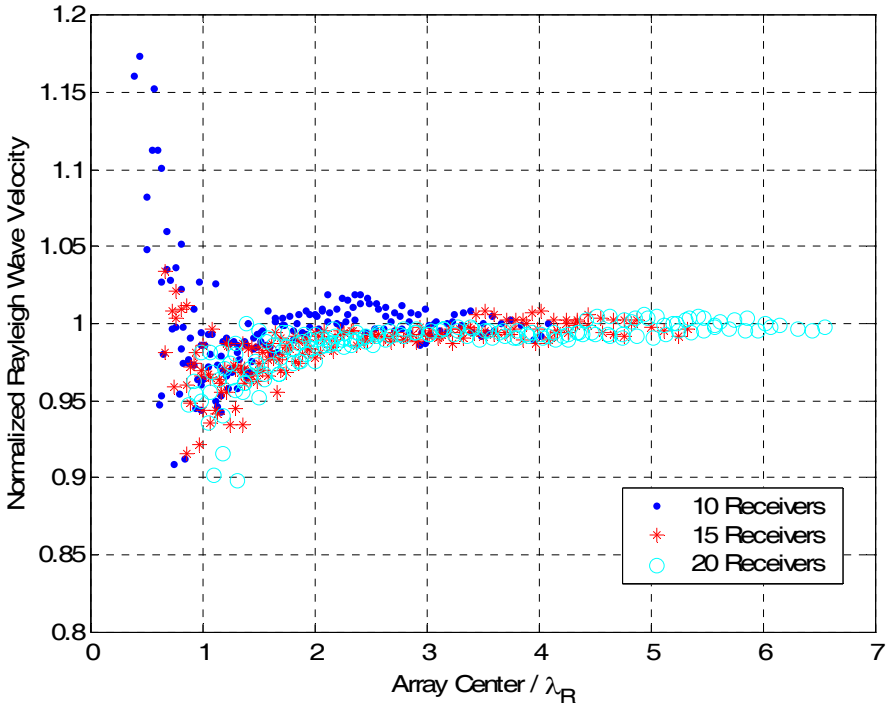

Figure 4.28 Near-field effects captured by normalized parameters with laboratory simulation results

4.4 FIELD TESTS

4.4.1 Oakridge Landfill Site

For the study of near-field effects, a series of surface wave field tests including active and passive tests was performed at the Oakridge landfill site in Dorchester, South Carolina on June 4~5, 2004. The site at the latitude of N33.0808º and the longitude of W80.2208º has a sufficiently large area for performing both active and passive surface wave tests with various arrays. Since the site was surrounded by excellent passive sources from downtown Charleston, Interstate Highway 26, and the Atlantic Ocean, successful passive wave tests were anticipated. The tests were done using the test equipment and data processing techniques presented in Chapter 2.

The soil conditions consist of approximately 2 m of tan loose, medium to fine sand underlain by 2~6 m of white loose, fine sand, 6~8 m of black dense, medium to fine sand, 8~11 m of loose sand, and 11~13 m of black dense, medium to fine sand. Beneath the dense sand layer are stiffer soils. The cone penetration test (CPT) data for the site is shown in Figure 4.29.

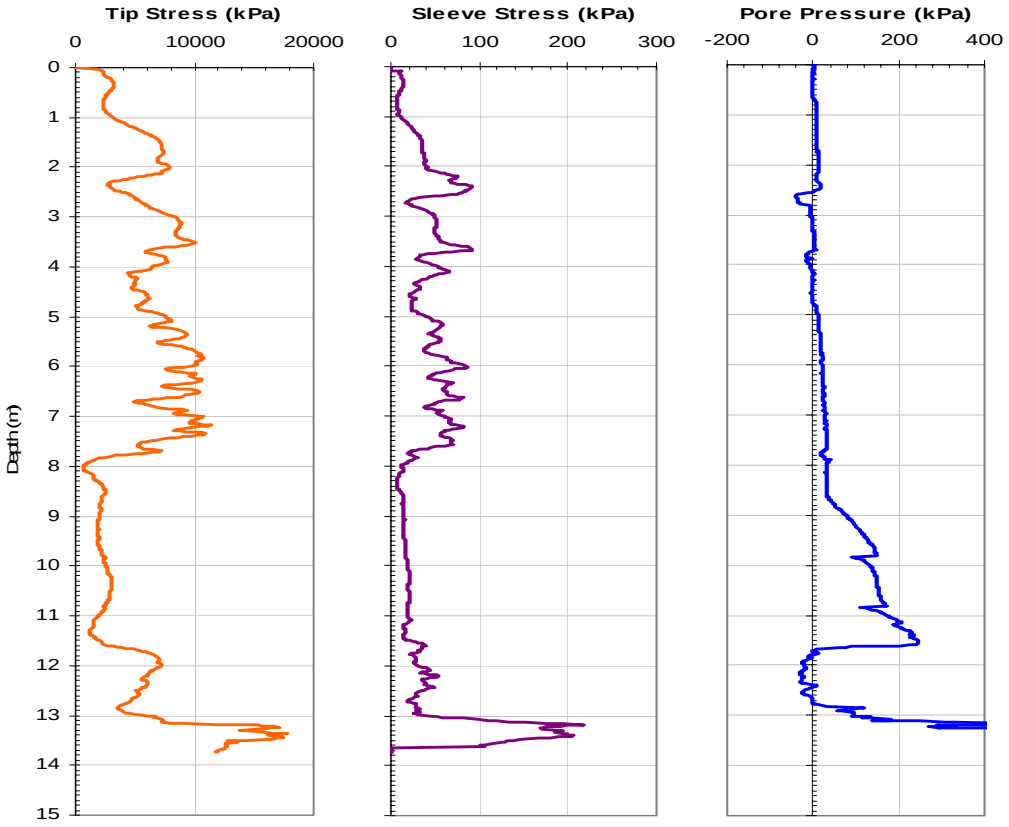

Figure 4.29 Soil profile at Oakridge landfill site

4.4.2 Test Configuration

To evaluate near-field effects, active surface tests were conducted with three different non-uniform arrays: (1) the standard array of 15 receivers spaced at 2.4, 3, 3.7, 4.6, 5.5, 6.7, 8.5, 10.4, 12.8, 15.2, 18.3, 21.3, 24.4, 29, and 33.5 m, (2) the standard array with the shift of 3.0 m (10ft), and (3) the standard array with the shift of 9.1 m (30ft) away from the source. A sledgehammer was used as a transient source and an electromagnetic shaker as a harmonic source. The measurements were made at a sampling frequency of 320 Hz for all the tests. Five repeated tests using the transient source were performed to average them with 2^{10} time domain records for reduced variation in the signal. For the tests using the harmonic source, 5 blocks of 2^{11} time domain records were measured for frequencies ranging 4 to 100 Hz and averaged.

4.4.3 Passive Test Results as Reference

One of the biggest challenges in parametric studies using field test results is having a "true" value that is used as a reference value. For example, to study near-field effects, a dispersion curve that is not contaminated by near-field effects is needed as a reference. Passive waves coming from a far distance may be reasonably considered as plane Rayleigh waves. If assuming that the passive surface wave tests provide unbiased results, the results can be used as reference values that are not contaminated by near-field effects. Three passive surface wave tests were conducted using a 16-receiver circular array with radius of 27.4 m (90 ft). The 16 receivers were placed at equal spacing along the circumference of the circle. During each passive testing, passive energy was collected for 256 seconds at a sampling frequency of 320 Hz. The 2^{16} time domain records in each passive test were divided into 16 blocks to average them in frequency domain to reduce the variance of the results.

4.4.4 Results of Field Tests

4.4.4.1 Active field tests with various SR distances

Figure 4.30 shows the comparison of the dispersion data from the active tests using the three arrays. The averaged dispersion curve from the three passive tests was also presented as a reference curve free of near-field effect since passive waves were considered plane Rayleigh waves. As shown in Figure 4.30, arrays further from the source produced dispersion curves closer to the assumed reference values. For frequencies over 10 Hz, similar dispersion curves are obtained regardless of array selection, indicating no serious near-field effects at higher frequencies.

Note that the minimum frequency in the dispersion curve becomes smaller as the array is shifted further away from a source. The minimum frequency is often limited by a wavenumber resolution determined by a total sampling distance of a given array. At frequencies below 10 Hz, Rayleigh wave velocities for the standard array with a shift of 9.1 m are higher than those for the standard array. Higher velocities correspond to smaller wavenumbers and the wavenumbers may not be successfully resolved by an improper wavenumber resolution. The two arrays have the same spatial resolution due to the same total sampling distance, and the wavenumber resolution may lead to unsuccessful detection of the smaller wavenumber for the shifted standard array at frequencies below 6 Hz.

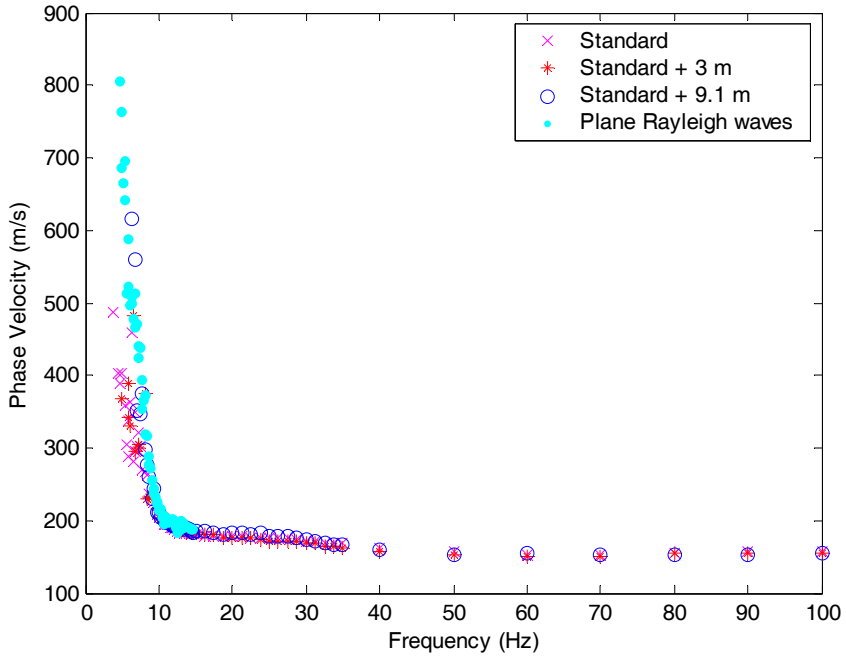

(a)

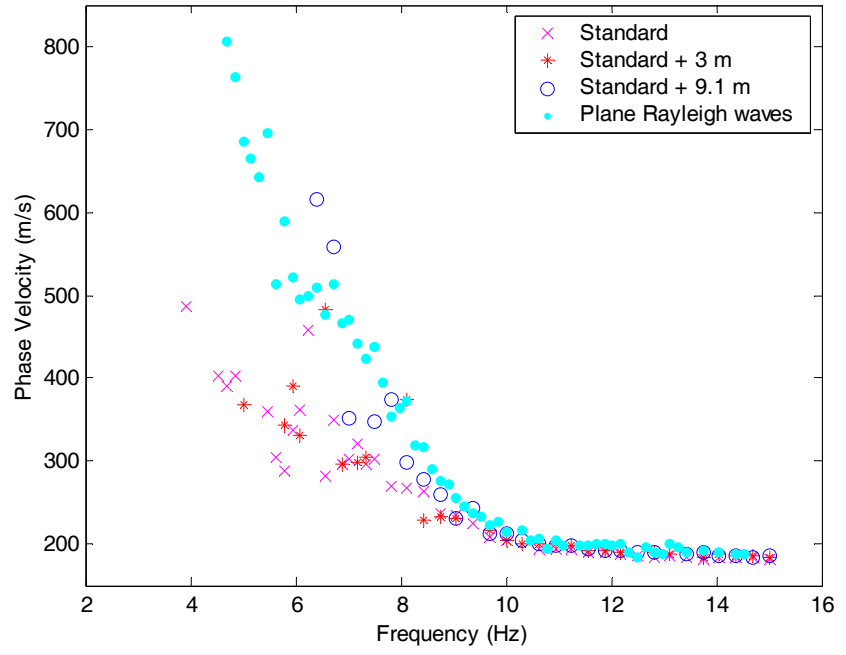

(b)

Figure 4.30 Comparison of dispersion curves from the filed tests for (a) frequencies up to 100 Hz and (b) frequencies ranging 2 to 16 Hz

4.4.4.2 Near-field effect according to source type

In the field tests, two types of active sources (i.e., active-transient and active-harmonic) were used. As discussed in Chapter 3, a harmonic source offers the following advantages over a transient source: (1) allowance of much greater control over the frequency content and (2) generation of meaningful lower-frequency energy compared to a transient source. It was anticipated that these advantages over a transient source provided a significant improvement in estimation of dispersion (or attenuation) data. The aforementioned advantages of a harmonic source may be visually shown by comparing dispersion curves from harmonic source tests to those from transient source tests.

It is helpful to see the frequency contents in each transient source test to better understand the dispersion curves from each test. Figure 4.31 shows the frequency content of the transient source in the active tests with the three arrays. The frequency contents are similar and are concentrated at frequencies greater than about 20 Hz, leading to anticipation of having meaningful dispersion data for frequencies over about 20 Hz.

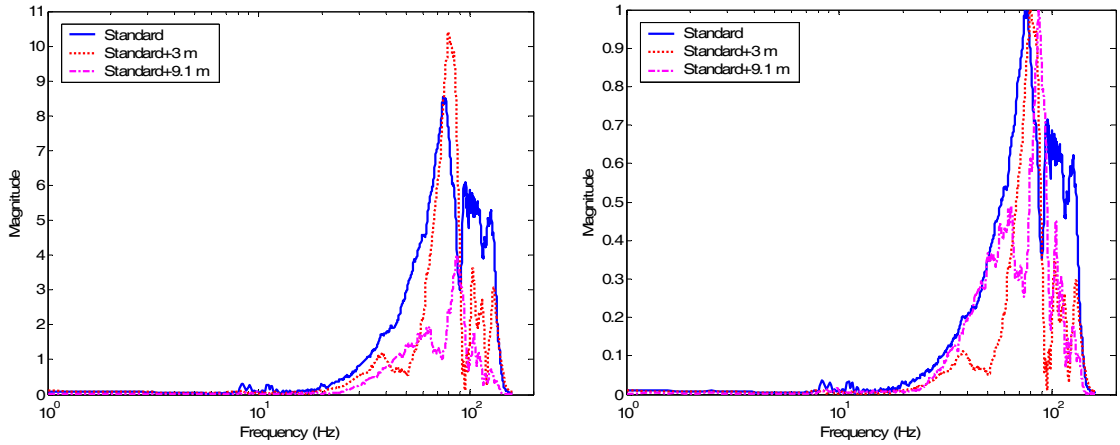

Figure 4.31 Frequency contents of energies generated by a transient source in tests with three arrays: (a) true magnitude and (b) normalized magnitude

Figure 4.32 presents f-k spectra associated with the transient source tests. As shown in Figure 4.32(a), severe noise interference is observed for the f-k spectrum associated with the standard array at frequencies lower than about 30 Hz. A similar observation was made for the 3 m shifted standard array from Figure 4.32(b). A small improvement in the f-k spectrum resulting from reduction in near-field effects was observed compared to that associated with the standard array having smaller AC. Finally, the near-field effects were significantly reduced by shifting the array further away from the source as shown in Figure 4.32(c).

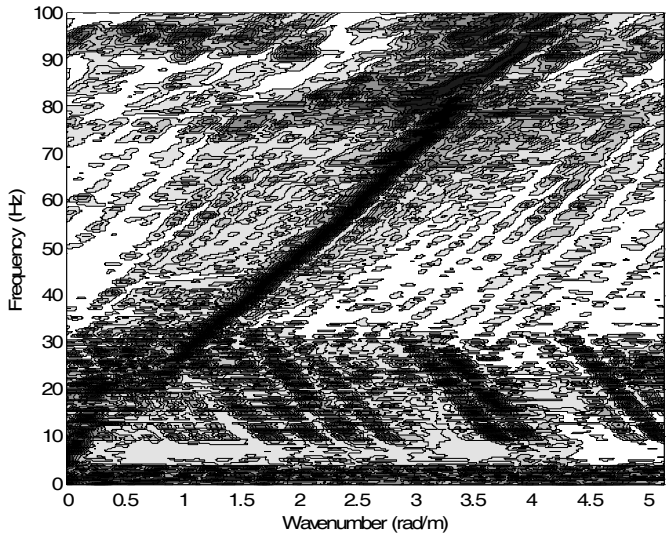

(a)

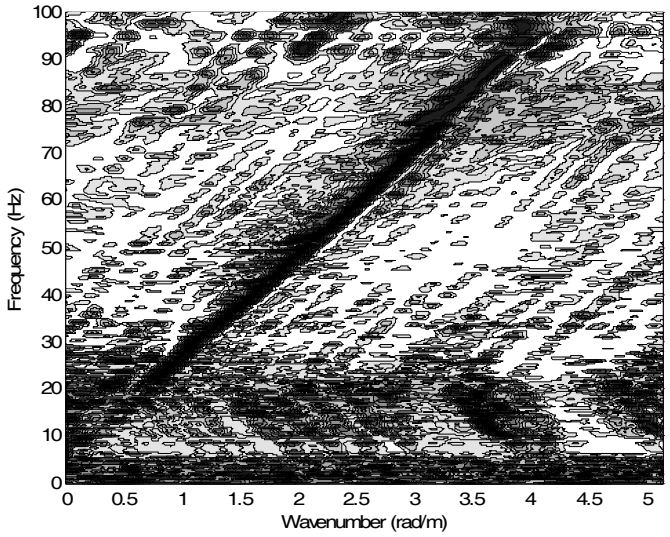

(b)

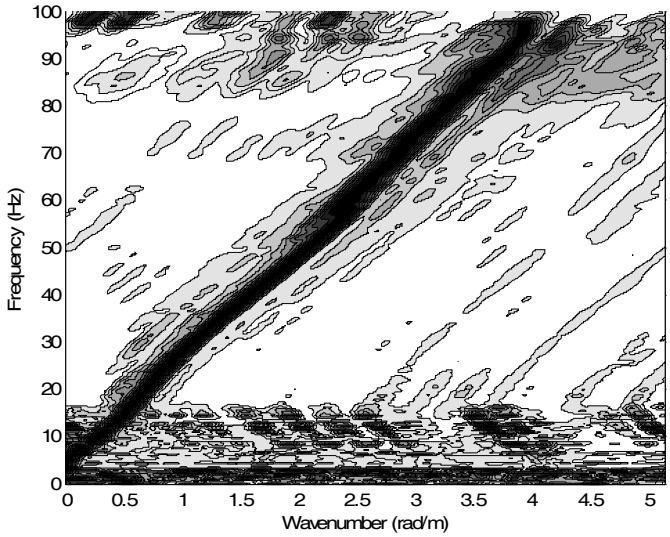

(c)

Figure 4.32 Frequency-wavenumber spectra for active tests using a transient source: (a) standard array, (b) standard + 3 m array, and (c) standard + 9.1 m array

Figure 4.33 shows the comparison of dispersion curves from the transient source tests and those from the harmonic source tests for the three arrays. As anticipated based on the f-k spectra in Figure 4.32 and directly shown in Figure 4.33, the transient source test with the standard array did not provide meaningful dispersion data for frequencies less than about 28 Hz, while the transient source tests with the shifted standard arrays provided those for lower frequencies. Since the same transient source (a sledgehammer) generating similar frequency content energy was used for the tests, it is considered that the availability of dispersion data at lower frequencies results from mitigating near-field effects via shifting the array further away from a source. Note that the harmonic tests provided meaningful dispersion data for relatively low frequencies regardless of array configuration, although some errors caused by near-field effects might be included in the data depending on a given array. It may be considered that transient source tests are more vulnerable to near-field effects than harmonic source tests because of their incapability to successfully remove noise interference.

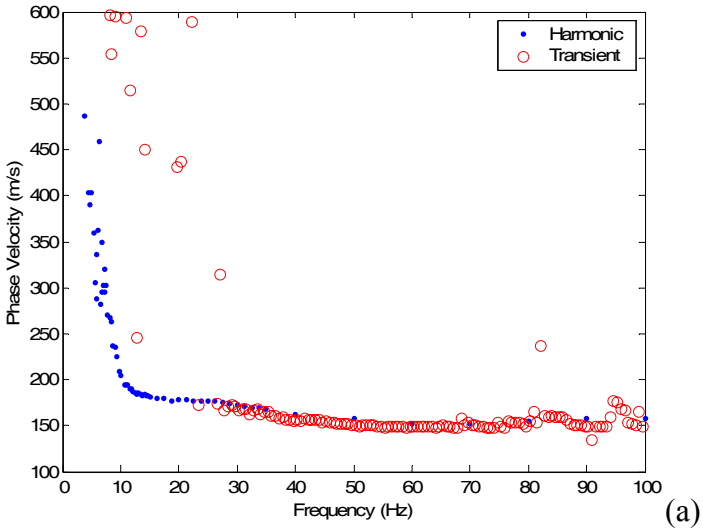

(a)

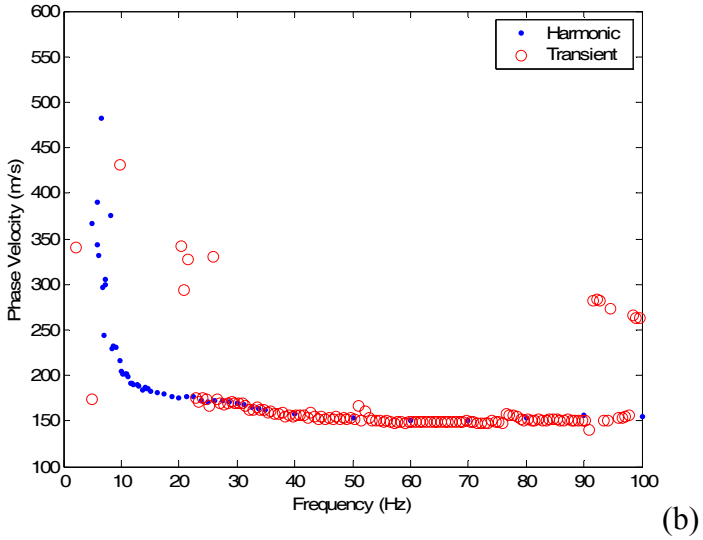

(b)

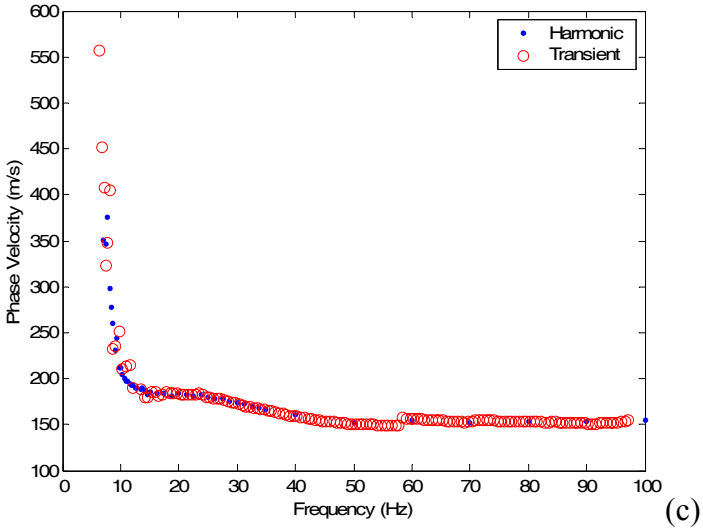

(c)

Figure 4.33 Comparison of dispersion curves of active tests using a transient source and a harmonic source: (a) standard array, (b) standard + 3 m array, and (c) standard + 9.1 m array

4.4.4.3 Near-field effect criteria in terms of normalized parameters

To evaluate near-field effects, normalized parameters were plotted using the dispersion data of the active and passive tests as shown in Figure 4.34. Rayleigh wave velocities from the passive tests were used as plane Rayleigh wave velocities (reference values). As observed in Figure 4.33, most of the dispersion data were underestimated due to near-field effects. At normalized values of AC of 1 and 0.5, lower-bound normalized Rayleigh wave velocities are about 0.92 and 0.80, respectively, indicating maximum probable errors up to 8 % and 20 %, respectively.

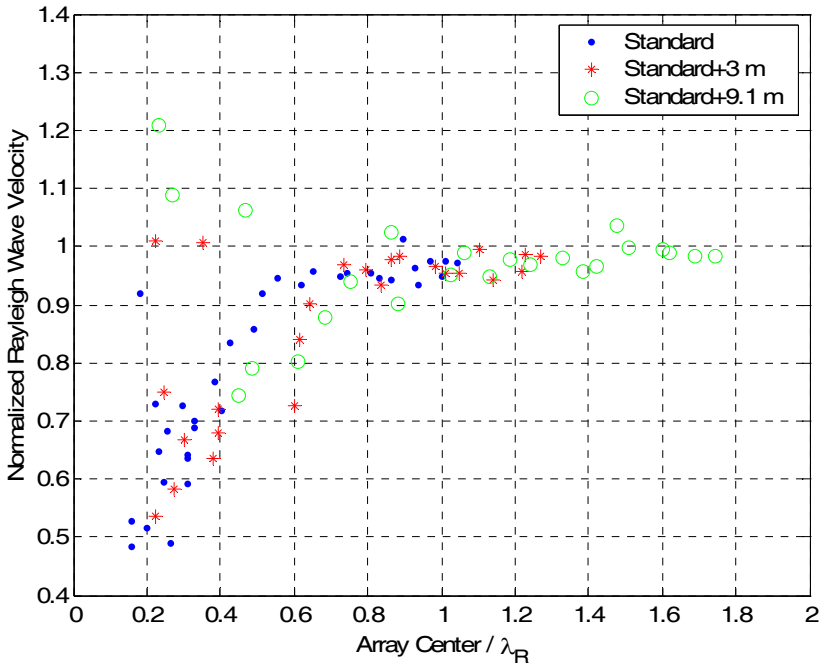

Figure 4.34 Near-field effects captured by normalized parameters with field test results

4.5 COMPARISON AND SYNTHESIS OF NUMERICAL, LABORATORY, AND FIELD RESULTS

4.5.1 Comparison of Numerical, Laboratory, and Field Results

Numerical and experimental methods have their own advantages and limitations in performing parametric studies. For the investigation of several issues in surface wave methods, numerical methods have been frequently used. However, to successfully apply numerical results to real cases, limitations of the methods should be carefully considered. In this study, two experimental methods (laboratory simulations and field tests) as well as numerical method have been developed and performed to investigate near-field effects on array-based surface wave methods. Comparison and synthesis of numerical, laboratory, and field results are expected to allow extracting conclusions for better practical applications.

Figure 4.35 shows the comparison of numerical simulation and laboratory simulation results. Due to dependency of near-field effects on soil condition, numerical results for Case 1 are compared with laboratory results, which have been obtained from tests with a homogeneous medium. For normalized AC greater than 1, numerical and laboratory results agree well although the plots of the laboratory simulation are slightly more scattered. However, many overestimated dispersion data were obtained from the laboratory simulation for normalized AC smaller than 1 unlike the numerical simulation results. Note that most of the overestimated data comes from the laboratory simulation results with the 10-receiver arrays as shown in Figure 4.28. If eliminating the data associated with the 10-receiver arrays, numerical and laboratory results agree better over the entire range of normalized AC.

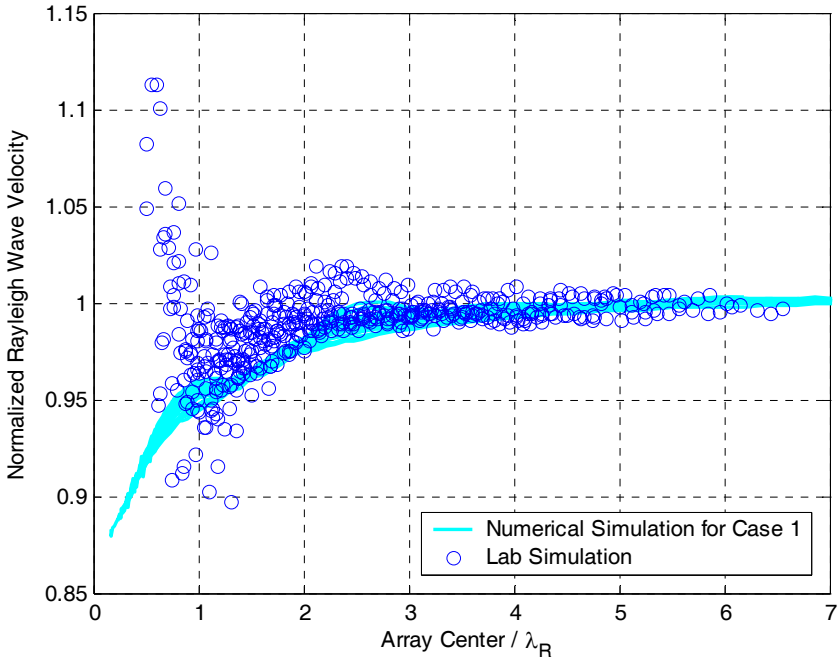

Figure 4.35 Comparison of near-field effect criteria in terms of normalized parameters from laboratory simulation results and numerical simulation results for Case 1

To successfully compare numerical simulation and field test results, soil conditions for the field test site needs to be identified. Figure 4.36 shows shear wave velocity profiles derived from active dispersion curves with three arrays at the Oakridge landfill site shown in Figure 4.30. As shown in Figure 4.36, a stiff layer between slightly softer layers is found indicating Case 4 type inversely dispersive soil condition. Based on general trend in the profiles, a soil condition may be considered as Case 2 type normally dispersive soil condition. Thus, the field test results were compared to numerical results for both Case 2 and Case 4 soil conditions.

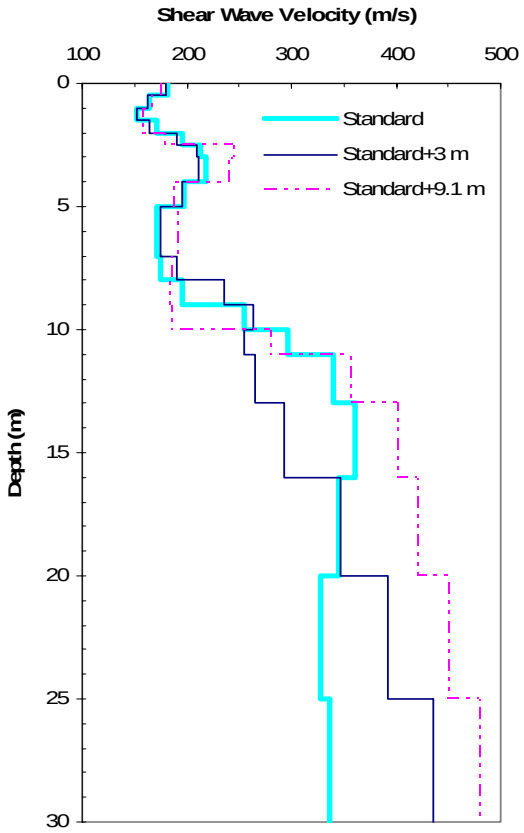

Figure 4.36 Shear wave velocity profiles at Oakridge landfill site

Figure 4.37(a) shows the comparison of near-field effects captured by normalized parameters with field test results and numerical simulation results associated with Case 2. As seen in Figure 4.37(a), excellent agreement between the two results was observed for normalized AC values greater than 0.6. At normalized AC values less than 0.6, near-field effects from the field test results are much more severe than those from the numerical simulations. Figure 4.37(b) shows another comparison of near-field effects captured by normalized parameters with field results and numerical results associated with Case 4. As seen in Figure 4.37(b), the two results show excellent agreement for normalized AC values greater than 0.4. For normalized AC values less than 0.4, the differences between the results are insignificant compared to those from the previous comparison of field results with numerical results associated with Case 2.

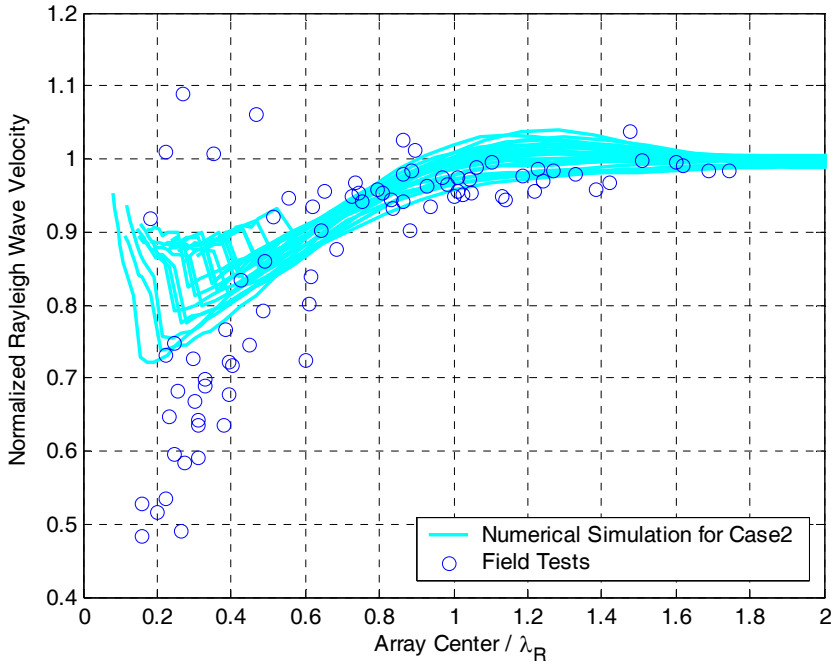

(a)

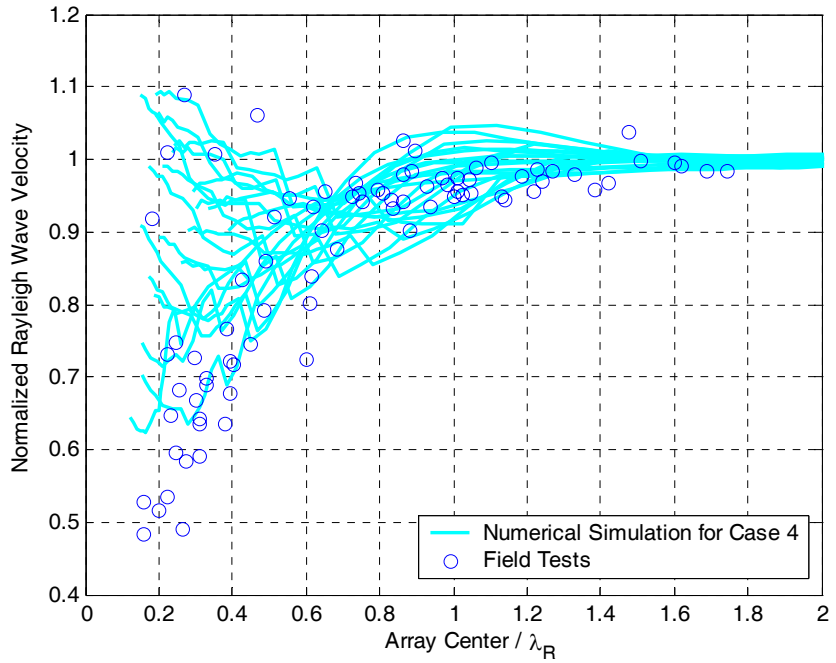

(b)

Figure 4.37 Comparison of near-field effect criteria in terms of normalized parameters from field test results and numerical simulation results for (a) Case 2 and (b) Case 4

4.5.2 Summary of Errors Due to Near-Field Effects

From the results of the studies with numerical simulations, laboratory simulations, and field tests, it was observed that majority of dispersion estimates contaminated by near-field effects were underestimated. Therefore, lower-bounds in the plots of normalized parameters can be used to approximate maximum probable errors caused by near-field effects for a given normalized AC depending on site conditions. Table 4.10 summarizes lower-bound normalized Rayleigh wave velocities at three normalized array centers for four soil profiles based on the numerical results. Table 4.11 presents a summary of lower-bound normalized Rayleigh wave velocities at three normalized Array centers for two soil conditions based on the laboratory and field results.

Table 4.10 Lower-bound normalized Rayleigh wave velocity based on numerical results

Normalized AC	Lower-bound normalized Rayleigh wave velocity			
	Case 1	Case 2	Case 3	Case 4
2	0.97	0.98	0.95	0.98
1	0.94	0.95	0.85	0.9
0.5	0.91	0.83	0.8	0.75

Table 4.11 Lower-bound normalized Rayleigh wave velocity based on laboratory and field results

Normalized AC	Lower-bound normalized Rayleigh wave velocity	
	Laboratory simulations	Field tests
2	0.97	0.98
1	0.9	0.92
0.5	N/A	0.8

4.6 SUMMARY AND CONCLUSIONS

From the results of numerical simulations, laboratory simulations, and field tests regarding near-field effects on array-based surface wave methods, the following conclusions are derived:

(1) Near-field filtering criteria previously suggested for traditional SASW methods do not apply to array-based surface wave methods. Since near-field effects rely on soil condition, the study of the near-field effects needs to be performed according to soil condition.

(2) Based on the two major causes of near-field effects, normalized array center (AC) and normalized Rayleigh wave velocity were proposed to perform the study of near-field effects and successfully captured near-field effects for various array configurations and various soil profiles. Plots of these dimensionless parameters can be applied to active surface wave tests with any scale for evaluation of near-field effects.

(3) Dispersion estimates from the array-based surface wave methods with limited number of receivers placed at limited space usually contain errors caused by array effects as well as near-field effects. In the numerical simulations, array-effects can be excluded by calculating a reference dispersion curve from Rayleigh Green's function solutions corresponding to the same array as a dispersion curve of combined body and Rayleigh waves.

(4) Underestimation of dispersion values is a primary impact caused by near-field effects. Therefore, lower boundaries in the plots of the normalized parameters for four different soil profiles are considered as criteria to approximate maximum

probable errors caused by near-field effects at a certain normalized AC for corresponding site conditions. For normalized AC of 2, normalized Rayleigh wave velocities corresponding to lower boundaries range from 0.95 to 0.98 depending on soil profiles. For normalized AC of 1 and 0.5, the lower boundary normalized Rayleigh wave velocities range from 0.86 to 0.95 and from 0.75 to 0.91, respectively, depending on soil profiles.

(5) Near-field effects become more significant for the inversely dispersive soil profiles due to much more complicated wavefields in these soil profiles compared to the homogeneous half-space and the normally dispersive soil profile. In addition to near-field effects, array effects become more serious for the inversely dispersive soil profiles than for the normally dispersive soil profile. The capabilities of the array-based surface wave methods with a certain array with a limited number of receivers to estimate accurate dispersion data are more restricted for the inversely dispersive soil profiles.

(6) Laboratory simulation using a thin PMMA plate was developed to investigate factors affecting surface wave measurements. The hypothesis regarding near-field effects was verified using dispersion curves from the laboratory simulations with various array configurations. Plots of the two normalized parameters with data from the laboratory simulations agree well with those with data from the numerical simulations for the homogeneous half-space.

(7) Active surface wave field tests with two different sources and three different linear arrays were performed to investigate near-field effects. Passive surface wave field tests were also performed to provide a dispersion curve that was

assumed to be free of near-field effects. Dispersion curves from the active tests satisfy the hypothesis regarding near-field effects. Active tests with the transient source appear to be more vulnerable to near-field effect than those with the harmonic source because of the insufficient low frequency energy and the lack of noise removal techniques.

(8) Field test results are compared with numerical simulation results associated with Case 2 and Case 4 soil profiles using normalized parameters. Field tests results show excellent agreement with numerical simulation results for both soil profiles at normalized AC values greater than 0.6. For normalized AC values less than 0.6, field test results agree more with numerical simulation results for Case 4 than those for Case 2, indicating the site condition more close to Case 4 type inversely dispersive condition.

CHAPTER 5

COMBINED ACTIVE-PASSIVE

SURFACE WAVE MEASUREMENTS

5.1 INTRODUCTION AND STATEMENT OF THE PROBLEM

As discussed in Chapter 3, surface wave methods may be divided into two types, active and passive methods, according to the source of the surface waves. Both methods have been used in geotechnical engineering as summarized in Table 5.1.

Table 5.1 Classification of surface wave methods (after Tokimatsu, 1995)

Method	Source	Period (Frequency)	Array Dimension	Applicable Depth	References
Active	Steady state point loading	Less than about 0.2~0.5 s (more than about 2~5 Hz)	linear	Less than 10~20 m	Jones (1958)
	Random point loading				Nazarian and Stokoe (1986)
Passive	Short-period microtremors	Less than 1 s (more than 1 Hz)	Two-dimensional	Less than 50~100 m	Tokimatsu et al. (1992a)
	Long-period microtremors	1~5 s (0.2~1 Hz)		Up to several km	Horike (1981)

Active tests can be performed using an active source and a one-dimensional (i.e., linear) array of receivers to monitor ground response caused by the propagating waves. Active tests, however, are limited in their ability to sample deep soils due to the difficulty of generating low-frequency energy with reasonably portable sources. Passive sources such as microtremors and cultural noise have been utilized as an alternative to overcome this limitation because passive waves typically contain more low-frequency energy and thus penetrate more deeply. The frequency range measured during passive testing is often

on the order of 1 to 10 Hz, depending on site conditions, characteristics of the passive source, and characteristics of the receiver array (Yoon and Rix, 2004). A two-dimensional array of receivers is required to collect passive waves because of the unknown locations of the passive sources during testing.

Active and passive tests may be combined to enable measurements of the shear wave velocity profile to greater depths without sacrificing the near-surface resolution offered by the active method (Hebeler, 2001; Rix et al., 2002; Yoon and Rix, 2004). Generally, the passive and active measurements overlap in the frequency range of approximately 4 to 10 Hz, and there are often systematic differences between the two measurements (Yoon and Rix, 2004). It is necessary to resolve these differences to obtain an accurate composite dispersion curve. In this chapter, features of active and passive measurements that are responsible for differences between them will be discussed using numerical simulations and field experiments.

The goal of this study is to develop a procedure to combine active and passive measurements to form an accurate composite dispersion curve over a broad range of frequencies.

5.2 FIELD MEASUREMENTS

5.2.1 Williams Street Park Site

Active and passive surface wave measurements were performed at the Williams Street Park site in San Jose, California on July 8, 2003. Since the site was surrounded by excellent passive sources from downtown San Jose, Interstate Highway 280, the Pacific

Ocean, and San Francisco Bay, successful passive tests were anticipated. A large, flat area at the site allowed for passive tests with circular arrays of large radii.

The soil conditions consist of approximately 9 m of sandy gravel underlain by 9 – 18 m of silty clay and 18 – 50 m of sandy gravel. Beneath the sandy gravel are stiffer sediments, which are composed of clay, silt, sand, and gravel. The gravels are composed largely of sandstone, basaltic volcanics, and red chert eroded from Franciscan bedrock in the surrounding mountains (Hanson et al., 2002). The based of the Holocene-aged sediments is marked at a depth of 23 m (Hanson et al., 2002).

5.2.2 Active and Passive Measurements

The 16-channel, VXI-based data acquisition unit described in Chapter 3 was used for recording test data from the field measurements. A mixture of Kinemetrics SS-1 Ranger, shown in Figure 5.1(a), and Mark Products L4-C, shown in Figure 5.1(b), geophones with a natural frequency of 1 Hz was used as receivers.

(a) (b)

Figure 5.1 Receivers used at the Williams Street Park site: (a) Kinemetrics SS-1 Ranger geophone and (b) Mark Products L4-C geophone

An active test was performed using an electromechanical harmonic source shown in Figure 3.3 and the standard, non-uniform array of 15 receivers spaced at 2.4, 3, 3.7, 4.6, 5.5, 6.7, 8.5, 10.4, 12.8, 15.2, 18.3, 21.3, 24.4, 29, and 33.5 m. The source generated Rayleigh waves at 54 frequencies ranging from 4 to 100 Hz that were monitored by the array of receivers. Five blocks of 2^{11} time domain records were measured by a sampling frequency of 320 Hz and averaged to reduce the variance of the calculated spectra.

In addition to the active test, nine passive surface wave tests were performed using 16-receiver circular arrays with radii of 30, 40, and 50 meters. The 16 receivers were equally spaced along the circumference of each circle. During each passive test, data were collected for 256 seconds at a sampling frequency of 320 Hz. The 2^{16} time domain records in each passive test were divided into 16 blocks for averaging. The frequency resolution in the passive tests was $\Delta f = f_S / N = 320 Hz / 4096 = 0.078$ Hz, where N is the number of time domain records for each block.

In both tests, time histories recorded at each receiver were used to calculate surface wave phase velocities using the frequency-wavenumber (f-k) analysis discussed in Chapter 3. The experimental dispersion curve from the active test is shown in Figure 5.2. Dispersion data were successfully obtained at frequencies up to 70 Hz. Spatial aliasing prevented the use of data at frequencies greater than 70 Hz.

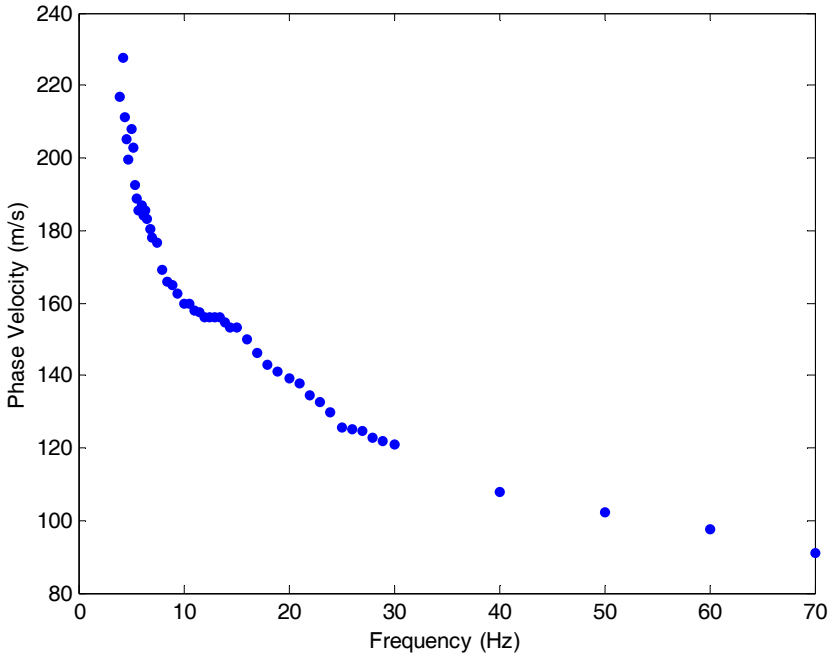

Figure 5.2 Active dispersion curve at Williams Street Park site

The frequency spectrum of measured passive waves is useful to determine the frequency range over which reliable dispersion data may be obtained in passive tests. Figure 5.3 shows the frequency content of passive waves collected by one receiver during a passive test using the array with a 30-m radius. The frequency content is concentrated at frequencies ranging from about 2 to 8 Hz, indicating the viability of passive measurements in this frequency range. In addition to the frequency content of the passive waves, the array's characteristics limit the frequency range of passive dispersion data. As shown in Figure 5.4, passive dispersion curves were obtained at frequencies ranging from about 2 to 8 Hz for the tests using the array with a 30-m radius and at frequencies ranging from about 2 to 7 Hz for the tests using the arrays with 40-m and 50-m radii, depending on the maximum wavenumbers determined by the minimum receiver-to-receiver (RR) distances. Figures 5.4(a) through 5.4(c) show experimental dispersion curves from the nine passive tests for the arrays with radii of 30 m, 40 m, and 50 m, respectively. For

each array, the three dispersion curves were averaged to yield a representative experimental dispersion curve.

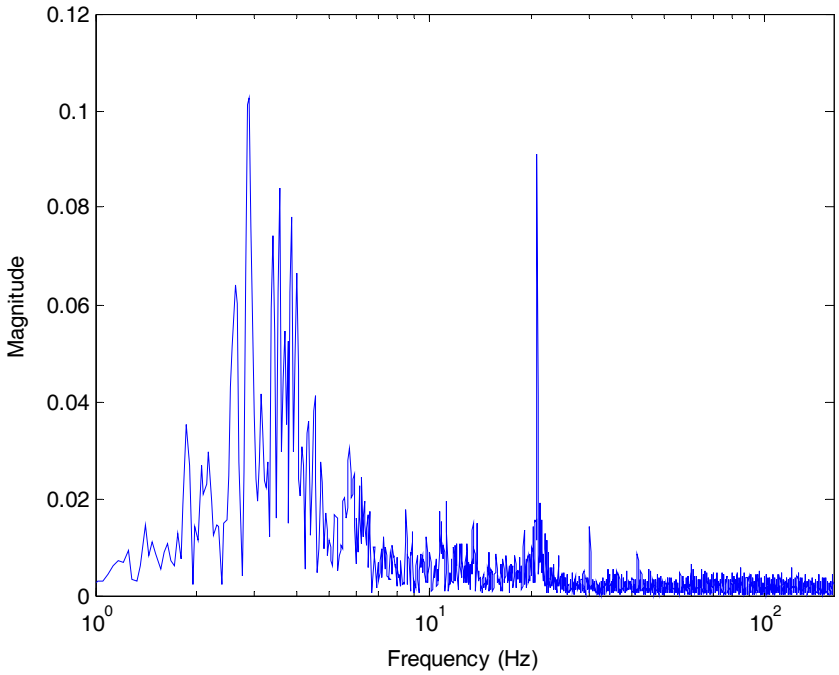

Figure 5.3 Frequency content of the passive energy at Williams Street Park site

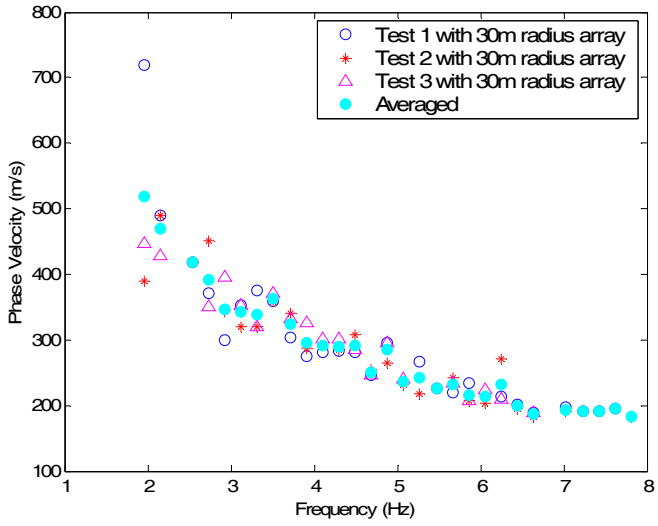

(a)

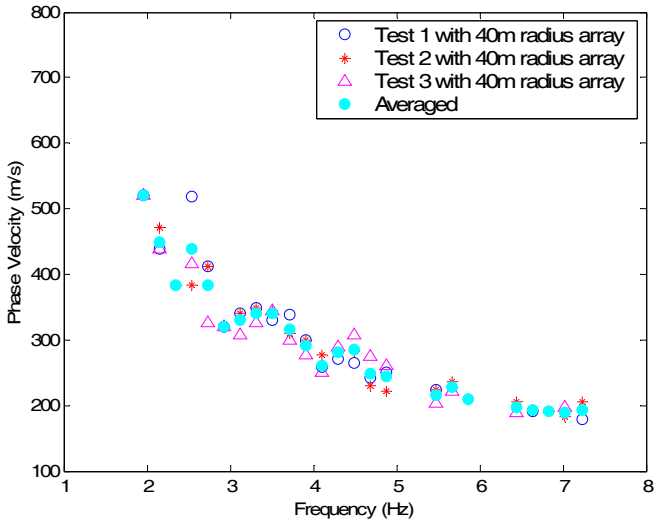

(b)

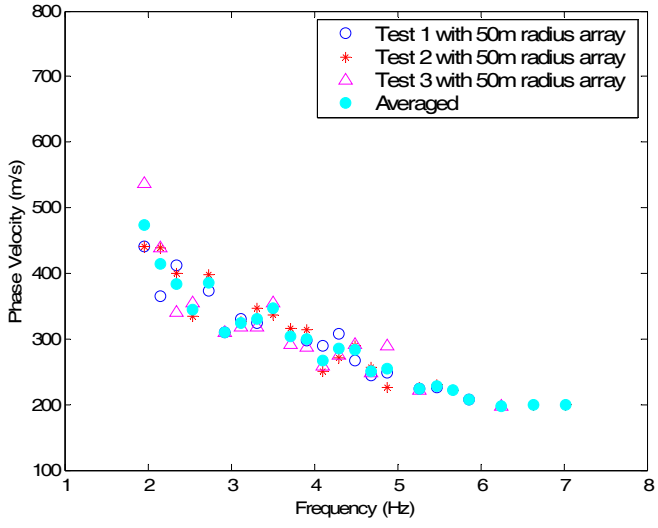

(c)

Figure 5.4 Dispersion curves from nine passive tests performed using the circular arrays with radii of (a) 30 m, (b) 40 m, and (c) 50 m

The averaged passive dispersion curves corresponding to the three different passive arrays are compared with the active dispersion curve in Figure 5.5. In Figures 5.5(a) and 5.5(b), the dispersion curves are compared for the entire frequency range and for the overlapping frequencies, respectively. The three averaged passive dispersion curves exhibit the same general trend, but phase velocities from the tests with larger arrays are generally less than those from smaller arrays, especially at low frequencies. From the comparison between the active and passive dispersion curves in Figure 5.5(b), it is apparent that the passive phase velocities exceed the active values, and that the difference decreases with increasing frequency.

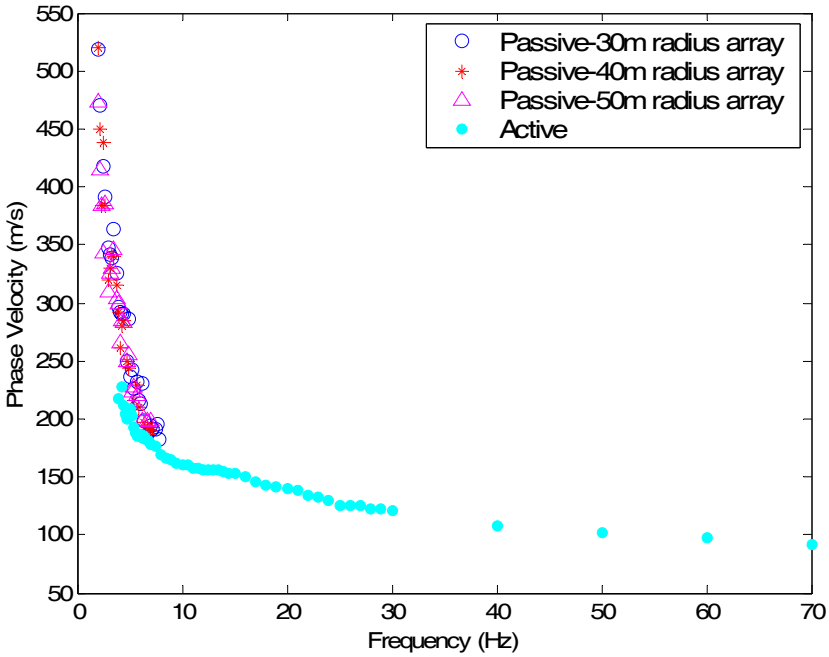

(a)

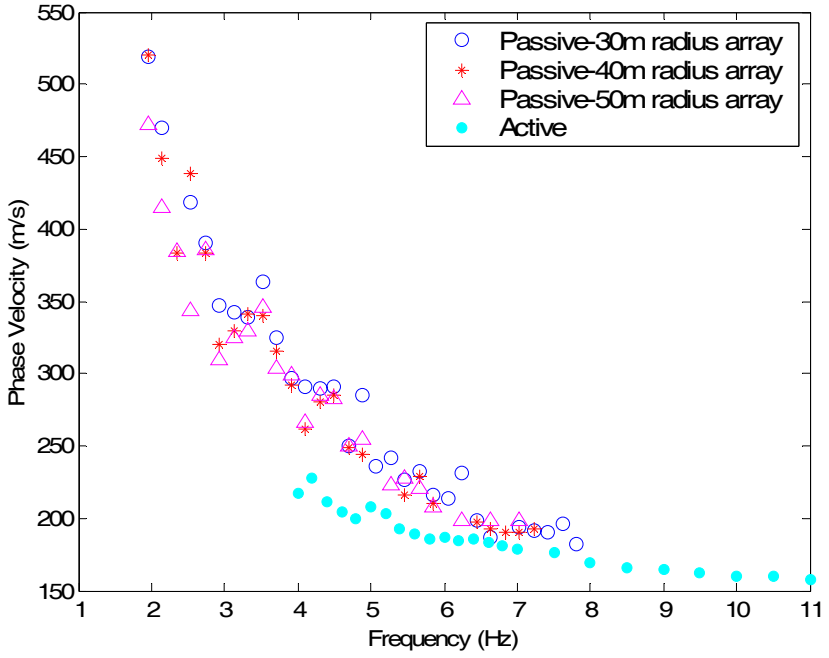

(b)

Figure 5.5 Comparison of average dispersion curves from passive tests with three arrays and an active test over frequencies from (a) 0 to 70 Hz and (b) 1 to 11 Hz

5.2.3 Differences between Active and Passive Dispersion Curves

Based on the observed differences between active and passive dispersion curves, it can be hypothesized that they result from phenomena that are frequency-dependent. Similar differences have been also observed by other investigators (Hebeler, 2001; Rix et al., 2002). In their study, a composite dispersion curve was formed by simply averaging the active and passive curves within this range of frequencies as shown in Figure 5.6. Hebeler (2001) stated that differences between active and passive estimates were thought to be a combination of random measurement errors as well as systematic errors in the two estimates. However, no further discussion about the differences and no method to resolve them have been suggested.

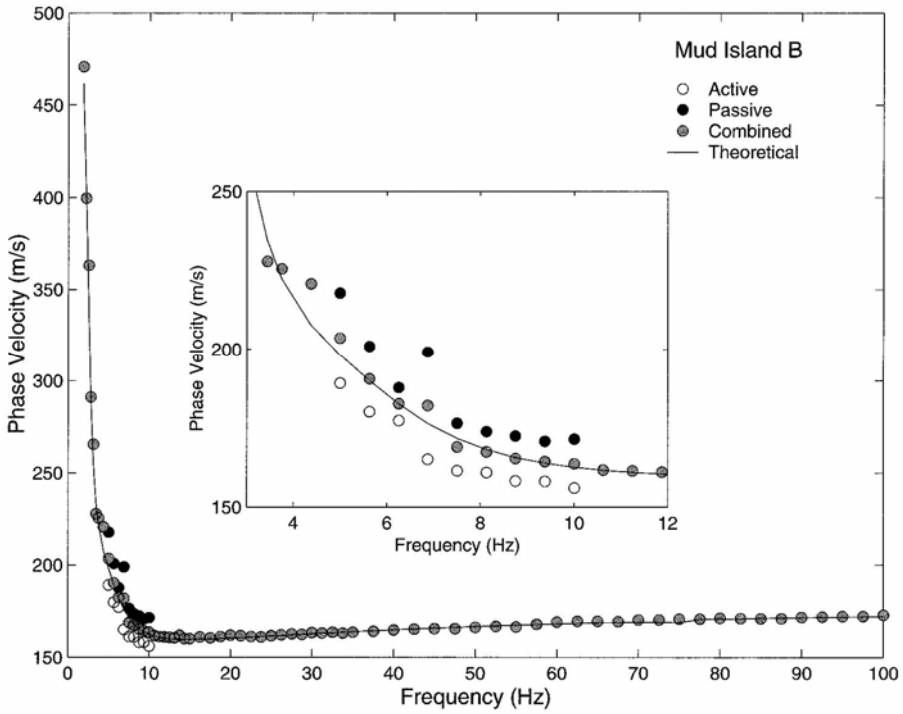

Figure 5.6 Active and passive dispersion curves for Mud Island B site (Rix et al., 2002). Combined active-passive dispersion curve was obtained by averaging the active and passive data in the overlapping frequencies.

Systematic errors included in active and passive dispersion data often limit the capability of the two methods to provide accurate dispersion estimates. These systematic errors are mainly explored as possible means to explain and resolve the difference between the active and passive dispersion curves. In active tests, significant systematic errors are caused by near-field effects, which tend to underestimate phase velocities at low frequencies as discussed in Chapter 4. In this chapter, the focus is on understanding systematic errors in passive tests, which may result from limited wavenumber resolution or energy leakage into sidelobes. It is anticipated that resolving differences between active and passive dispersion curves will lead to a more accurate composite dispersion curve.

5.3 WAVENUMBER PRECISION

The frequency domain beamformer (FDBF) searches for the largest peak in the wavenumber spectrum at a specific frequency to calculate the phase velocity at that frequency. The wavenumber spectrum is defined at a pre-selected number of discrete points. In the f-k analysis used in the active and passive tests, these points were defined by dividing a given wavenumber range by a selected number of trial wavenumbers. *Wavenumber precision* is defined by the increment between adjacent wavenumbers. Poor wavenumber precision can result in errors in selecting a dominant wavenumber up to a half of wavenumber increment used to define the wavenumber spectrum. In addition to poor wavenumber resolution and sidelobe leakage, poor wavenumber precision resulting from discretizing the wavenumber spectrum too coarsely must be investigated as another cause of error. Poor wavenumber precision can result in errors in selecting a dominant

wavenumber up to one half of the wavenumber increment used to define the wavenumber spectrum.

Errors due to poor wavenumber precision may become more significant in passive tests compared to active tests for two reasons: (1) wavenumbers in passive tests are usually very small compared to those from active tests because of the lower frequencies and higher phase velocities (in normally dispersive media), and (2) a larger wavenumber domain defined by positive and negative wavenumbers in both the x and y directions must be searched compared to that in active tests where the wavenumber domain includes only positive wavenumbers in the x direction. Improving the wavenumber precision can be achieved simply by increasing the number of trial wavenumbers. However, this requires more computation time. To optimize the required wavenumber precision, it is desirable to approximate the maximum probable errors that may be included in dispersion estimations due to limited wavenumber precision.

In this study, a wavenumber precision of 0.001 (rad/m) was selected for searching a peak in the wavenumber spectrum. At a wavenumber greater than 0.02 (rad/m), this wavenumber precision may create the maximum errors within ± 4 % of the true wavenumber.

5.4. WAVENUMBER RESOLUSION AND SIDELOBE LEAKAGE

As discussed in Chapter 3, perfect spatial sampling of a signal requires infinite integrals over space. In practice, however, the signal may be sampled only at a finite number of locations. This limitation influences the ability to determine a wavenumber associated with the signal from a steered response power spectrum. Errors in passive

dispersion estimates result mainly from: (1) poor wavenumber resolution and (2) energy leakage into sidelobes of the array smoothing function (ASF). The latter can be evaluated by examining the mainlobe width and sidelobe heights of the ASF for a selected array.

5.4.1 Wavenumber Resolution

Long (1964) pointed out a phenomenon in which two seismic waves with the same velocity combined, leading to measured phase velocity slower than the true velocity. During processing of passive measurements with f-k analysis, the presence of multiple waves close to one another in the 2-D wavenumber domain may lead to incorrect estimation of Rayleigh wave phase velocity. This problem occurs when the limited wavenumber resolution of a given array can not accurately separate the multiple waves, leading to an incorrectly-measured wavenumber that is smaller than the true value.

Assume two plane waves propagating from slightly different directions with the same velocity and unit amplitude. For a given frequency, Points A and B in Figure 5.7 indicate the true locations of the waves in 2-D wavenumber space. Since the velocity is the same for the two waves, the value of $|\mathbf{k}|$ is the same for the waves and thus Points A and B lie on the same circle. With limited wavenumber resolution that is insufficient to separate the two waves, the apparent peak would be located midway between two true wavenumbers, i.e., Point C in Figure 5.7.

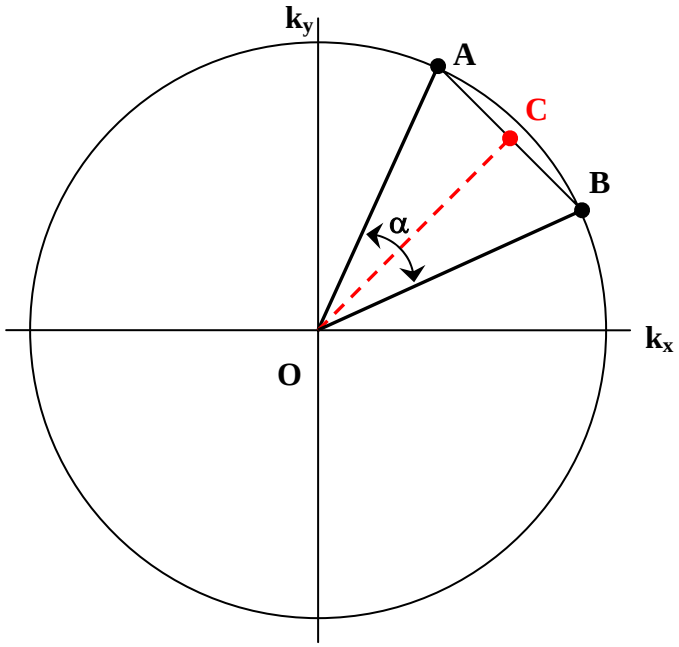

Figure 5.7 Two plane waves and a merged wave due to limited wavenumber resolution in 2-D wavenumber space

Since the measured wavenumber represented by the distance of Point C from the origin is smaller than a true wavenumber, i.e., distance AO or BO, the estimated phase velocity is greater than the true phase velocity.

The amount of the error induced by the limited wavenumber resolution is dependent on an angle α between the propagation directions of two waves. For a given frequency *f*, the ratio between the apparent wave velocity obtained from the merged peak and the true wave velocity can be calculated by:

$$\frac{V_{app}}{V_{true}} = \frac{2\pi f / k_{app}}{2\pi f / k_{true}} = \frac{k_{true}}{k_{app}} = \frac{1}{\cos(\frac{\alpha}{2})} = \sec(\frac{\alpha}{2}) \tag{5.1}$$

where, V_{app} = apparent velocity, V_{true} = true velocity, k_{app} = apparent wavenumber, and k_{true} = true wavenumber. Figure 5.8 shows the ratio in Equation 5.1 as a function of α.

The ratio is about 1.1 for an angle α of 50 degrees. The ratio increases with increasing the angle α, requiring more careful attention to this phenomenon for large values of α.

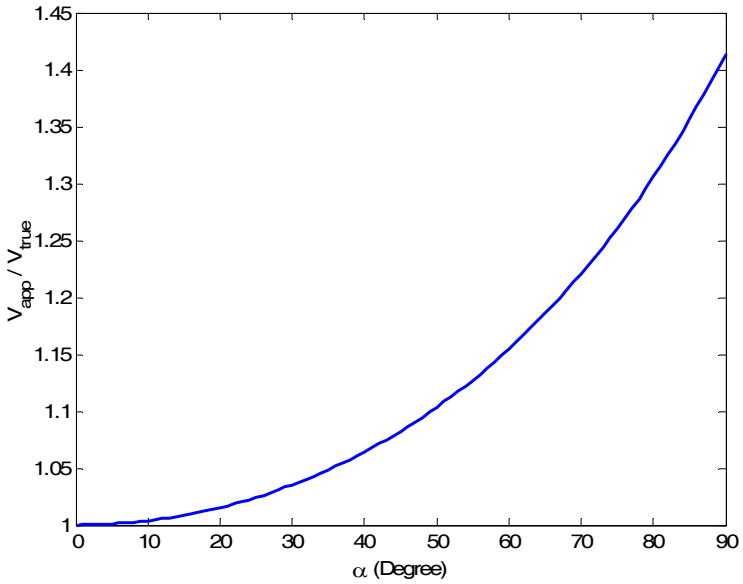

Figure 5.8 Ratio of V_{app} to V_{true} as a function of α

The phase velocities of the two waves can be calculated correctly only if the wavenumber resolution, which depends on the aperture of the array, is sufficient to isolate each wave. Wavenumber resolutions corresponding to half of the mainlobe widths for a uniform linear array and a uniform circular array are given by (Johnson and Dudgeon, 1993):

$$\Delta k_{Rayleigh} = \frac{2\pi}{D} \qquad \text{for a linear array} \qquad (5.2)$$

$$\Delta k_{Rayleigh} = \frac{2.44\pi}{D} = \frac{1.22\pi}{R} \qquad \text{for a circular array} \qquad (5.3)$$

where, D is a spatial extent of a linear array and R is a radius of a circular array.

To investigate the effects of limited wavenumber resolution, a circular array of 16 receivers deployed equally along the circumference of the circle with a 30-m radius is chosen. Figures 5.9(a), 5.9(b), and 5.9(c) present the array's geometry, the ASF of the array in 2-D space, and the ASF in 3-D space, respectively. As shown in Figures 5.9(b) and 5.9(c), a mainlobe is observed at the origin and first group of sidelobes with normalized magnitude greater than 0.5 are found at distance of about 0.6 (rad/m) from the mainlobe. The wavenumber resolution of the array (Δk) is calculated using Equation 5.3 and is equal to 0.1278 (rad/m).

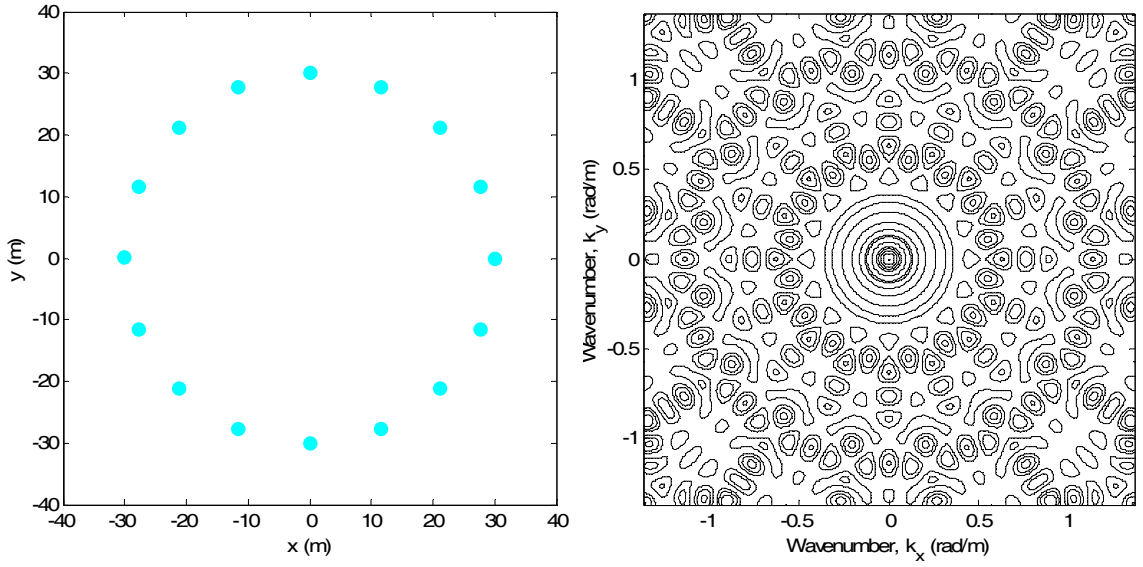

(a) (b)

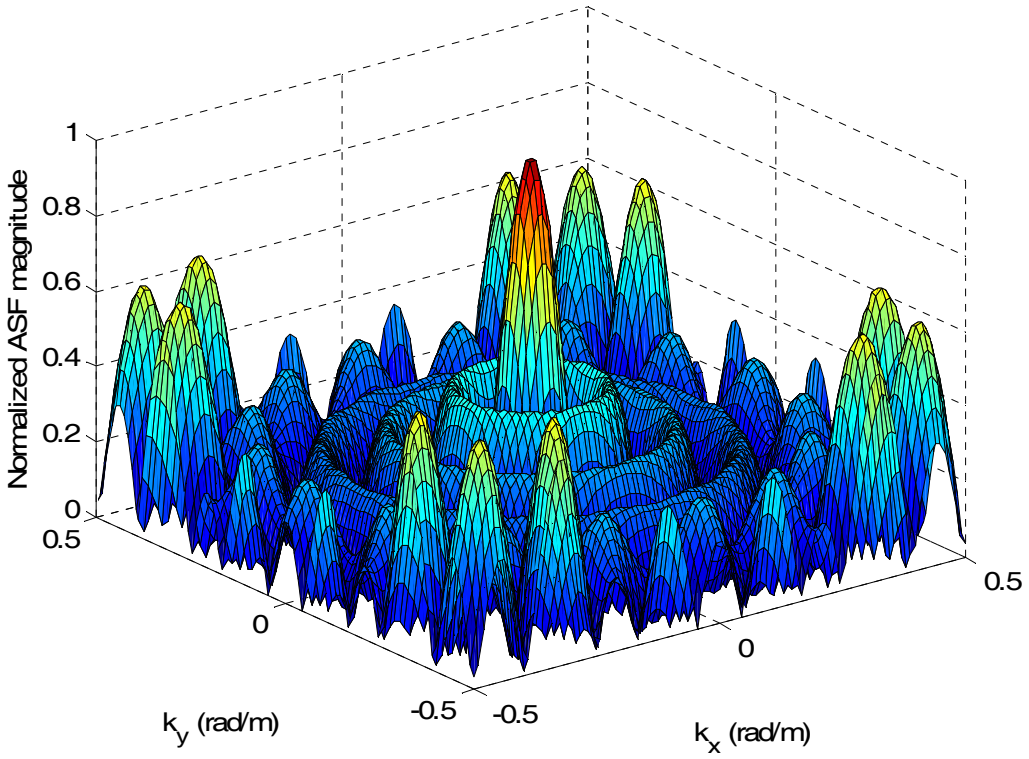

(c)

Figure 5.9 16-receiver circular array with a radius of 30 m: (a) geometry, (b) ASF in 2-D space, and (c) ASF in 3-D space

As a simple example of a wavefield consisting of multiple waves, assume a wavefield consisting of two unit amplitude monochromatic plane waves defined by a single frequency ω_0 and two wavenumber vectors $\mathbf{k}_1$ and $\mathbf{k}_2$ as described in Equation 5.4.

$$s(\mathbf{x},t) = s_1(\mathbf{x},t) + s_2(\mathbf{x},t) \tag{5.4}$$

where $s_1(\mathbf{x},t) = \exp\left[i(\omega_0 t - \mathbf{k}_1\mathbf{x})\right]$ and $s_2(\mathbf{x},t) = \exp\left[i(\omega_0 t - \mathbf{k}_2\mathbf{x})\right]$.

Let the two waves propagate with the same wave velocity of 200 (m/s) at 5 Hz and different directions separated by an angle α of 42°. The wavenumber corresponding to the velocity and frequency is 0.1571 (rad/m). Figure 5.10 shows the wavenumber spectrum of the two waves measured by the 16-receiver circular array with a 30-m radius. The wavenumber resolution defined by the aperture of the array is insufficient to isolate each wave, leading to incorrectly measured wavenumber. Note that the ratio of the measured velocity, 214 (m/s), to the true velocity, 200 (m/s), is 1.07 and is equal to the value from Equation 5.1 with the α of 42°.

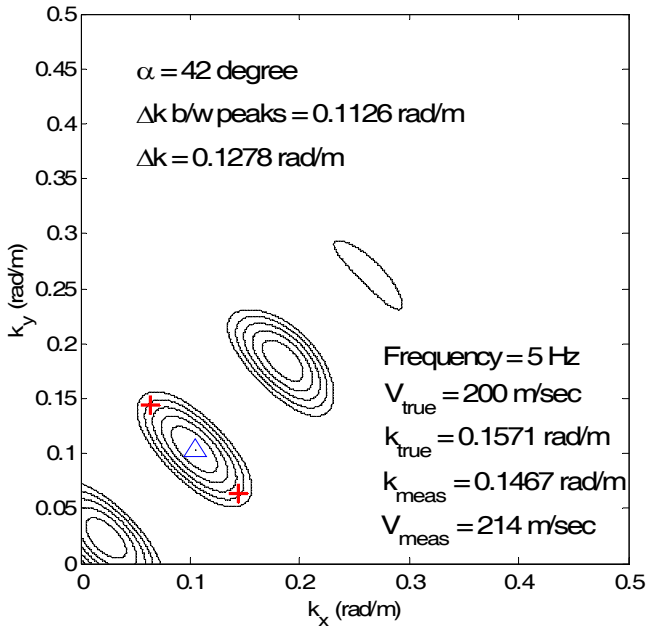

Figure 5.10 Example of unresolved waves by poor wavenumber resolution. Δk = array's wavenumber resolution and Δk b/w peaks = separation of two waves in the wavenumber domain. + indicates locations of the true wavenumbers and Δ indicates location of measured wavenumber.

5.4.2 Sidelobe Leakage

In addition to poor wavenumber resolution, energy leakage into sidelobes may cause incorrectly measured wavenumbers. As mentioned, the phenomenon deserves more attention for passive tests that normally deal with a wavefield consisting of multiple waves.

The investigation of the sidelobe leakage effect is performed with the same wavefield as previously used in Figure 5.10 except for the angle α. For values of αs of 43° and 87°, the wavenumber spectra of the two waves measured by the 16-receiver circular array with a 30-m radius are presented in Figures 5.11(a) and 5.11(b), respectively.

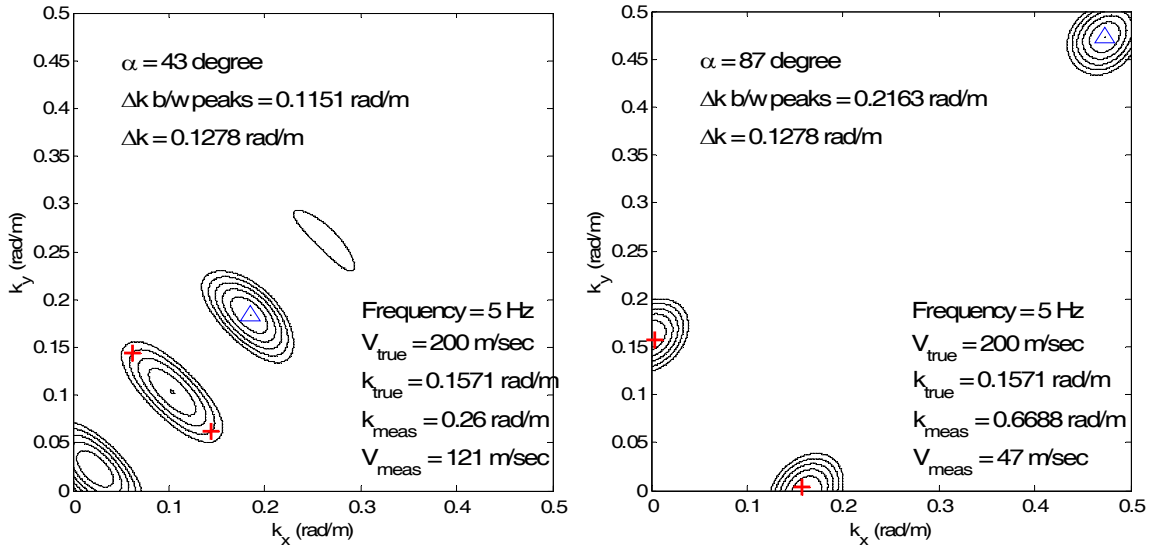

(a) (b)

Figure 5.11 Examples of spurious peaks due to sidelobe leakage for: (1) α = 43° and (2) α = 87°. Δk = array's wavenumber resolution and Δk b/w peaks = separation of two waves in the wavenumber domain. + indicates locations of the true wavenumbers and Δ indicates location of measured wavenumber.

For the angle α of 43º in Figure 5.11(a), energy leakage due to sidelobes creates a spurious peak in the wavenumber spectrum, yielding an incorrectly-measured wavenumber. Note that the measured wave velocity of 121 (m/s) is significantly different than the true wave velocity of 200 (m/s). Another incorrectly-measured wavenumber due to sidelobe leakage was observed for the angle α of 87º as shown in Figure 5.11(b). The location of the spurious wavenumber peak is different than that associated with the angle α of 43º. Difference between the measured velocity of 47 (m/s) and the true velocity is also significant.

From the investigation of sidelobe leakage effect on passive dispersion estimates, it was observed that the measured wavenumbers are significantly different from the true wavenumber. Thus, incorrectly measured wavenumbers due to sidelobe leakage can usually be easily identified.

5.4.3 Threshold Ratios Associated with Errors in Passive Data

Through the investigations using the two plane waves propagating with the same wave velocity of 200 (m/s) at 5 Hz and the angular separation of α, incorrectly measured wavenumbers due to poor wavenumber resolution and energy leakage into sidelobes were observed. Now, the angle α is increased up to 88°. Figure 5.12 shows the successful isolation of each wave by the wavenumber resolution for the 16-receiver circular array with a 30-m radium.

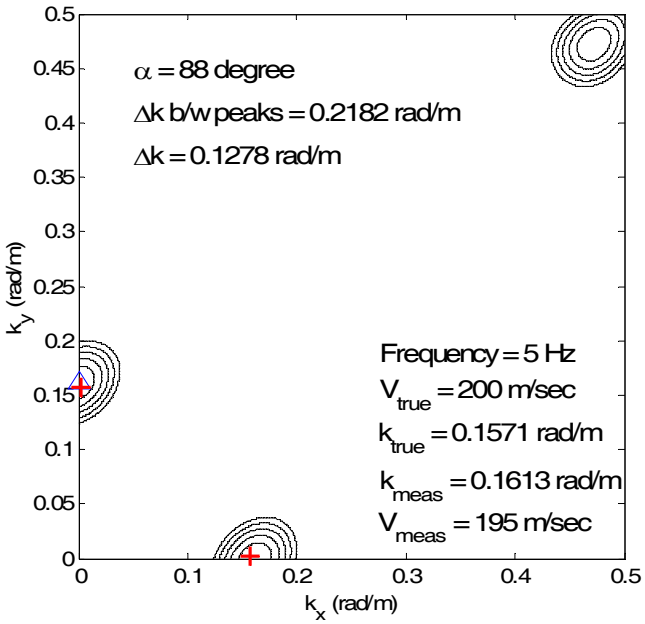

Figure 5.12 Example of resolved waves by a given wavenumber resolution. Δk = array's wavenumber resolution and Δk b/w peaks = separation of two waves in the wavenumber domain. + indicates locations of the true wavenumbers and Δ indicates location of measured wavenumber.

From Figures 5.10 through 5.12, it is important to notice that two important threshold angles appear at 43° and 88°. These are associated with the generation of a spurious peak due to sidelobe leakage and the isolation of each wave with the wavenumber resolution, respectively. At angular separation with α smaller than 43°, the

two waves can not be isolated by the given wavenumber resolution, yielding an incorrectly measured wavenumber, which can be estimated using Equation 5.1. At angular separation with α within 43° and 87°, sidelobe leakage creates a spurious peak, yielding an incorrectly measured wavenumber, which is significantly different from the true wavenumber. Finally, the waves may be successfully isolated for values of α greater than 87°.

More investigations regarding the threshold angle α's have been performed for two waves with different wavenumbers (i.e., different frequencies and different wave velocities). For a larger wavenumber, the 1st threshold angle, α_t^{1st}, and the 2nd threshold angle, α_t^{2nd} become smaller and for a smaller wavenumber, they become larger, indicating the dependency of the angles on wavenumber magnitude. Based on this result, it can be considered that α_t^{1st} and α_t^{2nd} are dependent only on the value of true wavenumber of two waves for the same array. As discussed, α_t^{1st} appears when sidelobe leakage starts creating a spurious peak. Two waves can not be successfully isolated due to sidelobe leakage until α reaches α_t^{2nd}. Important features associated with α_t^{1st} and α_t^{2nd} derived from these investigations are summarized in Table 5.2.

Table 5.2 Important features associated with α_t^{1st} and α_t^{2nd}

Angle α	$\alpha < \alpha_t^{1st}$	$\alpha_t^{1st} < \alpha < \alpha_t^{2nd}$	$\alpha_t^{2nd} < \alpha$
Cause of error	Poor wavenumber resolution	Sidelobe leakage	None
Status of measured waves	Non-isolated	Represented by a spurious peak	Isolated
Measured wavenumber	Underestimated	Either under- or overestimated	Correct
Measured wave velocity	Overestimated	Either over- or underestimated	Correct

Values of threshold angles α_t^{1st} and α_t^{2nd} are dependent on the wavenumber resolution of a given array and the wavenumber of each wave. It is desirable to develop a single term considering the two parameters simultaneously. An array's capability to isolate two waves propagating with different directions depends on a distance (in wavenumber space) between the two waves relative to the array's wavenumber resolution. Therefore, two important wavenumber distances between two waves (Δk^{1st} and Δk^{2nd} associated with α_t^{1st} and α_t^{2nd}, respectively) are dependent only on the wavenumber of a given array. Therefore, it appears to be more effective to use a term of *threshold ratio* between a wavenumber distance associated with α_t^{1st} or α_t^{2nd} and the wavenumber resolution. From the investigation results with the given example shown in Figures 5.10 through 5.12, two threshold ratios are calculated as follows:

$$1^{st} \text{ threshold ratio} = \frac{\Delta k^{1st} \text{ at } \alpha_t^{1st}}{\Delta k_{Rayleigh}} = \frac{0.1151 \text{ rad/m}}{0.1278 \text{ rad/m}} = 0.90 \tag{5.5a}$$

$$2^{nd} \text{ threshold ratio} = \frac{\Delta k^{2nd} \text{ at } \alpha_t^{2nd}}{\Delta k_{Rayleigh}} = \frac{0.2163 \text{ rad/m}}{0.1278 \text{ rad/m}} = 1.69 \tag{5.5b}$$

The wavenumber distance between two waves at a certain α is linearly proportional to a true wavenumber of the two waves. The wavenumber distance for a certain α can be simply calculated with a true wavenumber. Using the threshold ratios given from Equations 5.5a and 5.5b, the ratio of a wavenumber distance to a wavenumber resolution of a selected array can be used to determine status of the two waves measured by the array. Figure 5.13 presents V_{app}/V_{true} associated with the maximum errors due to poor wavenumber resolution as a function of true wavenumbers for the 16-receiver circular array with a 30-m radius. Since poor wavenumber resolution influences measurements

for α smaller than α_t^{1st}, V_{app}/V_{true} was calculated based on the 1st threshold ratio in Equation 5.5(a).

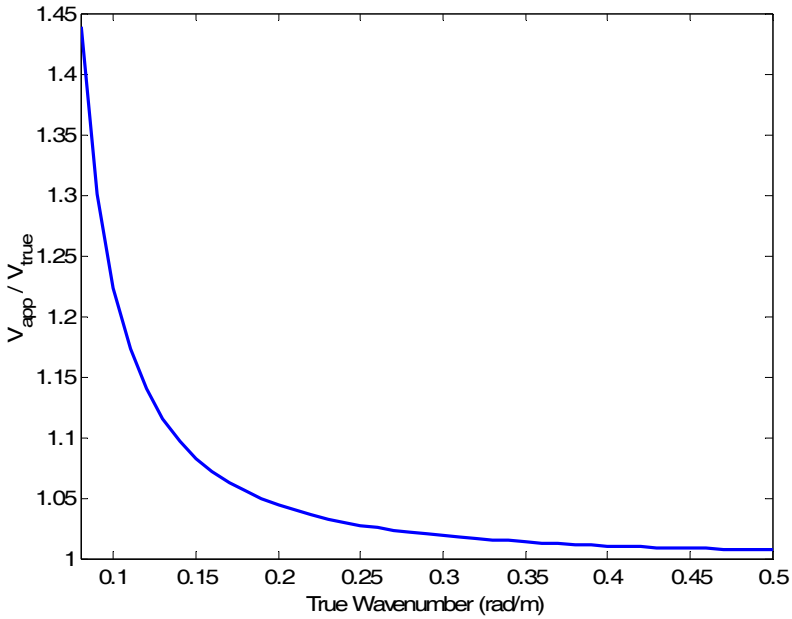

Figure 5.13 Ratio V_{app}/V_{true} corresponding to limited wavenumber resolution effect as a function of true wavenumber for 16 receiver circular array with 30 m radius

5.4.4 Two Waves with Different Amplitudes

The investigation summarized in Figures 5.10 through 5.12 was performed assuming that the two waves each have the same amplitude. Thus, the ratio V_{app}/V_{true} in Figure 5.13 corresponds to the maximum probable error associated with this ideal condition. In practice, this condition is rarely satisfied. Usually, there is a dominant passive source at a certain frequency, and one wave is superior to the others in terms of energy. Therefore, additional investigation regarding wavenumber resolution and energy leakage into sidelobes is conducted with two waves with different amplitudes.

Table 5.3 presents the summary of the results of the investigation. The first threshold angle α_t^{1st} appears at 43º for the ratios of 1:1 and 1:0.9 and at 44º for the ratio of 1:0.8.

The first threshold angle α_t^{1st} is very stable for these amplitude ratios. It may be deduced that α_t^{1st} is determined more dominantly by the array characteristics rather than the wave characteristics. For the ratio of 1:0.7, α_t^{1st} was not observed. As summarized in Table 5.3, the values of α_t^{2nd} corresponding to the separation of two waves are 88º, 78º, and 62º for the respective ratios of 1:1, 1:0.9, and 1:0.8. With increasing difference in amplitudes, the two waves can be successfully separated at smaller values of α. The second threshold angle α_t^{2nd} appears when the two waves are sufficiently apart from each other compared to the wavenumber resolution. It is observed that sidelobe leakage becomes less significant with increasing difference in amplitudes. For the amplitude ratio of 1:0.7, no value of α_t^{2nd} was observed. For waves with this amplitude ratio, the sidelobes do not reinforce to yield a spurious peak larger than the true peak.

Table 5.3 Values of α_t^{1st} and α_t^{2nd} associated with various amplitude ratios between two waves

Amplitude ratio	α_t^{1st} (º)	α_t^{2nd} (º)
1:1	43	88
1:0.9	43	78
1:0.8	44	62
1:0.7	Not observed	Not observed

5.5 RECOMMENDATIONS FOR IMPROVING PASSIVE MEASUREMENTS

5.5.1 Improvement of Array Characteristics

Poor wavenumber resolution and energy leakage into sidelobes may distort calculations of passive dispersion data if they are not properly handled. Both errors can be minimized by improving the array characteristics to the extent possible to obtain more

accurate dispersion data. For a surface wave test at the site, the number of receivers and the geometry of an array are limited by equipment conditions, an available area for placing the receivers, and testing time. For these constraints, it is required to optimize array geometry to obtain a good balance between wavenumber resolution and sidelobe height.

Wavenumber resolution can be simply improved by increasing the spatial extent of an array. However, for passive testing, increasing the spatial extent is often limited due to several considerations: First, for a fixed number of receivers it can only be achieved at the expense of increased energy leakage. For this condition, increasing an array's spatial extent increases sidelobe heights in the ASF, leading to increased energy leakage. Figure 5.14 shows ASF's of three 16-receiver circular arrays with radii of 30 m, 40 m, and 50 m. As shown in Figure 5.14, the width of a mainlobe decreases with increasing spatial extent, indicating improved wavenumber resolution. However, increasing the spatial extent with the same number of receivers results in more sidelobes located at closer distances from a mainlobe, indicating more severe sidelobe leakage. As discussed, the increased energy leakage may produce incorrectly measured wavenumbers during the f-k analysis. Second, a large flat area for a spatial array such as a circular array that must be used in passive testing is not always available depending on location of a site. For the passive test in urbanized area, such a limitation becomes significant and the test often must be performed with an array with poor wavenumber resolution.

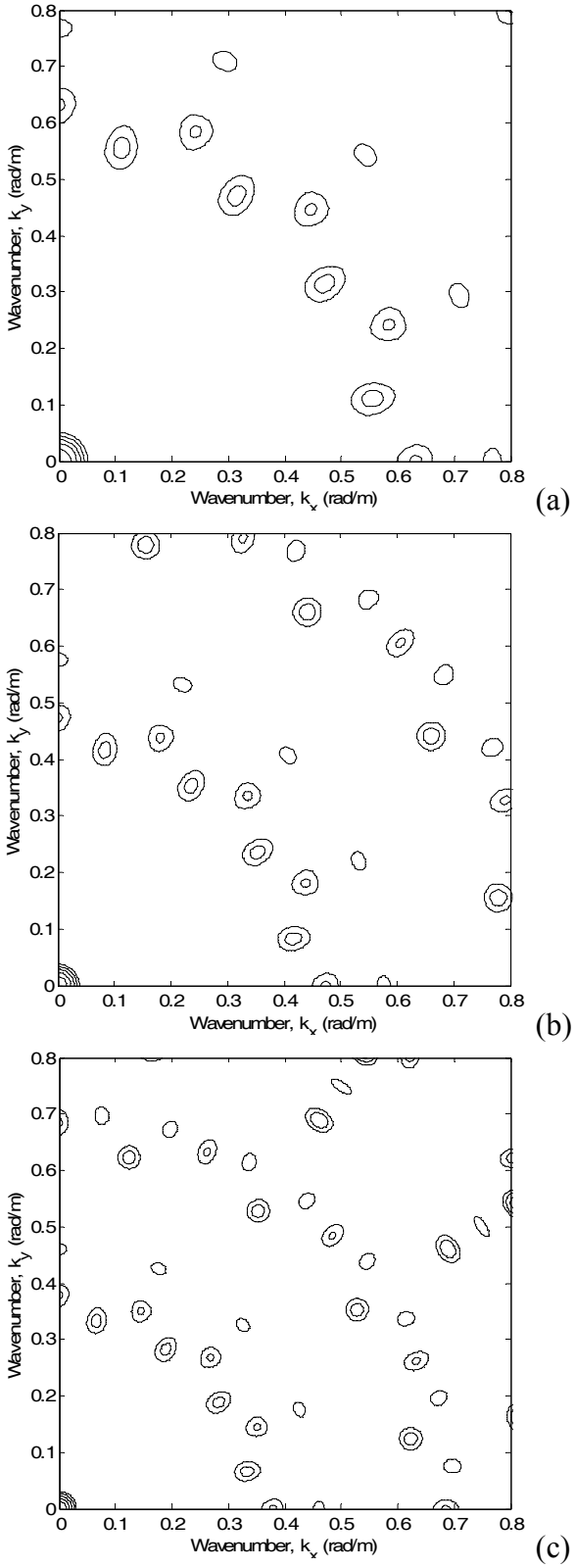

Figure 5.14 Comparison of ASFs of three circular arrays with different radii of: (a) 30 m, (b) 40 m, and (c) 50 m. Contours are plotted for normalized magnitudes over 0.5 with 0.1 intervals.

If available, increasing the number of receivers to increase spatial sampling is a good means to improve wavenumber resolution without sacrificing energy leakage control. However, in practice the number of receivers is often limited by testing devices as well as testing time.

Poor wavenumber resolution and sidelobe leakage become more important in passive tests because: (1) a focus is placed on waves with very small wavenumbers and (2) the limitation resulting from given devices and site condition becomes more stringent to a two-dimensional array with a given number of receivers. Therefore, poor wavenumber resolution and sidelobe leakage deserve more attenuation for passive tests.

As discussed in the previous section, the 1st and 2nd threshold ratios in Equations 5.5a and 5.5b are valid for 16-receiver circular arrays with various spatial extents. The maximum errors due to poor wavenumber resolution can be presented in terms of V_{app}/V_{true} and true wavenumber depending on spatial extent of an array. As shown in Figure 5.15, V_{app}/V_{true} associated with the maximum errors caused by limited wavenumber resolution can be reduced significantly by increasing the spatial extent of an array.

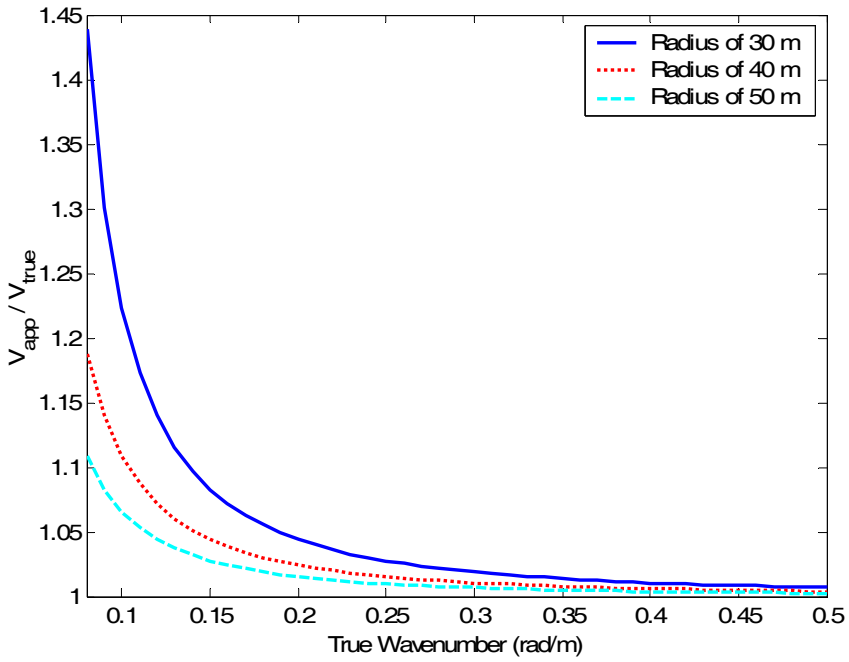

Figure 5.15 Errors due to poor wavenumber resolution in terms of V_{app}/V_{true} and true wavenumber for 16-receiver circular arrays with various spatial extents

Focus on significant reduction in V_{app}/V_{true} by increasing spatial extent of an array for low wavenumbers in Figure 5.15. For passive tests exposed to waves with very small wavenumbers, an array with sufficiently large spatial extent is primarily required to yield data with reasonably acceptable errors due to limited wavenumber resolution. In practice, the maximum spatial extent of a circular array often depends on the size of flat area at the testing site. From a rule of thumbs based on the author's experience with passive data analysis, a 16-receiver circular array with a 30-m or larger radius would be necessary for accurately measuring waves with wavenumbers as small as 0.02 rad/m. If having no prior information regarding a dispersion curve at the site, passive tests using two circular arrays with different radii would be desirable to approximate severity of errors due to poor wavenumber resolution.

5.5.2 Refining Process to Remove Passive Data with Significant Errors

In addition to optimizing the array configuration prior to performing a passive test, it is also helpful to carefully examine the dispersion data following the test to identify and remove errors due to poor wavenumber resolution and sidelobe leakage.

From the dispersion curves for various soil profiles derived from numerical simulations in Chapter 4, it was observed that for low frequencies, the fundamental Rayleigh mode is dominant. For passive tests focusing on dispersion data at low frequencies, usually below 10 Hz, a dispersion curve with a smooth general trend is expected rather than one with transitions in modes. Therefore, any dispersion datum that differs significantly from a general trend can be suspected of being created by poor wavenumber resolution or sidelobe leakage. Another fact that might be useful for identifying dispersion data with significant errors due to poor wavenumber resolution or sidelobe leakage is that propagation directions of passive waves are expected to be reasonably consistent for frequencies in particular range. If sidelobe leakage creates a spurious peak in wavenumber domain, its direction must be different than a true one that is expected to be consistent with other adjacent ones.

A manual process based on these two facts can be useful to find and delete dispersion data with significant errors due to poor wavenumber resolution or sidelobe leakage. In this study, this manual process is named *manual refining process* or *refining process*. Figures 5.16 through 5.18 illustrate the refining processes applied to the nine sets of passive dispersion data at the Williams Street Park site over frequencies ranging from about 2 to 8 Hz. In each refining process, measured Rayleigh wave velocities, propagation directions of the waves, and P_{max} (maximum in the steered response power

spectrum) magnitudes are presented as functions of frequency. For dispersion data significantly different from the general trend, their propagation directions are compared with other adjacent ones. Dispersion data with propagation directions much different from others may have significant errors due to wavenumber resolution or sidelobe leakage. Too large or too small wave velocities with inconsistent propagation directions are also indicative of having serious errors due to poor wavenumber resolution or sidelobe leakage. As expected, more serious sidelobe leakage and spatial aliasing are observed in refining processes with dispersion data associated with a larger radius array.

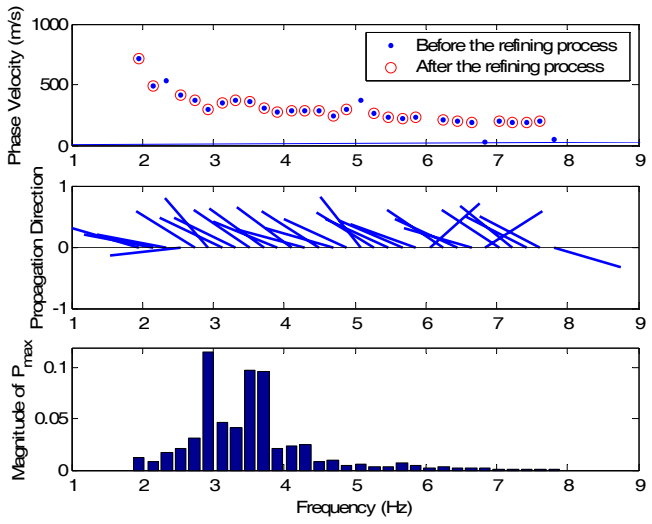

(a)

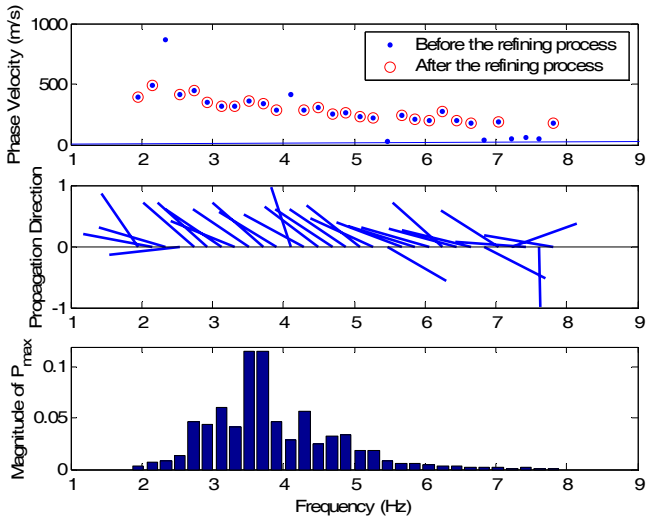

(b)

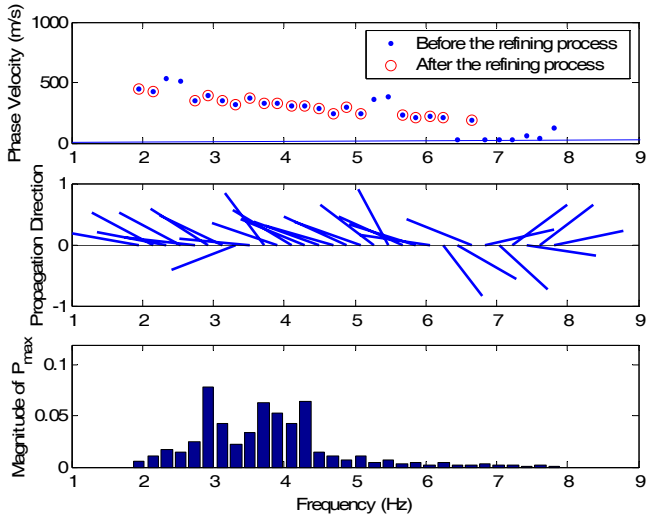

(c)

Figure 5.16 Refining process applied to dispersion data from three passive tests using a circular array with 30 m radius: (a) test 1, (b) test 2, and (c) test 3. A solid line in each dispersion plot indicates a $k_{Nyquist}$ criterion.

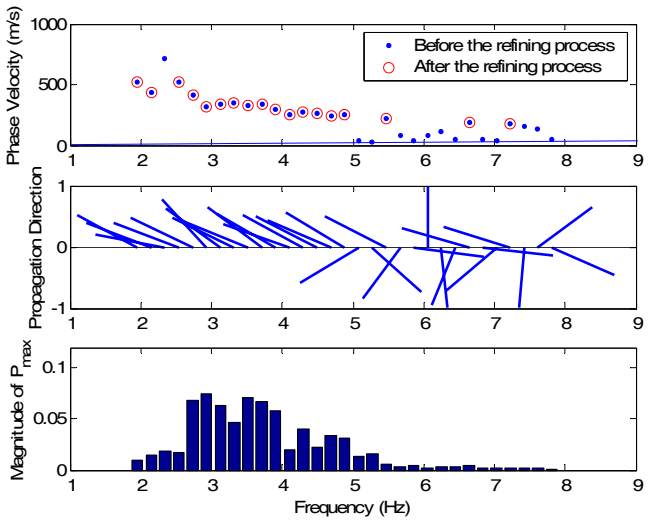

(a)

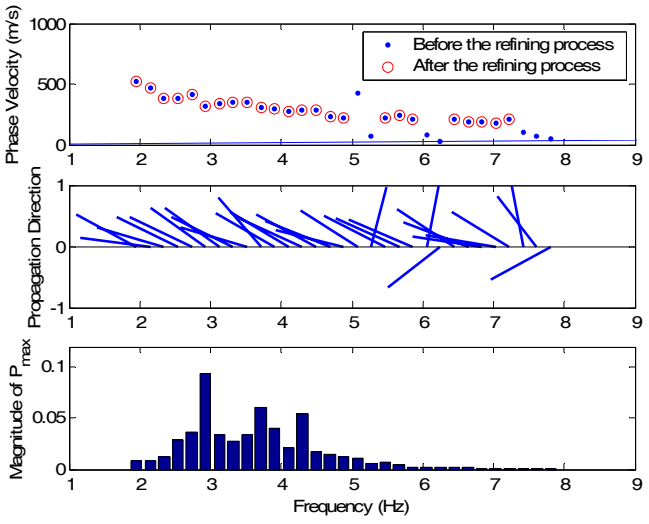

(b)

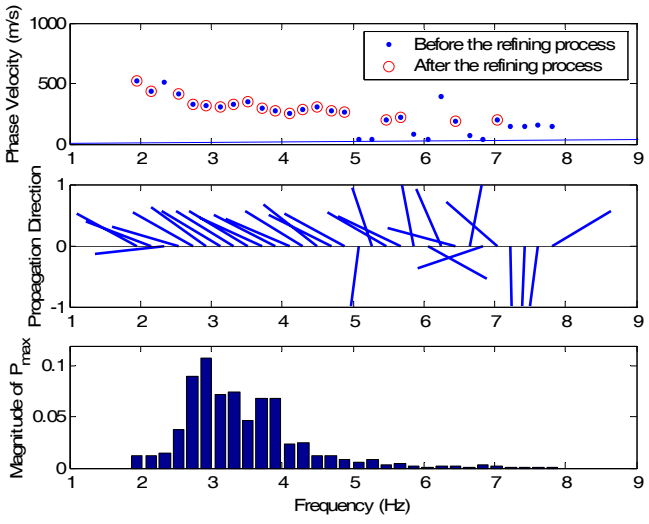

(c)

Figure 5.17 Refining process applied to dispersion data from three passive tests using a circular array with 40 m radius: (a) test 1, (b) test 2, and (c) test 3. A solid line in each dispersion plot indicates a $k_{Nyquist}$ criterion.

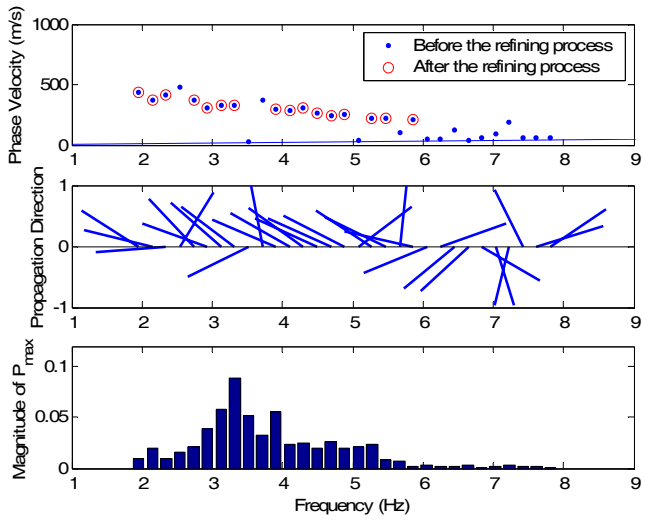

(a)

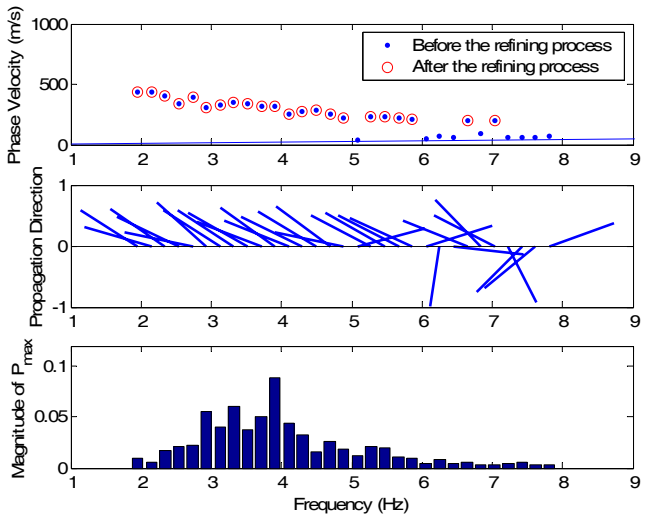

(b)

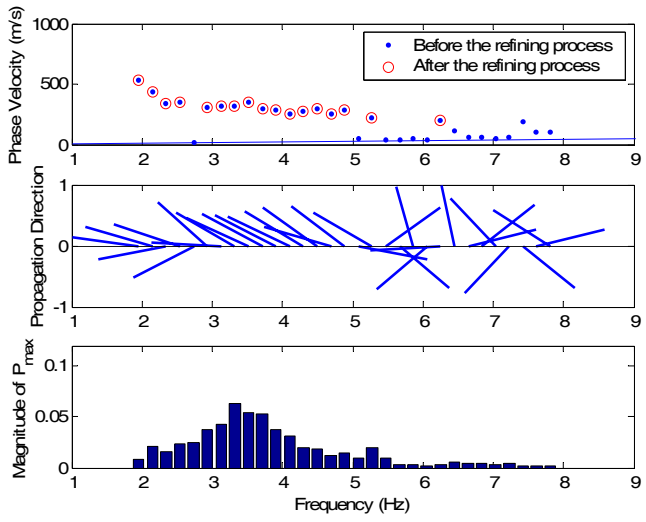

(c)

Figure 5.18 Refining process applied to dispersion data from three passive tests using a circular array with 50 m radius: (a) test 1, (b) test 2, and (c) test 3. A solid line in each dispersion plot indicates a $k_{Nyquist}$ criterion.

5.5.3 Validation of the Recommendations

It is desirable to estimate remained errors in passive dispersion curves associated with the three circular arrays after the refining process to validate the recommendations for improving passive measurements. As discussed, the differences between active and passive dispersion curve over the overlapping frequencies are caused mainly by errors due to near-field effects in active tests and errors due to poor wavenumber resolution or sidelobe leakage in passive tests. If the recommendations are successful, the differences are attributed to only near-field effects in active tests. Since passive waves are free of near-field effects, passive dispersion curves can offer plane Rayleigh wave velocities as references to estimate near-field effects in active dispersion curves. To validate the recommendations, active dispersion data normalized by passive dispersion data with the three arrays for the overlapping frequencies are compared to the normalized Rayleigh wave velocities (see Equation 4.2) from numerical simulations for soil profiles corresponding to the site condition for the field tests. Figure 5.19 shows a shear wave velocity profile derived from active measurements at the Williams Street Park site. An estimated uncertainty in shear wave velocity of each layer is calculated using Equation 3.12 (Lai et al., 2005) with assumed σ_{V_R} (standard deviation associated with the experimental dispersion data) of 5% and also shown as a horizontal bar in Figure 5.19. Based on the shape of the profile, the site condition may be categorized as normally dispersive or inversely dispersive (Case 4 type) conditions.

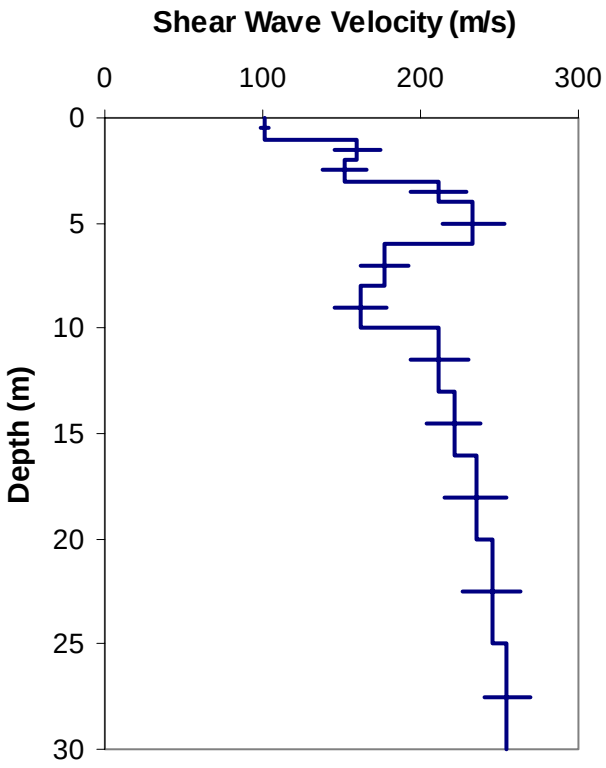

Figure 5.19 Shear wave velocity profile at Williams Street Park site

If the site condition is considered to be normally dispersive, normalized Rayleigh wave velocities from the filed tests can be compared with those from numerical simulation with Case 2. If the site condition is considered to be inversely dispersive, normalized Rayleigh wave velocities from the field tests can be compared with those from numerical simulation with Case 4. Figure 5.20 shows the comparison of normalized Rayleigh wave velocities from the field tests and numerical simulations as functions of normalized AC. The overlapping frequencies ranging from about 4 to 8 Hz correspond to normalized AC's ranging from about 0.2 to 0.6 for the three circular arrays. For this range of normalized AC, normalized Rayleigh wave velocities derived from field test data agree very well with those from numerical simulations for both Case 2 and Case 4, indicating that no significant error remains after applying the refining process.

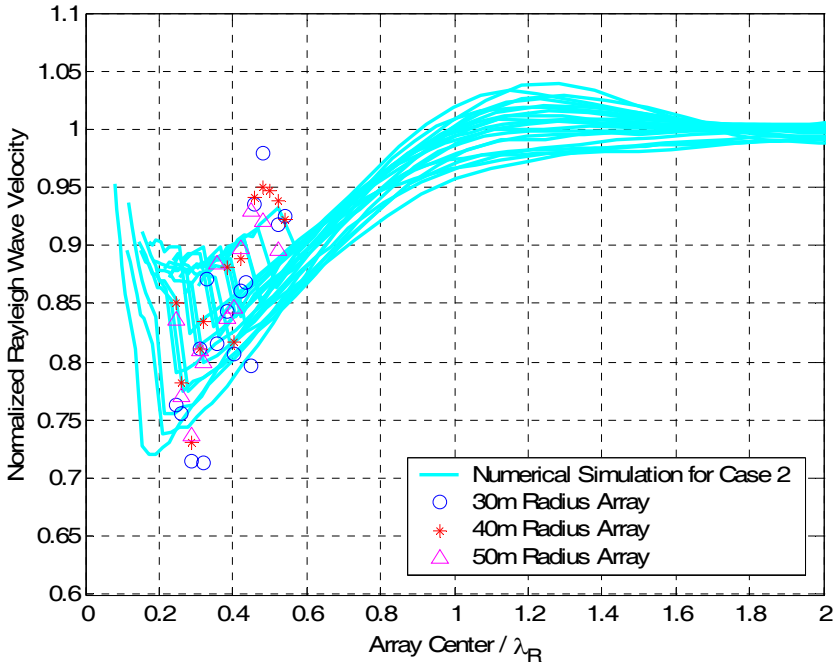

(a)

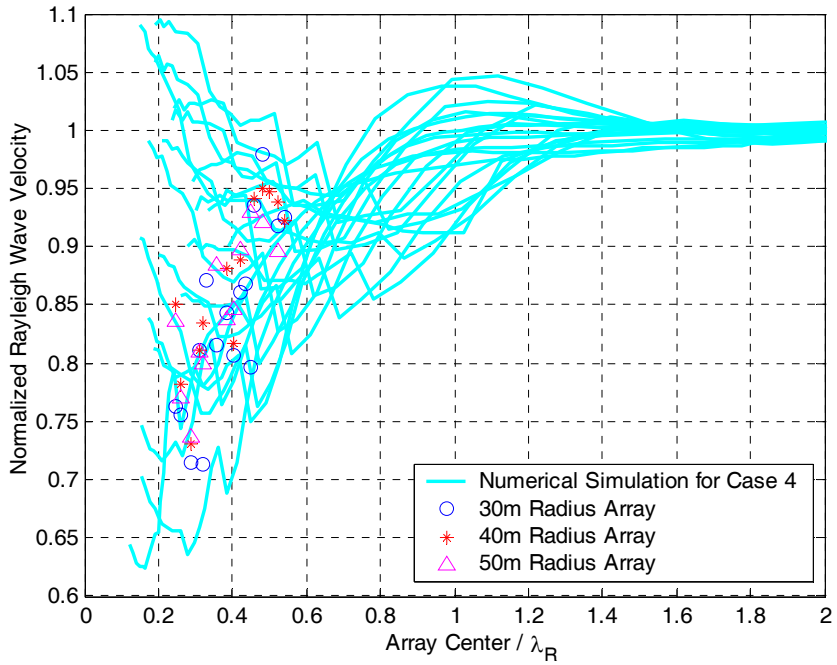

(b)

Figure 5.20 Comparison of normalized Rayleigh wave velocities associated with field experimental results at Williams Street Park site and numerical results for (a) Case 2 (normally dispersive) and (b) Case 4 (inversely dispersive)

5.5.4 Shear Wave Velocity Profiles from Composite Dispersion Curves

From this comparison, it can be concluded that the refining process applied to the passive dispersion data can eliminate data with significant errors due to poor wavenumber resolution or sidelobe leakage. Thus, the difference between active and passive dispersion data over the overlapping frequencies results mostly from errors caused by near-field effects in active measurements. Therefore, it is recommended that a composite dispersion curve be obtained by using only passive dispersion data over the overlapping frequencies.

The active dispersion curve and the averaged passive dispersion curves corresponding to the three arrays are combined to form three composite dispersion curves as shown in Figures 5.21(a) through 5.21(c), respectively. The three composite dispersion curves corresponding to the arrays with radii of 30 m, 40 m, and 50 m are named as Composite 1, Composite 2, and Composite 3, respectively. Shear wave velocity profiles are subsequently determined from the experimental dispersion curves via the non-linear, constrained least squares inversion algorithm (Lai, 1998) described in Chapter 3. For inversions with the three composite dispersion curves, the theoretical dispersion curves corresponding to the shear wave velocity profiles at the site are obtained and shown in Figures 5.21(a) through 5.21(c), respectively. The good agreements between experimental and theoretical dispersion curves are indicative of successful inversions. The shear wave velocity profiles corresponding to the composite dispersion curves are presented in Figures 5.22(a) through 5.22(c). An estimated uncertainty in shear wave velocity of each layer is calculated using Equation 3.12 (Lai et al., 2005) with assumed

σ_{V_R} (standard deviation associated with the experimental dispersion data) of 5 % and is shown as a horizontal bar in Figure 5.22.

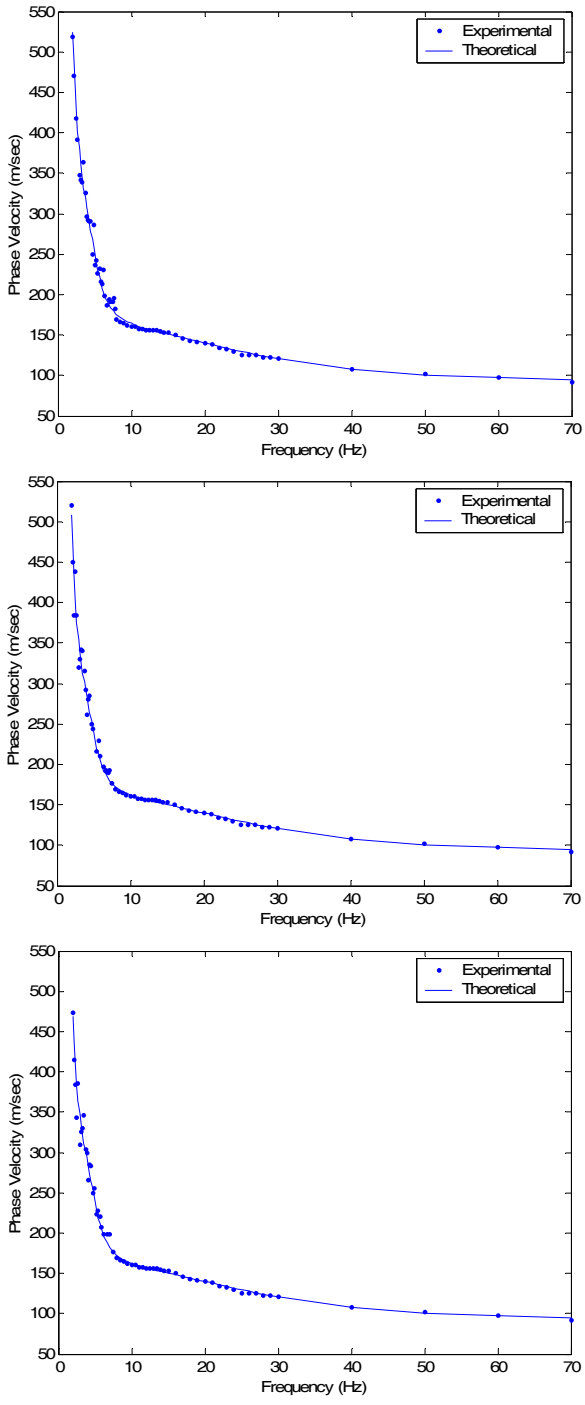

Figure 5.21 Comparison of experimental and theoretical dispersion curves at Williams Street Park site: (a) Composite 1, (b) Composite 2, and (c) Composite 3.

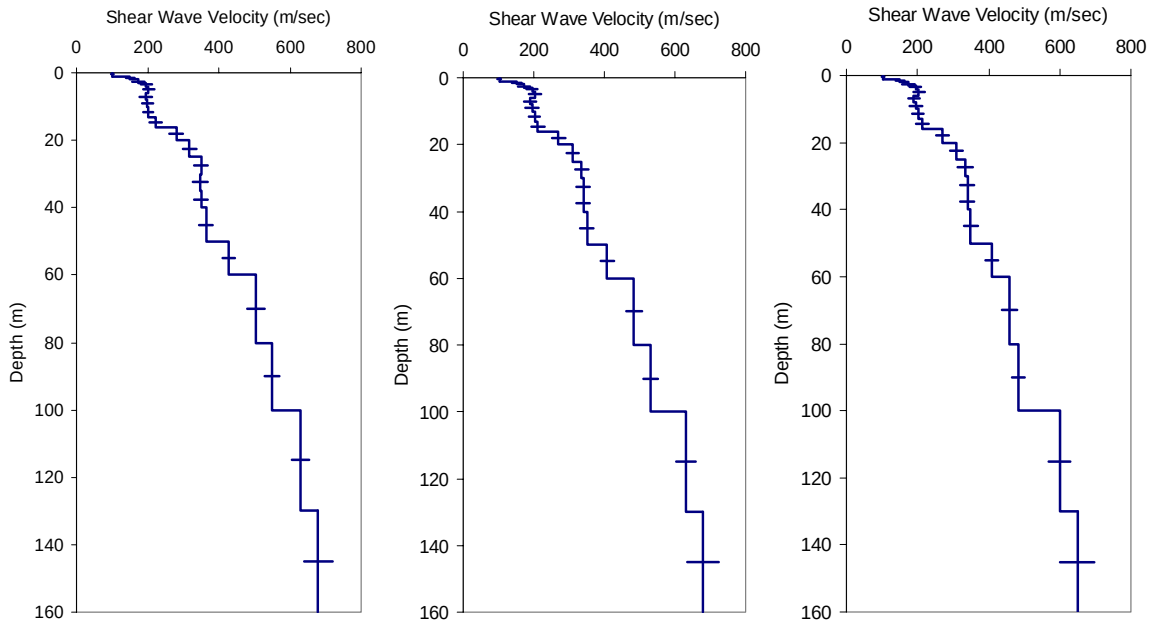

Figure 5.22 Shear wave velocity profiles at Williams Street Park site from: (a) Composite 1, (b) Composite 2, and (c) Composite 3.

Figure 5.23 shows the comparison of shear wave velocity profiles corresponding to the three composite dispersion curves and the active dispersion curve. Adding the passive data to the active data increases the maximum depth from 35 m to 160 m. Rayleigh wave velocities in the composite dispersion curves are greater than those in the active dispersion curve in the overlapping frequencies. Consequently, higher shear wave velocities were obtained from the composite dispersion curves compared to those from the active dispersion curve at depths between 16 to 35 m as shown in Figure 5.23. From the comparison between the shear wave velocity profiles corresponding to the three composite dispersion curves, slightly higher shear wave velocities were obtained from the composite dispersion curve corresponding to a shorter radius array.

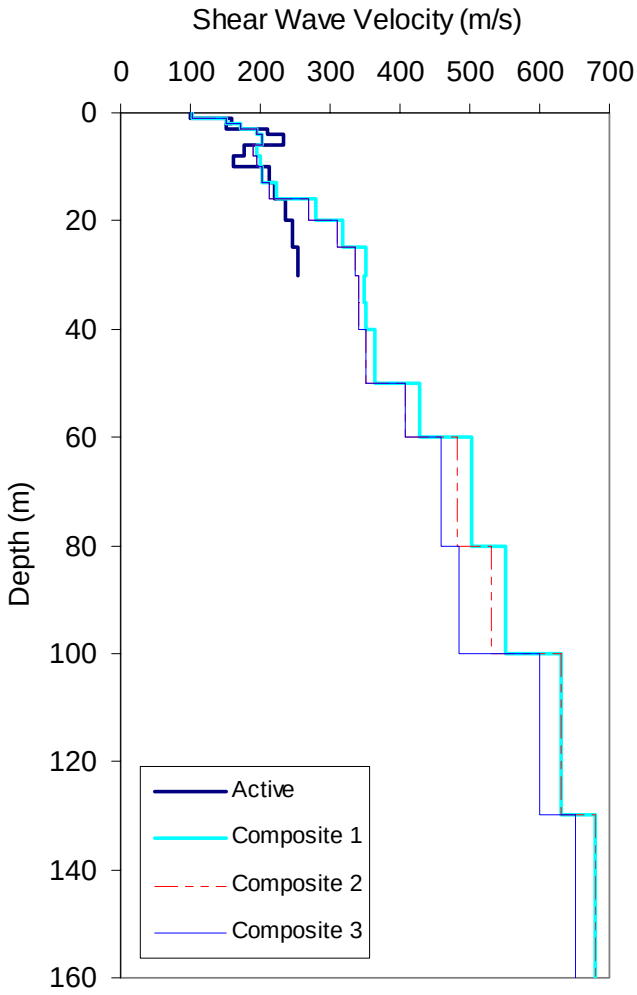

Figure 5.23 Comparison of shear wave velocity profiles at Williams Street Park site

5.6 SUMMARY AND CONCLUSIONS

A study to resolve the differences between active and passive dispersion estimates within the range of overlapping frequencies has been performed using experimental synthetic data. Near-field effects on active estimates and array effects on passive estimates were suspected of causing the systematic errors responsible for the differences. Array effects that include both limited wavenumber resolution and sidelobe leakage have been investigated in this chapter, with the following conclusions:

(1) If two waves are not successfully separated by the wavenumber resolution of a selected array, errors in measured dispersion estimates are dependent on the angular separation α between the waves.

(2) Separation of two waves is dependent on a ratio between a wavenumber resolution and a wavenumber distance between the two waves if no sidelobe effect exists.

(3) Sidelobe leakage may become significant for passive tests and yields a measured wavenumber significantly different than the true value. Dispersion data corresponding to the incorrect wavenumber can be detected and eliminated by the refining process.

(4) Improving an array's characteristics may significantly reduce the errors resulting from poor wavenumber resolution and sidelobe leakage depending on site conditions. The improvement of the characteristics via increasing the number of receivers or increasing the spatial extent of the array is often limited in practice. The optimization of the array is required for test result with minimized errors based on the test and site conditions.

(5) The refining process can be very useful to eliminate dispersion data contaminated by array effects, resulting in a more reliable dispersion curve.

(6) It is recommended that a fixed wavenumber precision for any spatial array be used for the approximated wavenumber range using active dispersion data. For the wavenumber of 0.02 rad/m, the wavenumber precision of 0.001 rad/m may create an error up to 4 %. If necessary, greater precision can be selected based on given time and analysis system as well as measured wavenumbers.

(7) If the refining process successfully removes data with significant errors due to the array effect, only slight errors remain on a final dispersion curve. Comparison between the experimental data and the numerical simulation result showed that no serious error due to the array effect was found for the passive dispersion curves at the Williams Street Park site.

(8) It might be concluded that the differences between the active and passive dispersion curves at overlapping frequencies resulted from errors caused by near-field effects in the active data. It is recommended that a composite dispersion curve be obtained by using only passive dispersion data for these frequencies.

CHAPTER 6

ATTENUATION MEASUREMENTS BY FREQUENCY-WAVENUMBER ANALYSIS

6.1 INTRODUCTION AND STATEMENT OF THE PROBLEM

In addition to stiffness, material damping ratio is another important property of a medium to understand and predict its response to dynamic loads. Attenuation properties of soils are often determined based on results of laboratory measurements of damping ratio using resonant column or torsional shear tests. Laboratory tests are useful for parametric studies of factors affecting damping ratio, however the effect of specimen disturbance on the measured values is uncertain (Rix et al., 2000).

In-situ damping measurements provide small-strain material damping ratio without the effect of specimen disturbance. In geotechnical engineering and seismology, borehole methods such as cross-hole or downhole tests have been utilized to measure the attenuation of body waves (Hoar and Stokoe, 1984; Redpath and Lee, 1986; Mok et al., 1988; Jongmans, 1990; Stewart, 1992; Gibbs et al., 1994; Liu et al., 1994).

Surface wave methods have been also used in recent years for damping measurements (Rix and Spang, 1995; Spang, 1995; Lai, 1998; Zywicki, 1999; Rix et al., 2000) with several advantages compared to borehole methods (Rix et al., 2000): (1) better soil-receiver coupling that is essential for accurate measurements of particle motion amplitudes, (2) operating frequencies approximating the frequencies of interest in earthquake site response analyses, and (3) non-invasive testing to save time and money. Despite these advantages, surface wave methods were not widely used in geotechnical

engineering for damping measurements until recently except for studying the attenuation of construction-induced vibrations (Rix et al., 2000).

In surface wave methods, measurements of vertical particle displacement amplitudes at various offsets from a source are utilized to determine the frequency-dependent Rayleigh wave attenuation coefficient α_R. A plot of the attenuation coefficient as a function of frequency is called an *attenuation curve*. Figure 6.1 presents an example of an experimental attenuation curve with error bars of ± one standard deviation of the attenuation coefficient at each frequency. The shear damping ratio profile is subsequently obtained from the experimental attenuation curve via inversion.

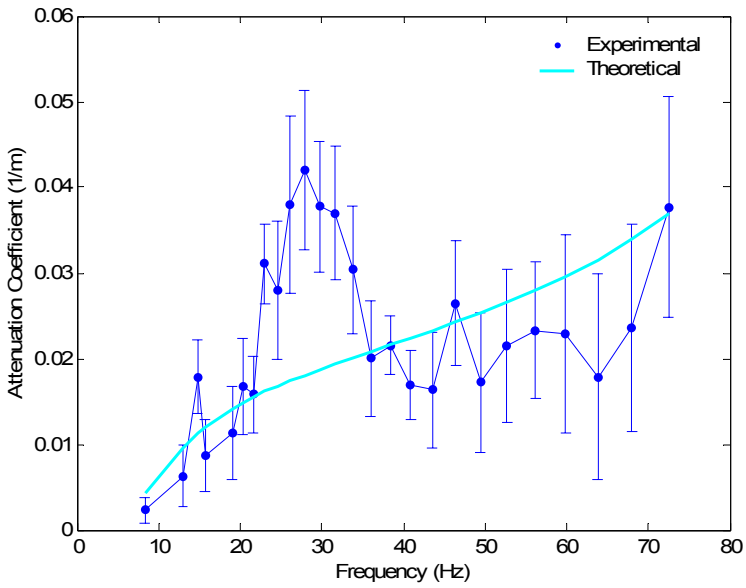

Figure 6.1 Example of experimental and theoretical attenuation curves (modified from Rix et al., 2000)

The accurate measurement of α_R is a basis for accurate determination of a shear damping ratio profile of near-surface soils. The accuracy of the measured attenuation coefficients from surface wave field measurements is improved by properly accounting

for three factors: (1) geometric spreading, (2) near-field effects, and (3) ambient noise. Several surface wave attenuation estimation methods have been developed with different techniques to account for these factors (Rix and Spang, 1995; Spang, 1995; Lai, 1998; Zywicki, 1999; Rix et al., 2000). Lai (1998) and Rix et al. (2000) pointed out the limitations of the $1/\sqrt{x}$ approximation for geometric spreading in vertically heterogeneous media and proposed the use of the geometric spreading function based on Green's function solutions in vertically heterogeneous media. Two techniques were used to remove ambient noise included in measurements (Spang, 1995; Lai, 1998; Rix et al., 2000). Near-field effects on surface wave attenuation estimates have not been studied and deserve more attention.

In this study, the traditional estimation method by Lai (1998) and Rix et al. (2000) and the frequency-wavenumber (f-k) estimation method utilizing sub-arrays are investigated with the displacement data from numerical simulations, focusing on near-field and ambient noise effects. The f-k estimation method was suggested by Zywicki (1999). In this study, detailed procedures are developed based on a study of the main factors affecting attenuation estimates. The two methods are also evaluated using experimental displacement data obtained from surface wave field measurements with three different arrays.

6.2 MECHANISMS AND DEFINITIONS OF ATTENUATION

6.2.1 Mechanisms of Attenuation

Seismic wave attenuation occurs due to: (1) geometric spreading, (2) apparent attenuation, and (3) material attenuation. Geometric spreading accounts for energy losses

with increasing distance due to spreading of a fixed amount of energy over a larger area. Apparent attenuation is due to scattering, reflection, and mode conversion at material boundaries and inclusions. Finally, material attenuation is an intrinsic property of the material (Spang, 1995). Apparent attenuation is often lumped into and is difficult to separate from material attenuation.

Measured displacement data from surface wave field measurements reflect the combination of all three mechanisms. To correctly estimate material attenuation from the data, geometric spreading must be accounted for properly.

As discussed in Chapter 2, the displacement Green's function provides a means to calculate a response of a linear system to an arbitrary source. The Green's function for vertically heterogeneous media with no material damping has the important physical interpretation of modeling geometric spreading in the media. For a vertical harmonic point source $F_z \cdot e^{i\omega t}$ located at x = 0 and z = 0, the vertical particle displacement amplitude $|u_z(x,\omega)|$ at the ground surface (z = 0) resulting from the superposition of the modes of Rayleigh propagation is calculated by:

$$|u_z(x,\omega)| = F_z \cdot G(x,\omega) \tag{6.1}$$

where $G(x,\omega)$ is called the *Rayleigh geometric spreading function* and is defined by:

$$G(x,\omega) = \frac{1}{4\sqrt{2\pi x}} \left\{ \sum_{i=1}^{M} \sum_{j=1}^{M} \frac{r_1(k_i,\omega) r_1(k_j,\omega) r_2(k_i,\omega) r_2(k_j,\omega) \cos\left[x(k_i - k_j)\right]}{\sqrt{k_i k_j}\,(V_i U_i I_i)(V_j U_j I_j)} \right\}^{0.5} \tag{6.2}$$

where k_i, V_i, U_i are the wavenumber, phase velocity, and group velocity, respectively, of the ith mode of propagation of Rayleigh waves (i=1, m). The term I_i is the first energy integral (Aki and Richards, 1980) associated with the ith mode and is defined by Equation 2.40. Displacement eigenfunctions $r_1(k_i,\omega)$ and $r_2(k_i,\omega)$ are associated with the

solution of the Rayleigh eigenproblem in elastic layered media. For more details about individual terms used in Equation 6.2, refer to the section 2.4.3.

The geometric spreading function $G(x,\omega)$ represents the geometric attenuation law in vertically heterogeneous media. It can be approximated by $1/\sqrt{x}$ derived for homogeneous media (i.e., a single mode of propagation). Figure 6.2 illustrates the effect of site conditions on the geometric spreading function and illustrates that the geometric spreading functions in vertically heterogeneous media are different than that in homogeneous media (i.e., $1/\sqrt{x}$). This approximation was adopted in some of the previous surface wave attenuation studies for vertically heterogeneous media (Spang, 1995; Rix and Spang, 1995), leading to errors in material attenuation estimates due to the use of the incorrect physical model to account for the geometrical spreading.

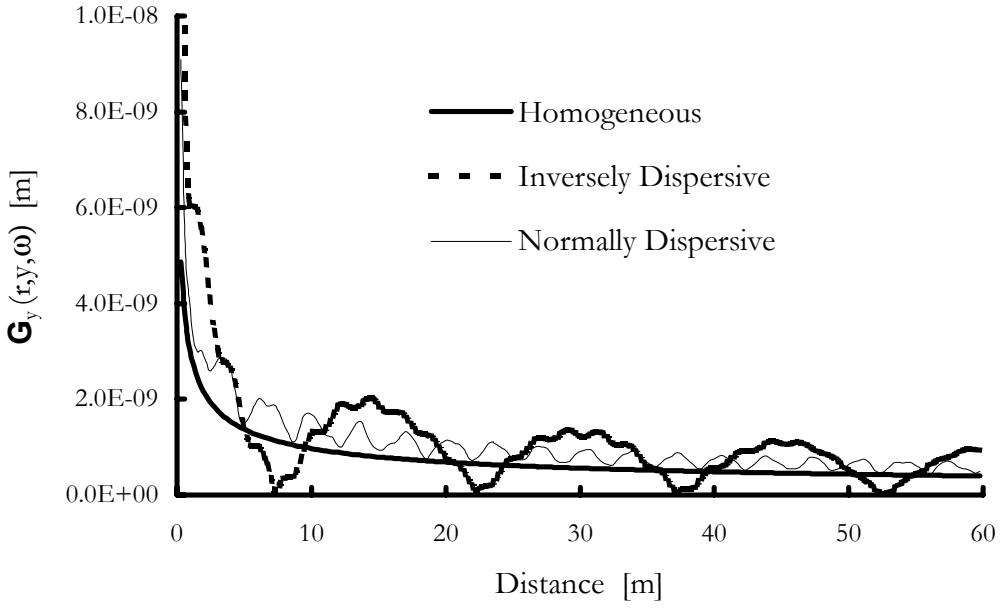

Figure 6.2 Geometric spreading function for various medium conditions (Lai, 1998)

6.2.2 Definitions of Material Attenuation

Surface wave methods measure dynamic soil properties, G_{max} and D_{Smin}, at very small strain levels, where the theory of linear viscoelasticity is appropriate. According to the elastic-viscoelastic correspondence principle (Read, 1950; Christensen, 1971), the viscoelastic solution is obtained directly from the solution of the corresponding elastic problem by replacing real-valued moduli with complex-valued moduli. As a general solution of the wave propagation equation in a viscoelastic medium, the particle motion is given by:

$$u(x,t) = A \cdot \exp[\omega t - k^* x] \tag{6.3}$$

where A is a constant to be determined from the boundary conditions and k^* is a complex wavenumber. Using a subscript χ (=P, S, or R) to denote P-, S-, and Rayleigh waves, the complex wavenumber k_χ^* is defined by:

$$k_\chi^* = k_\chi - i\alpha_\chi = \frac{\omega}{V_\chi} - i\alpha_\chi \tag{6.4}$$

where, k_χ, V_χ and α_χ are the real wavenumber, real phase velocity and attenuation coefficient, respectively, of the χ wave.

Waves experiencing attenuation due to intrinsic material losses are mathematically expressed with complex parameters. The complex phase velocity of the χ wave, V_χ^*, is given by:

$$V_\chi^* = \frac{\omega}{k_\chi^*} \tag{6.5}$$

For the P- and S-waves, $V_P^* = \sqrt{M^*/\rho}$ and $V_S^* = \sqrt{G^*/\rho}$, respectively, where ρ is the mass density of a medium, and M^* and G^* are complex constrained and shear moduli,

respectively. The complex moduli can be divided into real and imaginary parts. For example, the complex constrained modulus can be expressed by:

$$M^* = \mathrm{Re}(M^*) + i\,\mathrm{Im}(M^*) = M' + iM'' \tag{6.6}$$

where M' and M'' are real and imaginary parts of M^*, respectively and are related to the stored and dissipated energies, respectively. The ratio M''/M' that is called the loss tangent $tan\ \phi_P$ and can be used to define the quality factor Q_P of the P- wave as follows:

$$\frac{1}{Q_P} = \frac{M''}{M'} = \tan\phi_P \tag{6.7}$$

A quality factor Q_χ or its inverse, a specific dissipation factor Q_χ^{-1} associated with the χ wave is often used in geophysics and seismology for attenuation measurements. The specific dissipation factor can be also computed as a ratio of dissipated energy ΔW_χ to stored energy W_χ per unit volume:

$$\frac{1}{Q_\chi} = \frac{\Delta W_\chi}{2\pi W_\chi} \tag{6.8}$$

The linear hysteretic material damping ratio D_χ associated with the χ wave can also be defined in terms of the ratio of dissipated energy to stored energy per loading cycle:

$$D_\chi = \frac{\Delta W_\chi}{4\pi W_\chi} = \frac{1}{2Q_\chi} \tag{6.9}$$

The material damping ratio of most soils is less than 5 percent ($Q^{-1} < 0.1$) at very small strain levels, which allows the use of simplified approximations based on the assumption of low loss. For low-loss materials, the attenuation coefficient α_χ of the χ wave is related to other parameters as follows:

$$\alpha_\chi = \frac{2\pi D_\chi}{\lambda_\chi} = k_\chi D_\chi = \frac{k_\chi}{2Q_\chi} \tag{6.10}$$

where λ_χ is the wavelength of the χ wave.

For low-loss materials, the complex velocity can be calculated using the real-valued velocity and the damping ratio:

$$V_\chi^* = \frac{V_\chi}{1 - iD_\chi} = V_\chi \frac{1 + iD_\chi}{1 + D_\chi^2} \tag{6.11}$$

If only first-order terms are retained, the equation can be simplified to:

$$V_\chi^* = V_\chi (1 + iD_\chi) \tag{6.12}$$

Lai and Rix (2002) compared the real and imaginary parts of Equations 6.11 and 6.12 to those of the exact equation and found no significant difference between them for Q^{-1} less than 0.1.

The complex Poisson's ratio ν^* can be calculated by:

$$\nu^* = \frac{1}{2}\left(\frac{V_P^{*2} - 2V_S^{*2}}{V_P^{*2} - V_S^{*2}}\right) \tag{6.13}$$

For low-loss materials, Equation 6.13 can be rewritten using Equation 6.12 and retaining only the first-order terms of the damping ratios:

$$\nu^* = \nu + i\left[\frac{V_P^2 V_S^2 (D_P - D_S)}{(V_P^2 - V_S^2)^2}\right] \tag{6.14}$$

From Equations 6.14, it can be observed that if $D_P = D_S$, $\nu^* = \nu$.

6.2.3 Attenuation of Rayleigh Waves in Homogeneous Media

The complex Rayleigh wave equation for a homogeneous medium can be obtained by replacing real phase velocities in Equation 2.23 with corresponding complex phase velocities:

$$\left(2-\frac{V_R^{*2}}{V_S^{*2}}\right)^4 -16\left(1-\frac{V_R^{*2}}{V_P^{*2}}\right)\cdot\left(1-\frac{V_R^{*2}}{V_S^{*2}}\right)=0 \tag{6.15}$$

Macdonald (1959) derived a simplified equation relating the quality factors for P-, S-, and Rayleigh waves using Equations 6.11 and 6.15 for low-loss materials:

$$\frac{1}{Q_R}=(1-m)\frac{1}{Q_S}+m\frac{1}{Q_P} \tag{6.16}$$

where $m=\dfrac{a(2-b)(1-b)}{a(2-b)(1-b)-b(1-a)(2-3b)}$, $a=(V_R/V_P)^2$ and $b=(V_R/V_S)^2$.

6.3 MEASUREMENT OF SURFACE WAVE ATTENUATION

6.3.1 Rayleigh Wave Attenuation in Vertically Heterogeneous Media

In low-loss vertically heterogeneous media, the vertical displacement may be expressed as follows:

$$\left|u_z(x,\omega)\right| = F_z\cdot G(x,\omega)\cdot e^{-\alpha_R(\omega)x} \tag{6.17}$$

which includes the effect of both geometric and material attenuation.

Correcting for geometric attenuation leads to the normalized displacement amplitude $\left|u_z(x,\omega)\right|_{norm}$:

$$\left|u_z(x,\omega)\right|_{norm}=\frac{\left|u_z(x,\omega)\right|}{G(x,\omega)}=F_z\cdot e^{-\alpha_R(\omega)x} \tag{6.18}$$

Equation 6.18 can be used directly to determine the value of α_R that best matches the experimental displacement amplitudes through a non-linear regression analysis or one can take the natural logarithm for both sides, resulting in a linear relationship between α_R and x as follows:

$$Ln\left(\left|u_z(x,\omega)\right|_{norm}\right) = Ln(F_z) - \alpha_R(\omega)\cdot x \tag{6.19}$$

Spang (1995) used Equation 6.19 with $G(x,\omega) = 1/\sqrt{x}$ to account for geometric spreading to estimate frequency-dependent attenuation coefficients. Zywicki (1999) also used Equation 6.19, but with the geometric spreading function in Equation 6.2 to estimate frequency-dependent attenuation coefficients.

A linear regression analysis with log-scale displacement amplitude data versus distance magnifies uncertainties for the displacement data with small magnitude (i.e., large distance). To overcome this shortcoming in the linear regression analysis, a non-linear regression analysis can be utilized to determine the value of α_R by fitting Equation 6.18 to the experimental displacement amplitude data. Lai (1998) and Rix et al. (2000) used the non-linear regression technique to the experimental amplitudes normalized by the geometric spreading function in Equation 6.2.

In addition to accounting for geometric spreading, ambient noise included in the measured data should be removed for accurate measurement of displacements. Two noise removal techniques have been used with the assumption of a stationary noise environment, that is, the statistical characteristics of the noise do not change during the measurements. Spang (1995) independently measured the ambient noise and removed noise included in surface wave measurements by subtracting the spectrum of measured noise from the spectra of the measured displacements. This technique is quite sensitive to

temporal variations in noise power. Lai (1998) and Rix et al. (2000) used an ordinary coherence function $\gamma_{sr}^2(x,\omega)$ between source input and receiver output to correct the spectral amplitudes. The noise-corrected spectra are given by:

$$G_{vv}(x,\omega) = \gamma_{sr}^2(x,\omega) G_{yy}(x,\omega) \tag{6.20}$$

where $G_{vv}(x,\omega)$ and $G_{yy}(x,\omega)$ = auto-power spectra of the measured signal $v(x,t)$ free from noise and the measured signal $y(x,t)$ with noise, respectively.

Once the geometric spreading and noise are successfully removed from the displacement amplitudes, the application of a regression analysis to the amplitudes yields two parameters $F_z(\omega)$ and $\alpha_R(\omega)$. The value of $F_z(\omega)$ determined by the regression analysis using the displacement amplitudes is not exactly equal to the source amplitude since only a portion of source energy contributes to the formation of Rayleigh waves (Zywicki, 1999). However, the accuracy of F_z measurement does not influence the value of α_R. Moreover, the value of F_z is not required for the subsequent inversion process to yield a damping ratio profile.

6.3.2 Frequency-Wavenumber (f-k) Estimation Method

The key idea of the sub-array technique introduced by Zywicki (1999) is the decomposition of a single array into several sub-arrays and the estimation of the representative displacement amplitude for each sub-array. The f-k analysis of each sub-array allows one to estimate an *equivalent displacement amplitude* corresponding to the sub-array center. The steps in the f-k estimation method to obtain an attenuation curve are as follows:

(1) Perform surface wave field measurements with an array of n receivers.

(2) Decompose the array into m sub-arrays of l receivers. Note that $m = n - l + 1$.

(3) For each sub-array, perform frequency domain beamforming analysis with the displacement amplitude data corresponding to the sub-array that are corrected for geometric spreading and ambient noise. To correct the displacement amplitude data for geometric spreading, the data are weighted by a diagonal matrix **W** whose diagonal elements are the inverse of the geometric spreading function $G(x_m, \omega)$ for the mth receiver. The steered response power for a frequency ω_0 is given by:

$$P(\mathbf{k}, \omega_0) = \mathbf{e}^H \mathbf{W}\mathbf{R}\mathbf{W}^H \mathbf{e} \tag{6.21}$$

(4) The largest peak $P_{max}(\omega_0)$ in the steered response power spectrum for a given frequency ω_0 corresponds to the dominant Rayleigh wave propagating across the sub-array. The amplitude of the largest peak is also considered to be the power at a virtual receiver that is placed at the sub-array center for a given frequency ω_0. The equivalent normalized displacement amplitude corrected for geometric spreading can be obtained by taking the square root of the P_{max}. Additional equivalent normalized displacement amplitudes can be obtained via the same process for other frequencies in the same sub-array. The process can be repeated for other sub-arrays, leading to equivalent normalized displacement amplitude spectra as functions of the sub-array centers and frequencies. According to the type of receiver used in field measurements, the experimental equivalent normalized displacement amplitude spectra are calculated using:

$$\left|u_z(SC,\omega)\right|_{equi} = \frac{\sqrt{P_{\max}(SC,\omega)}}{\omega \cdot C_{vel}(\omega)} \text{ (For velocity transducers)} \quad (6.22a)$$

$$\left|u_z(SC,\omega)\right|_{equi} = \frac{\sqrt{P_{\max}(SC,\omega)}}{\omega^2 \cdot C_{accel}(\omega)} \text{ (For accelerometers)} \quad (6.22b)$$

where SC denotes sub-array center, and C is the frequency-dependent calibration factor of the receiver. Subscripts in C_{vel} and C_{accel} denote a velocity transducer and accelerometer as the receiver, respectively.

(5) Once the experimental equivalent normalized displacement amplitudes spectra are obtained for frequency range of interest, the non-linear regression analysis is used to determine the value of α_R in Equation 6.18 that best matches the experimental displacement amplitudes.

In the f-k estimation method, the number of receivers in each sub-array must be optimized. In the following section, a study of the effect of the number of receivers in each sub-array on the f-k estimation method will be presented.

6.4 NUMERICAL SIMULATION RESULTS

Since the surface wave attenuation estimation procedure is based on a regression analysis of measured displacement amplitude data, near-field effects and ambient noise play important roles in the accuracy of the derived attenuation coefficients. For the f-k estimation method, the number of receivers in each sub-array is also an important factor because the sub-array's characteristics limit its capability to correctly estimate power spectra of measured displacement amplitudes.

Numerical simulation using the PUNCH program to calculate the explicit Green's function solutions for vertically heterogeneous media offers a means to perform

parametric studies of the factors affecting surface wave attenuation measurements. As the first step, a validation of the traditional and f-k estimation methods is performed with the synthetic displacement data from the numerical simulations for an ideal homogeneous soil profile. For near-field effects, the traditional and f-k estimation methods are evaluated and compared for three typical soil profiles. Then, the effect of the number of receivers in each sub-array on the f-k estimation method is investigated with the data for the same three typical profiles.

6.4.1 Soil Profiles Used in Numerical Simulations

A homogeneous half-space and three typical soil profiles with small damping ratio, as tabulated in Tables 6.1 through 6.4, have been used in the numerical simulations to perform parametric studies of the two attenuation estimation methods. The homogeneous half-space is used only to validate the procedures in the two methods. The three remaining soil profiles (one normally dispersive and two inversely dispersive profiles) are used to simulate typical soil conditions that are encountered in the field. For simplicity, the values of D_P and D_S are assumed to be equal for the soil profiles.

Table 6.1 Properties of a soil profile (Case 1)

Layer No.	Thickness (m)	V_S (m/sec)	Poisson's ratio, ν	Damping ratio, D (%)	Mass density, ρ (t/m^3)
Half-Space	∞	200	0.3	2	1.8

Table 6.2 Properties of a soil profile (Case 2)

Layer No.	Thickness (m)	V_S (m/sec)	Poisson's ratio, ν	Damping ratio, D (%)	Mass density, ρ (t/m^3)
1	5	200	0.3	2	1.8
2	10	300	0.3	2	1.8
3	10	400	0.3	2	1.8
Half-Space	∞	500	0.3	2	1.8

Table 6.3 Properties of a soil profile (Case 3)

Layer No.	Thickness (m)	V_S (m/sec)	Poisson's ratio, ν	Damping ratio, D (%)	Mass density, ρ (t/m^3)
1	5	300	0.3	2	1.8
2	10	200	0.3	2	1.8
3	10	400	0.3	2	1.8
Half-Space	∞	500	0.3	2	1.8

Table 6.4 Properties of a soil profile (Case 4)

Layer No.	Thickness (m)	V_S (m/sec)	Poisson's ratio, ν	Damping ratio, D (%)	Mass density, ρ (t/m^3)
1	5	200	0.3	2	1.8
2	10	400	0.3	2	1.8
3	10	300	0.3	2	1.8
Half-Space	∞	500	0.3	2	1.8

From Equation 6.10, the attenuation coefficient of Rayleigh wave in low-loss medium is estimated by:

$$\alpha_R = \frac{2\pi f}{V_R} D_R = k_R D_R \tag{6.23}$$

Equation 6.23 can be usefully used to calculate a reference Rayleigh wave attenuation curve. With a constant Rayleigh damping ratio, α_R is a function of only the Rayleigh wavenumber. In order to use Equation 6.23 to obtain a reference attenuation curve that is simply a function of wavenumber, a constant damping ratio with depth is used in the four soil profiles.

6.4.2 Validation of Two Attenuation Estimation Methods

Before performing extensive parametric studies, it is desirable to validate the traditional method by Lai (1998) and Rix et al. (2000) and the f-k estimation method (Zywicki, 1999). The validation was performed using synthetic Rayleigh displacement data at various receiver offsets from the Green's function solutions of plane Rayleigh

waves (Lai, 1998) in a homogeneous half-space defined by the parameters in Table 6.1. The Rayleigh wave displacement data are then used to estimate attenuation curves with these two estimation methods.

The plane Rayleigh displacement data were calculated at receiver offsets of a uniform array 1SR1RR-15 (source–to-first receiver (SR) distance of 1 m, receiver-to-receiver (RR) distance of 1 m, and 15 receivers in the array) for a set of 69 frequencies ranging from 5 to 100 Hz. The f-k estimation method was performed with 5 receivers in each sub-array, which is denoted by 1SR1RR-15-S5.

Figure 6.3 shows the comparison of the normalized displacement amplitudes and the equivalent normalized displacement amplitudes calculated from the plane Rayleigh displacement data at the frequencies of 10 and 70 Hz. Since these normalized displacement amplitudes from plane Rayleigh waves do not contain geometric spreading, decays in the amplitudes with increasing distance from the source are due solely to material attenuation. Note that the two normalized displacement amplitudes follow an exponential function with the same slope, indicating that the attenuation coefficients calculated from the two methods are identical. Figure 6.4 presents the comparison of the reference attenuation curve from Equation 6.23 and the attenuation curves from the two methods. For this ideal soil condition with only plane Rayleigh waves, the two methods both yield accurate values of the frequency-dependent attenuation coefficients.

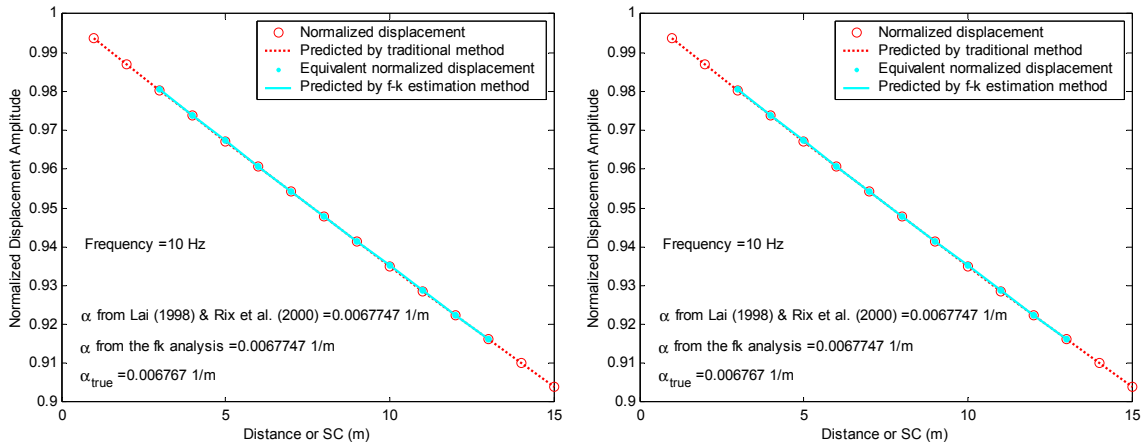

(a) (b)

Figure 6.3 Comparison of normalized displacement amplitudes and equivalent normalized displacement amplitudes for two attenuation estimation methods at frequencies of (a) 10 Hz and (b) 70 Hz.

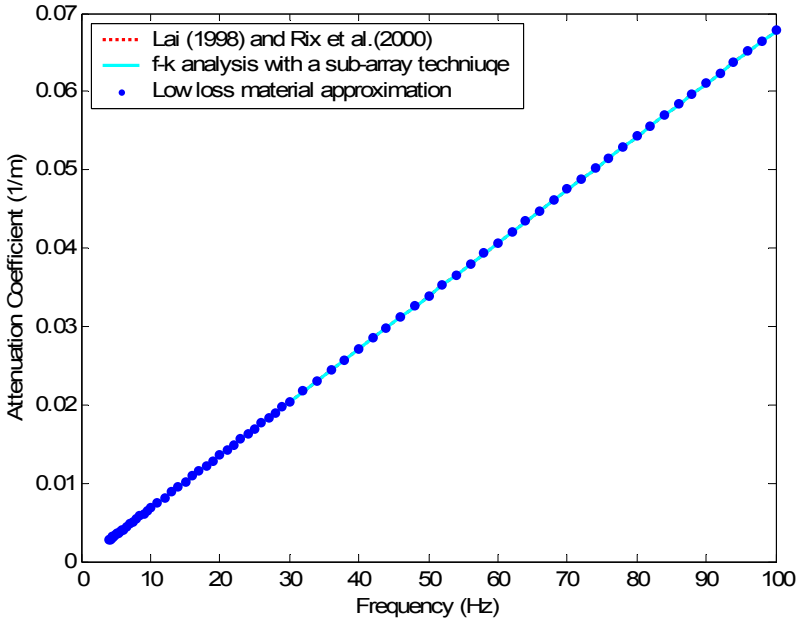

Figure 6.4 Comparison of attenuation curves from two attenuation estimation methods and from low-loss material approximation

6.4.3 Near-field Effects

In Chapter 4, near-field effects on dispersion estimates were discussed. In addition, near-field effects on attenuation estimates deserve attention. Based on the numerical studies by Holzlohner (1980), Vrettos (1991), and Tokimastu (1995), Rix et al. (2000)

suggested that displacement data measured inside the near-field extending up to $\lambda/2$ (where λ = wavelength) and 2λ from a source in normally dispersive and inversely dispersive soil profiles, respectively, be excluded. However, the near-field effect criterion appears to be excessively conservative and may result in insufficient displacement data for accurate attenuation measurements. In order to suggest more rational near-field effect criteria for attenuation measurements, it is necessary to investigate near-field effects on attenuation estimates.

Although the same near-field exists for a surface wave test with given test condition, the near-field effects on dispersion estimates are not identical to those on attenuation estimates due to difference in dispersion and attenuation estimation procedures. Near-field effects become more severe for attenuation estimates compared to dispersion estimates due to the following reasons: (1) near-field effects independently influence two individual procedures including the geometric spreading calculation and the attenuation estimation, and (2) a regression analysis procedure to determine α_R from experimental displacement data appears to be prone to variation in a few displacement data induced by near-field effects. In this section, a study of near-field effects on attenuation estimates is performed using the synthetic displacement data. The attenuation estimates were obtained from the f-k estimation and traditional methods and were compared to reference values to investigate the impact of near-field effects on both methods.

To study near-field effects on surface wave attenuation estimates for typical soil conditions, the synthetic displacement data were obtained from the Green's function solutions of the entire wavefield generated by a vertical load through the numerical simulations with three typical soil profiles in Tables 6.2 through 6.4. Reference

attenuation curves for the three typical soil profiles are calculated using Equation 6.23. Three different arrays consisting of 15 receivers, as listed in Table 6.5, are used for the numerical simulations. Note that in f-k estimation method, each sub-array is composed of 9 receivers.

Table 6.5 Array sets used to investigate near-field effects on attenuation estimates

Array	Array parameter		Sub-array parameter
	Array Center (m)	Number of receivers	Number of receivers
1SR1RR-15	8	15	9
5SR1RR-15	12		
10SR1RR-15	17		

Figure 6.5 shows the comparison of the attenuation curves from the two methods with the three arrays for the three soil profiles. As expected, near-field effects become more significant with decreasing frequency, leading to significant errors is estimated attenuation coefficients. The frequency at which significant near-field effects develop is called the *transition frequency*. For Case 2 and Case 4, the transition frequency decreases for larger values of the array center (AC). For Case 3, significant errors are observed at a broader range of frequencies, indicating the difficulty of the methods with a 15-receiver array to yield accurate attenuation data for this soil condition. The transition frequency is not clearly observed for this profile. Figure 6.6 shows the transition frequencies in the attenuation curves associated with the three arrays for the Case 2 profile.

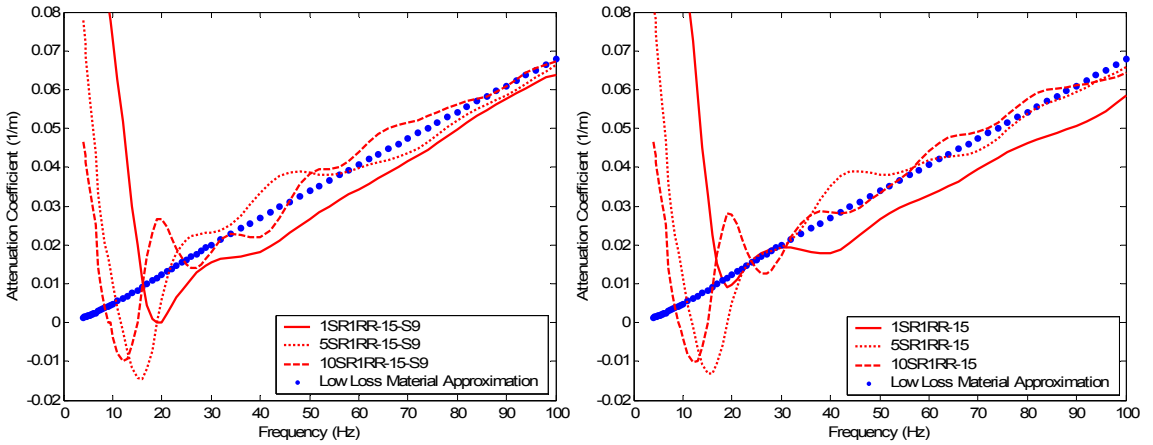

(a) f-k estimation method (Case 2)

(b) traditional method (Case 2)

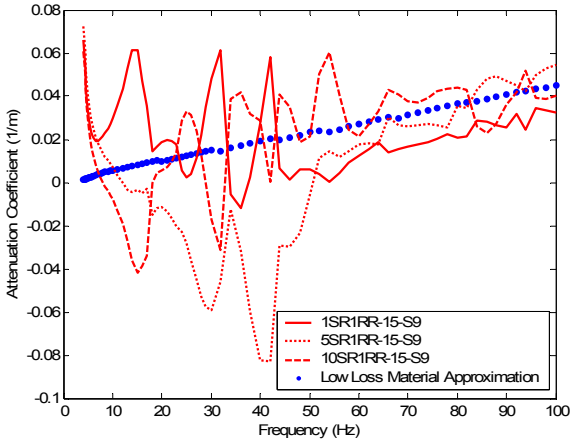

(c) f-k estimation method (Case 3)

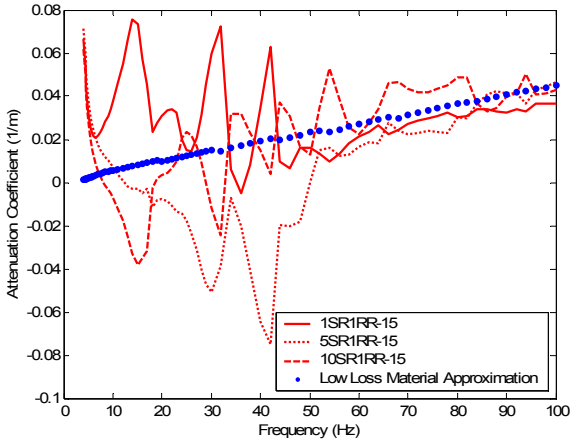

(d) traditional method (Case 3)

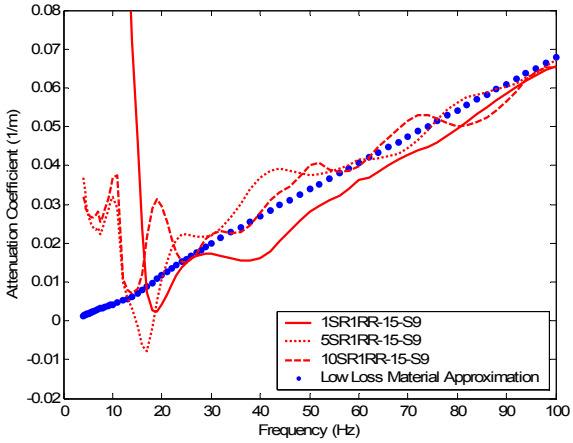

(e) f-k estimation method (Case 4)

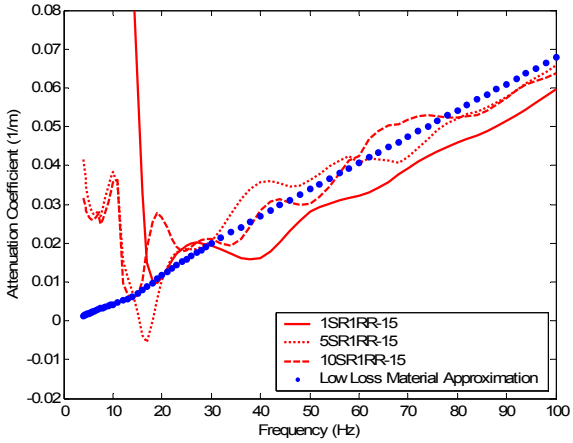

(f) traditional method (Case 4)

Figure 6.5 Comparison of attenuation curves corresponding to three different arrays of 15 receivers with various array centers

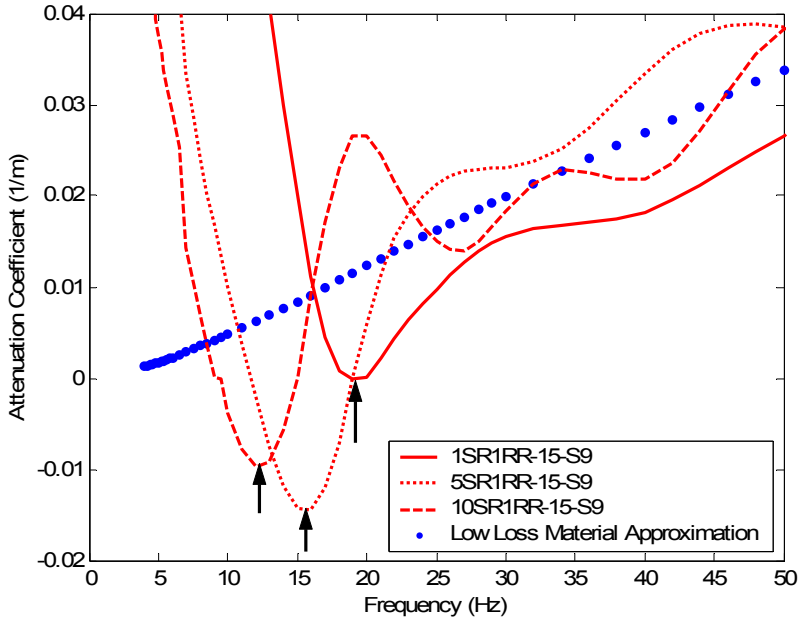

Figure 6.6 Transition frequencies (indicated with black arrows) in attenuation curves associated with three arrays for the Case 2 profile

In Chapter 4, two normalized parameters were successfully used to capture the influence of near-field effects on dispersion estimates with array-based surface wave methods. A normalized Rayleigh attenuation coefficient, that is a ratio of measured α_R to α_R of plane Rayleigh waves, however, is not appropriate because α_R of plane Rayleigh wave ($\alpha_{R,plane}$)approaches zero at low frequencies. As an alternate parameter, the absolute error, that is $|\alpha_R - \alpha_{R,plane}|$, is selected and near-field effects are evaluated in terms of absolute error and normalized AC.

Figure 6.7 shows plots of the absolute errors and normalized array centers for the three typical soil profiles using arrays of 15 receivers. Note that the errors for the Case 3 profile are much more significant than those for the Case 2 and Case 4 profiles. From Figure 6.7, the transition points associated with the transition frequencies are observed at a single normalized AC for the three arrays. For Case 2 and Case 4, the transition points are found at the normalized AC of 0.8. In this study, it is recommended that the transition

point in the normalized AC be used as a filtering criterion for near-field effects on attenuation estimates using 15-receiver arrays in the Case 2 and Case 4 profiles. For Case 3, no apparent transition point is found. Note that all of the errors due to near-field effects can not be removed by applying this near-field effect filtering criterion.

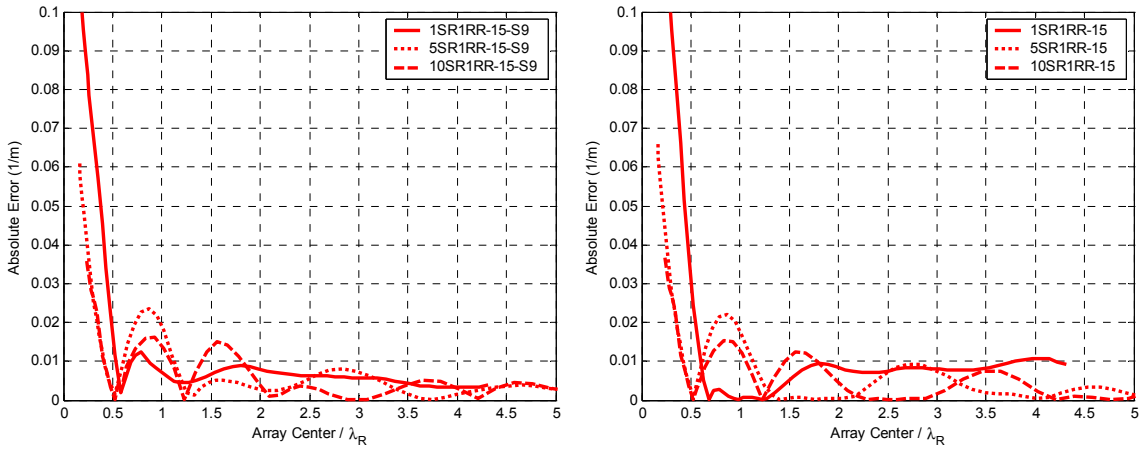

(a) f-k estimation method (Case 2)

(b) traditional method (Case 2)

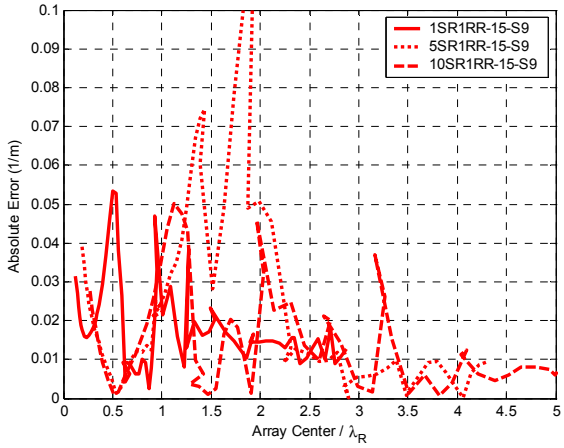

(c) f-k estimation method (Case 3)

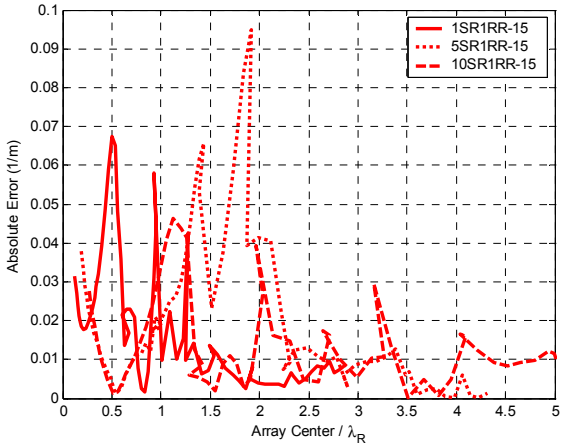

(b) traditional method (Case 3)

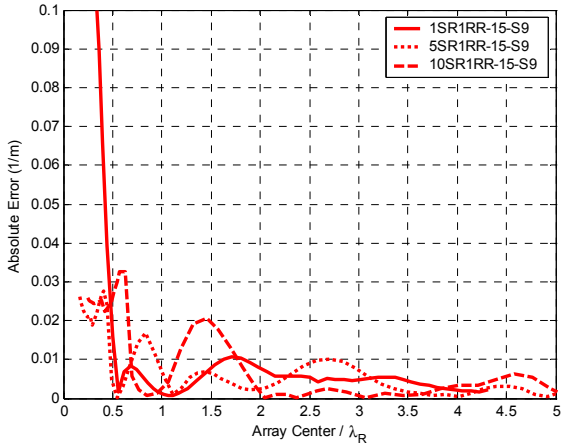

(e) f-k estimation method (Case 4)

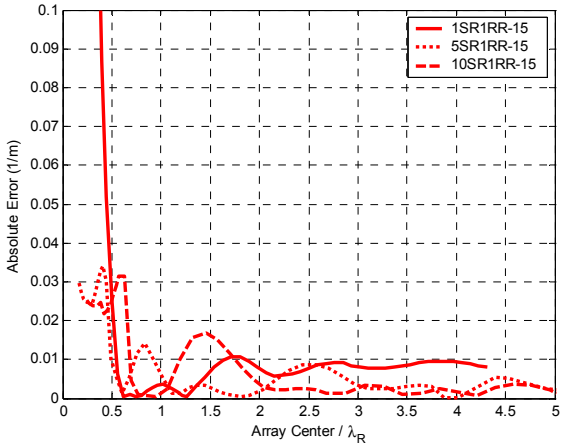

(f) traditional method (Case 4)

Figure 6.7 Near-field effects on attenuation estimates with three 15-receiver arrays for three typical soil profiles

6.4.4 Effect of the Number of Receivers in Each Sub-Array

In the f-k estimation method, the number of receivers used in each sub-array is a factor affecting attenuation estimation results and should be optimized. For a fixed number of total receivers in an array, the number of receivers in each sub-array defines the sub-array's capability to resolve dominantly propagating Rayleigh waves as well as the number of experimental displacement data that are included in a regression analysis to determine α_R. Increasing the number of receivers in each sub-array may lead to more accurate equivalent normalized displacement data, but will reduce their number, leading to increasing uncertainty in the regression analysis.

To investigate the effect of the number of receivers in each sub-array on attenuation estimates, numerical simulations using PUNCH are carried out with an array of 1SR1RR-15 for the three typical soil profiles. The synthetic Rayleigh displacement data from the numerical simulations are then processed by the f-k estimation method with four different numbers (5, 7, 9, and 11) of receivers in a single sub-array. Figure 6.8 shows the effect of the number of receivers in each sub-array on the calculated equivalent normalized displacement amplitudes from numerical data for the three soil profiles.

Theoretical attenuation curves in Figure 6.8 are obtained from Equation 6.18 with the estimated attenuation coefficients. If no near-field or ambient noise effects are present, the normalized displacement amplitudes corresponding to a set of sub-arrays should decay with distance due to only material attenuation. Therefore, the level of near-field effects may be estimated by evaluating the agreement between the experimental and theoretical attenuation curves. At the low frequency of 10 Hz, the displacement amplitudes obtained with more receivers in each sub-array deviate less from the

exponential trend with the estimated attenuation coefficients. When a larger number of receivers comprise each sub-array, the center of the closest (to the source) sub-array is further from the source and is thus less affected by near-field effects. At 70 Hz, the differences associated with the number of receivers in each sub-array are less pronounced. This phenomenon results from the different levels of near-field effects at these two frequencies.

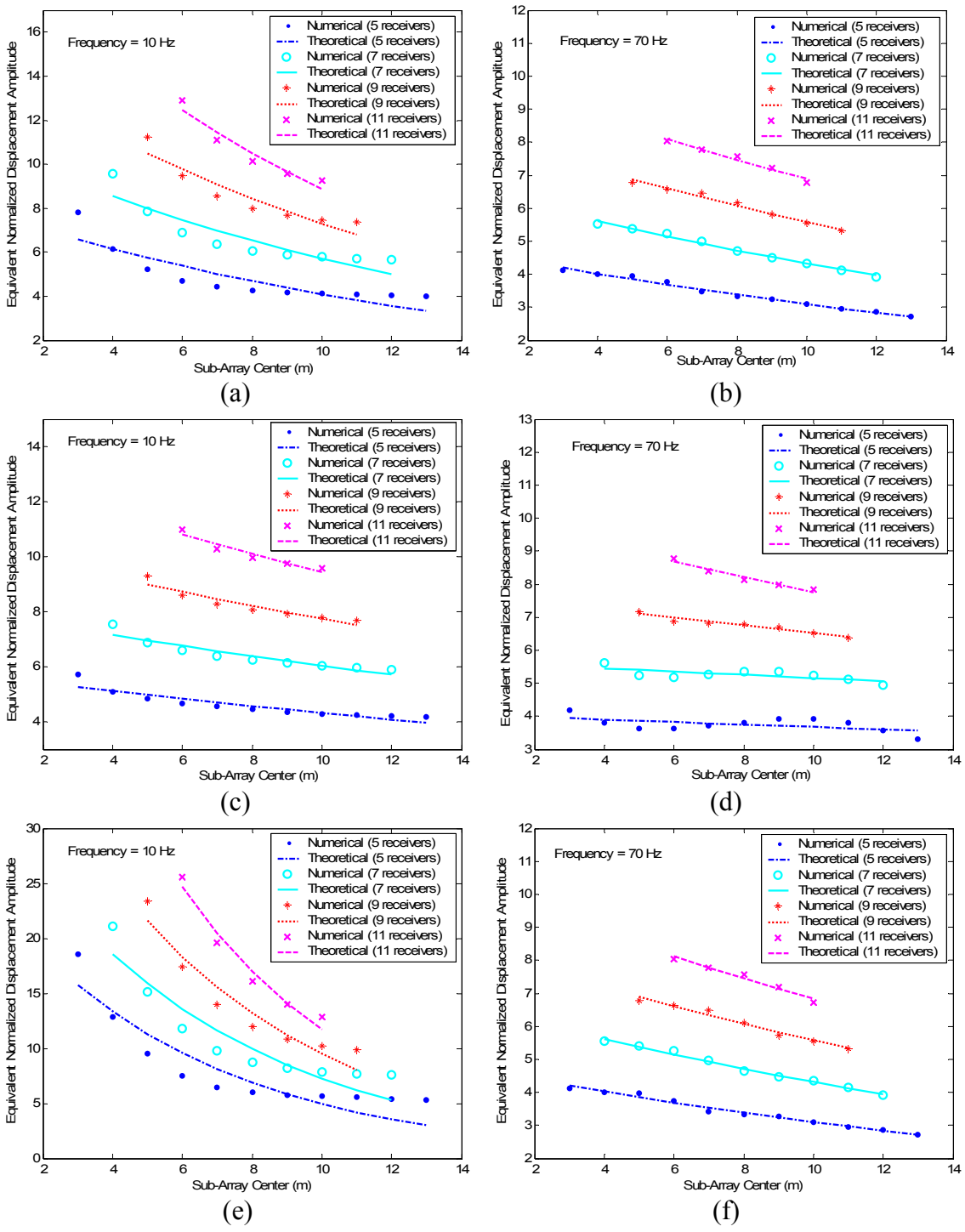

Figure 6.8 Effect of the number of receivers in each sub-array on equivalent normalized displacement amplitudes for normally dispersive (Case 2, (a) and (b)), inversely dispersive (Case 3, (c) and (d)), and another inversely dispersive (Case 4, (e) and (f)) soil profiles at frequencies of 10 and 70 Hz.

The effect of the number of receivers in each sub-array can be also investigated by comparing the attenuation curves with different numbers of the receivers, as shown in Figure 6.9. From the comparison in Figure 6.9(a), five and seven receivers in each sub-array provide attenuation curves that are closer to the reference curve than those corresponding to more receivers at frequencies over about 30 Hz. At frequencies between about 20 and 30 Hz, the attenuation curve corresponding to a larger number of receivers in each sub-array provides the attenuation curve closer to the reference one, confirming that the f-k estimation method with an increasing number of receivers in each sub-array reduces near-field effects. At frequencies below around 20 Hz, near-field effects become more significant with decreasing frequency regardless of the number of the sub-array receivers, leading to the incorrect attenuation estimates.

The comparison in Figure 6.9(b) illustrates the difficulty of measuring attenuation coefficients via surface wave tests for certain inversely dispersive site conditions. Case 3 represents a soil profile containing a softer layer between adjacent stiff layers. The inclusion of the softer layer between stiff layers leads to an increase in higher mode contributions to displacement amplitudes. Complicated wavefields due to the higher modes effectively prohibits estimating attenuation coefficients based on the displacement amplitudes. Moreover, significant near-field effects for this type of profile, as discussed in Chapter 4, influence the estimation procedures for geometric spreading as well as attenuation coefficients. It appears that an array with 15 total receivers is not sufficient to successfully estimate attenuation coefficients for this type of inversely dispersive soil profile.

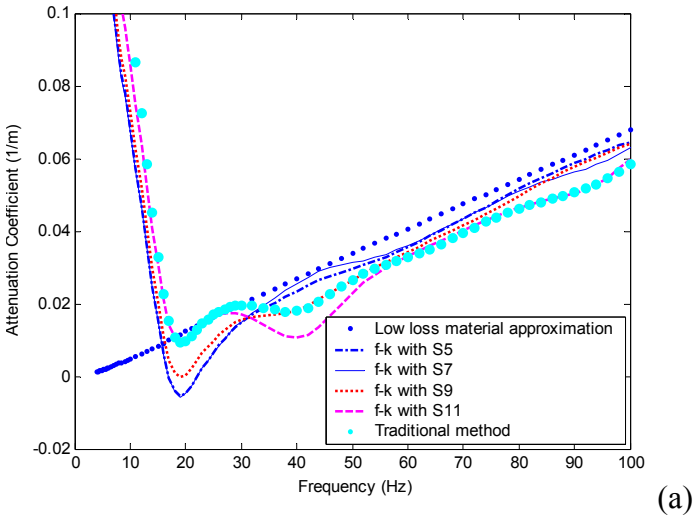

(a)

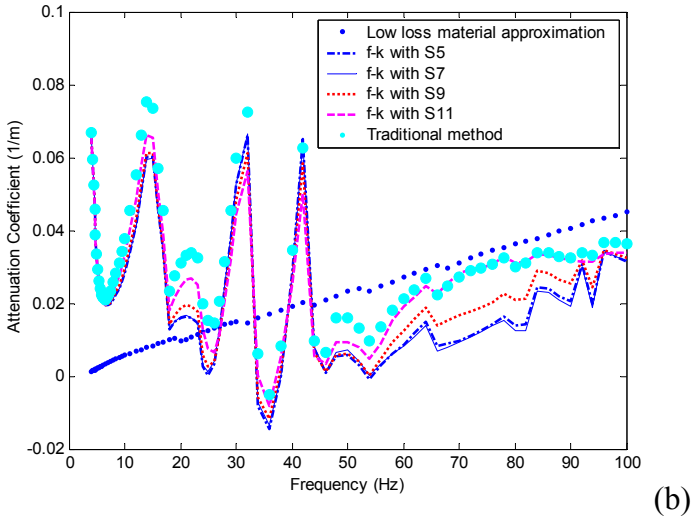

(b)

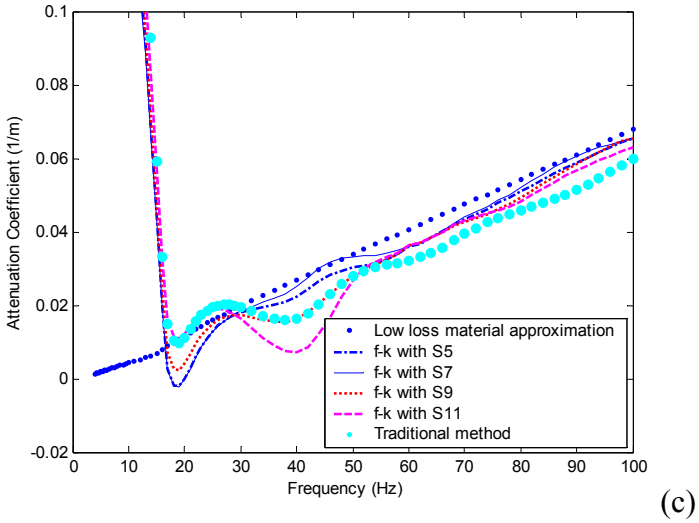

(c)

Figure 6.9 Effect of the number of receivers in each sub-array on attenuation estimates for (a) normally dispersive (Case 2), (b) inversely dispersive (Case 3), and (c) another inversely dispersive (Case 4) soil profiles

Attenuation curves with various numbers of receivers in each sub-array for another inversely dispersive soil condition, Case 4, are compared in Figure 6.9(c). Because this profile with a stiffer layer between adjacent soft layers is somewhat similar to a normally dispersive condition, attenuation curves similar to those presented in Figure 6.9(a) are obtained. At frequencies over about 30 Hz, five and seven receivers in each sub-array provide attenuation curves closer to the reference curve than more receivers in each sub-array. As noted above, the f-k estimation method with more receivers in each sub-array provides an attenuation curve with reduced near-field effects at frequencies ranging from about 20 to 30 Hz. At frequencies below 20 Hz, near-field effects become more significant with decreasing frequency regardless of the number of receivers in each sub-array much like Case 2.

Additional comparisons were made to investigate the difference in attenuation curves from the f-k estimation and traditional methods. For frequencies greater than 30 Hz, the f-k estimation method provides attenuation coefficients closer to the reference values than does the traditional method by Lai (1998) and Rix et al. (2000). However, the traditional method provides better attenuation curves at frequencies ranging from about 20 to 30 Hz than does the f-k estimation method. It is interesting to notice that the f-k estimation method with a large number (9 and 11) of receivers in each sub-array provides attenuation curves very similar to those from the traditional method over the entire frequency range. For arrays of 15 receivers, the f-k estimation method with nine receivers in each sub-array may be considered to provide more reliable attenuation curves over the entire frequency range.

6.4.5 Noise Inclusion Effects

Field measurements of particle displacement amplitudes induced by wave propagation are always exposed to ambient noise. Adequate noise control can improve the accuracy of the attenuation measurements as well as phase velocity measurements. As discussed, the several noise control techniques have been suggested to reduce or remove noise from the measured displacement data. However, it is impossible to completely remove all noise included in the measured data, and therefore, it is necessary to study which method works more effectively in the presence of noise.

The f-k method is known to provide more accurate dispersion estimates than other approaches. In conjunction with the use of a harmonic source, the f-k analysis is also more robust for attenuation estimation due to its ability to effectively control noise based on known frequency components of generated waves.

In this section, the traditional method and the f-k estimation method with nine receivers in each sub-array have been applied to the same synthetic displacement data and the attenuation curves estimated from them have been compared. To investigate the two methods in the presence of noise, Gaussian random noise with various magnitudes is generated and added to the synthetic displacement data from the numerical simulations with the arrays of 1SR1RR-15. Figure 6.10 shows the comparison of the attenuation curves obtained from the two methods with the added noise. Very similar observations to the noise-free condition can be made. For a limited number of total receivers (15) in the array, neither method is clearly superior over the entire frequency range under either noise-free or noisy conditions. The beneficial effects of increasing the total number of receivers are explored in the following section.

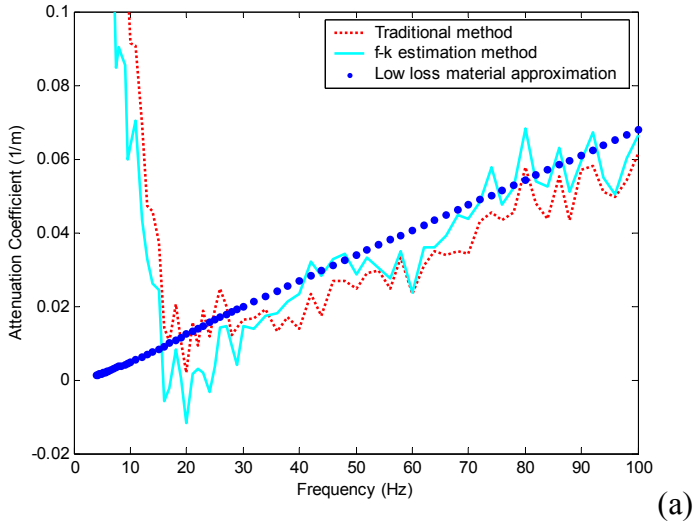

(a)

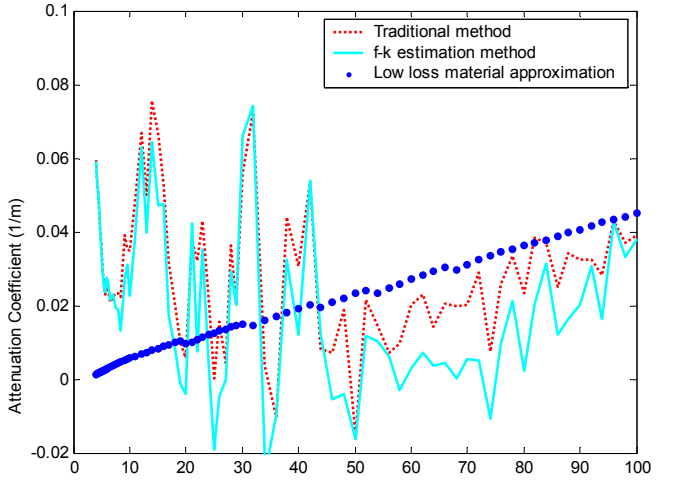

(b)

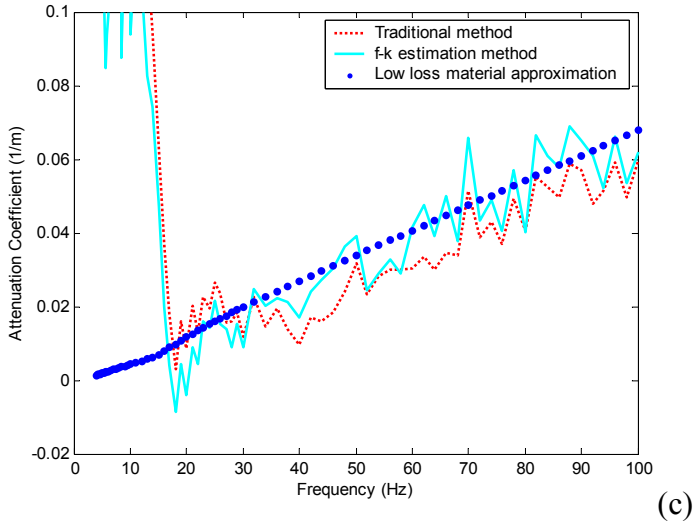

(c)

Figure 6.10 Noise inclusion effects on attenuation estimates from two methods for (a) normally dispersive (Case 2), (b) inversely dispersive (Case 3), and (c) another inversely dispersive (Case 4) soil profiles

6.4.6 Improvement of the Methods by Increasing the Total Number of Receivers in an Array

As discussed in the previous section, 15 receivers may not be sufficient to yield accurate attenuation values for some site conditions. Specifically, based on the simulation results for the three typical soil profiles, a surface wave test with a 15-receiver array does not allow the two methods to provide reliable attenuation estimates at frequencies less than about 20 Hz. For a fixed total number of receivers in an array, increasing the AC can be a means to reduce near-field effects. However, in practice, increasing the AC is limited due to the difficulty of generating sufficient energy at large distances. To have a shear damping ratio profile at greater depth, it appears to be necessary to reduce near-field effects by having displacement amplitude data at more offsets, leading to a reliable attenuation curve for lower frequencies. Increasing the total number of receivers in an array allows improving several characteristics of the array simultaneously without sacrificing others.

In this section, the improvement of the two methods by increasing the total number of receivers will be discussed based on the results of the numerical simulations. Numerical simulations with an array of 30 receivers (1SR1RR-30) are performed for the three typical soil profiles at 69 frequencies ranging 5 to 100 Hz. Attenuation curves obtained from the f-k estimation method and traditional method with data from the numerical simulations are compared with those associated with the 15-receiver array (1SR1RR-15).

Figure 6.11 illustrates the improvement of the methods by increasing the total number of receivers in an array. The 30-receiver array is superior in many aspects such as

the total number of receivers, AC, and characteristics of the array and sub-array to the 15-receiver array. Attenuation curves in the left figures are obtained from the traditional method with the array of 1SR1RR-15 and the f-k analysis with the sub-arrays of 1SR1RR-15-S9, while those in the right figures are obtained from the two methods with 1SR1RR-30 and 1SR1RR-30-S15, respectively. The first observation from Figure 6.11 is the improvement in the attenuation estimates from the f-k and traditional methods for all three soil profiles by increasing the total number of receivers in an array. Note the improvement in the attenuation estimates at low frequencies for all of the soil profiles and the significant improvement in the estimates at all frequencies for Case 3.

The second observation is the superiority of the f-k estimation method over the traditional method with 30 receivers in the array. From the comparison of the two methods with an array of 15 receivers for Case 2 and Case 4, it was observed that the f-k analysis yielded more accurate estimates than the traditional method at frequencies greater than about 30 Hz depending on the number of receivers in each sub-array. The same comparison with an array of 30 receivers for Case 2 and Case 4 indicates that the f-k estimation method is more accurate than the traditional method at all frequencies. For Case 3, the traditional method with 1SR1RR-30 provides better attenuation estimates than the f-k analysis with 1SR1RR-30-S15, but the errors in the attenuation estimates obtained by both methods are still significant. Given a sufficient receivers to measure vertical displacements at various offsets, the f-k estimation method is considered to estimate the attenuation coefficients more correctly than the traditional method.

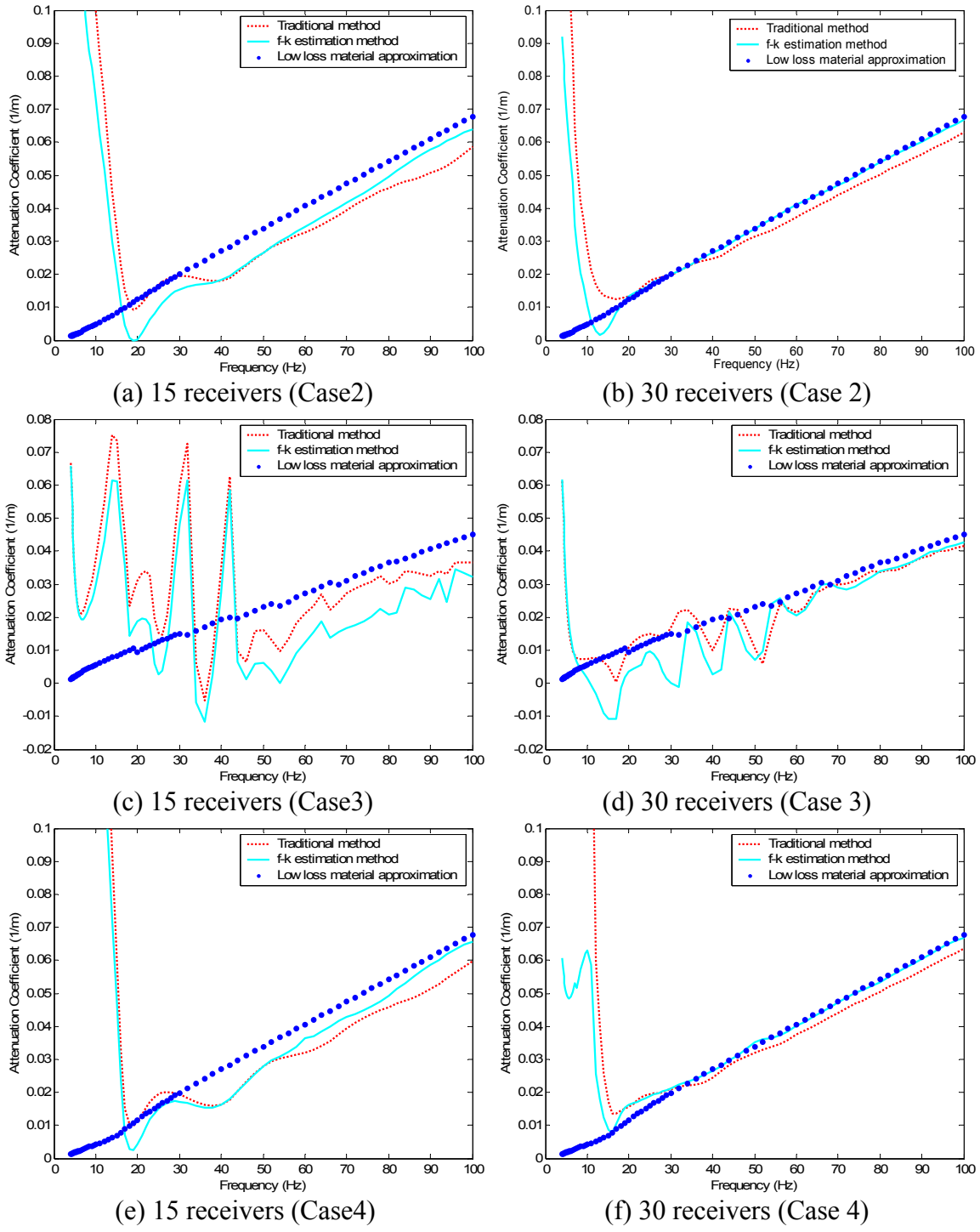

(a) 15 receivers (Case2)

(b) 30 receivers (Case 2)

(c) 15 receivers (Case3)

(d) 30 receivers (Case 3)

(e) 15 receivers (Case4)

(f) 30 receivers (Case 4)

Figure 6.11 Comparison of attenuation curves corresponding to two arrays consisting of 15 and 30 receivers that are obtained by two estimation methods

6.5 FIELD EXPERIMENTAL RESULTS

6.5.1 Surface Wave Field Tests with Various Arrays

In the previous section, numerical simulations were used to investigate factors affecting attenuation estimation procedures. As a result of the investigation, it was recommended that wavelengths greater than 0.8 times the array center should be omitted to avoid significant errors due to near-field effects for arrays of 15 receivers. In addition, it was recommended that the f-k estimation method using 15-receiver arrays be performed with 9 receivers in each sub-array. To investigate the applicability of these recommendations from numerical simulation results, a series of active surface wave tests was performed at the Oakridge Landfill site in Dorchester, South Carolina on June 4~5, 2004. The site was located at the latitude of N33.0808º and the longitude of W80.2208º. The tests were conducted using the test equipment and data processing techniques presented in Chapter 3.

To evaluate near-field effects on attenuation estimates, active surface tests with three different non-uniform arrays: (1) the standard array of 15 receivers spaced at 2.4, 3, 3.7, 4.6, 5.5, 6.7, 8.5, 10.4, 12.8, 15.2, 18.3, 21.3, 24.4, 29, and 33.5 m from the source, (2) the standard array shifted 3.0 m (10ft) further from the source, and (3) the standard array shifted 9.1 m (30ft) further from the source were conducted using a harmonic source. The measurements were made at a sampling frequency of 320 Hz. Five blocks of 2^{11} time domain records were measured for frequencies ranging 4 to 100 Hz and averaged to reduce the variance of the calculated spectra.

Dispersion data from the three arrays were used to obtain the shear wave velocity profiles shown in Figure 6.12. Each shear wave velocity profile was used as an input

profile to calculate the displacement Green's function solutions to account for geometric spreading. From the general trends of the shear wave velocity profiles, the site is considered to be normally dispersive similar to Case 2 or slightly inversely dispersive similar to Case 4.

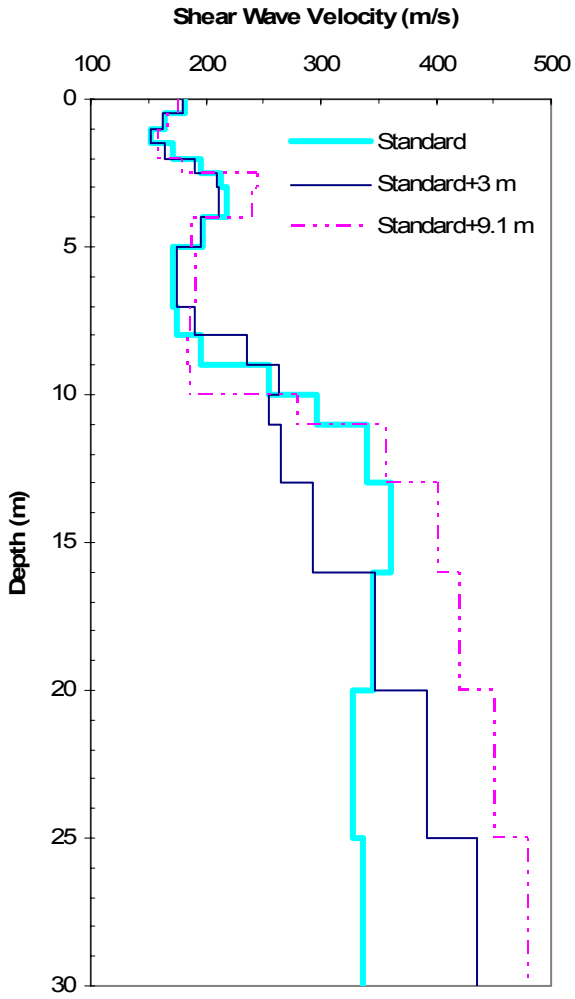

Figure 6.12 Shear wave velocity profiles at Oakridge landfill site

6.5.2 Measurements of Displacement Amplitudes

Attenuation coefficients are determined through a regression analysis using measured vertical displacement amplitudes at various locations from the source. Since field measurements in surface wave testing are always exposed to ambient noise, the measurements should be corrected to reduce the effect of ambient noise. In this study, the technique suggested by Lai (1998) and Rix et al. (2000) and defined in Equation 6.20 was used to remove ambient noise. After being corrected to reduce the effect of ambient noise, the experimental vertical displacement spectra are calculated from the field measurements in this study using:

$$\left|u_z(x,\omega)\right| = \frac{\sqrt{G_{ii}(x,\omega)}}{\omega^2 \cdot C(\omega)} \tag{6.24}$$

where G_{ii} = auto-power spectra of output at the *i*th receiver corrected for ambient noise and $C(\omega)$ = frequency-dependent calibration factor of the accelerometer.

Figure 6.13 shows the frequency-dependent normalized calibration factors of the 15 receivers used in the surface wave field measurements in this study. The normalization to the first receiver was conducted for the 15 receivers. Since only correct relative relationships between displacement amplitudes measured from receivers at various offsets from the source are required for the attenuation measurements, the receivers were calibrated using a reference receiver.

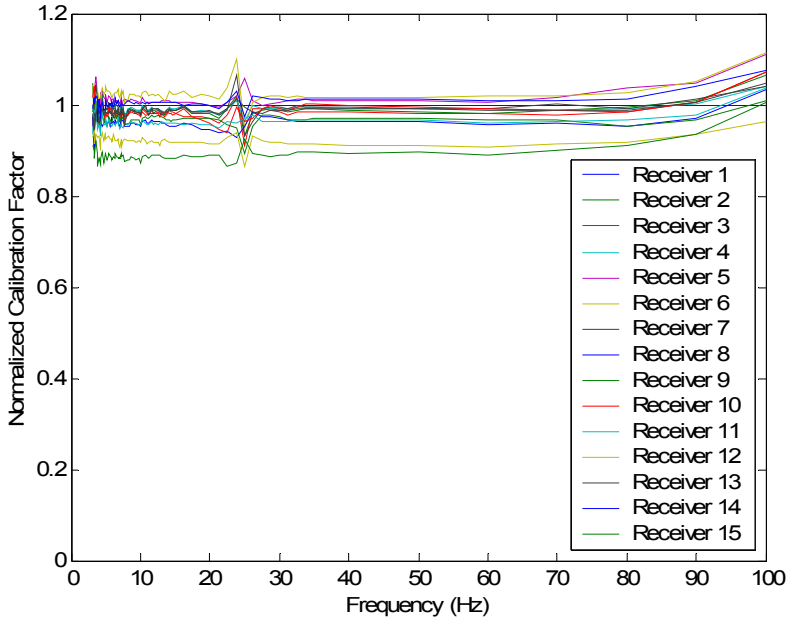

Figure 6.13 Frequency-dependent normalized calibration factors of 15 receivers used in surface wave field tests

6.5.3 Validation of the Recommendation for Near-Field Effects

Figure 6.14 shows attenuation curves obtained by the f-k estimation method with 9 receivers in each sub-array using experimental displacement data measured with the three arrays of 15 receivers. Since negative attenuation coefficients are not physically possible, only positive attenuation coefficients are plotted. To avoid significant errors due to near-field effects, it was recommended that wavelengths greater than 0.8 times the array center be omitted for Case 2 and Case 4 types of soil profiles. The figures in the left column show attenuation curves with the three arrays before applying the filtering criterion to reduce near-field effects and the figures in the right column show attenuation curves after applying the filtering criterion.

First, as expected, it was observed that significant errors due to near-field effects were reduced by shifting the array further from the source. This observation agrees well

with that already found from the study of near-field effects on dispersion estimates in Chapter 4. Comparing the figures in the left column with those in the right column validates the applicability of the suggested filtering criterion. It is apparent that the filtering criterion further reduced errors due to near-field effects.

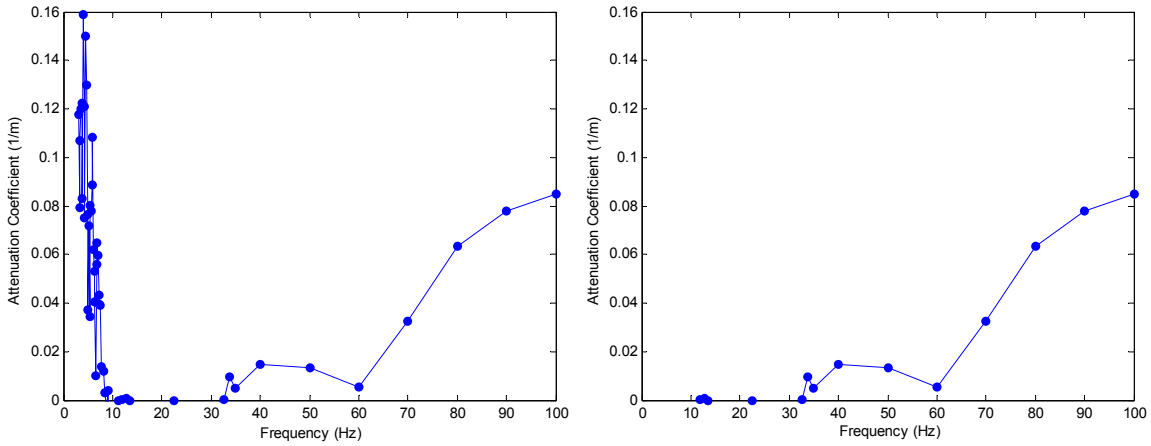

(a) Standard array (before filtering)

(b) Standard array (after filtering)

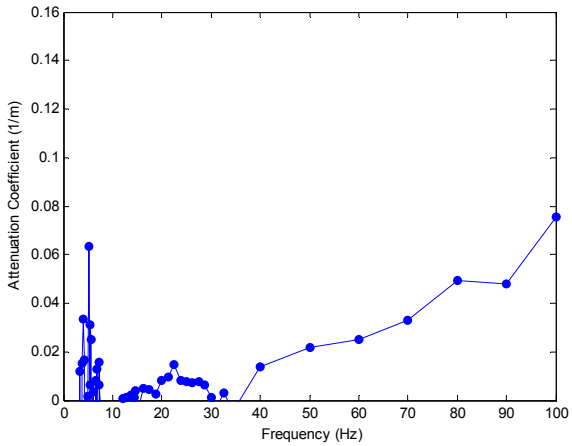

(c) Standard+3 m (before filtering)

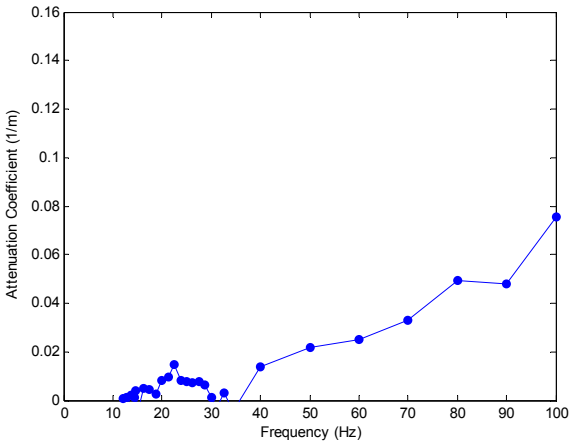

(d) Standard+3 m (after filtering)

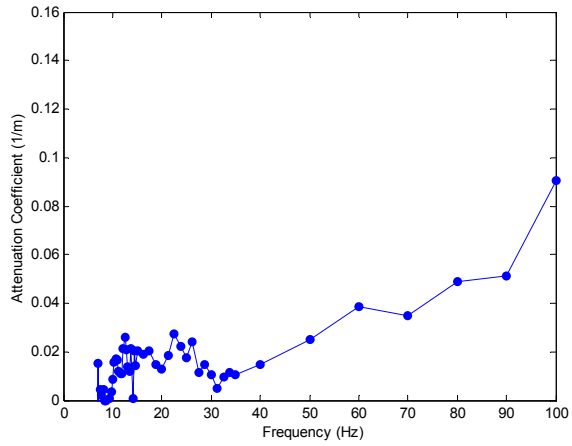

(e) Standard+9.1 m (before filtering)

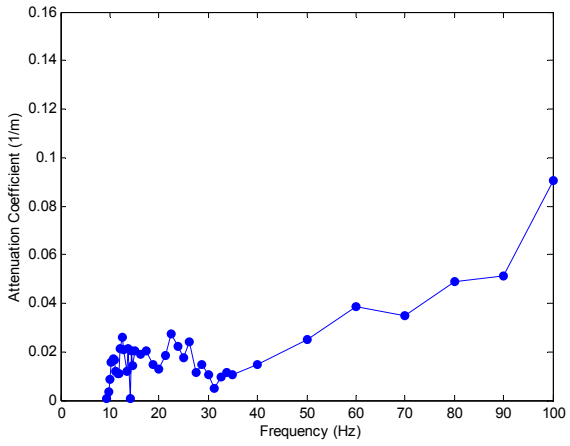

(f) Standard+9.1 m (after filtering)

Figure 6.14 Comparison of attenuation curves obtained from f-k estimation method with three arrays before filtering and after filtering

6.5.4 Validation of the Recommendation for Effect of the Number of Receivers in Each Sub-Array

From the numerical results, it was recommended that for arrays of 15 receivers, the f-k estimation method be performed with 9 receivers in each sub-array. In this section, the recommendation for the number of receivers in each sub-array is validated using experimental data from a field test. Figure 6.15 shows the effect of the number of receivers in each sub-array on attenuation estimates from the surface wave test with the standard non-uniform array with the shift of 9.1 m. As expected, attenuation curves estimated from the f-k estimation method vary according to the number of receivers in each sub-array. For frequencies ranging 10 to 30 Hz, the estimated attenuation curve from the f-k estimation method agree more closely with that of the traditional method with increasing number of the receivers in each sub-array. Recall the observation from the numerical results that the traditional method yields more accurate attenuation estimates at low frequencies for Case 2 and Case 4. An attenuation curve associated with 11-receiver sub-arrays in the f-k estimation method agrees most closely with an attenuation curve from the traditional method for frequencies ranging from about 10 to 30 Hz. Also, recall another observation that the f-k estimation method with 5-, 7-, or 9-receiver sub-array yields more accurate attenuation estimates at high frequencies for Case 2 and Case 4. Attenuation curves associated with the 5-, 7-, and 9-receiver sub-arrays are similar to one another but, different from that associated with the 11-receiver sub-array. Considering the balance in accuracy of attenuation estimates over the entire frequency range, the f-k estimation method with the 9-receiver sub-array may be considered to yield

the most reliable attenuation curve, indicating agreement with the recommendation from the numerical results.

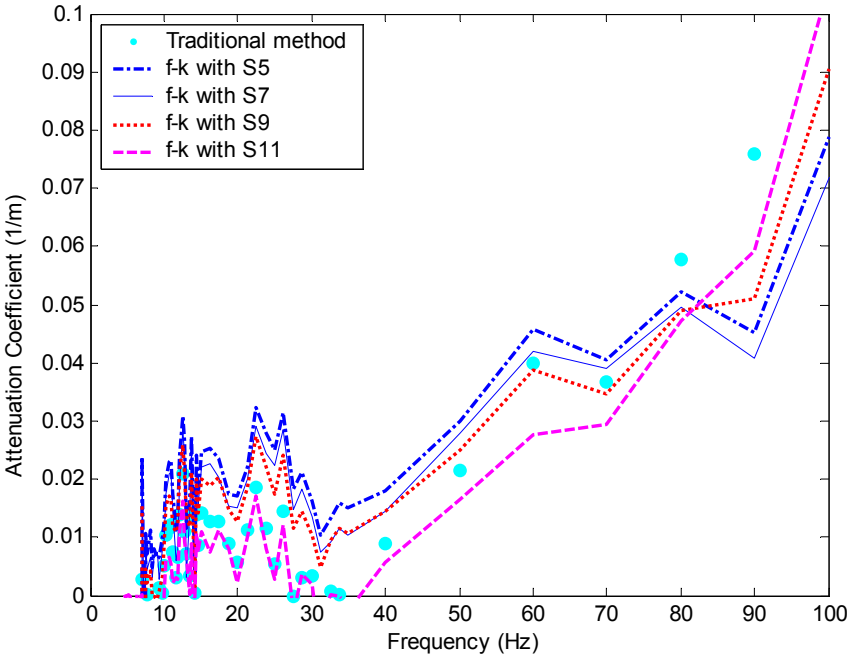

Figure 6.15 Effect of the number of receivers in each sub-array in f-k estimation method

6.6 SUMMARY AND CONCLUSIONS

An investigation of two attenuation estimation methods has been performed using synthetic displacement data from numerical simulations and experimental data from surface wave field tests with various arrays. From the investigation, the following conclusions can be made:

(1) The f-k estimation method provided different attenuation curves according to the number of receivers in each sub-array. For arrays of 15 receivers, the method with 9 receivers in each sub-array may be considered to provide more reliable attenuation curves.

(2) For the tests with arrays of 15 receivers, the f-k estimation method estimated the attenuation coefficient more accurately at high frequency than the traditional method, while the latter performed better at low frequency. However, the difference in the estimated attenuation coefficients from the two methods was not significant. For the tests with arrays of 30 receivers, the f-k estimation method estimated attenuation coefficient more correctly than the traditional method over the entire frequency range.

(3) The two methods suffered from significant near-field effects at low frequency. Near-field effects can be reduced by shifting an array further away from a source. To avoid significant errors due to near-field effects for arrays of 15 receivers, wavelengths greater than 0.8 times the array center for Case 2 and Case 4 should be omitted.

(4) For inversely dispersive soil profiles containing a softer layer between stiff layers represented by Case 3 in this study, surface wave tests with 15 receivers did not provide reliable attenuation curves. Surface wave tests with more receivers can be performed by combining two successive surface wave tests with two different array configurations (e.g., an array of 15 receivers placed between 1 and 15 m from a source and another array of 15 receivers placed between 16 and 30 m from a source) at the same site. The use of a harmonic source is necessary to keep the magnitude of generated signal constant.

(5) From the results of the numerical simulations with noise, no significant improvement in the accuracy of attenuation estimates by using the f-k estimation method instead of the traditional method has been observed.

CHAPTER 7

SUMMARY, CONCLUSIONS AND RECOMMENDATIONS

7.1 SUMMARY AND CONCLUSIONS

In this study, numerical simulations based on displacement Green's functions, laboratory simulations using a 2-D experimental model, and field tests have been used to evaluate near-field effects on array-based surface wave methods, combine active and passive measurements, and evaluate surface wave attenuation measurements. The main conclusions on each topic are presented as follows:

Near-field effects on array-based surface wave methods

(1) Near-field filtering criteria previously suggested for traditional spectral analysis of surface waves (SASW) methods do not apply to array-based surface wave methods.

(2) Near-field effects depend on the soil profile. They are more severe for inversely dispersive profiles compared to normally dispersive profiles.

(3) Normalized parameters are useful means to express near-field effects. Near-field criteria developed for a certain type of soil profile in terms of these dimensionless parameters may be used to estimate and reduce near-field effects in array-based, active tests with similar soil profiles.

(4) Array effects due to finite spatial sampling of the wavefield and near-field effects should not be confused.

(5) Underestimation of Rayleigh phase velocities is the primary symptom of near-field effects. Therefore, the lower-bound normalized Rayleigh wave velocity

corresponding to a given normalized array center (AC) may be used to estimate the maximum error due to near-field effects for a given wavelength (or frequency).

(6) Results of the study of near-field effects using numerical simulations, laboratory simulations, and field tests agree very well.

Combined active and passive measurements

(1) The differences between active and passive dispersion curves at overlapping frequencies result from systematic errors in active and passive tests. Major causes of the systematic errors are near-field effects in active tests and poor wavenumber resolution and sidelobe leakage in passive tests.

(2) Errors in passive dispersion data due to poor wavenumber resolution are always positive and depend on the angular separation between two adjacent waves and the ratio of their amplitudes.

(3) Sidelobe leakage may create a spurious peak in the wavenumber domain, leading to an incorrectly estimated wavenumber. Sidelobe leakage is more troublesome in passive tests. However, incorrectly measured wavenumbers due to sidelobe leakage are usually significantly different from true wavenumbers, and thus may be easily identified and removed.

(4) Examining the propagation direction and power at each frequency in addition to the phase velocity can be very useful to eliminate passive dispersion data with significant errors due to poor wavenumber resolution or sidelobe leakage, yielding a more accurate final dispersion curve.

(5) Insufficient wavenumber precision may create significant errors, particularly for low-frequency, high velocity data.

(6) The differences between active and passive dispersion curves at overlapping frequencies result mainly from near-field effects in active tests. It is recommended that a composite dispersion curve be obtained by using only passive dispersion data at overlapping frequencies.

Attenuation measurements by frequency-wavenumber analysis

(1) For tests with arrays of 15 receivers, the use of 9 receivers in each sub-array provides more accurate attenuation curves over the entire range of frequencies.

(2) For arrays of 15 receivers, neither the f-k estimation method nor the traditional method is clearly superior over the entire frequency range. For tests with arrays of 30 receivers, the f-k estimation method is more accurate than the traditional method over the entire frequency range.

(3) Significant errors due to near-field effects for arrays of 15 receivers can be reduced by removing wavelengths longer than 0.8 times the array center for Case 2 and Case 4 types of soil profiles.

(4) For inversely dispersive soil profiles containing a softer layer between stiff layers represented by Case 3 in this study, surface wave tests with 15 receivers did not provide accurate attenuation curves.

(5) From the results of the numerical simulations with Gaussian noise, no significant improvement in the accuracy of attenuation estimates is obtained by using the f-k estimation method instead of the traditional method.

7.2 RECOMMENDATIONS

Based on the results of this study, recommendations to improve the accuracy of measured dispersion and attenuation data include:

For more accurate active dispersion data:

(1) Use the normalized parameters to estimate errors in active dispersion data due to near-field effects depending on the type of soil profile.

(2) Increase the AC to reduce near-field effects. Increasing the number of total receivers serves to increase the AC and improve other array characteristics as well.

For more accurate passive dispersion data:

(1) To the extent possible, increase the aperture of the array and the number of receivers.

(2) Use a wavenumber precision of 0.001 (rad/m) to define the wavenumber spectrum and locate peak values.

(3) For a given test situation, passive dispersion data should be carefully checked using the manual refining process to eliminate questionable data due to sidelobe leakage, aliasing, insufficient passive energy, and inconsistent propagation directions.

For more accurate attenuation data:

(1) To the extent possible, increase the total number of receivers in an array. If the number of receivers is not sufficient, repeat tests with different array configurations several times at the same site to create a synthetic array. Then,

combine measurements with various array configurations. The use of a harmonic source is very helpful to generate a repeatable signal.

(2) Use the filtering criterion (remove wavelengths greater than 0.8 times the AC) to avoid significant errors due to near-field effects on attenuation estimates obtained from active tests with 15-receiver arrays in the Case 2 or Case 4 types of soil profiles.

REFERENCES

Abbiss, C. P. (1981). "Shear wave measurements of the elasticity of the ground." *Geotechnique*, 31(1), 91-104.

Abo-Zena, A. M. (1979). "Dispersion function computations for unlimited frequency values." *Geophys. J. R. Astr. Soc.*, 58, 91-105.

Achenbach, J.D. (1973). *Wave propagation in elastic solids*, North-Holland, 425p.

Aki, K. (1957). "Space and time spectra of stationary stochastic waves, with special reference to microtremors." *Bull. Earthquake Res. Inst.*, 35, 415-456.

Aki, K. (1965). "A note on the use of microseisms in determining the shallow structures of the earth's crust." *Geophysics*, 30, 665-666.

Aki, K., and Richards, P.G. (1980). *Quantitative Seismology - Theory and Methods*, Vol. 1 and 2, Freeman Company, San Francisco, 932p.

Al-Hunaidi, M. O. (1993). "Insights on SASW nondestructive testing method." *Can. J. Civil Eng.*, 20, 940-950.

Alleyen, D., and Cawley, P. (1991). "A two-dimensional Fourier transform method for the measurement of propagating multimode signals." *J. Acoustical Society America*, 89(3), 1159-1168.

Bendat, J. S. and Piersol, A. G. (2000). *Random data - analysis and measurement procedures*, John Wiley and Sons, Inc. 594p.

Bracewell, R. N. (2000). *The Fourier transform and its applications*, International Edition, McGraw-Hill, Inc., 616p.

Bolt, B. A. (1993). *Earthquakes*, W. H. Freeman, New York, 331p.

Buckingham, E. (1915). "Model experiments and the forms of empirical equations." *Transactions*, ASME, 37, 263-297.

Butterfield, R. (1999). "Dimensional analysis for geotechnical engineers." *Geotechnique*, 49, 357-366.

Capon, J. (1969). "High-resolution frequency-wavenumber spectrum analysis." *Proc. of the IEEE*, 57(8), 1408-1418.

Clough, G. W. and Chameau, J. L. (1980). "Measured effects of vibratory sheetpile driving." *J. Geotech. Engrg. Div.*, ASCE, 106(10), 1081-1099.

Constable, S., Parker, R., and Constable, G. (1987). "Occam's inversion: A practical algorithm for generating smooth models from electromagnetic sounding data." *Geophysics*, 52, 289-300.

Ewing, W. M., Jardetzky, W. S., and Press, F. (1957). *Elastic waves in layered media* McGraw-Hill, New York. 380p.

Ferry, J. D. (1980). *Viscoelastic properties of polymers*, John Wiley & Sons, Inc., New York, 641p.

Foti, S., (2000). Multistation methods for geotechnical characterization using surface waves, PhD dissertation, Politecnico di Torino, 229p.

Ganji, V., Gukunski, N., and Nazarian, S. (1998). "Automated inversion procedure for spectral analysis of surface waves." *J. Geotech. and Geoenv. Eng.*, ASCE, 124(8), 757-770.

Graff, K. F. (1975). *Wave motion in elastic solids*, Dover Publications, New York, 649p.

Gibbs, J. F., Boore, D. M., Joyner, W. B., and Fumal, T. E. (1994). "The attenuation of seismic shear waves in quaternary alluvium in Santa Clara Valley, California." *Bulletin of the Seismological Society of America*, 84(1), 76-90.

Gucunski, N. and Woods, R. D. (1992). "Numerical simulation of the SASW test." *Soil Dynamics and Earthquake Engineering*, 11, 213-227.

Haskell, N.A. (1953). "The dispersion of surface waves in multilayered media." *Bulletin of the Seismological Society of America*, 43, 17-34.

Hanson, R. T., Newhouse, M. W., Wentworth, C. M., Williams, C. F., Noce, T. E., and Bennett, M. J. (2002). "Santa Clara valley water district multi-aquifer monitoring-well site, Coyote Creek outdoor classroom, San Jose, California." *Open-File Report 02-369*, USGS.

Hardin, B. O. and Black, W. L. (1968). "Vibration modulus of normally consolidated clay." *J. of the Soil Mechanics and Foundations Division*, Proc. of the ASCE, 94(SM2), 353-369.

Hardin, B. O. and Drnevich, V. P. (1972). "Shear modulus and damping in soils: measurement and parameter effects." *J. of the Soil Mechanics and Foundations Division*, Proc. of the ASCE, 98(SM6), 603-624.

Hebeler, G. L. (2001). *Site characterization in Shelby County, Tennessee using advanced surface wave methods*, MS dissertation, Georgia Institute of Technology, 148p.

Heisey, J. S., Stokoe, II, K. H., Hudson, W. R., and Meyer, A. H. (1982). "Determination of in-situ shear wave velocities from spectral analysis of surface waves." *Research Report N. 256-2*, Center for Transportation Research, University of Texas of Austin, 277p.

Heisey, J. S., Stokoe, K. H., and Meyer, A. H. (1982). "Moduli of pavement system from spectral analysis of surface waves." *Transportation Research Record 852*, TRB, National Research Council, 22-31.

Hisada, Y. (1994). "An efficient method for computing Green's functions for a layered half-space with sources and receivers at close depths." *Bulletin of the Seismological Society of America*, 84(5), 1456-1472.

Hisada, Y. (1995). "An efficient method for computing Green's functions for a layered half-space with sources and receivers at close depths (Part 2)." *Bulletin of the Seismological Society of America*, 85(4), 1080-1093.

Horike, M. (1981). "Estimation of phase velocity of microtremors." *Zishin* (*J. of Seismological Society of Japan*), Ser 2, 34, 535-550.

Holzlohner, U. (1980). "Vibrations of the elastic half-space to vertical surface loads." *Earthquake Engrg. and Struct. Dyn.*, 8, 405-414.

Hossain, M. M. and Drnevich, V. P. (1989). "Numerical and optimization techniques applied to surface waves for backcalculation of layer moduli." *Nondestructive Testing of Pavements and Backcalculation of Moduli*, ASTM STP 1026, A.J. Bush and G.Y. Baladi, Eds., American Society for Testing and Materials, Philadelphia, 649-669.

Ishihara, K. (1996). *Soil behavior in earthquake geotechnics*, Oxford Science Publications, Oxford, UK, 350p.

Jones, R. B. (1958). "In-situ measurement of the dynamic properties of soil by vibration methods." *Geotechnique*, 8(1), 1-21.

Jones, R. B. (1962). "Surface wave technique for measuring the elastic properties and thickness of roads: theoretical development." *British J. of Applied Physics*, 13, 21-29.

Johnson, D. H., and Dudgeon, D. E. (1993). *Array signal processing: concepts and techniques*, PTR Prentice-Hall, Inc., Upper Saddle River, New Jersey, 533p.

Jongmans, D. (1990). "In-situ attenuation measurements in soils." *Engrg. Geology*, 29, 99-118.

Jongmans, D. and Demanet, D. (1993). "The importance of surface waves in vibration study and the use of Rayleigh waves for estimating the dynamic characteristics of soils." *Engrg. Geology*, 34, 105-113.

Kalinski, M. E., Stokoe II, K. H., Jirsa, J. O., and Roesset, J. M. (1994). "Nondestructive identification of internally damaged areas of concrete beam using the spectral analysis of surface wave method." *Transportation Research Record 1458*, 14-19.

Kausel, E. (1981). *An explicit solution for the Green functions for dynamic loads in layered media*, Research Report R81-13, MIT, Cambridge, 79p.

Kausel, E., and Roesset, J. M., (1981). "Stiffness matrices for layered soils." *Bulletin of the Seismological Society of America*, 71(6), 1743-1761.

Kennet, B. L. N. (1974). "Reflections, rays, and reverberations." *Bulletin of the Seismological Society of America*, 64, 1685-1696.

Kennet. B. L. N., and Kerry, N. J. (1979). "Seismic waves in a stratified half space." *Geophysical J. Royal Astronomical Society*, 57, 557-583.

Kopplemann, V. J. (1958). "Über die Bestimmung des dynamischen Elastizitatsmodulus und des dynamischen Schubmodulus im Frequenzbereich von 10^{-5} bis 10^{-1} Hz." *Rheology Acta*, No.1, 20-28.

Lacoss, R. T., Kelly, E. J., and Toksoz, M. N. (1969). "Estimation of seismic noise structure using arrays." *Geophysics*, 34, 21-38.

Lai, C. G. (1998). *Simultaneous inversion of Rayleigh phase velocity and attenuation for near-surface site characterization*, PhD dissertation, Georgia Institute of Technology, 370p.

Lai, C. G., Foti, S., and Rix, G. J. (2005). "Propagation of data uncertainty in surface wave inversion." *J. of Envir. and Engrg. Geophysics*, 10(2), 219-228.

Lai, C. G. and Rix, G. J. (2002). "Solution of the Rayleigh eigenproblem in viscoelastic media." *Bulletin of the Seismological Society of America*, 92(6), 2297-2309.

Lai, C. G., Rix, G. J., Foti, S., and Roma, V. (2002). "Simultaneous measurement and inversion of surface wave dispersion and attenuation curves." *Soil Dynamics and Earthquake Engineerin*g, 22, 923-930.

Lamb, H. (1889). "On waves in an elastic plate." *Proc. of the London Mathematical Society*, 21, 85p.

Lamb, H. (1904). "On the propagation of tremors over the surface of an elastic solid." *Philosophical Transactions of the Royal Society of London*, A203, 1-42.

Lamb, H. (1917). "On waves in an elastic plate." *Proc. Royal Society London*, A93, 114p.

Liu, H. P., Boore, D., Joynar, W. B., Oppenheimer, D. H., Warrick, R. E., Zheng, W., Hamilton, J. C., and Brown, L. T. (2000). "Comparison of phase velocity from array measurements of Rayleigh waves associated with microtremors and results

calculated from borehole shear-wave velocity profiles." *Bulletin of the Seismological Society of America*, 90, 666-678.

Liu, H. P., and Warrick, R. E., Westerlund, R. E., and Kayen, R. E. (1994). "In situ measurement of seismic shear-wave absorption in the San Francisco Holocene bay mud by the pulse-broadening method." *Bulletin of the Seismological Society of America*, 84(1), 62-75.

Long, L. T. (1964). *A study of short-period microseisms*, MS dissertation, New Mexico Institue of Mining and Technology, 54p.

Love, A. E. H. (1944). *A treatise on the mathematical theory of elasticity*, Dover Publications, New York.

Luco, J. E. and Apsel, R. J. (1983). "On the Green's function for a layered half-space." Part I, *Bulletin of the Seismological Society of America*, 73, 909-929.

Lysmer, J. and Drake, L. A. (1972). "A finite element method for seismology." *Seismology: Surface Waves and Earth Oscillations*, Methods in Computational Physics, 11, B. A. Bolt, Ed., Academic Press, New York, 181-216.

Macdonald, J. R. (1959). "Rayleigh-wave dissipation functions in low-loss media." *Geophys. J. of the Roy. Astronomical Soc.*, 2, 132-135.

Meng, J. (2003). *The influence of loading frequency on dynamic soil properties*, PhD dissertation, Georgia Institute of Technology, 174p.

Miller, G. F., and Pursey, H. (1955). "On the partition of energy between elastic waves in a semi-infinite solid." *Proc. of the Royal Society of London*, A233, 55-59.

Mindlin, R. D. (1960). "Waves and vibrations in isotropic, elastic plates." *Proc. of the 1st Symposium on Naval Structural Mechanics*, Pergamon Press, New York, 199-232.

Mok, Y. J., Sanchez-Salinero, I., Stokoe, K. H., and Roesset, J. M. (1988). "In situ damping measurements by crosshole seismic method." *Earthquake engineering and soil dynamics II-Recent advances in ground motion evaluation, Geotech. Spec. Publ. No. 20*, J. L. Von Thun, ed., ASCE, New York, 305-320.

Nazarian, S. (1984). *In situ determination of elastic moduli of soil deposits and pavement systems by Spectral-Analysis-of-Surface-Waves method*, PhD dissertation, Univ. of Texas of Austin.

Nazarian, S., and Stokoe, K. H. (1986). "Use of surface waves in pavement evaluation." *Transportation Research Record 1070*, TRB, National Research Council, 132-144.

Ohori, M., Nobata, A., and Wakamatsu, K. (2002). "A comparison of ESAC and FK methods of estimating phase velocity using arbitrarily shaped microtremor arrays." *Bulletin of the Seismological Society of America*, 92, 2323-2332.

Okada, H. (2003). *The microtremor survey method*, SEG, 135p.

Okada, H. and Matsushima, T. (1986). "Estimation of underground structures down to a depth more than several hundreds of meters using long-period microtremors." *Proceedings, 7th Japan Earthquake Engineering Symposium*, 211-216 (in Japanese).

Oliver, J., Press, F., and Ewing, M. (1954). "Two-dimensional model seismology." *Geophysics*, 19, 202-219.

Orozco, M. C. (2004). *Inversion method for Spectral Analysis of Surface Waves (SASW)*, PhD dissertation, Georgia Institute of Technology, 287p.

Parham, R. T. and Sutton, D. J. (1971). "The transition between 2- and 3-dimensional waves in seismic models." *Bulletin of the Seismological Society of America*, 61(4), 957-960.

Park, C. B., Miller, R. D., and Xia, J. (1999). "Multichannel analysis of surface waves." *Geophysics*, 64, 691-700.

Rayleigh, L. (1885). "On waves propagated along the plane surface of an elastic solid." *London Mathematical Society*, 17, 4-11.

Rayleigh, L. (1988). "On the free vibrations of an infinite plate of homogeneous isotropic matter." *Proc. of the London Mathematical Society*, 20, 225p.

Redpath, B. B. and Lee, R. C. (1986). "In-situ measurements of shear-wave attenuation at a strong motion recording site." *Earthquake Notes*, 57, 8.

Richart, F. E. Jr., Hall, J. R., and Woods, R. D. (1970). *Vibrations of soils and foundations*, Prentice-Hall, Inc., Englewood Cliffs, New Jersey, 414p.

Rix, G. J. (1988). *Experimental study of factors affecting the Spectral-Analysis-of-Surface Waves method*, PhD dissertation, Univ. of Texas of Austin, 315p.

Rix, G. J. (2000). "Site characterization using surface waves." Short course notes.

Rix, G. J. (2004). "Near-surface site characterization using surface waves." *Surface waves in geomechanics: direct and inverse modeling for soils and rocks*, Lai, C. G. and Wilmanski, K. (Eds.) (In press).

Rix, G. J. and Spang, A. W. (1995). "Measurement of in situ damping ratio using surface waves." *Proc. of the 1st Int. Conf. on Earthquake Geotech. Eng.*, Balkema, Rotterdam, 345-350.

Rix, G. J. and Lai, C. G. (1998). "Simultaneous inversion of surface wave velocity and attenuation." *Proc. of the 1st International Conf. on Site Characterization – ISC '98*, April 19-22, Atlanta, GA, 503-508.

Rix, G. J., Lai, C. G., and Spang, W. Jr. (2000). "In situ measurement of damping ratio using surface waves", *J. Geotech. and Geoenv. Eng.*, ASCE, 126(5), 472-480.

Rix, G. J., Lai, C. G., and Foti, S. (2001a). "Simultaneous measurement of surface wave dispersion and attenuation curves." *Geotechnical Testing Journal*, 24(4), 350-358.

Rix, G. J., Hebeler, G. L., and Orozco, M. C. (2002). "Near-surface V_s profiling in the New Madrid Seismic Zone using surface wave methods." *Seismological Research Letters*, 73(3), 380-392.

Rix, G. J., Lai, C. G., Orozco, M. C., Hebeler, G. L., and Roma, V. (2001b). "Recent advances in surface wave methods for geotechnical site characterization." *15th ICSMGE Conf.*

Roesset, J. M., Chang, W., Stokoe, K. H., and Aouad, M. (1990). "Modulus and thickness of the pavement surface layer from SASW tests." *Transportation Research Record 1260*, TRB, National Research Council, 53-63.

Roma, Vitantonio. (2001). *Soil properties and site characterization by means of Rayleigh waves*, PhD dissertation, Technical University of Turin (Politecnico), 246p.

Rose, J. L. (1999). *Ultrasonic waves in solid media*, Cambridge University Press.

Sanchez-Salinero, I. (1987). *Analytical investigation of seismic methods used for engineering applications*, PhD dissertation, Univ. of Texas of Austin. 401p.

Sanchez-Salinero, I., Roesset, J. M., Shao, K., Stokoe, K. H., and Rix, G. J. (1987). "Analytical evaluation of variables affecting surface wave testing of pavements." *Transportation Research Record 1136*, TRB, National Research Council, 86-95.

Santamatina, J. C. in collaboration with Kleigh, K. A., and Fam, M. A. (2001). *Soils and waves-particulate materials behavior, characterization and process monitoring*, John Wiley and Sons, New York, 488p.

Santamarina, J. C., and Fratta, D. (1996). *Introduction to discrete signals and inverse problems in civil engineering*, ASCE Press, Virginia, 327p.

Seligson, C. D. (1970). Comment on "High-resolution frequency-wavenumber spectrum analysis." *Proc. IEEE*, 58, 947-949.

Schwab, F., and Knopoff, L. (1970). "Surface-wave dispersion computations." *Bulletin of the Seismological Society of America*, 60, 321-344.

Schwab, F., and Knopoff, L. (1971). "Surface waves on multilayered anelastic media." *Bulletin of the Seismological Society of America*, 61, 893-912.

Schwab, F., and Knopoff, L. (1972). "Fast surface wave and free mode computations." *Seismology: Surface Waves and Earth Oscillations*, Methods in Computational Physics, 11, B. A. Bolt, Ed., Academic Press, New York, 87-180.

Spang, A. W., Jr. (1995). *In situ measurements of damping ratio using surface waves*, PhD dissertation, Georgia Institute of Technology, 347p.

Stewart, W. P. (1992). *In situ measurement of dynamic soil properties with emphasis on damping*, PhD dissertation, Univ. of British Columbia, Vancouver.

Stokoe, K. H., and Santamarina, J. C. (2000). "Seismic-wave-based testing in geotechnical engineering." *GeoEng 2000*, November, Australia.

Stokoe, K. H., Wright, S. G., Bay, J. A., and Roesset, J. M., (1994). "Characterization of geotechnical sites by SASW method." *XIII ICSMFE*, New Delhi, India, Oxford & IBH Publishing, 15-25.

Takeuchi, H., and Saito, M. (1972). "Seismic surface waves." *Seismology: Surface Waves and Earth Oscillations*, Methods in Computational Physics, 11, B.A. Bolt, Ed., Academic Press, New York, 217-296.

Tarantola, A. (1987). *Inverse problem theory*, Elsevier, Amsterdam.

Thomson, W.T. (1950). "Transmission of elastic waves through a stratified solid." *J. of Applied Physics*, 21, 89-93.

Tokimatsu, K., (1995). "Geotechnical site characterization using surface waves." *Proc. of the First Int. Conf. on Earthquake Geotech. Eng. IS-Tokyo '95*, Tokyo, November 14-16, Balkema, Rotterdam, 1333-1368.

Tokimatsu, K., Shinzawa, K., and Kuwayama, S. (1992a). "Use of short-period microtremors for V_S profiling." *J. Geotech. Eng.*, ASCE, 118(10), 1544-1558.

Tokimatsu, K., Tamura, S., and Kojima H. (1992b). "Effects of multiple modes on Rayleigh wave dispersion." *J. Geotech. Eng.*, ASCE, 118(10), 1529-1543.

Viktorov, I. A. (1957). *Rayleigh and Lamb waves: physical theory and applications*, Plenum Press, New York, 154p.

Vrettos, C. (1991). "Time-harmonic Boussinesq problem for a continuously non-homogeneous soil." *Earthquake Engrg. and Struct. Dyn.*, 20, 961-977.

Vucetic, M., and Dobry, R. (1991). "Effect of soil plasticity on cyclic response." *J. Geotech. Eng.*, ASCE, 117(1), 89-107.

White, J. E. (1983). *Underground sound*, Elsevier, New York, 253p.

Winkler, K. and Nur, A. (1979). “Pore fluids and seismic attenuation in rocks.” *Geophys. Res. Lett.*, 6, 1-4.

Woods, R. D. (1968). “Screening of surface waves in soils.” *J. Soil Mechanics and Foundations Division*, ASCE, 94(4), 951-979.

Woods, R. D. and Jedele, L. P. (1985). “Energy-attenuation relationships from construction vibrations.” *Vibration problems in geotechnical engineering*, G. Gazetas, and E. T. Selig, eds., ASCE, New York, 229-246.

Yoon, S., Rix, G. J. (2004). “Combined active-passive surface wave measurements for near-surface site characterization.” *Proc. Symposium on the Application of Geophysics to Engineering and Environmental Problems*, Denver, CO, 1156-1164.

Yuan, D. and Nazarian, S. (1993). “Automated surface wave method: inversion technique.” *J. Geotech. Eng.*, ASCE, 119(7), 1112-1126.

Zerwer, A. (1999). *Near surface fracture detection in structural elements: Investigation using Rayleigh waves*, PhD dissertation, Univ. of Waterloo, 348p.

Zerwer, A., Polak, M. A., and Santamarina, J. C. (2000). “Wave propagation in thin Plexiglas plates: implication for Rayleigh waves.” *NDT & E Int.*, 33, 33-41.

Zywicki, D. J. (1999). *Advanced signal processing methods applied to engineering analysis of seismic surface waves*, PhD dissertation, Georgia Institute of Technology, 228p.

Zywicki, D. J., and Rix, G. J. (1999). “Frequency-wavenumber analysis of passive surface waves.” *Proc. Symposium on the Application of Geophysics to Engineering and Environmental Problems*, Oakland, CA, 75-84.

VITA

Sungsoo Yoon was born in Seoul, Korea on June 7, 1972, the son of Jiehyun Yoon and Byungsook Bae. He entered the Civil Engineering department of Korea University in Seoul, Korea in March 1991 and received his Bachelor degree in February 1997. Between 1993 and 1994, he served his military duty in the Korean army for one and a half years. He was awarded his Master degree in Civil and Environmental Engineering from Korea University in February 1999. In August 2000, he entered the Georgia Institute of Technology in Atlanta, Georgia as a Ph.D. student in Civil and Environmental Engineering. He received his Ph.D. degree in August, 2005. During years at the Georgia Institute of Technology, he worked as a graduate research assistant.

In 1999, he married Soojin Kim. They have a daughter named Heewon Yoon who was born in Atlanta on November 20, 2004.